BIOPROCESS OPTIMIZATION FOR RECOMBINANT PROTEIN PRODUCTION FROM MAMMALIAN CELLS

by

CHETAN T. GOUDAR
B.Tech., Regional Engineering College Trichy, 1995
M.S., University of Oklahoma, 1998

A THESIS SUBMITTED IN PARTIAL FULFILMENT OF
THE REQUIREMENTS FOR THE DEGREE OF

DOCTOR OF PHILOSOPHY

in

THE FACULTY OF GRADUATE STUDIES

(Chemical and Biological Engineering)

THE UNIVERSITY OF BRITISH COLUMBIA

August 2006

Abstract

Mammalian cells are being increasingly used to manufacture complex therapeutic proteins given their ability to properly fold and glycosylate these proteins. However, protein yields are low and process enhancements are necessary to ensure economically viable processes. Methods for yield improvement, bioprocess development acceleration and rapid quantification and monitoring of cell metabolism were investigated in this study. Recognizing the adverse effect of high pCO_2 on cell growth, metabolism and protein productivity, a novel pCO_2 reduction strategy based on $NaHCO_3$ elimination was investigated that decreased pCO_2 by 65 – 72%. This was accompanied by 68 – 123% increases in growth rate and 58 – 92% increases in productivity. To enable rapid and robust data analysis from early stage process development experiments, logistic equations were used to effectively describe the kinetics of batch and fed-batch cultures. Substantially improved specific rate estimates were obtained from the logistic equations when compared with current modeling approaches. Metabolic flux analysis was used to obtain quantitative information on cellular metabolism and the validity of using the balancing method for flux estimation was verified with data from isotope tracer studies. Error propagation from prime variables into specific rates and metabolic fluxes was quantified using Monte-Carlo analysis which indicated 8 – 22% specific rate error for 5 – 15% error in prime variable measurement. While errors in greater metabolic fluxes were similar to those in the corresponding specific rates, errors in the lesser metabolic fluxes were extremely sensitive to greater specific rate errors such that lesser fluxes were no longer representative of cellular metabolism. The specific rate to metabolic flux error relationship could be accurately described by the corresponding normalized sensitivity coefficient. A framework for quasi-real-time estimation of metabolic fluxes was proposed and implemented to serve as a bioprocess monitoring and early warning system. Methods for real-time oxygen uptake and carbon dioxide production rate estimation were developed that enabled rapid flux estimation. This framework was used to characterize cellular response to pH and dissolved oxygen changes in a process development experiment and can readily be applied to a manufacturing bioreactor. Overall, the approaches for protein productivity

enhancement and rapid metabolism monitoring developed in this study are general with potential for widespread application to laboratory and manufacturing-scale perfusion and fed-batch mammalian cell cultivations.

Contents

List of Tables

List of Figures

Acknowledgements

I express my deepest gratitude and appreciation to Konstantin, whose vision, support and encouragement made this possible. He has been a great role model and has touched my life in many ways for which I will forever be grateful. I sincerely thank Jamie for his outstanding guidance and for believing this was possible. I am especially appreciative of his insistence on rigor and hope to write as well as him some day. My committee members, Douglas Kilburn and Charles Haynes provided valuable feedback that has greatly enhanced the presentation in Chapter 7 and Appendix I. I thank them for very productive progress update meetings. I am grateful to Bruce Bowen and Ross MacGillivray for their insightful feedback during the final exam.

Richard Biener helped program early versions of the QRT-MFA software. Our cell metabolism and computer programming discussions have always been very productive and his advice has been invaluable on multiple occasions. NMR flux analysis was performed in collaboration with METabolic EXplorer, especially Albert de Graaf, whose expertise enabled effective application of this technique to mammalian cells in perfusion culture

I have benefitted immensely from interactions with my Bayer colleagues. Chun Zhang provided the flexible and open environment that was so vital to bring this to fruition. I thank Jim Michaels for his friendship, support and consistent demonstration that operation outside the realm of the second law of themodynamics was possible. Cary Matanguihan was involved with early work on pCO_2 reduction and has taught many of us the nuances of operating a manufacturng-scale bioreactor in a process development laboratory. Rüdiger Heidemann introduced me to mammalian cell culture and more importantly to the microbreweries in Berkeley. His friendship over all these years is greatly appreciated. Demonstrating pCO_2 reduction at manufacturing-scale would not have been possible without assistance from Edward Long and Chris Cruz. I thank them for their outstanding commitment and for putting up with me. Mehdi Saghafi, Doan Tran, Meile Liu, Ricardo Ibarra and David Hou are continuing on that path and we collectively hope to develop a process that will result in an improved product for our patients.

Keith Strevett, Joseph Suflita, Michael McInerney and Mark Nanny have played a pivotal role in my development as a researcher. I have benefitted from my interactions with Gregory Stephanopoulos and from the Metabolic Engineering research from his laboratory. I thank him for his insight and kindness. Donald Knuth's TEX and Leslie Lamport's LATEX helped make this dissertation Microsoft Office-free.

What I am today is in large part due to my parents effort and sacrifice. I thank Harpreet for her unconditional love and unwavering support. While I tried hard to ensure $\Delta G < 0$ for thesis completion, I had much reduced impact on the rate of progress. The kinetics improved substantially with Niah's arrival and I look forward to introducing her to Metabolic Engineering in the coming months. Timely completion of this dissertation would not have been possible without help from Harpreet's parents over the last six months.

Finally, I thank my employer, Bayer HealthCare, for letting me pursue my Ph.D. while working full-time and for the opportunity to make products that dramatically improve patient quality of life.

Dedication

To action alone hast thou a right and never at all to its fruits. Let not the fruits of action be thy motive. Neither let there be in thee any attachment to inaction.

Bhagavad Gita

To
my Teachers, Parents, Harpreet and Niah

Part I

Introduction and Literature Review

Chapter 1

Introduction

Protein biopharmaceuticals that are manufactured through modern molecular biology techniques have revolutionized the way many life threatening illnesses are treated. These products comprise a global annual market of $30 billion and this number is expected to increase exponentially in the future with about 500 products currently undergoing clinical evaluation [1] and thousands more being actively researched. The first biopharmaceutical to be approved was recombinant insulin in 1982 [2] and since then a total of 84 biopharmaceuticals were approved in the United States and the European Union by the year 2000 [3]. The most rapid increase was during the 2000 – 2003 period with a total of 64 products receiving regulatory approval [1].

Mammalian cells have played an increasingly important role in the development of new biopharmaceuticals over the past decade. For instance, 64% (21 out of 33) of the biopharmaceuticals that were approved between January 1996 and November 2000 were manufactured by mammalian cells [4]. This number is likely to increase in the future as mammalian cells have the ability to perform complex post-translational modifications which enable them to produce proteins that have the desired biological activity for therapeutic and diagnostic applications. Current products of mammalian cell culture include therapeutics in the form of recombinant proteins or antibodies, vaccines, tissue-replacement products, and diagnostic products such as monoclonal antibodies.

Despite the advantages of post-translational modifications, mammalian cell culture has several challenges. Mammalian cell growth rates are typically an order of magnitude lower than bacterial cells and protein productivity is also low, typically less than 0.1% of the total protein concentration in the cell [5]. This places an enormous burden on downstream protein concentration and purification steps. In addition to lower growth and productivity, mammalian cells have complex nutritional requirements and are sensitive to shear during

bioreactor cultivation. Significant progress has been made over the last two decades to address these limitations resulting in suspension cultivation using serum-free media.

It is the general perception that the low hanging fruits in mammalian cell culture have been gathered. These include products with low dosage and high market value such as Erythropoietin (EPO) which generated worldwide annual revenues of $7 billion in 2002 [6]. Products of the future are likely to have dosage requirements that are orders of magnitude higher than those for EPO with substantially smaller revenues. Thus protein productivity increase along with reduction in the cost of goods will be an underlying theme for manufacturing the next generation of biopharmaceuticals. Robust cell line engineering coupled with bioprocess improvements can provide economically feasible manufacturing options.

The first section of this study is introductory and presents an overview of mammalian cell metabolism (Chapter 2) and the methods used to determine intracellular fluxes from bioreactor experiments (Chapter 3). While metabolic flux analysis essentially involves the solution of mass balance expressions, a formal method of flux estimation was proposed only 15 years ago while methods of flux estimation from labeled substrates, albeit mature, are still in late stages of development. The important features of both these flux estimation methods have been reviewed with an emphasis on error identification in input data and robust flux estimation. Each of the following chapters, structured like an article, includes an introductory review.

The second section presents a detailed description of the dynamics of dissolved carbon dioxide in mammalian cell perfusion bioreactors. High values of dissolved carbon dioxide ($pCO_2 > 200$ mm Hg) are commonly encountered in high-density perfusion bioreactors and have been shown to adversely affect growth, metabolism, productivity and protein glycosylation. A robust method of reducing bioreactor pCO_2 by ~70% (final values close to 70 mm Hg) has been proposed by eliminating $NaHCO_3$ from the medium and for bioreactor pH control (Chapter 4). This pCO_2 reduction was achieved with no changes to bioreactor operation and only a marginal increase in raw material cost while resulting in substantially increased specific protein productivity. Detailed oxygen and carbon dioxide mass balances were developed for a perfusion system that enabled the determination of oxygen uptake and carbon dioxide evolution rates (OUR and CER, respectively) from which the respiratory quotient (RQ) was estimated (Chapter 5). While mammalian cell RQ's are typically close to unity, OUR and CER are affected by bioreactor operating conditions and are also necessary for metabolic flux estimation.

Robust methods of batch and fed-batch culture specific rate estimation along with a detailed analysis of error propagation during specific rate and metabolic flux estimation in perfusion systems are presented in Section 3. Analytically differentiable logistic equa-

tions were used to describe time profiles of cell density, nutrient, metabolite, and product concentrations in batch and fed-batch cultures resulting in robust specific rate estimates which were in most instances statistically superior to current specific rate estimation methods (Chapter 6). Error propagation from experimental measurements into specific rates and subsequently into metabolic fluxes was quantified using Monte-Carlo analysis (Chapter 7). This analysis helped quantify the uncertainty inherent in metabolic flux estimates due to experimental measurement errors. This information was critical to meaningfully compare flux data across different experimental conditions and for decoupling the effect on flux estimates of measurement error and cell physiology.

Application of metabolic flux analysis to mammalian cell cultivation is presented in Section 4. The use of ^{13}C labeled glucose for detailed flux estimation in a CHO perfusion culture is described in Chapter 8. The biomass hydrolysates from these experiments were analyzed by 2D-NMR which allowed flux estimation in reversible and cyclical reactions, something not possible using the metabolite balancing approach. Besides providing a comprehensive description of CHO cell metabolism, the extended flux data set allowed validation of flux data obtained using the metabolite balancing approach. A framework for quasi-real-time metabolic flux estimation is presented in Chapter 9 that provides rapid quantification of cell physiology and metabolism in both process development and commercial bioreactors.

Bibliography

[1] Walsh, G. Biopharmaceutical benchmarks - 2003. *Nat. Biotechnol.*, **2003**, *21*(8), 865–870.

[2] Gosse, M.; Manocchia, M. The first biopharmaceuticals approved in the United States: 1980-1994. *Drug Inf. J.*, **1996**, *30*, 991–1001.

[3] Walsh, G. Biopharmaceutical benchmarks. *Nat. Biotechnol.*, **2000**, *18*, 831–833.

[4] Chu, L.; Robinson, D. Industrial choices for protein production by large-scale cell culture. *Curr. Opin. Biotechnol.*, **2001**, *12*, 180–187.

[5] Nyberg, G. B.; Balcarcel, R. R.; Follstad, B. D.; Stephanopoulos, G.; Wang, D. I. Metabolism of peptide amino acids by Chinese hamster ovary cells grown in a complex medium. *Bioctechnol Bioeng*, **1999**, *62*(3), 324–35.

[6] Stix, G. Making Proteins without DNA. *Sci.Am.*, **2004**, *290*, 38–40.

Chapter 2

Overview of Cellular Metabolism

2.1 Introduction

Before analyzing the fluxes through a metabolic network, the biochemical reactions that make up the metabolic pathway of interest must be identified. A recombinant mammalian cell converts nutrients (primarily glucose and glutamine) into energy, biomass and waste products along with production of the therapeutic protein of interest. Energy in a cell is present primarily in the form of adenosine tri-phosphate (ATP), while reducing power is provided by the reduced forms of nicotinamide adenine dinucleotide (NADH) and nicotinamide adenine dinucleotide phosphate (NADPH). Biosynthetic reactions use NADPH while NADH is used primarily for the production of ATP. Mammalian cell biochemistry has been the subject of extensive research and detailed information on cellular metabolism can be found in standard biochemistry textbooks [1]. Only a brief summary of the primary pathways of mammalian cells metabolism will be presented here along with the effect of environmental conditions on cell growth, metabolism and protein productivity.

2.2 Glycolysis

2.2.1 Overview of Glycolysis

Glycolysis involves the degradation of a molecule of glucose through a series of enzyme-catalyzed reaction resulting in two molecules of pyruvate

$$\text{Glucose} + 2\text{NAD}^+ + 2\text{ADP} + 2\text{P}_\text{i} \longrightarrow 2\text{Pyruvate} + 2\text{NADH} + 2\text{ATP} + 2\text{H}^+ + 2\text{H}_2\text{O} \tag{2.1}$$

This conversion of glucose to pyruvate occurs in ten steps (Figure 2.1), the first five of which constitute the preparatory phase where 2 molecules of ATP are used to convert 1 molecule of glucose into 2 molecules of glyceraldehyde 3-phosphate. In the payoff phase that comprises the latter five reactions, 2 molecules of glyceraldehyde 3-phosphate are converted to 2 molecules of pyruvate resulting in the formation of 4 molecules of ATP and 2 molecules of NADH. Since 2 molecules of ATP are used in the preparatory phase, the net ATP yield in glycolysis per molecule of glucose is 2.

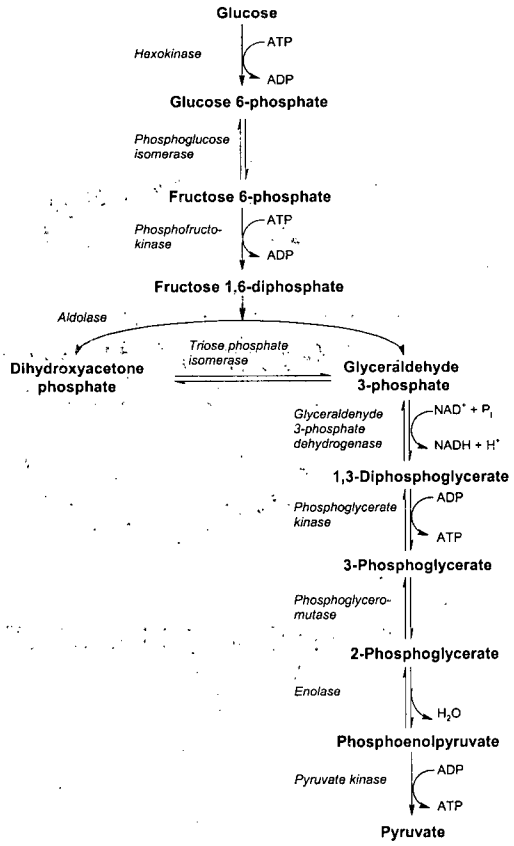

Figure 2.1: Conversion of glucose to pyruvate via the glycolytic pathway in mammalian cells.

2.2.2 Energetics of Glycolysis

The overall glycolytic reaction presented as Eq.(2.1) can be split into the exergonic and endergonic components which are the conversion of glucose to pyruvate and the formation

of ATP from ADP and P_i, respectively

$$\text{Glucose} + 2\text{NAD}^+ \longrightarrow 2\text{Pyruvate} + 2\text{NADH} + 2\text{H}^+; \quad \Delta G_1^0 = -146 \text{ kJ/mol} \tag{2.2}$$

$$2\text{ADP} + 2\text{P}_i \longrightarrow 2\text{ATP} + 2\text{H}_2\text{O}; \quad \Delta G_2^0 = 61 \text{ kJ/mol} \tag{2.3}$$

It follows from Eqs.(2.2) and (2.3) that the overall standard free-energy change for glycolysis is −85 kJ/mol. This large decrease in net free energy makes glycolysis in the cell an essentially irreversible process and the energy released in glycolysis is recovered as ATP with efficiencies greater than 60%. It is also important to note that only a small portion of the total available energy from glucose is released during glycolysis. The total standard free-energy change for complete oxidation of glucose to CO_2 and H_2O is −2,480 kJ/mol while that for the degradation of glucose to pyruvate is only −146 kJ/mol. Thus only about 5% of the energy available from glucose is released during glycolysis. Pyruvate retains most of the chemical potential energy from glucose which is subsequently extracted by the oxidative reactions of the citric acid cycle and by oxidative phosphorylation.

2.2.3 Regeneration of NAD^+ Consumed during Glycolysis

It follows from Eq.(2.1) that glycolysis involves consumption of NAD^+ for the production of NADH. Thus regeneration of NAD^+ is necessary to sustain glycolysis and this can happen in several ways in mammalian cells. One mechanism is the reoxidation of NADH to NAD^+ by electron transfer through the respiratory chain located in the mitochondria. These electrons are then passed on through the respiratory chain to oxygen, the terminal electron acceptor

$$2\text{NADH} + 2\text{H}^+ + \text{O}_2 \longrightarrow 2\text{NAD}^+ + 2\text{H}_2\text{O} \tag{2.4}$$

Alternatively, the production of lactate from pyruvate can also serve as a mechanism for the production of NAD^+

$$\text{Pyruvate} + \text{NADH} + \text{H}^+ \longrightarrow \text{Lactate} + \text{NAD}^+ \tag{2.5}$$

2.2.4 Regulation of Glycolysis

Glucose flux through glycolysis is regulated to achieve constant ATP levels and to maintain adequate amounts of glycolytic intermediates that are used for biosynthesis. Three enzymes - hexokinase (HK), phosphofructokinase (PFK) and pyruvate kinase (PK) are are considered to play a key role in controlling the glycolytic flux by regulating metabolite concentrations

such that balance between ATP production and consumption is maintained.

2.2.4.1 Hexokinase

Hexokinase catalyzes the first step of glycolysis where glucose is phosphorylated to glucose 6-phosphate

$$\text{Glucose} + \text{ATP} \longrightarrow \text{Glucose 6-phosphate} + \text{ADP} + \text{H}^+ \tag{2.6}$$

Mammalian cells have several forms of hexokinase, all of which catalyze the above reaction. Muscle hexokinase is allosterically inhibited by glucose 6-phosphate such that high concentrations of glucose 6-phosphate temporarily and reversibly inhibit hexokinase. This reduces the rate of formation of glucose 6-phosphate from glucose and helps reestablish a steady state for the glycolytic flux. The hexokinase found in the liver is also referred to as glucokinase and is not inhibited by glucose 6-phosphate but instead is inhibited by fructose 6-phosphate.

2.2.4.2 Phosphofructokinase

Phosphofructokinase (PFK) catalyzes the phosphorylation of fructose 6-phosphate to fructose 1,6-diphosphate

$$\text{Fructose 6-phosphate} + \text{ATP} \longrightarrow \text{Fructose 1,6-bisphosphate} + \text{ADP} \tag{2.7}$$

This is often considered as the step that commits the cell to channeling glucose into glycolysis. PFK has in addition to its substrate binding sites, several regulatory sites where allosteric activators or inhibitors can bind. The activity of PFK is influenced by the concentrations of ATP, AMP, citrate, fructose 1,6-bihosphate and fructose 2,6-biphosphate. High ATP concentrations inhibit PFK by binding to an allosteric site thereby lowering the affinity of PFK for fructose 6-phosphate. This inhibition is relieved by an increase in the concentration of ADP and AMP which results from consumption of ATP. Citrate also serves as an allosteric regulator for PFK with high citrate concentration increasing the inhibitory effect of ATP. The most significant allosteric regulator of PFK is fructose 1,6-bihosphate which is not an intermediate in glycolysis.

2.2.4.3 Pyruvate Kinase

Pyruvate kinase catalyzes the conversion of phosphoenolpyruvate (PEP) to pyruvate and is the last step in glycolysis

$$\text{PEP} + \text{ADP} + \text{H}^+ \longrightarrow \text{Pyruvate} + \text{ATP} \tag{2.8}$$

High ATP concentrations allosterically inhibit PK by decreasing its affinity for PEP as well as acetyl-CoA and long-chain fatty acids. Both acetyl-CoA and long-chain fatty acids are important fuels for the citric acid cycle and when these are present in high concentrations, ATP is readily produced by the citric acid cycle. Low ATP concentrations increase the affinity of PK for PEP resulting in the formation of ATP through substrate-level phosphorylation, thereby maintaining the steady-state concentration of ATP.

2.3 Pentose Phosphate Pathway (PPP)

2.3.1 Overview of PPP

The primary function of the PPP is the generation of NADPH and five carbon sugars. The PPP consists of an oxidative branch which produces NADPH (Figure 2.2) and a nonoxidative branch (Figure 2.3) that interconverts various sugars and connects the PPP to glycolysis. The overall reaction through the oxidative branch of the PPP is

$$\text{G6P} + 2\text{NADP}^+ + \text{H}_2\text{O} \longrightarrow \text{Ribose 6-phosphate} + \text{CO}_2 + 2\text{NADPH} + 2\text{H}^+ \tag{2.9}$$

which results in the production of NADPH, a reductant for biosynthetic reactions and ribose 5-phosphate which is a precursor for nucleotide synthesis.

2.3.2 Regulation of PPP

The first step in the oxidative branch of the PPP is the dehydrogenation of glucose 6-phosphate (Figure 2.2) and this reaction is essentially irreversible under physiological conditions. Also, this reaction is frequently limiting and serves as the main control point in the PPP. In the nonoxidative branch of the PPP, all the reactions are readily reversible (Figure 2.3) and the direction and magnitude of their fluxes are likely to be determined by simple mass action. The control of this branch however, is not explicitly known. It is likely that cellular demand for NADPH and ribose 5-phosphate will determine the flux through the pentose phosphate pathway.

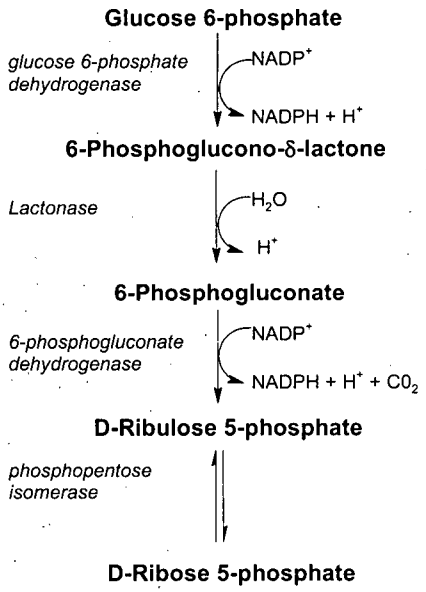

Figure 2.2: The oxidative branch of the pentose phosphate pathway.

2.4 Tricarboxylic Acid (TCA) Cycle

2.4.1 Overview of the TCA Cycle

The TCA cycle (Figure 2.4) has the dual role of generating energy in the form of ATP from the oxidation of carbon compounds and also of generating biosynthetic precursors for a wide variety of products. The pyruvate produced during glycolysis is converted to acetyl-CoA and CO_2 through an oxidative decarboxylation reaction that is catalyzed by the pyruvate dehydrogenase complex which is made up of three distinct enzymes - pyruvate dehydrogenase, dihydrolipoly transacetylase, and dihydrolipoly dehydrogenase. This conversion of pyruvate to acetyl-CoA and CO_2 is an irreversible reaction. The acetyl-CoA formed above enters the TCA cycle where the first of eight reactions is the condensation of acetyl-CoA with oxaloacetate to form citrate under the action of citrate synthase (Figure 2.4). The overall reaction of the TCA cycle can be written as

$$\begin{aligned} & \text{Acetyl-CoA} + 2\text{NAD}^+ + \text{FAD} + \text{GDP} + \text{P}_i + 2\text{H}_2\text{O} \\ \rightarrow\ & 2\text{CO}_2 + 3\text{NADH} + \text{FADH}_2 + \text{GTP} + 2\text{H}^+ + \text{CoA} \end{aligned} \tag{2.10}$$

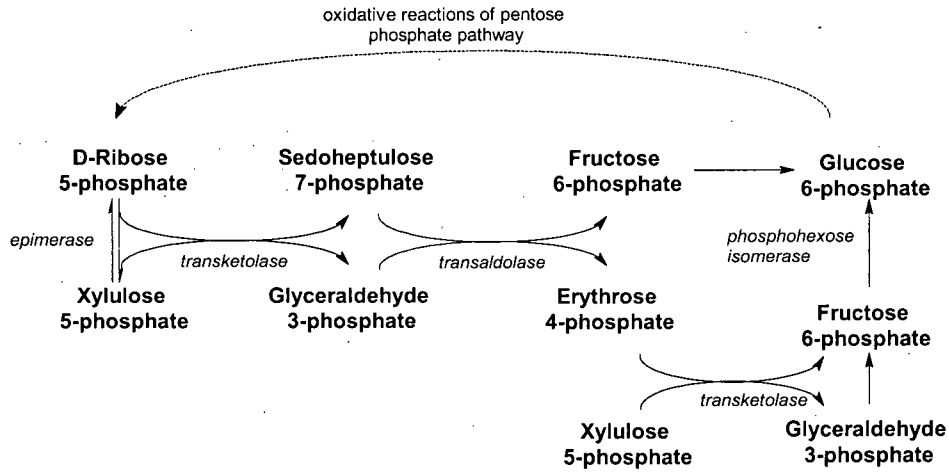

Figure 2.3: The nonoxidative branch of the pentose phosphate pathway.

2.4.2 Energetics of the TCA Cycle

For one turn of the TCA cycle, two molecules of CO_2 are formed from the oxidation of isocitrate and α-ketoglutarate. The energy from these oxidation reactions is conserved in the reduction of three NAD^+ and one FAD molecule coupled with the production of one GTP molecule. While only one molecule of GTP is generated per turn of the TCA cycle, the oxidation steps of the TCA cycle (four in all) are electron sources. These electrons are transported to the respiratory chain via NADH and $FADH_2$ where additional ATP molecules are formed during oxidative phosphorylation. When coupled with glycolysis and assuming that both the pyruvate molecules are oxidized to CO_2 via the citric acid cycle, about 32 ATP molecules are generated per molecule of glucose.

2.4.3 Regulation of the TCA Cycle

The TCA cycle is controlled to meet the energetic needs of the cell in addition to precursors for biosynthesis. The most important regulation is via the NAD^+/NADH ratio with many reactions requiring NAD^+ as an electron acceptor and other being allosterically regulated by NAD^+ or NADH. Concentrations of other substrates such as succinyl-CoA, oxaloacetate, ATP and ADP also serve to control the activity of the TCA cycle. The key enzymes that

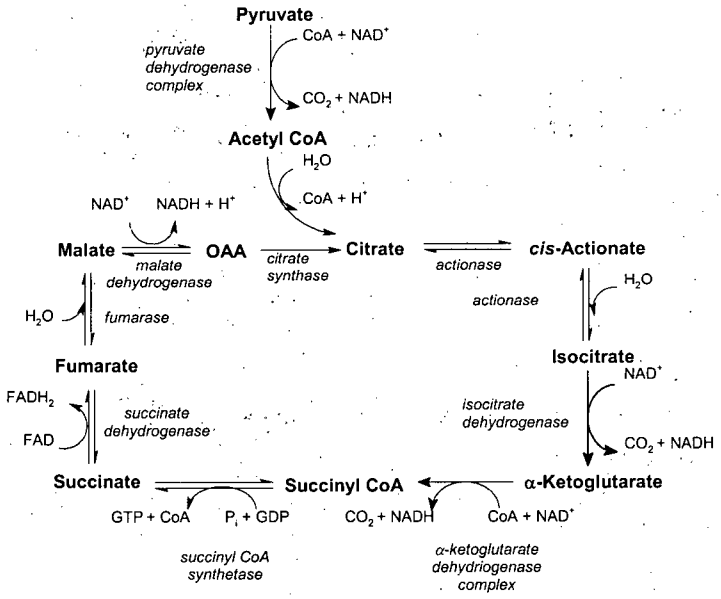

Figure 2.4: Reactions of the TCA cycle.

control TCA cycle activity are pyruvate dehydrogenase complex (PDC), citrate synthase (CS), isocitrate dehydrogenase (ID) and α-ketoglutarate dehydrogenase.

2.4.3.1 Pyruvate Dehydrogenase Complex

The PDC catalyzes conversion of pyruvate into acetyl-CoA

$$\text{Pyruvate} + \text{CoA} + \text{NAD}^+ \longrightarrow \text{Acetyl-CoA} + \text{CO}_2 + \text{NADH} + \text{H}^+ \tag{2.11}$$

The products of the above reaction, acetyl-CoA and NADH are inhibitory to PDC and this inhibition is relieved by CoA and NAD^+. Also, GTP inhibits PDC activity while AMP activates it. PDC is also activated by phosphorylation which is simulated by high ATP/ADP, acetyl-CoA/CoA, and $NADH/NAD^+$ ratios. Dephosphorylation however increases the activity of PDC. It appears that PDC is active when there is a need for acetyl-CoA, either for biosynthesis, or for the production of NADH.

2.4.3.2 Citrate Synthase

Citrate synthase (CS) catalyzes the first step of the TCA cycle where oxaloacetate and acetyl-CoA are converted to citrate

$$\text{Acetyl-CoA} + \text{oxaloacetate} \longrightarrow \text{citrate} + \text{CoA} \tag{2.12}$$

Activity of CS is strongly influenced by the concentrations of oxaloacetate and acetyl-CoA which are the reactants in the above reaction. The concentrations of these substrates vary with the metabolic state of the cell and hence affect the rate of citrate production. Succinyl-CoA, NADH, and NADPH act as inhibitors by decreasing the affinity of CS for acetyl-CoA

2.4.3.3 IsoCitrate Dehydrogenase

Isocitrate dehydrogenase catalyzes the conversion of isocitrate to α-ketoglutarate

$$\text{Isocitrate} + \text{NAD}^+ \longrightarrow \alpha\text{-ketoglutarate} + \text{CO}_2 + \text{NADH} + \text{H}^+ \tag{2.13}$$

The activity of isocitrate dehydrogenase is strongly affected by the NAD^+/NADH ratio and is allosterically activated by ADP. Increased ATP concentrations adversely affect the activity of isocitrate dehydrogenase.

2.4.3.4 α-Ketoglutarate Dehydrogenase

Conversion of α-ketoglutarate to succinyl-CoA is catalyzed by α-ketoglutarate dehydrogenase

$$\alpha\text{-ketoglutarate} + \text{CoA} + \text{NAD}^+ \longrightarrow \text{Succinyl-CoA} + \text{NADH} + \text{H}^+ \tag{2.14}$$

The activity of this enzyme is inhibited by succinyl-CoA and NADH, which are the products in the above reaction. A high ATP/ADP ratio is also known to inhibit α-ketoglutarate dehydrogenase.

2.5 Glutamine Metabolism

2.5.1 Overview of Glutamine Metabolism

Glutamine is a major source of energy and nitrogen for mammalian cells. The anabolic reactions of glutamine typically take pace in the cytosol while the catabolism of glutamine

occurs in the mitochondria. Detailed reviews on the metabolism of glutamine are available [2] and, given the dominant role that glutamine plays in catabolism, only this component will be discussed here.

2.5.2 Catabolism of Glutamine

The use of glutamine for energy production is also referred to as glutaminolysis and results in the production of pyruvate with the concomitant production of NADH (Figure 2.5).

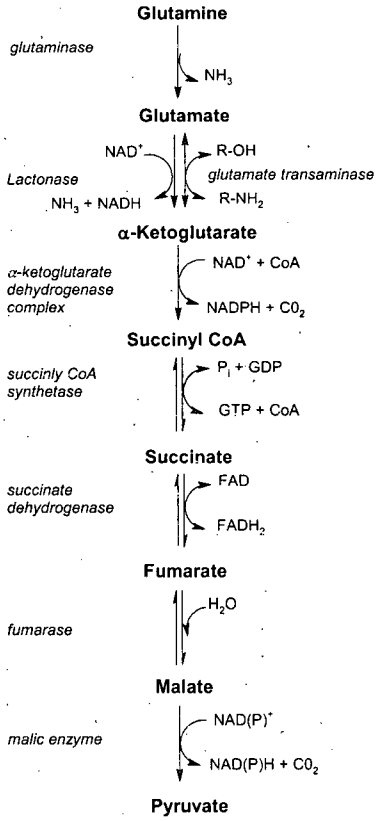

Figure 2.5: Reactions involved in glutamine catabolism.

Glutamine is first converted to glutamate which subsequently is converted to α-ketoglutarate and enters the TCA cycle. While five carbon atoms enter the TCA cycle through α-ketoglutarate, only two are removed as CO_2 for each turn of the TCA cycle. The remaining carbon atoms are removed by the conversion of malate to pyruvate, a reaction that is catalyzed by the malic enzyme. The pyruvate formed can either be converted to lactate or it can enter the TCA cycle via acetyl-CoA.

Glutamine is first converted to glutamate in the following reaction

$$\text{Glutamine} + H_2O \longrightarrow \text{Glutamate} + NH_4^+ \tag{2.15}$$

Subsequent conversion of glutamate to α-ketoglutarate can occur through either glutamate dehydrogenase (GLDH) or via a transaminase reaction (Figure 2.5). Alanine transaminase and aspartate transaminase are abundant in most cells and are likely to be major contributors for the conversion of glutamate to α-ketoglutarate. In addition to the transamination reaction, glutamate can also be deaminated by GLDH as

$$\text{Glutamate} + NAD(P)^+ \longrightarrow \alpha\text{-ketoglutarate} + NH_4^+ + NAD(P)H \tag{2.16}$$

and the α-ketoglutarate formed in the above reaction enters the TCA cycle.

Of special interest is the conversion of malate to pyruvate through the action of the malic enzyme

$$\text{Malate} + NAD(P)^+ \longrightarrow \text{Pyruvate} + CO_2 + NAD(P)H \tag{2.17}$$

This action of the malic enzyme serves to remove the excess carbons from the TCA cycle and also allows for complete oxidation of glutamine.

2.6 Oxidative Phosphorylation

In aerobic metabolism, oxidative phosphorylation is the final step in the energy production process. The electrons released during the TCA cycle are carried by the energy rich molecules NADH and $FADH_2$ and are subsequently transferred to oxygen, the terminal electron acceptor. In mammalian cells, this process occurs in the mitochondria where the respiratory assemblies that carry out the electron transfer steps are located. The overall reaction can be written as

$$NADH + H^+ + \frac{1}{2}O_2 + \left(\frac{P}{O}\right) ADP + \left(\frac{P}{O}\right) P_i \longrightarrow NAD^+ + \left(\frac{P}{O}\right) H_2O + \left(\frac{P}{O}\right) ATP \tag{2.18}$$

where $\frac{P}{O}$ is the ratio of the number of ATP atoms formed per atom of oxygen. For mammalian this ratio is usually between two and three.

2.7 An Integrated View of Cellular Metabolism

As the primary role of metabolism is to produce and maintain biomass, cells consume nutrients to produce energy, reducing power and biosynthetic precursors. The primary pathways that form the core of mammalian cell metabolism are glycolysis, TCA cycle, pentose phosphate cycle, glutaminolysis and oxidative phosphorylation. Having examined these pathways individually, it is important to view them in an integrated fashion as their numerous connections and interactions contribute to the overall behavior of the bioreaction network. Glycolysis and the PPP are connected by glucose-6-phosphate as well as several other glycolytic intermediates. Also, glycolysis is connected to the TCA cycle through pyruvate. Glutamine, which is first metabolized to glutamate, enters the TCA cycle as α-ketoglutarate. It is important to note that while the regulation of an individual enzyme can be evaluated fairly completely *in vitro*, understanding the role of regulation in the overall control of metabolism is extremely difficult. While significant progress has been made in trying to quantify the control of cellular metabolism through metabolic control analysis [3], much work still remains to be done.

2.8 Environmental Effects on Cellular Metabolism

Bioreactor operating conditions have a significant effect on the growth and productivity of mammalian cells. The most commonly monitored parameters during routine cell cultivation include nutrient and metabolite concentration, pH, dissolved oxygen and temperature. All of these parameters have been known to have a significant influence on cellular metabolism and a summary is presented in the following sections.

2.8.1 Nutrients

2.8.1.1 Glucose

Glucose is the primary source of energy and carbon for mammalian cells while glutamine is a source of both nitrogen and energy. A key observation in the metabolism of glucose and glutamine is that their uptake rates are highly concentration dependent. Early investigations [2, 4, 5] have shown that at low glucose concentration, glutamine becomes the dominant source of energy. Also, glucose metabolism itself is a strong function of the glucose concentration in the bioreactor. At high glucose concentrations, specific glucose uptake rates are higher with a majority of glucose converted to lactate and only a small portion entering the TCA cycle [5–7]. At low glucose levels, a majority of the glucose enters the

TCA cycle where it is completely oxidized to CO_2. This difference in glucose utilization patterns has been used to optimize the operation of fed-batch bioreactors where glucose concentration was maintained at a minimum level to minimize the production of lactate [8, 9]. However, it is important to note that a reversal of cellular metabolism can occur when cells are reintroduced into a high glucose environment. For instance, an increase in the molar stoichiometric ratio of lactate to glucose from 0.05 to 1.8 was observed within a few hours of reintroducing glucose starved cells into a glucose rich environment [6].

2.8.1.2 Glutamine

Glutamine concentration also has an effect on the specific uptake rate of glutamine [10–13]. In continuous culture experiments with hybridoma cells, medium glutamine concentrations in the 0.5 – 2 mM range were limiting and were characterized by reduced rates of ammonium and alanine production [10]. Specific ammonium production rates were almost 2-fold higher at elevated glutamine concentrations when compared with those under glutamine-limiting conditions. Consumption rates of other amino acids decreased at higher glutamine concentration in the medium and it was hypothesized that their metabolic function was partially replaced by glutamine. Glutamine uptake rates exhibited a Michaelis-Menten type relationship with the glutamine concentration for BHK cells in batch culture and the kinetic parameters were dependent on the glucose concentration in the medium as glutamine consumption rates were higher at low glucose concentration [14]. However, no significant differences in the oligosaccharide structures of a human IgG-IL2 fusion protein were detected under glutamine limiting conditions [15].

Metabolic flux analysis was used to investigate the metabolism of human 293 cells under low glutamine conditions [16]. At limiting amounts of glutamine, the consumption rates of other essential amino acids increased indicating that these could provide intermediates to the TCA cycle in the absence of glutamine. Replacement of glutamine with glutamate has also been proposed as a strategy to minimize ammonium accumulation [17] which is a consequence of both chemical decomposition of glutamine and the conversion of glutamine to glutamate.

2.8.2 Metabolites

2.8.2.1 Lactate

A significant portion of glucose is converted to lactate in cultured mammalian cells and high lactate concentrations are toxic to cells. Moreover, glucose conversion to lactate is energetically inefficient. A 20% reduction in hybridoma cell growth was observed at 10 mM

(0.9 g/L) lactate concentration [18] while a 50% reduction in hybridoma cell growth rate were observed at 22 mM [19], 40 mM [12, 20] and 55 mM [21] concentrations. As with other variables, the detrimental effects of lactate accumulation are cell line specific but concentrations in excess of 1 g/L have the potential to adversely affect growth and metabolism. Uptake rates of glucose and glutamine also decreased with increase in bioreactor lactate concentration (20 – 70 mM) while death, oxygen uptake and specific antibody production rates were not affected [21]. For CHO cells in batch culture, lactate concentrations in excess of 30 mM inhibited cell growth with 25% growth rate reduction at 60 mM lactate while no reduction was seen in specific productivity and glucose and glutamine uptake [22].

2.8.2.2 Ammonium

Ammonium in mammalian cell bioreactors is produced both from cellular metabolism and from the chemical decomposition of glutamine. Ammonium has significant effects on cellular metabolism [23] including reduction in cellular growth rates and decline in protein productivity along with alteration of protein glycosylation [24–29]. Reviews on the mechanism of ammonium inhibition are available [30, 31]. In contrast to lactate, ammonium can inhibit cellular growth at much lower concentrations. Growth of several cell lines was inhibited at 2 mM ammonium concentration [18]. However, no inhibition was seen with hybridoma cells at 3 mM NH_4Cl concentration while significant growth inhibition was observed at 10 mM NH_4Cl [30]. As both lactate and ammonium can be toxic at elevated concentrations, it is desirable to keep their bioreactor concentrations as low as possible.

2.8.2.3 Dissolved Carbon Dioxide

Carbon dioxide is a product of cellular respiration and indirect sources include $NaHCO_3$ which is typically a buffer in the cultivation medium. If $NaHCO_3$ or Na_2CO_3 are used as base to neutralize cellular lactate, these will be additional CO_2 sources. Bioreactor CO_2 concentration is measured as CO_2 partial pressure (pCO_2) and the physiological range is 30 – 50 mm Hg. Cell growth can be inhibited at $pCO_2 < 30$ mm Hg while elevated pCO_2 has been implicated in reduced growth, metabolism and productivity in addition to adverse effects on glycosylation [32–43]. There is thus an optimial bioreactor pCO_2 concentration close to the physiological range where bioreactor operation is desirable.

For BHK cells in perfusion culture, a 40 to 280 mm Hg pCO_2 increase resulted in 30% growth rate and specific productivity decreases [40]. A 57% growth rate decrease was observed for CHO cells in perfusion culture under high glucose concentrations when the pCO_2 was increased from 53 to 228 mm Hg [44]. The specific antibody productivity,

however, was almost unchanged [44]. Increasing pCO_2 from 36 to 148 mm Hg during perfusion cultivation decreased CHO cell density by 33% (reflecting reduced growth rate) and specific productivity by 44% [37]. Under glucose limiting conditions, for a similar pCO_2 increase the growth rate decreased by 38% along with a 15% reduction in specific antibody productivity. The growth rate of NS/0 cells decreased when pCO_2 increased from 60 to 120 mm Hg [33]. Scale-up of a fed-batch process resulted in pCO_2 values of 179 $\pm$ 9 mm Hg in a 1000 L bioreactor and a 40% decrease in specific productivity was seen under these conditions compared to a pCO_2 value of 68 $\pm$ 13 mm Hg in a 1.5 L laboratory-scale bioreactor [41]. Glucose consumption rates decreased in a dose-dependent fashion for hybridoma cells in T-25 flasks [35] with a 40% decrease observed when pCO_2 increased from 40 to 250 mm Hg. Similar observations were made for lactate production that decreased by 45% for the same pCO_2 increase. Bioreactor pCO_2 control close to the physiological range is thus critical given the substantial impact on cell growth, metabolism and protein productivity.

2.8.3 Amino Acids

Amino acid metabolism in mammalian cell cultures is significantly different from that in microbial cultures as mammalian cells are incapable of synthesizing 10 of the 20 standard amino acids. These 10 are referred to as essential amino acids implying that they must be present in the culture medium to promote cell growth and function. A list of essential and non-essential amino acids is presented in Table 2.1. This representation, however, is for classical human nutrition and all 20 amino acids are present in mammalian cell culture media to promote cell growth and productivity. Amino acid catabolism will be examined first followed by an examination of the pathways through which the nonessential amino acids are synthesized.

2.8.3.1 Amino Acid Catabolism

Only about 10 – 15% of energy is generated from amino acid catabolism (excluding glutamine) indicating that these pathways are significantly less active compared with glycolysis and fatty acid oxidation. All products of amino acid catabolism enter the TCA cycle and a summary of the pathways is shown in Figure 2.6. Arganine, glutamine, histidine and proline are first converted to glutamate through different pathways. Glutamate is subsequently converted to α-ketoglutarate either through transamination or deamination. Isoleucine, methionine, threonine and valine are all first converted to propionyl-CoA which is subsequently converted to succinyl-CoA by the action of methylmalonyl-CoA mutase. Phenylalanine and

Table 2.1: Essential and Nonessential Amino Acids for Mammalian Cell Metabolism

Essential amino acids	Nonessential amino acids
Arginine	Alanine
Histidine	Asparagine
Isoleucine	Aspartate
Leucine	Cysteine
Lysine	Glutamate
Methionine	Glutamine
Phenylalanine	Glycine
Threonine	Proline
Tryptophan	Serine
Valine	Tyrosine

tyrosine can enter the TCA cycle either through fumarate or acetyl-CoA. Asparagine is converted to aspartate by the action of asparaginase and aspartate undergoes transamination with α-ketoglutarate yielding glutamate and oxaloacetate. A majority (10) of the amino acids yield acetyl-CoA which subsequently enters the TCA cycle. Leucine, lysine, phenylalanine, tryptophan and tyrosine are first converted to acetoacetyl-CoA which is subsequently cleaved to acetyl-CoA. Alanine, cysteine, glycine, serine and tryptophan are first converted to pyruvate and then to acetyl-CoA.

2.8.3.2 Amino Acid Biosynthesis

Of all the amino acids shown in Figure 2.6, the essential amino acids have to be supplied in the culture medium since they cannot be synthesized by the cells. Biosynthesis of only the non-essential amino acids is possible and an overview will be presented in this section. Alanine is produced by the transamination of pyruvate by alanine transaminase. The production of asparagine is catalyzed by asparagine synthetase and deamination of asparagine catalyzed by asparginase results in the formation of aspartate. The sulfur for cysteine comes from methionine, an essential amino acid and homocysteine is first produced. Homocysteine condenses with serine to produce cystathionine, which is subsequently cleaved by cystathionase to produce cysteine and a-ketobutyrate. Glutamine is produced by aminotransferase reactions, with a number of amino acids donating the nitrogen atom (Figure 2.6). It can also be synthesized by the reductive amination of α-ketoglutarate catalyzed by glutamate dehydrogenase. Glutamine can be produced by the action of glutamine synthetase or from glutamate by the direct incorporation of ammonia. Glycine is produced from serine in a one-step reaction catalyzed by serine hydroxymethyltransferase.

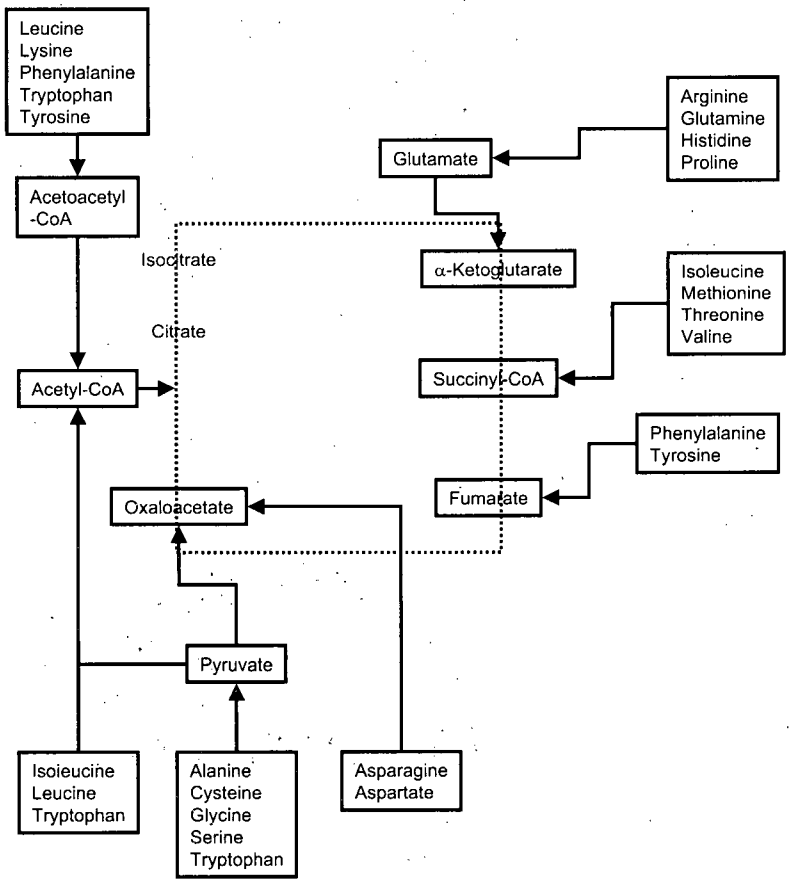

Figure 2.6: An overview of amino acid catabolism in mammalian cells.

Glutamate is the precursor for proline synthesis while serine is produced from the glycolytic intermediate 3-phosphoglycerate. An NADH-linked dehydrogenase converts 3-phosphoglycerate into a keto acid, 3-phosphopyruvate, suitable for subsequent transamination. Aminotransferase activity with glutamate as a donor produces 3-phosphoserine, which is converted to serine by phosphoserine phosphatase. Tyrosine is produced in cells by hydroxylating the essential amino acid phenylalanine with approximately half of the phenylalanine required going into the production of tyrosine.

2.8.4 pH

Bioreactor pH during mammalian cell cultivation is typically maintained close to neutral while optimal pH values for growth and protein production tend to be cell-line and product specific. For hybridoma cells in batch culture, maximum growth was seen at 7.4 and this

value decreased as the pH increased [45]. For hybridoma cells in batch culture, a decrease in bioreactor pH from 7.6 to 7.2 and subsequently to 6.8 decreased cell growth, glucose consumption and lactate production while glutamine uptake and ammonia production were not affected by pH changes [30]. Similar reductions in glucose uptake and lactate production rates at low bioreactor pH have been seen for hybridoma cells in batch and continuous culture [46] resulting in the substitution of glutamine for glucose as the energy source. It has been shown that a decrease in bioreactor pH can reduce the intracellular pH (pH_i) resulting in cytoplasmic acidification [47] which in turn is primarily responsible for the metabolism shifts in response to bioreactor pH changes.

Changes to pH_i have significant implications for cell growth and metabolism [48, 49]. Decrease in pH_i on the order of 0.2 units has been shown to significantly reduce the carbon flux through glycolysis [50–53]. One reason for this decrease is the strong dependence of the activity of the enzyme phosphofructokinase on pH_i [1]. Since changes to pH_i affect the ionization states of all peptides and proteins, pH_i is actively regulated [54, 55].

2.8.5 Dissolved Oxygen

The concentration of dissolved oxygen is a key variable in mammalian cell cultivation and is often controlled at a constant value in the vicinity of 50% air saturation. Oxygen is essential for ATP production through oxidative phosphorylation and is typically provided to the bioreactor using an air-oxygen mixture. Given the low solubility of oxygen in cell culture media, efficient aeration strategies need to be employed, especially in high-density cultivation.

It was observed early on that cell growth is sub-optimal in the absence of dissolved oxygen control and controlling pO_2 in the 40 – 100 mm Hg range (25 – 63% air saturation) resulted in maximum viable cell densities during batch cultivation of mouse LS cells [56]. Cell growth and maximum cell density, however, were significantly reduced at low (1%) and high (200%) DO concentrations [57]. Oxygen uptake rate was also lower at DO = 1% and this was attributed to oxygen-limiting conditions in the bioreactor. Glucose metabolism was also significantly affected by bioreactor DO concentration. At DO = 200%, only 60% of the glucose was converted to lactate when compared with 90% conversion for all other DO concentrations investigated (7.5, 20, 25, 60, 100%). Thus more glucose was drawn into the TCA cycle at DO = 200% which was also characterized by higher oxygen uptake rates. The lactate production rate was the highest at DO = 1% and decreased at higher DO values. High lactate production at low DO values is necessary to generate ATP from the conversion of glucose to lactate since there is a reduction in ATP production through the

TCA cycle. A build-up of pyruvate was also seen at DO = 1% indicating that the pyruvate flux into lactate was slower than the conversion of glucose to pyruvate, An analysis of the enzyme levels at various DO concentrations indicated low levels of isocitrate dehydrogenase and aldolase, and high levels of lactate dehydrogenase at low DO concentration [58]. Thus low DO concentration caused a reduction in the levels of enzymes involved in terminal respiration while the levels of those in glycolysis and the hexose-monophosphate pathway were increased.

The effect of dissolved oxygen concentration in the 0.1 – 100% air saturation range on hybridoma cell metabolism was examined in continuous culture [59]. Oxygen uptake rate was constant for DO in the 10 – 100% range but decreased by more than 50% when the DO dropped below 10%, suggesting oxygen limitation. Lactate production from glucose was higher at low DO concentrations while glutamine consumption decreased. In another study on hybridoma cells in continuous culture, cell growth was reduced both at DO $< 5\%$ and DO = 100% air saturation [60]. Glucose consumption and lactate production increased when the DO was $< 5\%$ while there was a significant reduction in the oxygen uptake rate and these findings are similar to those reported in earlier studies. Glutamine consumption and ammonium production rates were also higher under low DO conditions, in contrast to the observations in Miller et al. [59]. Amino acid consumption rates increased sharply at low DO concentration while the specific antibody production rate was DO independent.

Metabolic flux analysis has been applied to characterize the influence of DO on cell metabolism [61, 62]. For hybridoma cells in continuous culture [62], growth rate was not affected at DO values as low as 1% but was significantly reduced at DO = 0.1%. Glucose consumption and lactate production rates were significantly higher at DO = 0.1% as with previous studies. Metabolic flux analysis indicated that the fluxes of NAD(P)H–producing dehydrogenase reactions decreased under hypoxic conditions (low $NAD(P)^+$/NAD(P)H ratio) and increased at higher DO concentration (high $NAD(P)^+$/NAD(P)H ratio). For hybridoma cells in batch culture [61] there was no significant effect on metabolism when the DO was varied between 5 and 60% air saturation. At DO values of 1% and 0%, both oxygen uptake and carbon dioxide production rates were lower while those for glucose consumption and lactate production increased. Glutamine consumption and ammonia production decreased at low DO while glutamate production was high. Metabolic flux analysis indicated that the pyruvate flux into the TCA cycle was non-existent at DO = 0% and the flux through glutamate dehydrogenase was reversed at low DO resulting in increased glutamate production. The fraction of ATP from glycolysis increased from 34% at DO = 60% to 69% when the DO was 0% reflective of the increased rates of glucose and lactate metabolism at low DO.

All the above studies suggest that there is a threshold DO concentration below which dramatic changes in growth and metabolism are seen. This value is typically 1% air saturation or lower for most cell lines studied to date. It must however be noted that it is not clear if the DO was actually controlled at 1 and 0.1% saturation. DO probes are not characterized by that level of accuracy and it is possible that the cultivations were actually at even lower DO levels. DO concentrations greater than 100% also have the potential to adversely impact cellular metabolism clearly highlighting the need to control bioreactor DO concentration at lower levels. It is nonetheless important to note that DO concentrations in the 10 – 90% range have minimal impact on cell metabolism and protein productivity thereby minimizing the impact of DO excursions associated with operational error in a manufacturing scenario. Controlling DO at a defined set-point is rather straightforward and this is typically done using a PID controller that regulates the flow of a mixture of oxygen and nitrogen/air into the system.

2.8.6 Temperature

Temperature is a key variable in mammalian cell cultivation and most bioreactors are typically operated close to the physiological value of 37 °C. While reduction in cell growth and metabolism at lower temperatures have been long recognized [63, 64], manipulating temperature to improve protein productivity is relatively recent. Temperature effects on specific protein productivity are cell line-specific since observations to date include increased [65–70], decreased [19, 31, 71, 72] or unchanged productivity [31, 73–76] upon temperature reduction. While the advantages associated with increased specific productivity are obvious, even unchanged specific productivity can be beneficial in both fed-batch and perfusion systems. Since lower temperatures are typically accompanied by reduced growth and metabolic rates, fed-batch cultivation times can be extended without large decreases in culture viability. Along similar lines, perfusion rates can be reduced in perfusion cultivation reducing both medium usage and the volume of harvest generated. This concentrated harvest stream can significantly reduce the cost associated with subsequent protein purification operations.

2.8.6.1 Effect of Temperature on Growth and Metabolism

Both growth and metabolic rates are known to decrease sharply with temperature decreases. Reduction in growth rate is attributed to cell accumulation in the G0/G1 phase concomitant with a rapid reduction of cells in the S phase [66, 77, 78]. For BHK cells in batch culture, the growth rate was reduced by 25% when cultivation temperature was lowered from 37 to 33 °C [73] while a more dramatic decrease was seen for EPO-producing CHO cells in batch

culture (0.029 ± 0.003 h^{-1} at 37 °C; 0.016 ± 0.001 h^{-1} at 33°C) [65]. Cell cycle analysis for CHO cells revealed that at 74 hours into the cultivation, the percentages of cells in the G0/G1 phase was 75.8, 62.8 and 47.3% at 30, 33 and 37 °C, respectively, while that for the S phase were 11.6, 33.2 and 45.8%, respectively. Similar observations were made during batch cultivation of Anti-4-1BB producing CHO cells [79]. The growth rate decreased from 0.022 ± 0.003 h^{-1} at 37°C to 0.014 ± 0.004 h^{-1} at 33 °C and the percentages of cells in the G0/G1 phase 78 hours into the cultivation were 64.9, 59.1 and 36% at 30, 33 and 37 °C, respectively, while the S phase percentages were 17.4, 15.6 and 45.1%, respectively.

Just as with growth rate, lower cultivation temperatures are associated with reduced glucose uptake and lactate production rates. For hybridoma cells in batch bioreactors, glucose uptake rate was reduced by 41% at 34 °C compared to 37 °C [19] while a 2-5 fold decrease was observed for hybridoma cells for temperature reduction from 39 to 33 °C [71]. For BHK-21 cells in batch culture, the specific glucose uptake rate decreased from 0.58 ng/cell-d at 37 °C to 0.45 ng/cell-d when the temperature was lowered to 33°C [73] while a 50% reduction in both glucose uptake and lactate production rates was seen for CHO cells in a packed bed reactor for a temperature reduction from 37 to 32 °C [70]. For EPO-producing CHO cells in batch culture, there was no significant reduction in glucose uptake and lactate production rates for a temperature decrease from 37 to 33 °C [65] and similar observations were made for glutamine consumption and ammonium production. However, when the temperature was further lowered to 30 °C, glucose uptake and lactate production rates decreased by 44 and 56%, respectively (as compared to 37 °C) while the decreases in glutamine uptake and ammonium production were 47 and 36%, respectively.

2.8.6.2 Effect of Temperature on Oxygen Uptake Rate

An Arrhenius-type relationship has been proposed to describe the dependence of oxygen uptake rate on temperature in the 6 – 37 °C range [80]. At temperatures close to 37 °C, every 1 °C drop in temperature was accompanied by approximately 10% reduction in the oxygen uptake rate [74] and an order of magnitude decrease in the oxygen uptake rate was seen for temperatures below 15 °C. For CHO cells in a packed bed reactor, a 4 – 5 fold decrease in oxygen uptake rate was seen when the temperature was reduced from 37 to 32 °C [70]. For CHO cells in batch culture, a 50% reduction in oxygen uptake rate was seen when the temperature was reduced from 37 to 30 °C [77]. Temperature effects on oxygen consumption rate are thus consistent and follow an inverse relationship of the Arrhenius type.

2.8.6.3 Effect of Temperature on Cell Sensitivity to Shear

There has been one report where the effect of temperature on shear sensitivity was studied for BHK-21 cells [81]. Cultivation temperatures in the 28 – 39 °C range were examined and an improvement in shear resistance was observed at lower temperatures. It was hypothesized that increased rigidity of the lipid bi-layer at reduced temperatures was contributing to the increased shear resistance. Cell morphology was also influenced by cultivation temperature and cells were more spherical at lower temperatures. However, temperature reduction is unlikely to be used with the sole objective of improving shear resistance properties in light of subsequent advances in the use of shear protectants [82]. Components such as pluronic F-68 are routinely used in current cell cultivation media and provide adequate shear protection in serum-free media under a variety of agitation and oxygenation conditions.

2.8.6.4 Implications for Bioprocess Optimization

Reduced temperature cultivation has been suggested as a tool for increasing productivity in mammalian cell bioreactors. Higher productivity can be achieved rather easily when specific protein productivity is also higher at lower temperatures [65–70], and this has in one instance been linked to increased transcription level of the protein of interest [65]. A biphasic cultivation method has been proposed to maximize protein productivity which includes an initial phase of fast cell growth at 37 °C followed by cultivation at reduced temperatures where specific productivity is higher [66–70]. The shift in cultivation temperature has typically been determined arbitrarily and a model-based approach to cultivation temperature change has been proposed only recently [83]. Using simple Monod-type unstructured kinetic models to describe the dynamics of cell growth and metabolism, a temperature shift after 3 days of growth was found to result in optimal volumetric productivity, a 90% increase when compared with cultivation at 37 °C.

The lower rates of metabolite production at reduced temperatures allow perfusion cultivation at reduced perfusion rates since metabolite accumulation in the reactor is reduced. This lowers medium consumption thereby significantly reducing the cost of goods and also provides a harvest stream with increased product concentration that has positive implications for downstream purification operations. However, temperature shifts can potentially affect product quality [84, 85] and this must be taken into account before temperature-based bioprocess optimization is considered in both fed-batch and perfusion cultivations.

2.9 Conclusions

The primary pathways that form the core of mammalian cell metabolism are glycolysis, TCA cycle, pentose phosphate cycle, glutaminolysis and oxidative phosphorylation, and an overview of these pathways has been presented. Published information on the effect of bioreactor operating conditions such as nutrient and metabolite concentration, pH, dissolved oxygen and temperature has been reviewed and this information can be useful during the optimization of perfusion systems for high density cultivation of mammalian cells.

Bibliography

[1] Stryer, L. *Biochemistry.* W. H. Freeman and Company, San Francisco, 4th edition, 1995.

[2] Zielke, H.; Zielke, C.; Ozand, P. Glutamine: A major energy source for cultured mammalian cells. *Fed. Proc.*, **1984**, *43*, 121–125.

[3] Fell, D. Increasing the flux in metabolic pathways: A metabolic control analysis perspective. *Biotechnol. Bioeng.*, **1998**, *58*, 121–124.

[4] Reitzer, L.; Wice, B.; Kennell, D. Evidence that glutamine, not sugar, is the major energy source for cultured HeLa cells. *J. Biol. Chem.*, **1979**, *254*, 2669–2676.

[5] Zielke, H.; Ozand, P.; Tildon, J.; Sevdalian, D.; Cornblath, M. Reciprocal regulation of glucose and glutamine utilization by cultured human diploid fibroblasts. *J. Cell. Physiol.*, **1978**, *95*, 41–48.

[6] Europa, A. F.; Gambhir, A.; Fu, P. C.; Hu, W. S. Multiple steady states with distinct cellular metabolism in continuous culture of mammalian cells. *Biotechnol Bioeng*, **2000**, *67*(1), 25–34.

[7] Cruz, H. J.; Moreira, J. L.; Carrondo, M. J. Metabolic shifts by nutrient manipulation in continuous cultures of BHK cells. *Biotechnol Bioeng*, **1999**, *66*(2), 104–13.

[8] Zhou, W. C.; Chen, C.-C.; Buckland, B.; Aunins, J. Fed-batch culture of recombinant NSO myeloma cells with high monoclonal antibody production. *Biotechnol. Bioeng.*, **1997**, *55*, 783–792.

[9] Zhou, W. C.; Rehm, J.; Europa, A. F.; Hu, W. S. Alteration of mammalian cell metabolism by dynamic nutrient feeding. *Cytotechnology*, **1997**, *24*, 99–108.

[10] Vriezen, N.; Romein, B.; Luyben, A. M.; van Dijken, J. Effects of glutamine supply on growth and metabolism of mammalian cells in chemostat culture. *Biotechnol. Bioeng.*, **1997**, *54*, 272–286.

[11] Schmid, G.; Keller, T. Monitoring hybridoma metabolism in continuous suspension cultures at the intracellular level. *Cytotechnology*, **1992**, *9*, 217–229.

[12] Miller, W.; Wilke, C.; Blanch, H. Transient responses of hybridoma cells to nutrient additions in continuous culture: I. Glucose pulse and step changes. *Biotechnol. Bioeng.*, **1989**, *33*, 477–486.

[13] Jeong, Y.-H.; Wang, S. Role of glutamine in hybridoma cell culture: effects on cell growth, antibody production, and cell metabolism. *Enzyme Microb. Technol.*, **1995**, *17*, 45–55.

[14] Cruz, H. J.; Ferreira, A. S.; Freitas, C. M.; Moreira, J. L.; Carrondo, M. J. Metabolic responses to different glucose and glutamine levels in baby hamster kidney cell culture. *Appl. Microbiol. Biotechnol.*, **1999**, *51*(5), 579–585.

[15] Cruz, H. J.; Freitas, C. M.; Alves, P. M.; Moreira, J. L.; Carrondo, M. J. Effects of ammonia and lactate on growth, metabolism, and productivity of BHK cells. *Enzyme Microb Technol*, **2000**, *27*(1-2), 43–52.

[16] Nadeau, I.; Sabatié, J.; Koehl, M.; Perrier, M.; Kamen, A. Human 293 cell metabolism in low glutamine-supplied culture: Interpretation of metabolic changes through metabolic flux analysis. *Metab. Eng.*, **2000**, *2*, 277–292.

[17] Altamirano, C.; Paredes, C.; Cairo, J.; Gòdia, C. Improvement of CHO cell culture medium formulation: Simultaneous substitution of glucose and glutamine. *Biotechnol. Prog.*, **2000**, *16*, 69–75.

[18] Hassel, T.; Gleave, S.; Butler, M. Growth inhibition in animall cell culture: The effect of lactate and ammonia. *Appl. Biochem. Biotechnol.*, **1991**, *30*, 29–41.

[19] Reuveny, S.; Velez, D.; Macmillam, J.; Miller, L. Factors affecting cell growth and monoclonal antibody production in stirred reactors. *J. Immunol. Methods*, **1986**, *86*, 53–59.

[20] Glacken, M.; Adams, E.; Sinskey, A. J. Mathematical description of hybridoma culture kinetics: I. Initial metabolic rates. *Biotechnol. Bioeng.*, **1988**, *32*, 491–506.

[21] Ozturk, S.; Riley, M.; Palsson, B. Effects of ammonia and lactate on hybridoma growth, metabolismand ammonia production. *Biotechnol. Bioeng.*, **1992**, *39*, 418–431.

[22] Lao, M. S.; Toth, D. Effects of ammonium and lactate on growth and metabolism of a recombinant Chinese hamster ovary cell culture. *Biotechnol Prog*, **1997**, *13*(5), 688–91.

[23] Schnieder, Y.; Marison, I.; von Stockar, U. The importance of ammonia in mammalian cell culture. *J. Biotechnol.*, **1996**, *46*, 161–185.

[24] Yang, M.; Butler, M. Effects of ammonia on CHO cell growth, erythropoietin production, and glycosylation. *Biotechnol. Bioeng.*, **2000**, *68*, 370–380.

[25] Thorens, B.; Vassalli, P. Chloroquine and ammonium chloride prevent terminal glycosylation of immunoglobulins in plasma cells without affecting secretion. *Nature*, **1986**, *321*, 618–620.

[26] Gawlitzek, M.; Valley, U.; Wagner, R. Ammonium ion and glucose-dependent increases of oligosaccharide complexity in recombinant glycoproteins secreted from cultivated BHK-21 cells. *Biotechnol. Bioeng.*, **1998**, *57*, 518–528.

[27] Borys, M.; Linzer, D.; Papoutsakis, E. Ammonia affects the glycosylation patterns of recombinant mouse placental lactogen-I by Chinese hamster ovary cells in a pH-dependent manner. *Biotechnol. Bioeng.*, **1994**, *43*, 505–514.

[28] Borys, M.; Linzer, D.; Papoutsakis, E. Culture pH affects expression rates and glycosylation of recombinant mouse placental lactogen proteins by Chinese hamster ovary (CHO) cells. *Bio/Technology*, **1993**, *11*, 720–724.

[29] Anderson, D.; Goochee, C. The effect of ammonia on the O-linked glycosylation of granulocyte colony-stimulating factor produced by Chinese hamster ovary cells. *Biotechnol. Bioeng.*, **1995**, *47*, 96–105.

[30] McQueen, A.; Bailey, J. E. Mathematical modeling of the effects of ammonium ion on the intracellular pH of hybridoma cells. *Biotechnol. Bioeng.*, **1990**, *35*, 897–906.

[31] Ryll, T.; Dutina, G.; Reyes, A.; Gunson, J.; Krummen, L.; Etcheverry, T. Performance of small-scale perfusion cultures using an acoustic cell filtration device for cell retention: characterization of spearation efficiency and impact of perfusion on product quality. *Biotechnol. Bioeng.*, **2000**, *69*, 440–449.

[32] Anderson, D.; Goochee, C. The effect of cell culture conditions on the oligosaccharide structures of secreted glycoproteins. *Curr. Opin. Biotechnol.*, **1994**, *5*, 546–549.

[33] Aunins, J.; Henzler, H.-J. in *Biotechnology: A multi-volume comprehensive treatise*, Stephanopoulos, G.; Rehm, H.-J.; Reed, G.; Puhler, A.; Stadler, P., Eds., volume 3, p 817p. VCH Verlag, Weinheim, 1993.

[34] deZengotita, V.; Kimura, G.; Miller, W. Effects of CO2 and osmolality on hybridoma cells: Growth, metabolism and monoclonal antibody production. *Cytotechnology*, **1998**, *28*, 213–227.

[35] deZengotita, V.; Schmeizer, A.; Miller, W. Characterization of hybridoma cell response to elevated pCO2 and osmolality: Intracellular pH, cell size, apoptosis, and metabolism. *Biotechnol. Bioeng.*, **2002**, *77*, 369–380.

[36] Garnier, A.; Voyer, R.; Tom, R.; Perret, S.; Jardin, B.; Kamen, A. Dissolved carbon dioxide accumulation in a large scale and high density production ot TGFb receptor with baculovirus infected Sf-9 cells. *Cytotechnology*, **1996**, *22*, 53–63.

[37] Gray, D.; Chen, S.; Howarth, W.; Inlow, D.; Maiorella, B. CO2 in large-scale and high-density CHO cell perfusion culture. *Cytotechnology*, **1996**, *22*, 65–78.

[38] Kimura, R.; Miller, W. Effects of elevated pCO2 and/or osmolality on the growth and recombinant tPA production of CHO cells. *Biotechnol. Bioeng.*, **1996**, *52*, 152–160.

[39] Kimura, R.; Miller, W. Glycosylation of CHO-derived recombinant tPA produced under elevated pCO2. *Biotechnol. Prog.*, **1997**, *13*, 311–317.

[40] Matanguihan, R.; Sajan, E.; Zachariou, M.; Olson, C.; Michaels, J.; Thrift, J.; Konstantinov, K. Solution to the high dissolved DCO2 problem in high-density perfusion culture of mammalian cells. in *Animal Cell Technology: From Target to Market, 17th ESACT Meeting, Tylosand, Sweden*, pp 399–402. Kluwer, 2001.

[41] Mostafa, S.; Gu, X. Strategies for improved dCO2 removal in large-scale fed-batch cultures. *Biotechnol. Prog.*, **2003**, *19*, 45–51.

[42] Zanghi, J.; Schmelzer, A.; Mendoza, T.; Knop, R.; Miller, W. Bicarbonate concentration and osmolality are key determinants in the inhibition of CHO cell polysialylation under elevated pCO2 or pH. *Biotechnol. Bioeng.*, **1999**, *65*, 182–191.

[43] Zhou, W. C.; Rehm, J.; Hu, W. S. High viable cell concentration fed-batch cultures of hybridoma cells through on-line nutrient feeding. *Biotechnol. Bioeng.*, **1995**, *46*, 579–587.

[44] Takuma, S.; Hirashima, C.; Piret, J. in *Animal Cell Technology: Basic and Applied Aspects*, Yagasaki, K.; Miura, Y.; Hatori, M.; Nomura, Y., Eds., pp 99–103. Kluwer Academic Publishers, Netherlands, 2004.

[45] Doyle, C.; Butler, M. The effect of pH on the toxicity of ammonia to a murine hybridoma. *J. Biotechnol.*, **1990**, *15*, 91–100.

[46] Miller, W.; Blanch, H.; Wilke, C. A kinetic analysis of hybridoma growth and metabolism in batch and continuous suspension culture: Effect of nutrient concentration, dilution rate and pH. *Biotechnol. Bioeng.*, **1987**, *32*, 947–965.

[47] McQueen, A.; Bailey, J. E. Growth inhibition of hybridoma cells by ammonium ion: Correlation with effect on intracellular pH. *Bioprocess Engineering*, **1990**, *6*, 49–61.

[48] Roos, A.; Boron, W. Intracellular pH. *Physiol. Rev.*, **1981**, *61*, 296–434.

[49] Gillies, R.; Martinez-Zaguilan, R.; Peterson, E.; Perona, R. Role of intracellular pH in mammalian cell proliferation. *Cell Physiol. Biochem.*, **1992**, *2*, 159–179.

[50] Fidelman, M.; Seeholzer, S.; Walsh, K.; Moore, R. Intracellular pH mediates action of insulin on glycosysis in frog skeletal muscle. *Am. J. Physiol.*, **1982**, *242*, C87–C93.

[51] Busa, W. in *Na+/H+-exchange, intracellular pH and cell function*, Aronson, P.; Boron, W., Eds., p 291. Academic Press, New York, 1986.

[52] McQueen, A.; Bailey, J. E. Effect of ammonium ion and extracellular pH on hybridoma cell metabolism amd antibody production. *Biotechnol. Bioeng.*, **1990**, *35*, 1067–1077.

[53] Moore, R.; Fidelman, M.; Hansen, J.; Otis, J. in *Intracellular pH: Its measurement, regulation and utilization in cellular function*, Nuccitelli, R.; Deamer, D., Eds., p 385. John Wiley and Sons Inc., New York, 1982.

[54] Madshus, H. Regulation of intracellular pH in eukaryotic cells. *Biochem. J.*, **1988**, *250*, 1–8.

[55] Boron, W. Regulation of intracellular pH. *Adv. Physiol. Educ.*, **2004**, *28*, 160–179.

[56] Kilburn, D.; Webb, F. The cultivation of animal cells at controlled dissolved oxygen partial pressure. *Biotechnol. Bioeng.*, **1968**, *10*, 801–814.

[57] Kilburn, D.; Lilly, M.; Self, D.; Webb, F. The effect of dissolved oxygen partial pressure on the growth and carbohydrate metabolism of mouse LS cells. *J. Cell Sci.*, **1969**, *4*, 25–37.

[58] Self, D.; Kilburn, D.; Lilly, M. The influence of dissolved oxygen partial pressure on the level of various enzymes in mouse LS cells. *Biotechnol Bioeng*, **1968**, *10*, 815–828.

[59] Miller, W.; Wilke, C.; Blanch, H. Effects of dissolved oxygen concentration on hybridoma growth and metabolism in continuous cultures. *J. Cell. Physiol.*, **1987**, *132*, 524–530.

[60] Ozturk, S.; Palsson, B. Effects of dissolved oxygen on hybridoma cell growth, metabolism, and antibody production kinetics in continuous culture. *Biotechnol. Prog.*, **1990**, *6*, 437–446.

[61] Zupke, C.; Sinskey, A. J.; Stephanopoulos, G. Intracellular flux analysis applied to the effect of dissolved oxygen on hybridomas. *Appl. Microbiol. Biotechnol.*, **1995**, *44*(1-2), 27–36.

[62] Bonarius, H.; Houtman, J.; Schmid, G.; C.D., d. G.; Tramper, J. Metabolic-flux analysis of hybridoma cells under oxidative and reductive stress using mass balance. *Cytotechnology*, **2000**, *32*, 97–107.

[63] Watanabe, I.; Okada, S. Effects of temperature on growth rate of cultures mammalian cells (LY5178Y). *J. Cell Biol.*, **1967**, *32*, 309–323.

[64] Rao, P.; Engelberg, J. HeLa cells: Effects of temperture on the life cycle. *Science*, **1965**, *148*, 1092–1094.

[65] Yoon, S.; Song, J.; Lee, G. Effect of low temperature on specific productivity, transcription level, and heterogeneity of erythropoietin in chinese hamster ovary cells. *Biotechnol. Bioeng.*, **2003**, *882*, 289–298.

[66] Kaufmann, H.; Mazur, X.; Fussenegger, M.; Bailey, J. E. Influence of low temperature on productivity, proteome and protein phosphorylation of CHO cells. *Biotechnol. Bioeng.*, **1999**, *65*, 573–582.

[67] Hendrik, V.; Winnepenninckx, P.; Abdelkafi, C.; Vandeputte, O.; Cherlet, M.; Marique, T.; Renemann, G.; Loa, A.; Kretzmer, G.; Werenne, J. Increased productivity of tissular plasminogen activator (t-PA) by butyrate and shift of temperature: a cell cycle phases analysis. *Cytotechnology*, **2001**, *36*, 71–83.

[68] Furukawa, K.; Ohsuye, K. Enhancement of productivity of recombinant a-amidating enzyme by low temperature culture. *Cytotechnology*, **1999**, *21*, 85–94.

[69] Furukawa, K.; Ohsuye, K. Effect of culture temperature on a recombinant CHO cell line producing a C-terminal a-amidating enzyme. *Cytotechnology*, **1998**, *26*, 153–164.

[70] Ducommun, P.; Ruffieux, P.; Kadouri, A.; Stockar, U.; Marison, I. Monitoring of temperature effects on animal cell metabolism in a packed bed process. *Biotechnol. Bioeng.*, **2002**, *77*, 838–842.

[71] Sureshkumar, G.; Mutharasan, R. The influence of temperature on a mouse-mouse hybridoma growth and monoclonal antibody production. *Biotechnol. Bioeng.*, **1991**, *37*, 292–295.

[72] Barnabé, N.; Butler, M. Effect of temperature on nucleotide pools and mitochondrial antibody production in a mouse hybridoma. *Biotechnol. Bioeng.*, **1994**, *44*, 1235–1245.

[73] Weidemann, R.; Ludwig, A.; Kretzmer, G. Low temperature cultivation - a step towards process optimization. *Cytotechnology*, **1994**, *15*, 111–116.

[74] Chuppa, S.; Tsai, S.; Yoon, S.; Shackelford, S.; Rozales, C.; Bhat, R.; Tsay, G.; Matanguihan, R.; Konstantinov, K.; Naveh, D. Fermentor temperature as a tool for control of high-density perfusion cultures of mammalian cells. *Biotechnol. Bioeng.*, **1997**, *55*, 328–338.

[75] Broth, N.; Heider, R.; Assadian, A.; Katinger, H. Growth and production kinetics of human X mouse and mouse hybridoma cells at reduced temperature and serum content. *J. Biotechnol.*, **1992**, *25*, 319–331.

[76] Bloemkolk, J.; Gray, M.; Merchant, F.; Mosmann, T. Effect of temperature on hybridoma cell cycle and Mab production. *Biotechnol. Bioeng.*, **1992**, *40*, 427–431.

[77] Moore, A.; Mercer, J.; Dutina, G.; Donahue, C.; Bauer, K.; Mather, J.; Etcheverry, T.; Ryll, T. Effects of temperature shift on cell cycle, apoptosis and nucleotide pools in CHO cell batch cultures. *Cytotechnology*, **1997**, *23*, 47–54.

[78] Jenkins, N.; Hovey, A. Temperature control of growth and productivity in mutant Chinese hamster ovary cells synthesizing a recombinant protein. *Biotechnol. Bioeng.*, **1993**, *42*, 1029–1036.

[79] Yoon, S.; Kim, S.; Lee, G. Effect of low temperature on specific productivity and transcription level of anti-4-1BB antibody in recombinant Chinese Hamster Ovary cells. *Biotechnol. Prog.*, **2003**, *19*, 1383–1386.

[80] Jorjani, P.; Ozturk, S. Effects of cell density and temperature on oxygen consumption rate for different mammalian cell lines. *Biotechnol. Bioeng.*, **1999**, *64*, 349–356.

[81] Ludwig, A.; Tomeczkowski, J.; Kretzmer, G. Influence of the temperature on the shear stress sensitivity of adherent BHK 21 cells. *Appl. Microbiol. Biotechnol.*, **1992**, *38*, 323–327.

[82] Michaels, J.; Nowak, J. E.; Mallik, A. K.; Koczo, K.; Wasan, D. T.; Papoutsakis, E. Analysis of cell-to-bubble attachment in sparged bioreactors in the presence of cell-protecting additives. *Biotechnol. Bioeng.*, **1995**, *47*, 407–419.

[83] Fox, S.; Patel, U.; Yap, M.; Wang, D. Maximizing Interferon-g production by chinese hamster ovary cells through temperature shift optimization: Experimental and Modeling. *Biotechnol. Bioeng.*, **2004**, *85*(2), 177–184.

[84] Kaufmann, H.; Mazur, X.; Marone, R.; Bailey, J. E.; Fussenegger, M. Comparative analysis of two controlled proliferation strategies regarding product quality, influence on tetracycline-regulated gene expression and productivity. *Biotechnol. Bioeng.*, **2001**, *72*, 592–602.

[85] Anderson, D.; Bridges, T.; Gawlitzek, M.; Hoy, C. Multiple cell factors can affect the glycosylation of Asn-184 in CHO-produced tissue-type plasminogen activator. *Biotechnol. Bioeng.*, **2000**, *70*, 25–31.

Chapter 3

Methods for Metabolic Flux Estimation[1]

3.1 Introduction

Flux is defined as the rate with which material is processed through a bioreaction pathway [1]. While a reaction flux does not contain information on the activity of enzymes in that particular reaction, it does contain information on the extent of involvement of the enzymes in that reaction. For this reason, it has been argued that metabolic fluxes constitute a fundamental determinant of cell physiology and metabolic flux estimation is, therefore, the preferred method for characterizing the physiological state of a cell [2]. Metabolic fluxes can be estimated either by applying mass balances across intracellular metabolites or through isotope mass balances across every carbon atom in the metabolic network. An overview of these two flux estimation methods is presented in this chapter.

3.2 Flux Estimation from Metabolite Balancing

In the metabolite balancing approach, intracellular fluxes are estimated from experimentally measured extracellular rates [3–5]. Intracellular metabolites in the bioreaction network are identified and mass balance expressions are written around them resulting in a stoichiometric model of cellular metabolism. Specific uptake rates of key nutrients and specific production rates of some metabolites are experimentally measured and these constitute the input data

[1] A version of this chapter has been accepted for publication. Goudar, C.T., Biener, R., Piret, J.M. and Konstantinov, K.B. (2006) Metabolic Flux Estimation in Mammalian Cell Cultures, In R. Pörtner, (ed.), Animal Cell Biotechnology: Methods and Protocols, 2nd ed., Humana Press, Totowa, NJ.

for flux estimation. Intracellular fluxes are subsequently computed from experimental data and the network stoichiometry using linear algebra.

The earliest application of metabolite balancing to a fermentation process is for citric acid production by *Candida lipolytica* [6] and this approach was later used for validation of the bioreaction network of butyric acid bacteria [7, 8]. Metabolic flux analysis in its present form can be largely attributed to the seminal work on lysine fermentation [1] where metabolite balancing and extracellular fluxes were used to understand intracellular regulatory mechanisms during lysine production by *Corynebacterium glutamicum*. Metabolite balancing has since seen widespread application for bacterial, yeast and mammalian cell cultures. Mammalian cell applications include BHK [9, 10], CHO [4, 11, 12], hybridoma [3, 13–20] and human [21] cells.

3.2.1 Theory

Consider the reaction sequence $A \rightarrow B \rightarrow C$ where B is the intracellular metabolite. The mass balance expression for B can be written as

$$\frac{dB}{dt} = r_A - r_C - \mu B \tag{3.1}$$

where r_A is the rate of formation of B from A, r_C the rate of conversion of B to C and μB the conversion of B to biomass. Substituting $r_B = r_A - r_C$ for the net formation rate of metabolite B, the above equation can be rewritten as

$$\frac{dB}{dt} = r_B - \mu B \tag{3.2}$$

At low intracellular metabolite concentrations, the μB term is small and can be neglected. For aerobic chemostat cultivation of *S. cerevisiae* at a dilution rate of 0.1 h^{-1}, the intracellular concentrations of glycolytic pathway intermediates ranged between 0.05 – 1.0 μmol (g DW)$^{-1}$ [22], resulting in 0.005 – 0.1 μmol (g DW)$^{-1}h^{-1}$ μB values. These values were much lower than the glycolytic fluxes that were ~1.1 mmol (g DW)$^{-1}h^{-1}$, 4 – 6 orders of magnitude higher. A similar rationale can be applied to mammalian cells where intracellular metabolite concentrations are similar to those in yeast but with reduced growth and metabolic rates [2] such that

$$\frac{dB}{dt} = r_B \tag{3.3}$$

Invoking the steady-state hypothesis which suggests that the magnitude of change in intracellular metabolite concentrations are negligible [20], we get

$$r_B = 0 \tag{3.4}$$

which essentially states that the net rate of formation of intracellular metabolites in zero. For a bioreaction network with M intracellular metabolites we get

$$\mathbf{r_M} = 0 \tag{3.5}$$

where $\mathbf{r_M}$ is the vector of net metabolite formation rates. Mass transfer effects have not been included in the above derivation because substrate transfer from the cultivation medium into the cell and availability of intracellular metabolites are not considered to be rate limiting.

3.2.2 Flux Estimation Through Manual Substitution

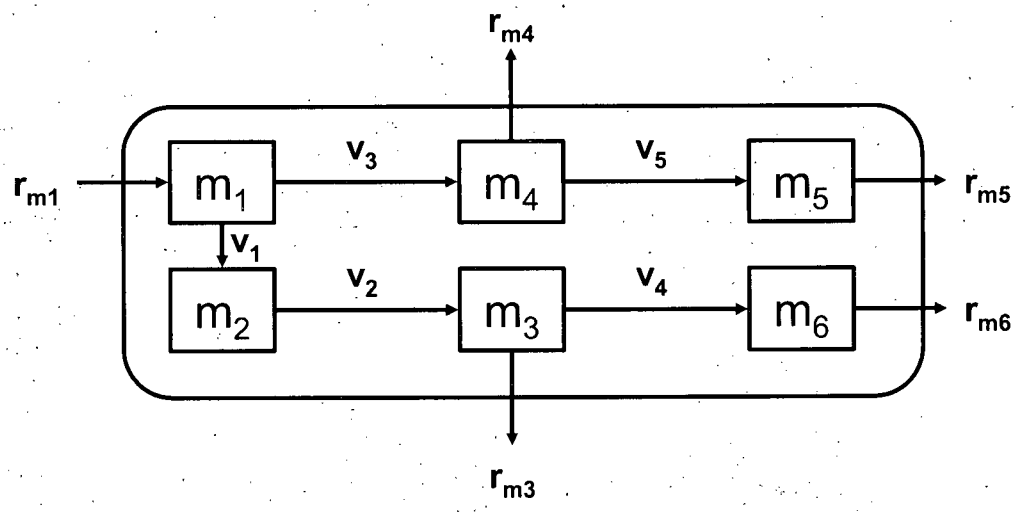

Figure 3.1: A simplified bioreaction network consisting of 6 intracelllular metabolies ($m_1 - m_6$), 5 measured extracellular rates ($r_{m1}, r_{m3} - r_{m6}$) and 5 unknown intracellular fluxes ($v_1 - v_5$).

The application of Eq.(3.5) for flux estimation is illustrated using the reaction network shown in Figure 3.1. This network consists of 6 intracellular metabolites ($m_1 - m_6$) and 5 measured extracellular rates ($r_{m_1}, r_{m_3} - r_{m_6}$) that have been arbitrarily selected to have enough measurements to solve for the 5 unknown intracellular fluxes ($v_1 - v_5$). Applying

Eq.(3.5) around metabolites $m_1 - m_6$ results in the following mass balance expressions

$$m_1 : r_{m_1} - v_1 - v_3 = 0 \tag{3.6}$$

$$m_2 : v_1 - v_2 = 0 \tag{3.7}$$

$$m_3 : v_2 - r_{m_3} - v_4 = 0 \tag{3.8}$$

$$m_4 : v_3 - r_{m_4} - v_5 = 0 \tag{3.9}$$

$$m_5 : v_5 - r_{m_5} = 0 \tag{3.10}$$

$$m_6 : v_4 - r_{m_6} = 0 \tag{3.11}$$

Estimating the unknown fluxes $v_1 - v_5$ from the above equations is straightforward. From Eq.(3.10), $v_5 = r_{m_5}$ and $v_4 = r_{m_6}$ from Eq.(3.11). Thus $v_3 = r_{m_4} + r_{m_5}$ from Eq.(3.9) and $v_2 = v_1 = r_{m_3} + r_{m_6}$ from Eqs.(3.7) and (3.8). The solution for the above bioreaction network can thus be summarized as

$$v_1 = r_{m_3} + r_{m_6} \tag{3.12}$$

$$v_2 = v_1 \tag{3.13}$$

$$v_3 = r_{m_4} + r_{m_5} \tag{3.14}$$

$$v_4 = r_{m_6} \tag{3.15}$$

$$v_5 = r_{m_5} \tag{3.16}$$

3.2.3 Flux Estimation Through Linear Algebra

The above approach of manual substitution works well for small bioreaction networks. For complicated networks that have multiple branch points and often include more than 30 metabolites and reactions, manual estimation of fluxes becomes cumbersome. An elegant alternative is to use matrix notation and linear algebra techniques for flux estimation. Eq.(3.5) can be written as

$$\mathbf{r_M} = \mathbf{G}^T\mathbf{v} = 0 \tag{3.17}$$

where $\mathbf{G}^T$ is the matrix containing the stoichiometric coefficients for the intracellular metabolites and $\mathbf{v}$ is the vector of reaction rates that includes both the measured uptake and production rates as well as the unknown intracellular fluxes. To solve Eq.(3.17), it is convenient to split the reaction rate vector $\mathbf{v}$ into two components, $\mathbf{v}_m$ and $\mathbf{v}_c$ for the measured and calculated rates, respectively. If $\mathbf{G}_m^T$ and $\mathbf{G}_c^T$ are the corresponding splits in the stoichiometric

matrix, $\mathbf{G}$, then Eq.(3.17) can be rewritten as

$$\mathbf{G}^T\mathbf{v} = \mathbf{G}_m^T\mathbf{v}_m + \mathbf{G}_c^T\mathbf{v}_c = 0 \tag{3.18}$$

from which $\mathbf{v}_c$ can be estimated (assuming $\mathbf{G}_c^T$ is a nonsingular square matrix) as

$$\mathbf{v}_c = -\left(\mathbf{G}_c^T\right)^{-1}\mathbf{G}_m^T\mathbf{v}_m \tag{3.19}$$

3.2.4 Application of the Matrix Approach for Flux Estimation

The first step in application of the matrix approach to the reaction network shown in Figure 3.1 involves construction of $\mathbf{G}^T$ and $\mathbf{v}$. The number of rows in $\mathbf{G}^T$ equals the number of intracellular metabolites (6) and the number of columns equals the sum of the measured extracellular rates (5) and the number of unknown intracellular fluxes (5). $\mathbf{G}^T$ is thus a 6 x 10 matrix while $\mathbf{v}$ is a 10 x 1 column vector whose elements include the measured extracellular rates and unknown intracellular fluxes. Eq.(3.17) can be written as

$$\underbrace{\begin{pmatrix} 1 & 0 & 0 & 0 & 0 & -1 & 0 & -1 & 0 & 0 \\ 0 & 0 & 0 & 0 & 0 & 1 & -1 & 0 & 0 & 0 \\ 0 & -1 & 0 & 0 & 0 & 0 & 1 & 0 & -1 & 0 \\ 0 & 0 & -1 & 0 & 0 & 0 & 0 & 1 & 0 & -1 \\ 0 & 0 & 0 & -1 & 0 & 0 & 0 & 0 & 0 & 1 \\ 0 & 0 & 0 & 0 & -1 & 0 & 0 & 0 & 1 & 0 \end{pmatrix}}_{(\mathbf{G}^T)_{5\text{x}10}} \underbrace{\begin{pmatrix} r_{m_1} \\ r_{m_3} \\ r_{m_4} \\ r_{m_5} \\ r_{m_6} \\ v_1 \\ v_2 \\ v_3 \\ v_4 \\ v_5 \end{pmatrix}}_{(\mathbf{v})_{10\text{x}1}} = \begin{pmatrix} 0 \\ 0 \\ 0 \\ 0 \\ 0 \\ 0 \end{pmatrix} \tag{3.20}$$

Multiplying the first row of $\mathbf{G}^T$ with the elements of $\mathbf{v}$ results in $r_{m_1} - v_1 - v_3 = 0$ which is identical to Eq.(3.6) and is the mass balance expression for metabolite m_1. Multiplications of rows 2 – 6 of $\mathbf{G}^T$ with $\mathbf{v}$ results in the mass balance expressions for metabolites $m_2 - m_6$ making the representation in Eq.(3.20) identical to Eqs.(3.6-3.11). The compact representation in Eq.(3.20) becomes especially important for typical mammalian cell bioreaction networks that have more than 30 metabolites and reactions.

Eq.(3.20) can be split into the measured and unmeasured components according to

Eq.(3.18)

$$\overset{(\mathbf{G}_m^T)}{\begin{pmatrix} 1 & 0 & 0 & 0 & 0 \\ 0 & 0 & 0 & 0 & 0 \\ 0 & -1 & 0 & 0 & 0 \\ 0 & 0 & -1 & 0 & 0 \\ 0 & 0 & 0 & -1 & 0 \\ 0 & 0 & 0 & 0 & -1 \end{pmatrix}} \overset{(\mathbf{v}_m)}{\begin{pmatrix} r_{m_1} \\ r_{m_3} \\ r_{m_4} \\ r_{m_5} \\ r_{m_6} \end{pmatrix}} + \overset{(\mathbf{G}_c^T)}{\begin{pmatrix} -1 & 0 & -1 & 0 & 0 \\ 1 & -1 & 0 & 0 & 0 \\ 0 & 1 & 0 & -1 & 0 \\ 0 & 0 & 1 & 0 & -1 \\ 0 & 0 & 0 & 0 & 1 \\ 0 & 0 & 0 & 1 & 0 \end{pmatrix}} \overset{(\mathbf{v}_c)}{\begin{pmatrix} v_1 \\ v_2 \\ v_3 \\ v_4 \\ v_5 \end{pmatrix}} = \begin{pmatrix} 0 \\ 0 \\ 0 \\ 0 \\ 0 \\ 0 \end{pmatrix} \tag{3.21}$$

The vector of unknown fluxes, $\mathbf{v}_c$, can now be estimated from Eq.(3.19)

$$\mathbf{v}_c = -\overset{\left((\mathbf{G}_c^T)^{-1}\right)}{\begin{pmatrix} -\frac{1}{2} & \frac{1}{2} & \frac{1}{2} & -\frac{1}{2} & -\frac{1}{2} & \frac{1}{2} \\ -\frac{1}{3} & -\frac{1}{3} & \frac{2}{3} & -\frac{1}{3} & -\frac{1}{3} & \frac{2}{3} \\ -\frac{1}{3} & -\frac{1}{3} & -\frac{1}{3} & \frac{2}{3} & \frac{2}{3} & -\frac{1}{3} \\ -\frac{1}{6} & -\frac{1}{6} & -\frac{1}{6} & -\frac{1}{6} & -\frac{1}{6} & \frac{5}{6} \\ -\frac{1}{6} & -\frac{1}{6} & -\frac{1}{6} & -\frac{1}{6} & \frac{5}{6} & -\frac{1}{6} \end{pmatrix}} \overset{(\mathbf{G}_m^T)}{\begin{pmatrix} 1 & 0 & 0 & 0 & 0 \\ 0 & 0 & 0 & 0 & 0 \\ 0 & -1 & 0 & 0 & 0 \\ 0 & 0 & -1 & 0 & 0 \\ 0 & 0 & 0 & -1 & 0 \\ 0 & 0 & 0 & 0 & -1 \end{pmatrix}} \overset{(\mathbf{v}_m)}{\begin{pmatrix} r_{m_1} \\ r_{m_3} \\ r_{m_4} \\ r_{m_5} \\ r_{m_6} \end{pmatrix}} \tag{3.22}$$

where $\left(\mathbf{G}_c^T\right)^{-1}$ is the inverse (actually a pseudoinverse as $\mathbf{G}_c^T$ is nonsquare) of $\mathbf{G}_c^T$. When experimentally measured extracellular rates are included in the $\mathbf{v}_m$ vector, $\mathbf{v}_c$ can be readily calculated from the above equation.

3.2.5 The Nature of Biochemical Networks

It follows from Eqs.(3.17 – 3.19) and the above example that intracellular flux estimation is a simple 3 step process that first involves formulation of the stoichiometric matrix, $\mathbf{G}^T$, from the reaction network, followed by separation of $\mathbf{G}^T$ into $\mathbf{G}_m^T$ and $\mathbf{G}_c^T$ and subsequent estimation of $\mathbf{v}_c$ by matrix inversion. However, computational complexities can arise due to singularities in $\mathbf{G}_c^T$ depending upon the number of metabolite mass balances (m) and reactions (r) and three scenarios are possible

1. Determined system ($m = r$)
2. Underdetermined system ($m < r$)
3. Overdetermined system ($m > r$)

Determined systems are computationally the simplest (assuming $\mathbf{G}_c^T$ is square and non-singular) and usually have a unique solution that can be determined from Eq.(3.19). They have little practical utility since $m \neq r$ for most biochemical networks.

Underdetermined systems are more common because adequate experimental measurements can often not be made. These systems are formulated as linear programming (LP) problems [5, 23–34] and do not have unique solutions suggesting flexibility in the intracellular metabolic fluxes

$$\text{Minimize } \sum c_i v_i \text{ subject to } \mathbf{G}^T\mathbf{v} = 0 \tag{3.23}$$

where c_i is the weight factor for flux v_i. The choice of c_i determines the objective function to be minimized (or maximized) and it is critical that this be physiologically relevant. Choices can include maximization of growth rate or production of a particular metabolite and minimization of ATP production and nutrient uptake. Despite the possibility of an infinite number of solutions, the solution is confined to a feasible domain, a polyhedron, conceptualized as the metabolic genotype. The stoichiometric constraints of the system determine the feasible region and in two-dimensional space, these stoichiometric constraints are lines and are the boundaries of the feasible domain (plane). These systems are typically solved using the simplex method and the solutions occur at the extreme points of the feasible domain. Sensitivity analysis of the optimal solution can be analyzed using shadow prices

$$p_i = \frac{\partial Z}{\partial r_i} \tag{3.24}$$

where Z is the optimal value of the objective function and r_i the extracellular production/consumption of metabolite i. This quantity helps determine the contribution (or lack thereof) of r_i to the stated objective function and provides useful information for designing rational metabolic engineering strategies for maximizing/minimizing Z. A major disadvantage of underdetermined systems is that the stated objective function may not reflect cell physiology. For instance, Bonarius et al, [3] used the minimum Euclidean norm constraint (minimize sum of flux values or the most efficient channeling of fluxes) for hybridoma cells in batch culture while experimental data indicated that cell physiology was more consistent with ATP and NADH maximization constraints rather than the minimum Euclidean norm constraint. Nonetheless, this approach can provide very useful information helping target genetic engineering efforts to maximize the outcome of interest [5, 35].

Overdetermined systems have more metabolite mass balances than the number of reactions ($m > r$) and are preferred over determined and underdetermined systems because excess experimental data can provide improved estimates of the metabolic fluxes and can

also be used to check the validity of the assumed biochemistry. The stoichiometric matrix, $\mathbf{G}_c^T$ is non-square for overdetermined systems and a pseudoinverse must be computed to determine $\mathbf{v}_c$. Singularities can arise when one or more rows in $\mathbf{G}_c^T$ can be expressed as a linear combination of the other rows, a condition referred to as linear dependency. These often result from parallel pathways in the network such as the transhydrogenase reaction for the interconversion of NADH and NADPH where the balances of the two cofactors are coupled resulting in linearly dependent stoichiometries. Flux estimation in overdetermined systems along with methods of error analysis are presented in detail below since such systems usually provide the most robust flux estimates.

3.2.6 Flux Determination in Overdetermined Systems

Overdetermined systems are those in which additional experimental measurements are available and the degrees of freedom are > 0. For these systems, $\mathbf{G}_c^T$ is not square and a pseudo-inverse of $\mathbf{G}_c^T$ is necessary to solve Eq.(3.19)

$$\mathbf{v}_c = -\left(\mathbf{G}_c^T\right)^{\#} \mathbf{G}_m^T \mathbf{v}_m \tag{3.25}$$

where $\left(\mathbf{G}_c^T\right)^{\#}$ is the pseudo-inverse of $\mathbf{G}_c^T$. Substituting for $\mathbf{v}_c$ from Eq.(3.25) in Eq.(3.18) results in

$$\mathbf{G}_m^T \mathbf{v}_m + \mathbf{G}_c^T \left\{ -\left(\mathbf{G}_c^T\right)^{\#} \mathbf{G}_m^T \mathbf{v}_m \right\} = 0 \tag{3.26}$$

or

$$\mathbf{v}_m \left\{ \mathbf{G}_m^T - \mathbf{G}_c^T \left(\mathbf{G}_c^T\right)^{\#} \mathbf{G}_m^T \right\} = 0 \tag{3.27}$$

which can be rewritten as

$$\mathbf{R}\mathbf{v}_m = 0 \tag{3.28}$$

where $\mathbf{R} = \mathbf{G}_m^T - \mathbf{G}_c^T \left(\mathbf{G}_c^T\right)^{\#} \mathbf{G}_m^T$ is called the redundancy matrix. The rank of $\mathbf{R}$ specifies the number of independent equations that must be satisfied by the measured and calculated rates. As extra measurements are available in an overdetermined system, the matrix $\mathbf{R}$ has dependent rows. Eliminating the dependent rows, Eq.(3.28) can be rewritten for only the independent rows as

$$\mathbf{R}_r \mathbf{v}_m = 0 \tag{3.29}$$

where $\mathbf{R}_r$ is referred to as the reduced redundancy matrix. In an ideal situation where experimental data are error free, the left hand side of Eq.(3.29) is exactly zero. However, all experimental data are characterized by measurement error, δ, which relates the measured

and actual $\mathbf{v}_m$ values as

$$\bar{\mathbf{v}}_m = \mathbf{v}_m + \delta \tag{3.30}$$

where $\bar{\mathbf{v}}_m$ is the measured value and $\mathbf{v}_m$ the actual value resulting in the following modification of Eq.(3.29)

$$\mathbf{R}_r \bar{\mathbf{v}}_m = \boldsymbol{\epsilon} \tag{3.31}$$

where $\boldsymbol{\epsilon}$ is the residual vector. Substituting $\bar{\mathbf{v}}_m = \mathbf{v}_m + \delta$ from Eq.(3.30) into Eq.(3.29) results in

$$\mathbf{R}_r \left(\mathbf{v}_m + \delta\right) = \boldsymbol{\epsilon} \tag{3.32}$$

which simplifies to

$$\mathbf{R}_r \delta = \boldsymbol{\epsilon} \tag{3.33}$$

as $\mathbf{R}_r \mathbf{v}_m = 0$ (Eq.3.29).

Under ideal conditions (with no error in the measured rates), $\delta = 0$, and Eq.(3.29) is valid. In the presence of measurement errors, however, the residual is not zero and it is possible to improve the measured rates such that the residual is minimized. The variance covariance matrix of the measured rates ($\mathbf{F}$) is first determined by assuming that the error vector is normally distributed with zero mean

$$E\left(\delta\right) = 0 \tag{3.34}$$

$$\mathbf{F} = E\left(\left(\bar{\mathbf{v}}_m - \mathbf{v}_m\right)\left(\bar{\mathbf{v}}_m - \mathbf{v}_m\right)^T\right) = E\left(\delta\delta^T\right) \tag{3.35}$$

It has been shown that the residuals are also normally distributed with zero mean [36] such that

$$E\left(\epsilon\right) = 0 \tag{3.36}$$

$$\varphi = E\left(\epsilon\epsilon^T\right) \tag{3.37}$$

where φ is the covariance matrix of the residuals. Substituting $\boldsymbol{\epsilon} = \mathbf{R}_r\delta$ from Eq.(3.33), φ can be expressed in terms of $\mathbf{R}_r$ and $\mathbf{F}$

$$\varphi = \mathbf{R}_r \mathbf{F} \mathbf{R}_r^T \tag{3.38}$$

The minimum variance estimate of δ is obtained by minimizing the sum of squared errors [36]

$$\hat{\delta} = \mathbf{F}\mathbf{R}_r^T \varphi^{-1} \mathbf{R}_r \mathbf{v}_m \tag{3.39}$$

from which the improved $\mathbf{v}_m$ estimates can be obtained

$$\hat{\mathbf{v}}_m = \bar{\mathbf{v}}_m - \hat{\delta} = \left(\mathbf{I} - \mathbf{F}\mathbf{R}_r^T \varphi^{-1} \mathbf{R}_r\right) \bar{\mathbf{v}}_m \tag{3.40}$$

where I is an identity matrix.

Statistical hypothesis testing can be used to identify gross measurement errors by computing a consistency index, h

$$h = \boldsymbol{\epsilon}^T \varphi^{-1} \boldsymbol{\epsilon} \tag{3.41}$$

It has been shown that h follows a χ^2 distribution with the degrees of freedom equal to the number of redundant equations [36]. Hence the h value computed from Eq.(3.41) for any bioreaction network can be used to check the quality of experimental measurements. If $h > \chi^2$ at a desired confidence level, it is an indication that either the measured values are in gross error or the assumed system biochemistry is incorrect. If excess measurements are present, h can be recalculated by eliminating a single measurement from the mass balances. If a dramatic reduction in h value is observed, it is likely that the eliminated measurement contained error. This process can be repeated for all the measured rates in the bioreaction network. Confidence can be placed in the unknown flux estimates only when $h < \chi^2$ at the desired confidence level (usually 90 or 95 %). The concepts presented above will be applied to a simplified biochemical network for mammalian cell metabolism.

Table 3.1: Reactions in the simplified bioreaction network of Figure 3.2

Glc+2NAD^++2ADP+2P_i	→	2Pyr+2NADH+2ATP+2H_2O+2H^+
Pyr+NADH+H^+	→	Lac+NAD^+
Pyr+4NAD^++FAD+ADP+3H_2O+P_i	→	3CO_2+4NADH+$FADH_2$+ATP+2H^+
0.5O_2+2.5 ADP+2.5P_i+NADH+3.5 H^+	→	2.5ATP+NAD^++3.5H_2O
0.5O_2+1.5 ADP+1.5P_i+$FADH_2$+1.5 H^+	→	1.5ATP+FAD^++2.5H_2O

3.2.7 Flux Estimation in an Overdetermined System describing Mammalian Cell Metabolism

Figure 3.2 shows a simplified bioreaction network that was originally proposed by Balcarcel and Clark [37] for flux analysis from well plate cultivations where limited measurements were available and the corresponding reactions are shown in Table 3.1. Glycolytic reactions have been lumped into a single reaction (Glucose → Pyruvate; flux v_{c1}) as have those for the TCA cycle (Pyruvate → CO_2; flux v_{c2}). Conversion of pyruvate to lactate is a dominant reaction in most mammalian cell culture and this has been included in the network (Flux

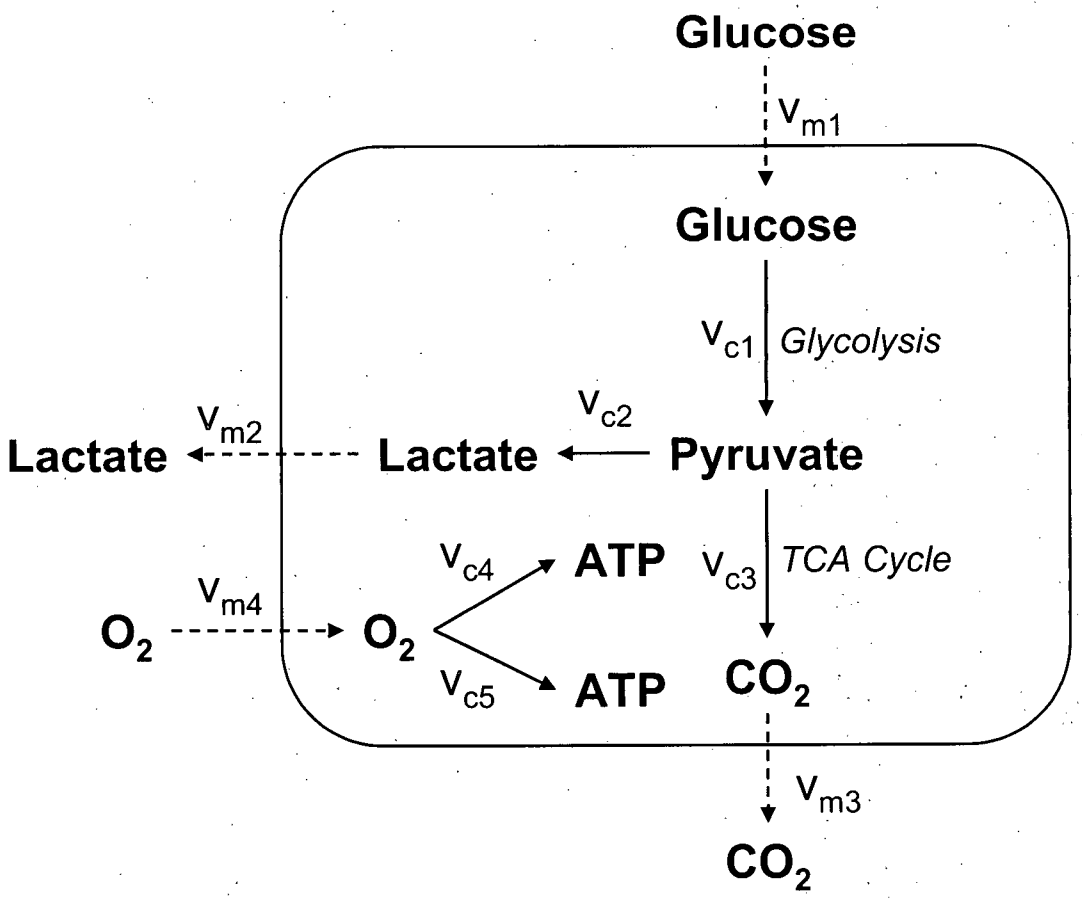

Figure 3.2: A simplified network for mammalian cell metabolism with lumped reactions for glycolysis and TCA cycle and those for lactate production and oxidative phosphorylation [37]. The network consists of 5 unknown intracellular fluxes (v_{c1}-v_{c5}) and 4 extracellular measured rates (v_{m1}-v_{m4}). Fluxes v_{c4} and v_{c5} involve NADH and $FADH_2$, respectively (Table 3.1).

v_{c3}) along with the oxidative phosphorylation reactions (v_{c4} and v_{c5}). Rates of glucose and oxygen consumption along with those for lactate and CO_2 production make up the measured extracellular rates. The network has a total of 4 measured extracellular rates (v_{m1}-v_{m4}) and 5 unknown intracellular fluxes that have to be estimated (v_{c1}-v_{c5}). Balcarcel and Clark [37] also included total ATP production as another unknown flux (v_{c6}) and considered the following 8 metabolites for writing the mass balance expressions: glucose, lactate, CO_2, O_2, pyruvate, NADH, $FADH_2$ and ATP resulting in a 8 x 10 stoichiometric matrix. The small size of this network makes it convenient for illustrating the concepts of consistency testing and gross error detection for overdetermined systems.

3.2.7.1 Determination of Intracellular Fluxes

Eq.(3.17) can be written for the network in Figure 3.2 as

$$\underbrace{\begin{pmatrix} -1 & 0 & 0 & 0 & -1 & 0 & 0 & 0 & 0 & 0 \\ 0 & -1 & 0 & 0 & 0 & 1 & 0 & 0 & 0 & 0 \\ 0 & 0 & -1 & 0 & 0 & 0 & 3 & 0 & 0 & 0 \\ 0 & 0 & 0 & 1 & 0 & 0 & 0 & -0.5 & -0.5 & 0 \\ 0 & 0 & 0 & 0 & 2 & -1 & -1 & 0 & 0 & 0 \\ 0 & 0 & 0 & 0 & 2 & -1 & 4 & -1 & 0 & 0 \\ 0 & 0 & 0 & 0 & 0 & 0 & 1 & 0 & -1 & 0 \\ 0 & 0 & 0 & 0 & 2 & 0 & 1 & 2.5 & 1.5 & -1 \end{pmatrix}}_{(\mathbf{G}^T)_{8\times 10}} \underbrace{\begin{pmatrix} v_{m1} \\ v_{m2} \\ v_{m3} \\ v_{m4} \\ v_{c1} \\ v_{c2} \\ v_{c3} \\ v_{c4} \\ v_{c5} \\ v_{c6} \end{pmatrix}}_{(\mathbf{v})_{10\times 1}} = \begin{pmatrix} 0 \\ 0 \\ 0 \\ 0 \\ 0 \\ 0 \\ 0 \\ 0 \end{pmatrix} \tag{3.42}$$

where the 8 rows of $\mathbf{G}^T$ represent the mass balance expressions for glucose, lactate, CO_2, O_2, pyruvate, NADH, $FADH_2$ and ATP, respectively, columns 1 – 4 represent the 4 extracellular reactions whose rates are measured (v_{m1}-v_{m4}) and columns 5 – 10 represent the 6 unknown intracellular fluxes (v_{c1}-v_{c6}). Examination of some basic properties of $\mathbf{G}^T$ is the first step towards determining the unknown fluxes. The rank of $\mathbf{G}^T$ was estimated to be 8 indicating all the 8 metabolites balance equations in $\mathbf{G}^T$ were independent and could not be expressed as a linear combination of the other mass balance expressions. The condition number of $\mathbf{G}^T$ was estimated as 7.6 and this low value indicates that estimated flux values are not overly sensitive to errors in the measured extracellular rates. Condition numbers < 100 have been considered acceptable for metabolic flux analysis [2].

Eq.(3.42) can be split into the measured and unmeasured components according to

Eq.(3.18)

$$\underbrace{\begin{pmatrix} -1 & 0 & 0 & 0 \\ 0 & -1 & 0 & 0 \\ 0 & 0 & -1 & 0 \\ 0 & 0 & 0 & -1 \\ 0 & 0 & 0 & 0 \\ 0 & 0 & 0 & 0 \\ 0 & 0 & 0 & 0 \\ 0 & 0 & 0 & 0 \end{pmatrix}}_{(\mathbf{G}_m^T)} \underbrace{\begin{pmatrix} v_{m1} \\ v_{m2} \\ v_{m3} \\ v_{m4} \end{pmatrix}}_{(\mathbf{v}_m)} + \underbrace{\begin{pmatrix} -1 & 0 & 0 & 0 & 0 & 0 \\ 0 & 1 & 0 & 0 & 0 & 0 \\ 0 & 0 & 3 & 0 & 0 & 0 \\ 0 & 0 & 0 & -0.5 & -0.5 & 0 \\ 2 & -1 & -1 & 0 & 0 & 0 \\ 2 & -1 & 4 & -1 & 0 & 0 \\ 0 & 0 & 1 & 0 & -1 & 0 \\ 2 & 0 & 1 & 2.5 & 1.5 & -1 \end{pmatrix}}_{(\mathbf{G}_c^T)} \underbrace{\begin{pmatrix} v_{c1} \\ v_{c2} \\ v_{c3} \\ v_{c4} \\ v_{c5} \\ v_{c6} \end{pmatrix}}_{(\mathbf{v}_c)} = \begin{pmatrix} 0 \\ 0 \\ 0 \\ 0 \\ 0 \\ 0 \\ 0 \\ 0 \end{pmatrix} \tag{3.43}$$

Using experimental values for the measured rates (CHO cells in perfusion culture), the vector of known rates is

$$\mathbf{v}_m = \begin{pmatrix} -1.4788 \\ 1.7293 \\ 5.8333 \\ -5.1369 \end{pmatrix} \tag{3.44}$$

and taking the pseudoinverse of $\mathbf{G}_c^T$ results in

$$\left(\mathbf{G}_c^T\right)^{\#} = \begin{pmatrix} -0.3172 & 0.3414 & 0.0103 & -0.1034 & 0.2897 & 0.0517 & 0.0517 & 0 \\ -0.3414 & 0.8293 & -0.0052 & 0.0517 & -0.1448 & -0.0259 & -0.0259 & 0 \\ -0.0034 & -0.0017 & 0.2121 & -0.1207 & -0.0621 & 0.0603 & 0.0603 & 0 \\ -0.2552 & -0.1276 & 0.6931 & -0.9310. & 0.4069 & -0.5345 & 0.4655 & 0 \\ 0.0483 & 0.0241 & 0.0310 & -0.3103 & -0.1310 & 0.1552 & -0.8448 & 0 \\ -1.2034 & 0.3983 & 2.0121 & -3.1207 & 1.3379 & -0.9397 & 0.0603 & -1 \end{pmatrix} \tag{3.45}$$

Once $\mathbf{v}_m$ and $\left(\mathbf{G}_c^T\right)^{\#}$ are known, the unknown fluxes can be estimated from Eq.(3.19) as

$$\mathbf{v}_c = \begin{pmatrix} 1.6512 \\ 1.6431 \\ 1.8592 \\ 8.9824 \\ 1.7456 \\ 30.2361 \end{pmatrix} \tag{3.46}$$

While this completes the flux analysis, it is perhaps just as important to analyze the biore-

action network for inconsistencies and to check for gross error in experimental data as shown in the subsequent sections.

3.2.7.2 Redundancy Analysis and Gross Error Detection

The above system has a total of 10 reaction rates (4 measured, 6 unknown) and 8 balances on pathway intermediates making it overdetermined with 2 degrees of freedom (Degrees of freedom = number of reaction rates - rank($\mathbf{G}^T$)). The redundancy matrix, $\mathbf{R}$, is first calculated as $\mathbf{R} = \mathbf{G}_m^T - \mathbf{G}_c^T \left(\mathbf{G}_c^T\right)^{\#} \mathbf{G}_m^T$

$$\mathbf{R} = \begin{pmatrix} -0.6828 & -0.3414 & -0.0103 & 0.1034 \\ -0.3414 & -0.1707 & -0.0052 & 0.0517 \\ -0.0103 & -0.0052 & -0.3638 & -0.3621 \\ 0.1034 & 0.0517 & -0.3621 & -0.3793 \\ -0.2897 & -0.1448 & -0.1862 & -0.1379 \\ -0.0517 & -0.0259 & 0.1810 & 0.1897 \\ -0.0517 & -0.0259 & 0.1810 & 0.1897 \\ 0 & 0 & 0 & 0 \end{pmatrix} \tag{3.47}$$

and the rank of $\mathbf{R}$ was calculated to be 2 and the reduced redundancy matrix $\mathbf{R_r}$ was obtained from singular value decomposition (SVD) of $\mathbf{R}$

$$\mathbf{R_r} = \begin{pmatrix} 0.8099 & 0.4049 & -0.2250 & -0.3599 \\ -0.3679 & -0.1839 & -0.6745 & -0.6131 \end{pmatrix} \tag{3.48}$$

Assuming 10% error in all the measured rates, the error vector, δ, can be written as

$$\boldsymbol{\delta} = \begin{pmatrix} 0.1479 \\ 0.1729 \\ 0.5833 \\ 0.5137 \end{pmatrix} \tag{3.49}$$

from which the variance covariance matrix, $\mathbf{F}$, is computed using Eq.(3.35)

$$\mathbf{F} = \begin{pmatrix} 0.0219 & 0 & 0 & 0 \\ 0 & 0.0299 & 0 & 0 \\ 0 & 0 & 0.3403 & 0 \\ 0 & 0 & 0 & 0.2639 \end{pmatrix} \tag{3.50}$$

It must be noted that the off-diagonal elements of **F** have been set to zero indicating that the measurements are uncorrelated. This assumption may not be valid under all experimental conditions and methods to obtain representative **F** estimates are available [2]. The variance covariance matrix of the residuals, φ, can now be calculated from Eq.(3.38) as

$$\varphi = \begin{pmatrix} 0.0707 & -0.1011 \\ -0.1011 & 0.2579 \end{pmatrix} \tag{3.51}$$

Once φ is known, h can be estimated from Eq.(3.41) as 3.36. This h value must be compared with the χ^2 distribution with 2 degrees of freedom. From Table 3.2, the h value of 3.36 is lower than the χ^2 distribution at a confidence level of 0.900 suggesting that the measured rates do not contain gross errors.

Table 3.2: Values of the chi^2 Distribution at varying Degrees of Freedom and Confidence Levels

	Confidence Level				
Degrees of freedom	**0.500**	**0.750**	**0.900**	**0.950**	**0.990**
1	0.46	1.32	2.71	3.84	6.63
2	1.39	2.77	4.61	5.99	9.21
3	2.37	4.11	6.25	7.81	11.3
4	3.36	5.39	7.78	9.49	13.3
5	4.35	6.63	9.24	11.10	15.1

Improved estimates of the measured rates can now be obtained from Eq.(3.40)

$$\hat{\mathbf{v}}_m = \bar{\mathbf{v}}_m - \hat{\delta} = \begin{pmatrix} -1.4788 \\ 1.7293 \\ 5.8333 \\ -5.1369 \end{pmatrix} - \begin{pmatrix} 0.191 \\ 0.1306 \\ 0.6090 \\ 0.0882 \end{pmatrix} = \begin{pmatrix} -1.6698 \\ 1.5987 \\ 5.2243 \\ -5.2251 \end{pmatrix} \tag{3.52}$$

It has been shown that the above $\hat{\mathbf{v}}_m$ estimates have a smaller standard deviation than the measured values ($\bar{\mathbf{v}}_m$) and are hence more reliable [36]. The differences between these two measured rate vectors is not substantial suggesting that the experimentally measured values are reasonably accurate. The unknown intracellular flux vector, $\mathbf{v}_c$, corrresponding

to the improved specific rate vector, $\hat{\mathbf{v}}_m$, can now be computed as

$$\hat{\mathbf{v}}_c = \begin{pmatrix} 1.6701 \\ 1.5986 \\ 1.7415 \\ 8.7078 \\ 1.7417 \\ 29.4638 \end{pmatrix} \tag{3.53}$$

and the corresponding h value is 2.49 x 10^{-8}, significantly smaller than the 3.36 obtained using the experimentally measured rates. From a comparison of Eqs.(3.46) and (3.53), however, there is only a small change in the estimated intracellular fluxes after correcting the measured specific rates. This may not be the case when measured data are in considerable error. A computer program that performs the above calculations is presented in Appendix A.

3.2.7.3 Error Diagnosis

If h values greater than the χ^2 distribution (for instance, a value >10 in the above example) are obtained, it could be due to either systematic or large random errors in the measured rates. It becomes important to identify the error source and an elegant method has been proposed for such an analysis in overdetermined systems with at least 2 degrees of freedom [36]. In this iterative approach, one of the measured rates is eliminated and the remaining are used to compute the consistency index which is subsequently compared with the χ^2 distribution at one lower degrees of freedom. This process is repeated by sequentially eliminating all the measured rates and the corresponding h values are recorded. If elimination of any single measured rate results in a dramatic decreases in the h value, that measurement is likely to contain systematic errors. Once the measured rate in error has been identified, it can be corrected as illustrated in the following example.

Let us assume that due to a measurement error, the CER has been inaccurately determined to be 7.2916 (25% error; actual value = 5.8333) and the other measurements are

unaffected. The unknown flux vector is calculated from Eq.(3.19) as

$$\mathbf{v}_c = \begin{pmatrix} 1.6663 \\ 1.6355 \\ 2.1684 \\ 9.9932 \\ 1.7902 \\ 33.1703 \end{pmatrix} \tag{3.54}$$

with a corresponding h value of 9.64 which is higher than the χ^2 distribution even at a confidence level of 0.99. It is thus clear that errors exist in the measured rates. The h values obtained by eliminating one measured rate at a time are shown in Table 3.3. CER elimination results in a significant reduction in h when compared with other specific rates indicating the presence of gross measurement error in CER. This problem can be adressed by making additional (accurate) CER measurements and if this not possible, experimental CER data must not be used for flux estimation.

Table 3.3: Values of h after Sequential Elimination of the Measured Rates

Measurement Eliminated	h value
None	9.64
Glucose uptake rate	5.87
Lactate production rate	5.87
CO_2 production rate	1.59
O_2 consumption rate	8.21

3.2.8 Summary of Flux Estimation in Overdetermined Systems

When overdetermined systems are characterized by at least two degrees of freedom, the consistency of experimental data and the presence of gross measurement errors can by analyzed as illustrated in the above example. A schematic of this approach is shown in Figure 3.3. The bioreaction network is first defined from which the stoichiometric matrix, $\mathbf{G}^T$, and the rate vector, $\mathbf{v}$, are derived. The unknown intracellular fluxes are then determined from Eq.(3.25) through matrix inversion. The redundancy matrix, $\mathbf{R}$, is then calculated as $\mathbf{R} = \mathbf{G}_m^T - \mathbf{G}_c^T \left(\mathbf{G}_c^T\right)^{\#} \mathbf{G}_m^T$ from which the reduced redundancy matrix $\mathbf{R}_r$ is derived by eliminating the dependent rows. The residual vector, $\boldsymbol{\epsilon}$, is subsequently determined using $\mathbf{R}_r$ and the measured rates (Eq.3.31). The variance-covariance matrix of the measured rates, $\mathbf{F}$, is then estimated from the measured rate errors (Eq.3.35) following which the covariance

matrix of the residuals, φ, is estimated from $\mathbf{R}_r$ and $\mathbf{F}$ (Eq.3.38). Finally, the consistency index, h, is estimated from φ and ϵ (Eq.3.41) and compared with the χ^2 distribution at the appropriate degrees of freedom.

If $h < \chi^2$, then no gross measurement errors are present and the assumed biochemistry is consistent. While the resulting fluxes constitute an acceptable solution, further improvement in the flux estimates is possible by improving the measured rates (Eq.3.40) followed by flux estimation. In addition to improved flux estimates, this approach will also significantly reduce the h value as demonstrated in the above example. While flux improvements for an accurate data set may be marginal, it is still useful to refine the flux estimates as this step requires minimal computational effort. For cases when $h < \chi^2$, either the experimental data contain gross errors or the assumed biochemistry is incorrect. Presence of gross errors can be determined by sequentially eliminating a measurement followed by flux estimation and h determination. If elimination of any single measurement results in a significant decrease in h, then that measurement contains gross errors. If additional accurate measurements are not available for that specific rate, it must not be used for flux estimation. However, if this analysis indicates no gross measurement error, then the likely source of high h is the bioreaction network. Appropriate modification of the network can result in flux estimates such that $h < \chi^2$.

3.3 Flux Estimation Using Isotopic Tracers

In isotopic tracer experiments, the cultivation medium contains a labeled substrate (usually ^{13}C glucose) that is stable and can be detected by NMR or GC-MS. Distribution of the label among the metabolites can be measured using either NMR or GC-MS and is a function of the intracellular metabolic fluxes. For simple biochemical networks, unknown intracellular fluxes can be directly determined by examining the fractional label enrichment either from transient intensity measurements or from experiments where both metabolic and isotopic steady states are reached. An elegant method to analyze data from complex metabolic networks is by using atom mapping matrices (AMMs) which describe the transfer of carbon atoms from reactants to products [19]. The primary advantage of the AMM approach is the decoupling of the steady-state isotope balance equations from the reactions in the biochemical network. Detailed information on the AMM approach is presented below while information on other related approaches can be found elsewhere [38–47].

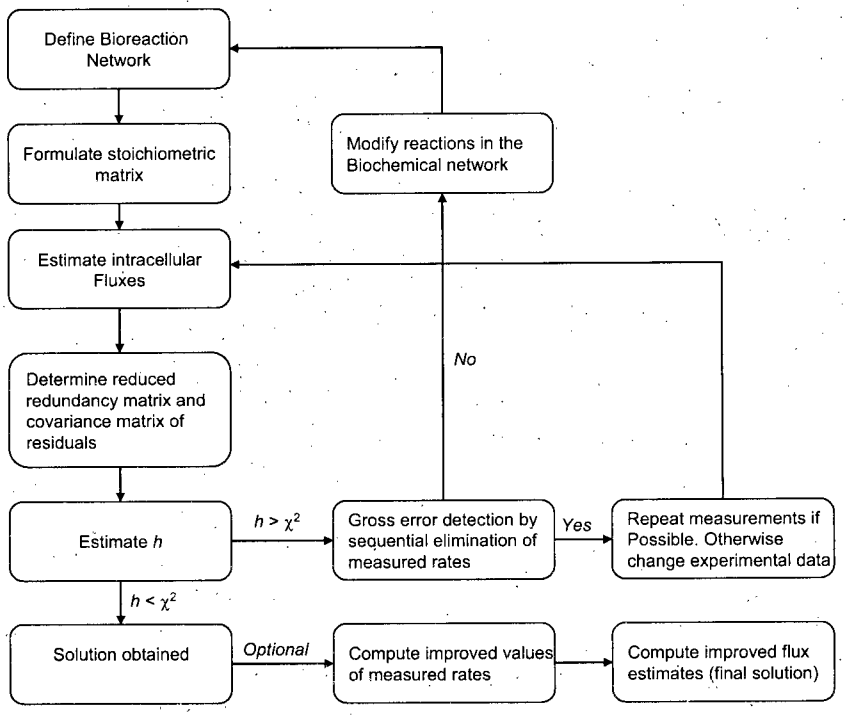

Figure 3.3: An illustration of the steps involved in overdetermined system flux estimation using the metabolite balancing approach.

3.3.1 Atom Mapping Matrices for Flux Estimation

^{13}C glucose is the most commonly used labeled substrate in the investigation of mammalian cell metabolism. When cells consume glucose, the carbon label gets incorporated into the various metabolites and for a metabolite with n carbon atoms, 2^n isotope isomers (isotopomers) are possible. Table 3.4 shows the isotopomer distribution for a 3-carbon molecule along with their binary and decimal indexes. Information on the isotopomers is contained in the NMR spectrum from which it is possible to quantify their relative distribution.

Consider a simple example where A and B (both 3-carbon molecules) react to form C (also a 3-carbon molecule) and x_1, x_2 and x_3 are the associated fluxes (Figure 3.4). The mass balance expression for this simple reaction network is straightforward ($x_1 + x_2 = x_3$) and isotopomer balances are necessary to determine the contributions from the isotopomers of A and B to the isotopomers of C. It follows from Table 3.4 that 8 isotopomers of A,B and C are possible since they all contain 3 carbon atoms. For instance, if the i^{th} isotopomer of A and the j^{th} isotopomer of B are transformed into the k^{th} isotopopmer of C, the steady-state

Table 3.4: Isotopomer distribution for a 3-carbon molecule along with their binary and decimal indexes

Carbon Atoms	Binary Index	Decimal Index	Index Vector
○ – ○ – ○	000	0	$\begin{pmatrix}0\\0\\0\end{pmatrix}$
○ – ○ – ●	001	1	$\begin{pmatrix}1\\0\\0\end{pmatrix}$
○ – ● – ○	010	2	$\begin{pmatrix}0\\1\\0\end{pmatrix}$
○ – ● – ●	011	3	$\begin{pmatrix}1\\1\\0\end{pmatrix}$
● – ○ – ○	100	4	$\begin{pmatrix}0\\0\\1\end{pmatrix}$
● – ○ – ●	101	5	$\begin{pmatrix}1\\0\\1\end{pmatrix}$
● – ● – ○	110	6	$\begin{pmatrix}0\\1\\1\end{pmatrix}$
● – ● – ●	111	7	$\begin{pmatrix}1\\1\\1\end{pmatrix}$

isotopomer balance is

$$x_1 A(i) + x_2 B(j) = x_3 C(k) \tag{3.55}$$

from which $C(k)$ can be determined only if the other quantities are known. In the above balance, the relationship between i, j and k was assumed and for complex metabolic networks, atom mapping matrices help define these relationships conveniently. AMMs describe the transfer of carbon items from the reactant to the product and are designated as **[reactant > product]** with the number of columns and rows equal to the number of carbon atoms in the reactant and product, respectively [19]. If the i^{th} carbon in the product is derived from the j^{th} carbon of the reactant, the element in the i^{th} row and the j^{th} column is 1 (this value is 0 otherwise).

For the reaction network in Figure 3.4, two AMMs (**[A > C]** and **[B > C]**) must be

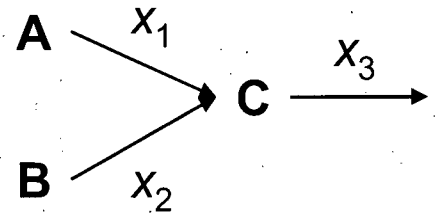

Figure 3.4: A simple reaction network where molecule C is formed from molecules A and B.

used to relate the reactant and product isotopomers. If carbon 1 of A becomes carbon 3 of C, carbon 2 of A becomes carbon 1 of C and carbon 3 of A becomes carbon 2 of C, then [**A** > **C**] can be written as

$$[\mathbf{A} > \mathbf{C}] = \begin{pmatrix} 0 & 1 & 0 \\ 0 & 0 & 1 \\ 1 & 0 & 0 \end{pmatrix} \tag{3.56}$$

and multiplying the AMM by a vector of the carbon atoms of A will result in the vector of carbon atoms for C

$$\begin{pmatrix} c_1 \\ c_2 \\ c_3 \end{pmatrix} = \begin{pmatrix} 0 & 1 & 0 \\ 0 & 0 & 1 \\ 1 & 0 & 0 \end{pmatrix} \begin{pmatrix} a_1 \\ a_2 \\ a_3 \end{pmatrix} = \begin{pmatrix} a_2 \\ a_3 \\ a_1 \end{pmatrix} \tag{3.57}$$

It must be noted that the vector of carbon atoms in A is not unique and 8 combinations are possible (Table 3.4). Each of these 8 carbon vectors of A will result in a corresponding carbon vector for C and this dependency is dictated by the AMM. If we consider the second index of A ($i = 2$), the index vector can be written as

$$[\mathbf{i}] = \begin{pmatrix} 1 \\ 0 \\ 0 \end{pmatrix} \tag{3.58}$$

The product vector [**k**] corresponding to the reactant vector [**i**] can be easily determined from the AMM

$$[\mathbf{k}] = [\mathbf{A} > \mathbf{C}]\ [\mathbf{i}] = \begin{pmatrix} 0 & 1 & 0 \\ 0 & 0 & 1 \\ 1 & 0 & 0 \end{pmatrix} \begin{pmatrix} 1 \\ 0 \\ 0 \end{pmatrix} = \begin{pmatrix} 0 \\ 0 \\ 1 \end{pmatrix} \tag{3.59}$$

indicating that $A(1) = C(4)$. A complete mapping of k at all 8 values of i results in

$$C(0) = A(0) \tag{3.60}$$
$$C(4) = A(1) \tag{3.61}$$
$$C(1) = A(2) \tag{3.62}$$
$$C(5) = A(3) \tag{3.63}$$
$$C(2) = A(4) \tag{3.64}$$
$$C(6) = A(5) \tag{3.65}$$
$$C(3) = A(6) \tag{3.66}$$
$$C(7) = A(7) \tag{3.67}$$

and a similar exercise can be done to develop the relationships between the isotopomers of reactant B and product $\dot{C}$. Eq.(3.55) can now be written as

$$x_1[\mathbf{A} > \mathbf{C}] \otimes \mathbf{A} + x_2[\mathbf{B} > \mathbf{C}] \otimes \mathbf{B} = x_3\mathbf{C} \tag{3.68}$$

where $\otimes$ is a mapping operator that helps generate all possible isotopomers of C from A and B. As metabolic fluxes are functions of the bioreaction network and isotopomer distribution, solution of the above equation followed by comparison with experimental NMR or GC-MS data in an iterative fashion (nonlinear least squares optimization) provides the desired flux estimates.

An alternative to AMMs is isotopomer distribution analysis where steady-state isotopomer balances are formulated for every metabolite in the network which allows determination of the metabolic fluxes as function of the isotopomer population. This has some advantages over the use of AMMs and detailed information is available [39, 44, 46–49].

3.3.2 Overview of Flux Estimation from Isotope Tracer Studies

For complex metabolic networks, flux estimation from NMR or GC-MS data is computationally intensive and iterative because of the nonlinear relationship between the isotopomer balances and the the metabolic fluxes. An overview of the flux estimation procedure is shown in Figure 3.5. The bioreaction network is first defined from which the metabolite and isotope balance equations are obtained. Either AMMs as described in the previous section or isotopomer mapping matrices can be used to formulate these equations. Once these equations are defined, an initial set of fluxes is assumed from which the metabolite isotopomer pools are calculated. This distribution of metabolite isotopomers helps predict

label enrichment, molecular weight distribution of the isotopomers (for GC-MS analysis) and the NMR fine structure. This theoretically predicted information (which is dependent on the assumed value of the fluxes) is subsequently compared with experimental GC-MS/NMR data and initial agreement is usually not satisfactory. The assumed flux values are refined and the calculation procedure is repeated until there is good agreement between theoretical and experimental data.

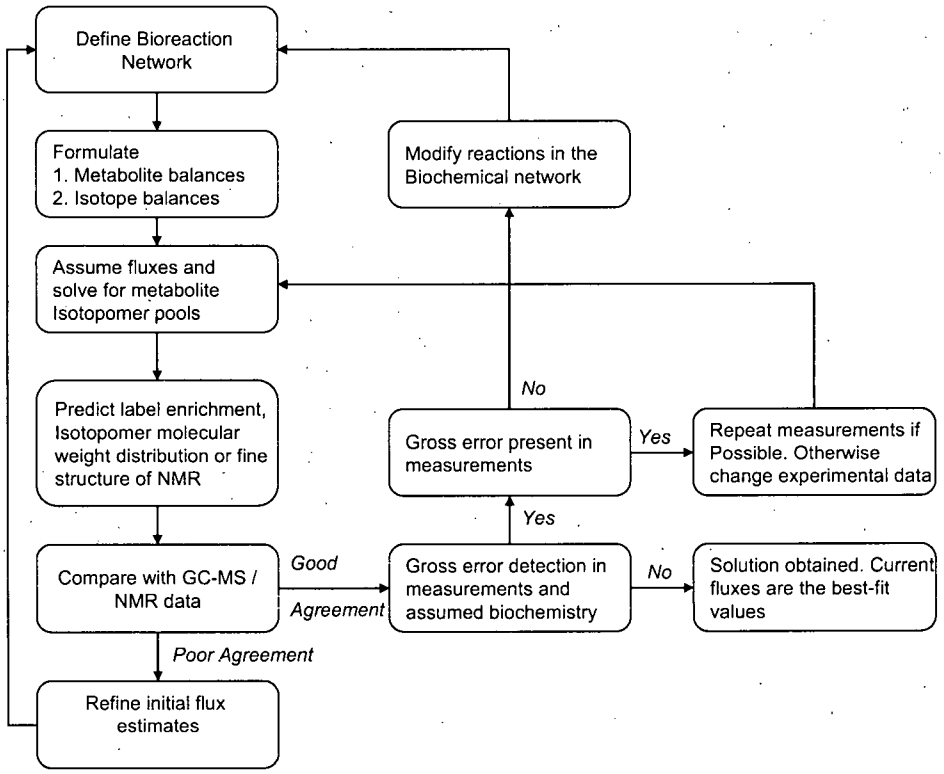

Figure 3.5: An overview of the flux estimation process for the isotope tracer approach.

Error diagnosis is an important component of flux estimation from isotope tracer studies as for the metabolite balancing approach. If no gross errors are detected, the obtained flux values are reliable and can be considered representative of cell physiology. However, if gross errors are detected, they could either be due to measurement error or inappropriate assumptions regarding system biochemistry. Depending upon the source of gross error, the existing experimental data must be reviewed and new measurements should be made if possible or the biochemical network must be modified to reflect cell physiology. Once either of these adjustments is done, the entire process of flux estimation must be repeated.

3.4 Summary

An overview of the two methods of flux estimation has been presented. Metabolite balancing is more commonly used because of experimental and computational simplicity. For mammalian cell culture, experimental data necessary for flux estimation by metabolite balancing include cell growth, nutrient uptake and metabolite/product formation rates along with uptake/production rates of amino acids. As these quantities are routinely measured in cell culture experiments, there is little need for additional measurements for flux estimation. The computational component of the metabolite balancing approach is simple and basic matrix manipulations are adequate for flux estimation. Overdetermined systems are preferable over determined and underdetermined systems as robust error diagnosis is possible in these systems, increasing the reliability of the flux estimates.

The use of isotope tracers helps determine fluxes in reversible and cyclical reactions which is not possible using metabolite balancing. This improved flux resolution is obtained at the expense of significantly increased experimental, analytical and computational effort which limits widespread application of this approach. Direct application to laboratory and manufacturing-scale perfusion systems is virtually impossible given the cost associated with using labeled substrates. Isotope tracer studies thus have to be performed in scaled-down systems which to the extent possible must be metabolically representative of the larger bioreactors. Comparison of flux estimates from these isotope tracer studies with those from metabolite balancing will help validate the metabolite balancing approach that can subsequently be directly applied to large-scale systems. This leverages the advantages of both methods of flux estimation and application of this approach for perfusion cultivation of CHO cells is presented in Chapter 8.

Bibliography

[1] Vallino, J. J; Stephanopoulos, G. in *Frontiers in Bioprocesing*, Sikdar, S.; Bier, M.; Todd, P., Eds., pp 205–219. CRC Press Inc., Boca Raton, FL, 1990.

[2] Stephanopoulos, G.; Aristodou, A.; Nielsen, J. *Metabolic Engineering. Principles and Methodologies.* Academic Press, San Diego, 1998.

[3] Bonarius, H.; Hatzimanikatis, V.; Meesters, K.; de Gooijer, C. D.; Schmid, G.; Tramper, J. Metabolic flux analysis of hybridoma cells in different culture media using mass balances. *Biotechnol. Bioeng.*, **1996**, *50*, 229–318.

[4] Follstad, B. D.; Balcarcel, R. R.; Stephanopoulos, G.; Wang, D. I. Metabolic flux

analysis of hybridoma continuous culture steady state multiplicity. *Biotechnol Bioeng*, **1999**, *63*(6), 675–83.

[5] Varma, A.; Palsson, B. Metabolic flux balancing: Basic concepts, scientific and practical use. *Bio/Technology*, **1994**, *12*, 994–998.

[6] Aiba, S.; Matsuoka, M. Identification of metabolic model: Citrate production from glucose by Candida lipolytica. *Biotechnol. Bioeng.*, **1979**, *21*, 1373–1386.

[7] Papoutsakis, E. Equations and calculations for fermentations of butyric acid bacteria. *Biotechnol. Bioeng.*, **1984**, *26*, 174–187.

[8] Papoutsakis, E. Equations and calculations of product yields and preferred pathways for butanediol and mixed-acid fermentations. *Biotechnol. Bioeng.*, **1985**, *27*, 50–66.

[9] Cruz, H. J.; Ferreira, A. S.; Freitas, C. M.; Moreira, J. L.; Carrondo, M. J. Metabolic responses to different glucose and glutamine levels in baby hamster kidney cell culture. *Appl. Microbiol. Biotechnol.*, **1999**, *51*(5), 579–585.

[10] Cruz, H. J.; Moreira, J. L.; Carrondo, M. J. Metabolic shifts by nutrient manipulation in continuous cultures of BHK cells. *Biotechnol Bioeng*, **1999**, *66*(2), 104–13.

[11] Altamirano, C.; Illanes, A.; Casablancas, A.; Gámez, X.; Cairo, J.; Gòdia, C. Analysis of CHO cells metabolic redistribution in a glutamate-based defined medium in continuous culture. *Biotechnol. Prog.*, **2001**, *17*, 1032–1041.

[12] Nyberg, G. B.; Balcarcel, R. R.; Follstad, B. D.; Stephanopoulos, G.; Wang, D. I. Metabolism of peptide amino acids by Chinese hamster ovary cells grown in a complex medium. *Biotechnol Bioeng*, **1999**, *62*(3), 324–35.

[13] Bonarius, H.; Timmerarends, B.; de Gooijer, C.; Tramper, J. Metabolite-balancing techniques vs. 13C tracer experiments to determine metabolic fluxes in hybridoma cells. *Biotechnol Bioeng*, **1998**, *58*(2-3), 258–262.

[14] Bonarius, H.; Houtman, J. H.; Schmid, G.; de Gooijer, C. D.; Tramper, J. Error analysis of metabolic-rate measurements in mammalian-cell culture by carbon and nitrogen balances. *Cytotechnology*, **1999**, *29*, 167–175.

[15] Bonarius, H.; Houtman, J.; Schmid, G.; C.D., d. G.; Tramper, J. Metabolic-flux analysis of hybridoma cells under oxidative and reductive stress using mass balance. *Cytotechnology*, **2000**, *32*, 97–107.

[16] Bonarius, H.; Ozemere, A.; B, T.; Skrabal, P.; Tramper, J.; Schmid, G.; Heinzle, E. Metabolic-flux analysis of continuously cultured hybridoma cells using 13CO2 mass spectrometry in combination with 13C-Lactate nuclear magnetic resonance spectroscoopy and metabolite balancing. *Biotechnol. Bioeng.*, **2001**, *74*, 528–538.

[17] Europa, A. F.; Gambhir, A.; Fu, P. C.; Hu, W. S. Multiple steady states with distinct cellular metabolism in continuous culture of mammalian cells. *Biotechnol Bioeng*, **2000**, *67*(1), 25–34.

[18] Zupke, C.; Sinskey, A. J.; Stephanopoulos, G. Intracellular flux analysis applied to the effect of dissolved oxygen on hybridomas. *Appl. Microbiol. Biotechnol.*, **1995**, *44*(1-2), 27–36.

[19] Zupke, C.; Stephanopoulos, G. Modeling of isotope distributions and intrecellular fluxes in metabolic networks using atom mapping matrices. *Biotechnol. Prog.*, **1994**, *10*, 489–498.

[20] Zupke, C.; Stephanopoulos, G. Intracellular flux analysis in hybridomas using mass balances and In Vitro 13C NMR. *Biotechnol. Bioeng.*, **1995**, *45*, 292–303.

[21] Nadeau, I.; Sabatié, J.; Koehl, M.; Perrier, M.; Kamen, A. Human 293 cell metabolism in low glutamine-supplied culture: Interpretation of metabolic changes through metabolic flux analysis. *Metab. Eng.*, **2000**, *2*, 277–292.

[22] Theobald, U.; Mailinger, W.; Baltes, M.; Rizzi, M.; Reuss, M. In vivo analysis of metabolic dynamics in Saccharomyces cerevisiae. *Biotechnol. Bioeng.*, **1997**, *55*, 303–319.

[23] Fell, D.; Small, J. Fat synthesis is adipose tissue. An examination of stoichiometric constraints. *J. Biochem. (Tokyo).*, **1986**, *238*, 781–786.

[24] Majewski, R.; Domach, M. Simple constrained optimization view of acetate overflow in E. coli. *Biotechnol. Bioeng.*, **1990**, *35*, 732–738.

[25] Pramanik, J.; Keasling, J. A stoichiometric model of Escherichia coli metabolism. Incorporation of growth-rate-dependent biomass composition and mechanistic energy requirements. *Biotechnol. Bioeng.*, **1997**, *56*, 398–421.

[26] Savinell, J.; Palsson, B. Network analysis of intermediary metabolism using linear optimization. I. Development of mathematical formulation. *J. Theor. Biol.*, **1992**, *154*, 421–454.

[27] Savinell, J.; Palsson, B. Network analysis of intermediary metabolism using linear optimization. II. Interpretation of hybridoma cell metabolism. *J. Theor. Biol.*, **1992**, *154*, 455–473.

[28] Varma, A.; Boesch, B.; Palsson, B. Biochemical production capabilities of Escherichia coli. *Biotechnol. Bioeng.*, **1993**, *42*, 59–73.

[29] Varma, A.; Boesch, B.; Palsson, B. Stoichiometric interpretation if Escherichia coli glucose catabolism under various oxygenation rates. *Appl. Environ. Microbiol.*, **1993**, *59*, 2465–2473.

[30] Varma, A.; Palsson, B. Metabolic capabilities of Escherichia coli. II. Optimal growth patterns. *J. Theor. Biol.*, **1993**, *165*, 503–522.

[31] Varma, A.; Palsson, B. Metabolic capabilities of Escherichia coli. I. Synthesis of biosynthetic precursors and cofactors. *J. Theor. Biol.*, **1993**, *165*, 477–502.

[32] Varma, A.; Palsson, B. Stoichiometric fkux balance models quantitatively predict growth and metabolic by-product secretion in wild-type Escherichia coli E3110. *Appl. Environ. Microbiol.*, **1994**, *60*, 3724–3731.

[33] Varma, A.; Palsson, B. Predictions for oxygen supply control to enhance population stability of engineered production strains. *Biotechnol. Bioeng.*, **1994**, *43*, 275–285.

[34] Varma, A.; Palsson, B. Parametric sensitivity of stoichiometric flux balance models applied to wild-type Escherichia coli metabolism. *Biotechnol. Bioeng.*, **1995**, *45*, 69–79.

[35] Edwards, J.; Palsson, B. How will bioinformatics influence metabolic engineering. *Biotechnol. Bioeng.*, **1998**, *58*, 162–169.

[36] Wang, N. S.; Stephanopoulos, G. Application of macroscopic balances to the identification of gross measurement errors. *Biotechnol. Bioeng.*, **1983**, *25*, 2177–2208.

[37] Balcarcel, R. R.; Clark, L. Metabolic screening of mammalian cell cultures using well-plates. *Biotechnol. Prog.*, **2003**, *19*, 98–108.

[38] van Winden, W.; Heijnen, J.; Verheijen, P.; Grievink, J. A priori analysis of metabolic flux identifiability from 13C-Labeling data. *Biotechnol. Bioeng.*, **2001**, *74*, 505–516.

[39] van Winden, W.; Heijnen, J.; Verheijen, P. Cumulative bandomers: A new concept in fluxanalysis from 2D[13C, 1H] COSY NMR data. *Biotechnol. Bioeng.*, **2002**, *80*, 731–745.

[40] van Winden, W.; Schipper, D.; Verheijen, P.; Heijnen, J. Innovations in generation and analysis of 2D [13C, 1H] COSY NMR spectra for metabolic flux analysis purposes. *Metab. Eng.*, **2001**, *3*, 322–343.

[41] van Winden, W.; van Guilk, W.; Schipper, D.; Verheijen, P.; Krabben, P.; Vinke, J.; Heijnen, J. Metabolic flux and metabolic network analysis of Penicillium chrysogenum using 2D [13C, 1H] COSY NMR measurements and cumulative bandomer simulation. *Biotechnol. Bioeng.*, **2003**, *83*, 75–92.

[42] van Winden, W.; Verheijen, P.; Heijnen, J. Possible pitfalls of flux calculations based on 13C-labeling. *Metab. Eng.*, **2001**, *3*, 151–162.

[43] van Winden, W.; Wittmann, C.; Heinzle, E.; Heijnen, J. Correcting mass isotopomer distributions for naturally occuring isotpoes. *Biotechnol. Bioeng.*, **2002**, *80*, 477–479.

[44] Wiechert, W. 13C Metabolic flux analysis. *Metab. Eng.*, **2001**, *3*, 195–206.

[45] Wiechert, W. Modeling and simulation: tools for metabolic engineering. *J. Biotechnol.*, **2002**, *94*, 37–63.

[46] Schmidt, K.; Carlsen, M.; Nielsen, J.; Villadsen, J. Modeling isotopomer distributions in biochemical networks using isotopomer mapping matrices. *Biotechnol. Bioeng.*, **1997**, *56*, 831–840.

[47] Wiechert, W.; de Graaf, A. A. Bidirectional reaction steps in metabolic networks: I. Modeling and simulation of carbon isotope labeling experiments. *Biotechnol. Bioeng.*, **1997**, *55*, 101–117.

[48] Wiechert, W.; Siefke, C.; de Graaf, A. A.; Marx, A. Bidirectional reaction steps in metabolic networks: II. Flux estimation and stastical analysis. *Biotechnol. Bioeng.*, **1997**, *55*, 118–135.

[49] Wiechert, W.; Möllney, M.; Isermann, N.; Wurzel, M.; de Graaf, A. A. Bidirectional steps in metabolic networks: III. Explicit solution and analysis of isotopomer labeling systems. *Biotechnol. Bioeng.*, **1999**, *66*, 69–85.

Part II

pCO_2 in High-Density Perfusion Culture

Chapter 4

pCO_2 Reduction in Perfusion Systems[1]

4.1 Introduction

Mammalian cells are being increasingly used to produce recombinant proteins, given their ability to properly fold and glycosylate these proteins. While the majority of current manufacturing-scale processes are fed-batch, perfusion cultures can be required, for instance, when the product of interest is relatively unstable. The continuous nature of the perfusion process allows higher cell density cultivation, since toxic metabolites, such as lactate and ammonium, do not accumulate in the bioreactor. Cell densities on the order of 20 x 10^6 cells/mL can be maintained in the steady-state phase of perfusion cultivation for 100 days or more [1, 2]. High cell density coupled with high perfusion rates yields high volumetric productivity from perfusion cultivation.

High density perfusion cultivation, however, results in elevated bioreactor pCO_2, often on the order of 200 mm Hg [3, 4], significantly higher than physiological values (30 – 50 mm Hg). Elevated pCO_2 has been implicated in reduced growth, metabolism and productivity in addition to adverse effects on glycosylation [3, 5–15]. As bioreactor pH during perfusion cultivation is controlled at a pre-defined set point, high pCO_2 results in increased osmolality which can also negatively impact cell growth, metabolism and productivity [7, 8, 10, 16–21]. High pCO_2 is a consequence of both the cellular metabolism and the $NaHCO_3$ that is widely used as a buffer in the medium. In addition, $NaHCO_3$ is often added as a base to neutralize

[1] A version of this manuscript has been accepted for publication. Goudar, C.T., Matanguihan, R., Long, E., Cruz, C., Zhang, C., Piret, J.M. and Konstantinov, K.B. (2006) Decreased pCO_2 accumulation by eliminating bicarbonate addition to high-density cultures. *Biotechnology & Bioengineering.*

the lactate produced by the cells. High pCO_2 can also be a concern in late stage fed-batch cultivation but the problem is greater in perfusion bioreactors, as high pCO_2 values are maintained over the entire length of the production phase due to the typically higher cell concentration (Figure 4.1).

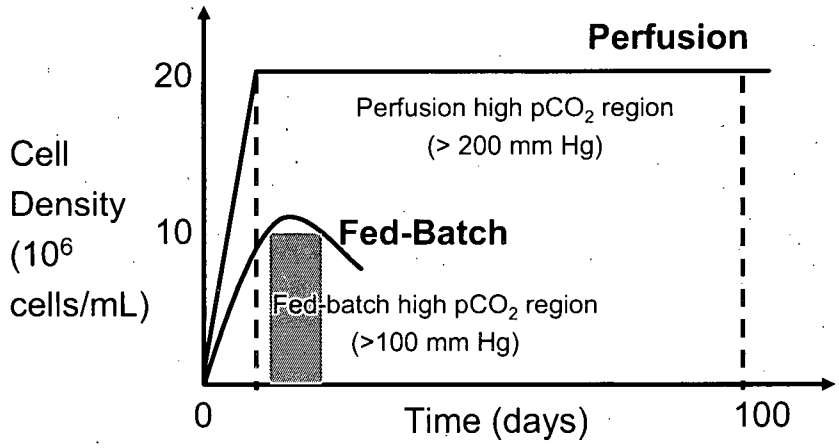

Figure 4.1: Bioreactor pCO_2 time profiles for mammalian cell cultivation in perfusion and fed-batch bioreactors. Perfusion pCO_2 remains high throughout steady-state operation while high pCO_2 can be a problem in late stages of fed-batch cultivation.

There is clearly a need for bioreactor pCO_2 reduction although there have been relatively few studies addressing pCO_2 removal and control in mammalian cell bioreactors [3, 12, 13]. Stripping is an obvious pCO_2 removal approach, but it has a limited impact in mammalian cell bioreactors. For CHO cells in a 500 L perfusion bioreactor, the ratio of oxygen and carbon dioxide transfer rates was 25:1 [3], thus much higher high gas flow rates would be necessary for adequate CO_2 stripping. There is an upper limit on sparging rates given the detrimental effects on cells [22, 23]. Macrosparging resulted in a significant pCO_2 reduction for CHO cells in fed-batch culture [13], but the maximum cell density was not reported and it is unlikely that it was high enough to be relevant to perfusion cultivation. Changing an impeller position yielded a 2-fold increase in the pCO_2 transfer rate [13], but such improvements cannot be expected in a well-mixed bioreactor. The inadequacy of stripping clearly indicates that a more attractive target to reduce bioreactor pCO_2 could be reduction at the source rather than removal after pCO_2 production and additions.

Engineering cellular metabolism to reduce pCO_2 production is not practical because cell lines are selected primarily on productivity and growth considerations. In fact, there are advantages to maintaining high rates of respiration to minimize lactic acid production.

The buffering components, on the other hand, offer the most potential for pCO_2 reduction and were the target of changes in this study. There have been some reports where reduced $NaHCO_3$ or $NaHCO_3$-free medium was used for mammalian cell cultivation [24–29], but pCO_2 reduction was not the primary objective in these studies and none were performed at manufacturing-scale.

This study evaluates the biotic and abiotic contributions to bioreactor pCO_2 in a perfusion system, and from these results, derives a simple pCO_2 reduction strategy based on minimizing abiotic pCO_2 contribution. The validity of this approach was verified both in laboratory and manufacturing-scale perfusion systems. Changes in cell growth, metabolism and protein productivity associated with pCO_2 reduction were also evaluated.

4.2 Theory

4.2.1 CO_2 Dynamics in a Mammalian Cell Bioreactor

Carbon dioxide produced by cells dissolves in the culture medium to form carbonic acid:

$$CO_{2(g)} \rightarrow CO_{2(aq)} \tag{4.1}$$

$$CO_{2(aq)} + H_2O \rightarrow H_2CO_3 \tag{4.2}$$

It is common practice [30] to combine the $CO_{2(aq)}$ and H_2CO_3 concentrations into H_2CO_3* ($CO_{2(aq)} + H_2CO_3 = H_2CO_3$*). Further dissociation of H_2CO_3* into HCO_3^- and CO_3^{2-} can be written as:

$$H_2CO_3^* \leftrightarrow HCO_3^- + H^+; \qquad K_1 = 10^{-6.35} \tag{4.3}$$

$$HCO_3^- \leftrightarrow CO_3^{2-} + H^+; \qquad K_2 = 10^{-10.33} \tag{4.4}$$

where K_1 and K_2 are equilibrium constants under standard conditions (temperature = 25 °C, ionic strength = 0). These must, however, be corrected to reflect cultivation conditions and K_1^c and K_2^c were estimated to be $10^{-6.07}$ and $10^{-10.04}$, respectively, at 37 °C and 0.1 M ionic strength using the vant-Hoff and Davies equations [31, 32]. Carbon dioxide produced by the cells thus exists as combination of H_2CO_3*, HCO_3^- and CO_3^{2-} whose relative amounts

at the cultivation pH of 6.8 were determined as:

$$\%\ \text{of}\ H_2CO_3^* = \left(\frac{[H^+]^2}{[H^+]^2 + [H^+]\,K_1^c + K_1^cK_2^c}\right) 100 = 15.7\% \quad (4.5)$$

$$\%\ \text{of}\ HCO_3^- = \left(\frac{[H^+]\,K_1^c}{[H^+]^2 + K_1^c + K_1^cK_2^c}\right) 100 = 84.3\% \quad (4.6)$$

$$\%\ \text{of}\ CO_3^{2-} = \left(\frac{K_1^cK_2^c}{[H^+]^2 + K_1^c + K_1^cK_2^c}\right) 100 = 5 \times 10^{-4}\% \quad (4.7)$$

Thus HCO_3^- is the dominant species at pH 6.8 followed by $H_2CO_3^*$ while CO_3^{2-} is virtually non-existent. Additional information on medium solution chemistry and associated computer programs are presented in Appendix B.

4.2.2 Buffering Action of $NaHCO_3$ and Na_2CO_3

The fate of added $NaHCO_3$, either through the medium or separately for pH control, is also governed by Eqs.(4.3) and (4.4). Complete dissociation of $NaHCO_3$ results in the formation of Na^+ and HCO_3^- ions, of which a portion of the latter is converted to $H_2CO_3^*$

$$NaHCO_3 \rightarrow Na^+ + HCO_3^- \quad (4.8)$$

$$HCO_3^- + H^+ \leftrightarrow H_2CO_3^* \quad (4.9)$$

The relative concentrations of $H_2CO_3^*$ and HCO_3^- at pH 6.8 are 15.7 and 84.3%, respectively (from Eqs. 4.5 and 4.6) such that 5.4 moles of $NaHCO_3$ are required to neutralize 1 mole of H^+ in the bioreactor.

If instead Na_2CO_3 is used as the base for pH control, complete dissociation results in the formation of CO_3^{2-}, which is essentially all converted to HCO_3^- under culture conditions:

$$Na_2CO_3 \rightarrow 2Na^+ + CO_3^{2-} \quad (4.10)$$

$$CO_3^{2-} + H^+ \leftrightarrow HCO_3^- \quad (4.11)$$

The significantly enhanced buffering capacity of Na_2CO_3 is due to Eq.(4.11) where 1 mole of Na_2CO_3 neutralizes 1 mole of H^+. Futher conversion of HCO_3^- to $H_2CO_3^*$ proceeds according to Eq.(4.9) such that 0.85 moles of Na_2CO_3 are required to neutralize 1 mole of H^+ in the bioreactor. A 84% improvement in buffer capacity and a corresponding decrease in the abiotic contribution to bioreactor pCO_2 can thus be expected when $NaHCO_3$ is replaced with Na_2CO_3.

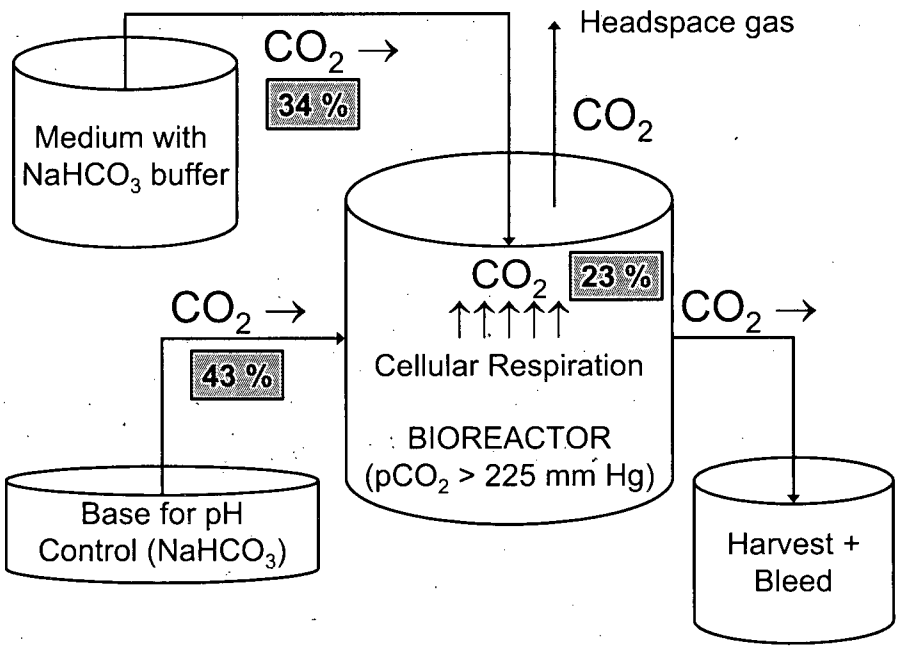

Figure 4.2: Calculated contributions from biotic (cellular respiration) and abiotic (medium and base $NaHCO_3$) sources to bioreactor pCO_2 during perfusion cultivation of BHK cells.

4.2.3 Contributors to Bioreactor pCO_2

Cellular respiration makes up the biotic component of bioreactor pCO_2 (abiotic contributors are $NaHCO_3$ and Na_2CO_3). For BHK cells in a perfusion bioreactor at 20 x 10^6 cells/mL, the carbon dioxide evolution rate was 8 pmol/cell-day, contributing 1.92 moles/day from cellular respiration to bioreactor pCO_2. Daily addition of 0.71 M $NaHCO_3$ as a base for pH control was 5 L, from which the contribution of the base was estimated as 3.57 moles/day. Medium (with 23.8 mM $NaHCO_3$) flow rate was 120 L/day resulting in a daily medium contribution of 2.86 moles. From the above data, the percentage contributions of cellular respiration, base, and medium to bioreactor pCO_2 were 23, 43 and 34%, respectively (Figure 4.2). Eliminating $NaHCO_3$ from the medium should thus reduce bioreactor pCO_2 by 34% while replacing $NaHCO_3$ with Na_2CO_3 as the base should reduce bioreactor pCO_2 by 36% (84% of 43). Overall, $NaHCO_3$ elimination from the medium and replacement with Na_2CO_3 as base are expected to lower bioreactor pCO_2 by 70% bringing it in the 60 – 80 mm Hg range, much closer to physiological values of 30 – 50 mm Hg.

4.3 Materials and Methods

4.3.1 Cell Line, Medium and Bioreactor System

Multiple perfusion BHK cell cultivations were performed with glucose and glutamine as the main carbon and energy sources in a proprietary medium formulation with either 2 g/L $NaHCO_3$ or a MOPS-Histidine mixture as the buffering component. Laboratory-scale experiments were conducted in 15 L bioreactors (Applikon, Foster City, CA) with a 12 L working volume. The temperature was maintained at 35.5 °C and the agitation at 70 rpm. The dissolved oxygen (DO) concentration was maintained at 50% air saturation using oxygen-nitrogen mixture aeration through a silicone membrane. Bioreactor pH was maintained at 6.8 by the addition of either 0.71 M $NaHCO_3$ or 0.57 M Na_2CO_3. The bioreactors were inoculated at an initial cell density of approximately 1 x 10^6 cells/mL and, with perfusion, the cells were allowed to accumulate up to a density of 20 x 10^6 cells/mL. Steady-state bioreactor cell density was maintained at this level by automatically discarding cells from the bioreactor based on optical density measurements [1]. Similar operating protocols and identical set points were maintained in the manufacturing-scale bioreactor. The effect of macrosparging on CO_2 stripping was also examined in the manufacturing-scale bioreactor.

4.3.2 Analytical Methods

Samples from the bioreactor were taken daily for cell density and viability analysis using the CEDEX system (Innovatis, Bielefeld, Germany). The samples were subsequently centrifuged (Beckman Coulter, Fullerton, CA) and the supernatants were analyzed for nutrient and metabolite concentrations. Glucose, lactate, glutamine and glutamate concentrations were determined using a YSI Model 2700 analyzer (Yellow Springs Instruments, Yellow Springs, OH) while ammonium was measured by an Ektachem DT60 analyzer (Eastman Kodak, Rochester, NY). The pH and DO were measured online using retractable electrodes (Mettler-Toledo Inc., Columbus, OH) and their measurement accuracy was verified through off-line analysis in a Rapidlab® 248 blood gas analyzer (Bayer HealthCare, Tarrytown, NY). The same instrument also measured the dissolved CO_2 concentration. On-line measurements of cell concentration were made with a retractable optical density probe (Aquasant Messtechnik, Bubendorf, Switzerland), calibrated with the CEDEX cell concentration estimates.

4.3.3 Estimation of Specific Rates

Growth rate, specific productivity, nutrient consumption and metabolite production rates were calculated from mass balance expressions across the bioreactor and cell retention device and details are presented in Appendix H. Since bioreactor cell density was held constant by bleeding cells from the bioreactor and death rates were not accounted for, the growth rate, μ (1/day), was a function of the bleed rate, F_b (L/day), and the viable cell density in the harvest stream, X_V^H (10^9 cells/L):

$$\mu = \frac{F_b}{V} + \frac{F_h}{V}\left(\frac{X_V^H}{X_V^B}\right) + \frac{1}{X_V^B}\left(\frac{dX_V^B}{dt}\right) \tag{4.12}$$

where V is the bioreactor volume (L), F_h the harvest flow rate (L/day), X_V^B the bioreactor viable cell density (10^9 cells/L) and t the time (day). The specific consumption rates of glucose and glutamine were determined from the glucose and glutamine concentrations in the bioreactor:

$$q_G = \frac{1}{X_V^B}\left(\frac{F_m\,(G_m - G)}{V} - \frac{dG}{dt}\right) \tag{4.13}$$

$$q_{Gln} = \frac{1}{X_V^B}\left(\frac{F_m\,(Gln_m - Gln)}{V} - \frac{dGln}{dt} - k_{Gln}\,Gln\right) \tag{4.14}$$

where F_m is the medium flow rate (L/day) q_G and q_{Gln} are the specific consumption rates of glucose and glutamine, respectively, (pmol/cell-day), G_m and Gln_m their respective concentrations in the fed medium (mM) and G and Gln their bioreactor concentrations (mM). The kinetics of abiotic glutamine degradation were assumed to be first-order with a rate constant k_{Gln} that was estimated as 8.94 x 10^{-4} h^{-1} [33]. Assuming the incoming medium to be free of lactate and ammonium, the specific production rates of lactate q_L and ammonium q_A were estimated as:

$$q_L = \frac{1}{X_V^B}\left(\frac{F_m L}{V} + \frac{dL}{dt}\right) \tag{4.15}$$

$$q_A = \frac{1}{X_V^B}\left(\frac{F_m A}{V} + \frac{dA}{dt} - k_{Gln}\,Gln\right) \tag{4.16}$$

where L and A are the bioreactor lactate and ammonium concentrations, respectively (mM). The expression for specific protein productivity is analogous to that for lactate production.

4.4 Results

4.4.1 Bioreactor pCO_2 before $NaHCO_3$ Elimination from Medium and Base

Figure 4.3 shows time profiles of viable cell density and bioreactor pCO_2 for BHK and CHO cells cultivated in manufacturing-scale perfusion reactors (100 – 500 L working volume). The medium for both cultivations contained 23.8 mM $NaHCO_3$ while the base added to control pH was 0.71 M $NaHCO_3$ for the BHK and 0.3 M NaOH for the CHO cultivation. In both cases, the bioreactors were inoculated at initial cell densities of ~1 x 10^6 cells/mL and the target steady-state cell density was 20 x 10^6 cells/mL (actual steady-state cell densities were 20.5 ± 1.6 x 10^6 cells/mL for the BHK and 21.2 ± 2.2 x 10^6 cells/mL for the CHO cultivation). Bioreactor pCO_2, in both cases, was ~70 mm Hg upon inoculation and this value increased over the cell accumulation phase, leveling out during steady-state cultivation. Average steady-state pCO_2 values were 238 ± 16 for the BHK and 193 ± 13 mm Hg for the CHO cultivation. Higher pCO_2 values would have resulted for the CHO cells if $NaHCO_3$ had been used in place of 0.3 M NaOH to control pH. The Figure 4.3 data illustrate the need for pCO_2 reduction during perfusion cultivation of mammalian cells at high densities.

4.4.2 pCO_2 Reduction Strategy

A strategy that involved the alteration of medium and external base compositions was used for bioreactor pCO_2 reduction. Candidates for $NaHCO_3$ replacement included histidine and iminodiacetic acid as complexing agents and 3 (N-morpholino) propanesulfonic acid (MOPS), N.N bis (2-hydroxyethyl) 2 aminoethanesulphonic acid (BES), N tris (hydroxymethyl) 2 aminoethanesulphonic acid (TES), tris (hydroxymethyl) aminoethane (TRIZMA), N (2-hydroxyethyl) piperazine N 2 ethanesulfonic acid (HEPES) and Piperazine 1,4 bis(2-ethanesulfonic acid) (PIPES) as buffers [34]. Based on the favorable growth, viability and metabolism obtained with a MOPS-histidine mixture, this was selected as the replacement for $NaHCO_3$ in the cultivation medium. The MOPS pK_a of 7.2 suggested an effective pH buffering range of 6.5 – 7.9 to ensure robust buffering during BHK cultivation (pH set point = 6.8). Histidine also serves as a minor contributor to buffering under culture conditions ($pK_a = 6$) but was primarily used to minimize precipitation in the medium feed line at the point of medium and base contact. This convergence of medium and base lines outside the bioreactor reduced localized areas of high pH in the bioreactor that result from direct base addition. Cell aggregation and death have been associated with direct base

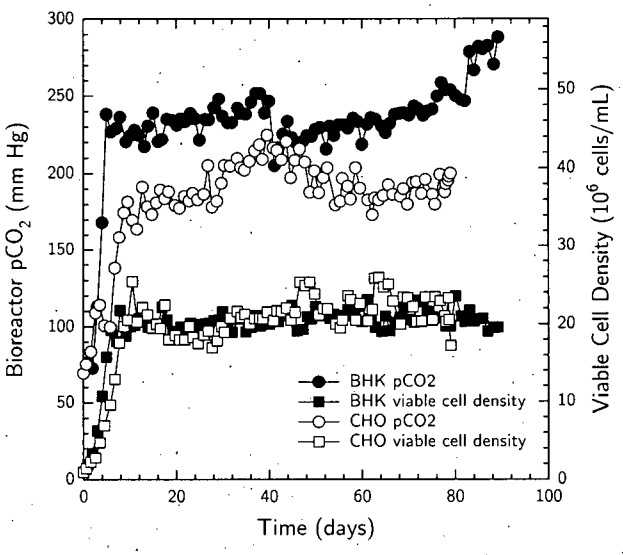

Figure 4.3: Time profiles of bioreactor pCO_2 and viable cell density for BHK and CHO cells in manufacturing-scale perfusion bioreactors. Bioreactor medium in both cases contained 23.8 mM $NaHCO_3$ as the buffer. Base usage was 0.71 M $NaHCO_3$ for the BHK cultivation and 0.3 M NaOH for the CHO cultivation.

addition and these problems are especially severe for perfusion systems given their long-term operation [35]. The imidazole moiety in histidine is primarily responsible for metal ion binding with the unshared electron pair on N-3, the most energetically favored coordination site for metal ions [36, 37]. Multiple bioreactor experiments (data not shown) defined, for our cells, estimated concentration ranges for MOPS and histidine that provide the required buffering and complexing action without adversely affecting cell growth (Figure 4.4). Histidine concentrations >10 mM were necessary to eliminate precipitation while concentrations >20 mM inhibited growth. MOPS did not inhibit the growth of the cells tested as long as the concentration was <30 mM.

Results from BHK cells in perfusion culture at 12 L working volume where sequential medium and base modifications were made are shown in Figure 4.5. The highest bioreactor pCO_2 levels were observed when $NaHCO_3$ was present both in the medium and base (229 $\pm$ 19 mm Hg) and these values decreased upon $NaHCO_3$ elimination (Figure 4.5). Eliminating $NaHCO_3$ from the medium reduced bioreactor pCO_2 to 150 $\pm$ 15 mm Hg, a 34.5% reduction close to the theoretically expected 34% reduction. When $NaHCO_3$ was eliminated from both the medium and the base, the pCO_2 was 96 $\pm$ 6 mm Hg, a 58.1% reduction, slightly lower than the expected 70%. This preliminary experiment confirmed that theoretically expected

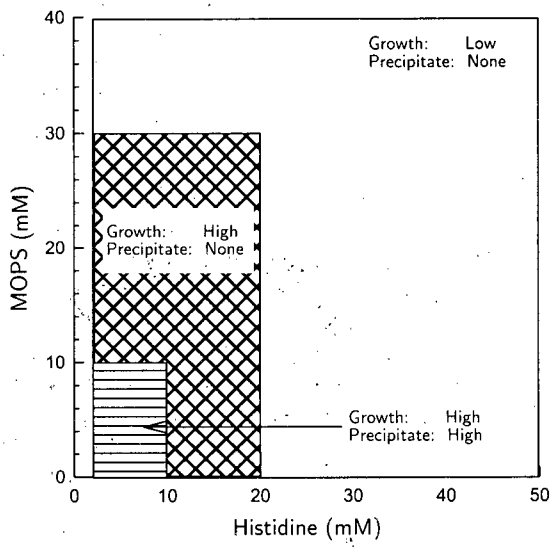

Figure 4.4: Influence of MOPS and histidine concentrations on cell growth and precipitation in the medium feed line. Histidine in the 10–20 mM range and MOPS in the 10–30 mM range did not adversely influence cell growth and prevented precipitation in the medium feed line.

pCO_2 reductions could be substantial and readily attained.

4.4.2.1 Bioreactor Operation after $NaHCO_3$ Elimination

Additional experiments were performed to verify the extent of pCO_2 reduction that could be obtained by eliminating $NaHCO_3$ from the cultivation medium and base. Time profiles of bioreactor pCO_2 and viable cell density for 4 long-term BHK perfusion cultivations are shown in Figure 4.6. The MOPS-histidine mixture was used as the medium buffer while Na_2CO_3 was the external base. Overall, average pCO_2 values ranged from 68 – 85 mm Hg and were significantly lower than the ~230 mm Hg observed when $NaHCO_3$ was present (Figures 4.3 and 4.5). Using a reference pCO_2 value of 229 mm Hg from phase A in Figure 4.5, bioreactor pCO_2 reductions were 63, 70, 69 and 66%, respectively, for Figures 4.6a, 4.6b, 4.6c and 4.6d, consistent with the theoretically expected 70% reduction.

A 33-day manufacturing-scale experiment was also performed under $NaHCO_3$-free conditions to check the transferability of results from laboratory-scale bioreactors. Time profiles of bioreactor pCO_2 and viable cell density from the manufacturing-scale bioreactor are shown in Figure 4.7 along with their respective steady-state averages. The steady-state pCO_2 average was 84 ± 7 mm Hg reflective of a 65% reduction compared to 238 ± 16

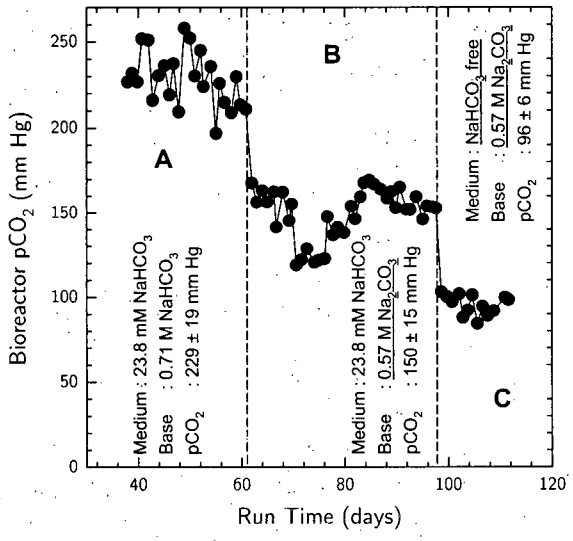

Figure 4.5: Average bioreactor pCO_2 for BHK cells in perfusion culture at 20 x 10^6 cells/mL. $NaHCO_3$ was present both in the medium and base for phase A and was replaced with Na_2CO_3 as the base for phase B. Phase C was $NaHCO_3$-free with MOPS-Histidine mixture replacing it in the medium and Na_2CO_3 replacing it as the base. Bioreactor pCO_2 reductions were 34.5 and 58.1% for phases B and C, respectively, when compared with phase A.

mm Hg that was observed when $NaHCO_3$ was present in both the medium and external base (Figure 4.3). Laboratory-scale pCO_2 reductions (Figure 4.6) were thus reproducible at manufacturing-scale (Figure 4.7).

4.4.3 Effect of Reduced pCO_2 on Growth, Metabolism and Productivity

Figure 4.8 shows a comparison of normalized growth rate and specific protein productivity between the reference condition (pCO_2 ~230 mm Hg) and the low pCO_2 cultivations from Figures 4.6 and 4.7. While both the specific growth rate and productivity averages were characterized by high standard deviations, results from a t-test (two-sided, assuming independent groups and unequal variances) indicated that growth rate and productivity increases at reduced pCO_2 values were significant in all 5 cultivations ($p<0.005$). The growth rate increase ranged from 68 – 123% while that for productivity was 58 – 92% under reduced pCO_2.

Glucose consumption and lactate production rates also increased ($p<0.005$) at reduced pCO_2 and ranged from 23 – 31% and 39 – 69%, respectively (Figure 4.9). There were thus

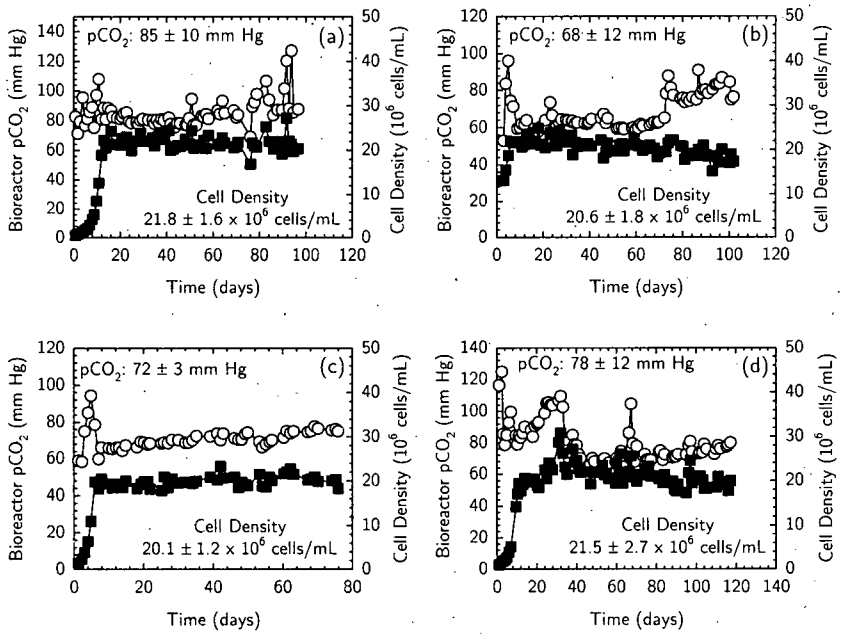

Figure 4.6: Time profiles of pCO_2 and viable cell density for BHK cells in 15 L perfusion bioreactors when medium containing MOPS-histidine buffer ($NaHCO_3$-free) was used along with 0.57 M Na_2CO_3 as the base for pH control. Bioreactor pCO_2 and cell density values are shown are mean ± standard deviation for the steady-state phase of the cultivation.

increases in cell growth, metabolism and protein productivity at reduced bioreactor pCO_2.

Metabolic flux analysis was performed using a reduced metabolic model [38] employing experimentally measured cell-specific rates for glucose, lactate and oxygen. All fluxes were higher at reduced pCO_2 indicating a general increase in metabolic activity at pCO_2 values closer to the physiological range. Increase in the glycolytic and lactate fluxes were 35 – 57% and 37 – 62%, respectively, while those for the TCA cycle and oxygen consumption fluxes were 35 – 55% and 34 – 52%, respectively (Figure 4.10). The consistency index, h, for these data sets was between 0.03 and 2.23 suggesting no gross error in experimental data.

4.5 Discussion

We have demonstrated pCO_2 reduction on the order of 60 – 70% in high-density BHK cell perfusion cultures. This reduction was achieved by eliminating additions of $NaHCO_3$ from the medium and the pH control base. The robustness of this preventive approach was shown by the relatively stable steady–state pCO_2 profiles in perfusion runs (Figures 4.6

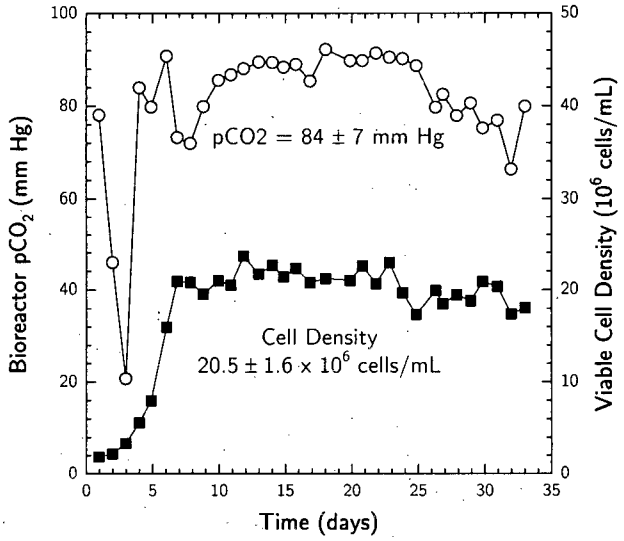

Figure 4.7: Time profiles of pCO_2 and viable cell density for BHK cells in a manufacturing-scale perfusion bioreactor when medium containing MOPS-histidine buffer ($NaHCO_3$-free) was used along with 0.57 M Na_2CO_3 as the base for pH control. Cell density and pCO_2 values are shown are mean ± standard deviation for the steady-state phase of the cultivation. Bioreactor pCO_2 and viable cell density for $NaHCO_3$ containing medium and base in an identical bioreactor are shown in Figure 4.3.

and 4.7) that together included over 400 days of bioreactor operation. Laboratory results were reproduced at the manufacturing scale, a major advantage as development work at this scale was minimized. It should be noted that there was no direct closed loop control of pCO_2 in any of these experiments. There was only an indirect control of bioreactor pCO_2 since all bioreactors were operated at a constant cell specific perfusion rate.

4.5.1 Comparison of Growth, Productivity and Metabolism with Previous Studies

The general trends in growth rate and specific protein productivity upon pCO_2 reduction observed here are similar to reports for other cell lines in perfusion or fed-batch cultures, though with cell-to-cell variability. A BHK perfusion culture bioreactor with a 40 to 280 mm Hg pCO_2 increase had both the growth rate and the specific productivity decrease by 30% [12]. For CHO cells in perfusion culture with a high glucose concentrations, the growth rate decreased by 57% when the pCO_2 was increased from 53 to 228 mm Hg, but the cell specific antibody productivity was almost unchanged [39]. Increasing pCO_2 from 36 to 148

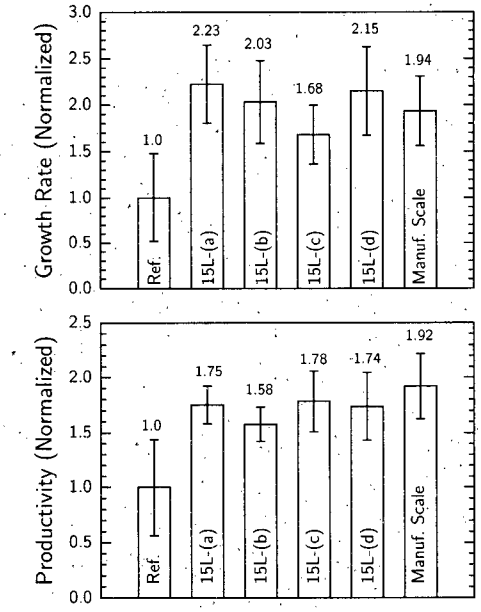

Figure 4.8: Comparison of normalized growth rate and specific productivity under reference ($NaHCO_3$-containing) conditions with $NaHCO_3$-free perfusion cultivations. Time profiles of bioreactor pCO_2 for the a to d 15 L bioreactors are shown in Figure 4.6 while that for the manufacturing-scale bioreactor is shown in Figure 4.7. There was a significant ($p<0.005$) increase in growth rate and specific productivity upon $NaHCO_3$ elimination in all cases.

mm Hg during perfusion cultivation decreased CHO cell density by 33% (reflecting reduced growth rate) and specific productivity by 44% [3]. Under glucose limiting conditions, for a similar pCO_2 increase, the growth rate decreased by 38% along with a 15% reduction in specific antibody productivity.

The growth rate of NS/0 cells decreased when pCO_2 increased from 60 to 120 mm Hg [6]. Scale-up of a fed-batch process resulted in pCO_2 values of 179 $\pm$ 9 mm Hg in a 1000 L bioreactor and a 40% decrease in specific productivity was seen under these conditions compared to a pCO_2 value of 68 $\pm$ 13 mm Hg in a 1.5 L laboratory-scale bioreactor [13]. Glucose consumption rates decreased in a dose-dependent fashion for hybridoma cells in T-25 flasks [8] with a 40% decrease observed when the pCO_2 increased from 40 to 250 mm Hg (osmolality held constant at 320 mOsm/kg). Similar observations were made for lactate production that decreased by 45% for the same pCO_2 increase. We have also observed increases in glucose consumption and lactate production rates at reduced pCO_2 (Figure 4.9).

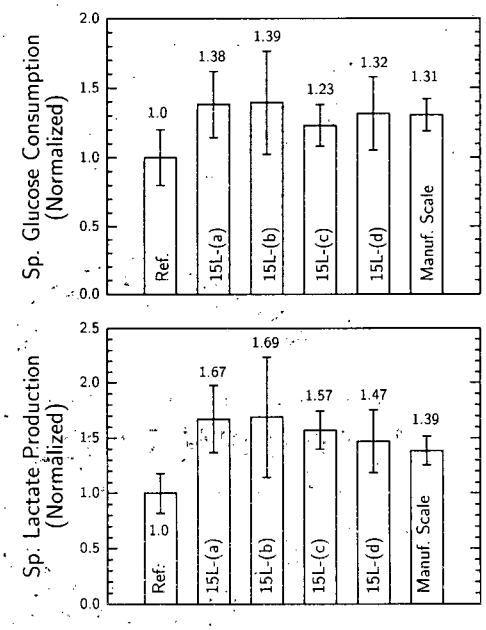

Figure 4.9: Comparison of normalized glucose consumption and lactate production rates under reference ($NaHCO_3$-containing) conditions with $NaHCO_3$-free perfusion cultivations. Time profiles of bioreactor pCO_2 for the a to d 15 L bioreactors are shown in Figure 4.6 while that for the manufacturing-scale bioreactor is shown in Figure 4.7. There was a significant ($p<0.005$) increase in glucose consumption and lactate production upon $NaHCO_3$ elimination in all cases.

4.5.2 Impact of high pCO_2 on Osmolality

High osmolality can be caused by high pCO_2 and while elevated osmolality has not been consistently shown to reduce growth rate and specific productivity, it has had a negative interaction effect when pCO_2 values were also high [8, 10]. For CHO cell cultivation in 6-well plates [10], growth rate and specific tissue plasminogen activator (tPA) productivity decreased 31% and 42%, respectively, when the pCO_2 increased from 36 to 250 mm Hg (constant osmolality at 310 mOsm/kg). An increase in osmolality from 310 to 376 mOsm/kg had no adverse impact on growth rate and tPA production for pCO_2 values in the 36 – 250 mm Hg range. The highest reduction in growth rate (53%) was seen when both pCO_2 (250 mm Hg) and osmolality values (376 mOsm/kg) were high. For CHO cells cultivated in 2 L batch bioreactors [21], the growth rate decreased, but only by 9% when the pCO_2 increased from 50 to 150 mm Hg (osmolality controlled at 350 mOsm/kg) while a 60% reduction was reported when the osmolality increased from 316 to 450 mOsm/kg (pCO_2 at 38 mm

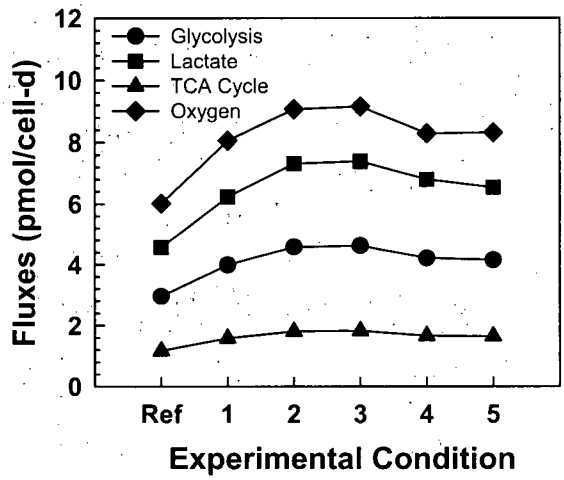

Figure 4.10: Effect of bioreactor pCO_2 on key metabolic fluxes. The presentation is similar to that in Figures 4.8 and 4.9. The reference condition indicates high pCO_2, conditions 1 – 4 are for low pCO_2 in 15 L bioreactors and condition 5 is low pCO_2 in a manufacturing-scale bioreactor.

Hg). For hybridoma cells cultivated in T-25 flasks [8], high pCO_2 and osmolality reduced growth rate in a dose-dependent fashion. The growth rate decreased by about 40% when pCO_2 increased from 40 to 250 mm Hg (osmolality constant at 320 mOsm/kg) and a similar decrease was seen when the osmolality increased to 435 mOsm/kg (pCO_2 constant at 40 mm Hg). Growth rate decreased by 84% for pCO_2 and osmolality values of 195 mm Hg and 435 mOsm/kg, respectively, suggesting a negative interaction effect. By reducing base addition, the pCO_2 reduction strategy proposed in this study also minimizes osmolality increases and the adverse effects associated with combined high pCO_2 and osmolality.

4.5.3 High pCO_2 and Intracellular pH

High pCO_2 has been reported to decrease intracellular pH (pH_i) with significant implications for cell growth and metabolism [40, 41]. For hybridoma cells cultivated in T-25 flasks, a 0.1 – 0.2 unit pH_i reduction was observed at pCO_2 values higher than 140 mm Hg when compared with a 40 mm Hg control [8]. While pH_i was not measured in this study, earlier work from our laboratory with BHK cells in perfusion culture observed a 0.2 unit reduction in pH_i when pCO_2 increased from 40 to 250 mm Hg [4]. Decreases in pH_i on the order of 0.2 units have been shown to significantly reduce the carbon flux through glycolysis [42–45]. One mechanism for this decrease is the strong dependence of phosphofructokinase activity

on pH [46]. This is consistent with the 23 – 31% increase in glucose consumption rates that were observed in this study at reduced pCO_2 values.

Since changes to pH_i affect the ionization states of all peptides and proteins, it is actively regulated [47, 48]. Under conditions of high external pCO_2, diffusion into the cell followed by rapid conversion to H_2CO_3 through the action of carbonic anhydrase can cause a decrease in pH_i [49–51]. Cells try to maintain pH homeostasis through the action of acid extruders which include the vacuolar-type H^+ pump [41], the Na^+/H^+ exchanger [52], the Na^+ driven Cl^-/HCO_3^- exchanger [51] and the electrogenic Na^+/HCO_3^- cotransporter [53]. The extrusion of H^+ from cells and the intake of HCO_3^- require energy [47] resulting in an increased energy demand for maintenance. This could be partially responsible for the reduced growth rate at elevated pCO_2 reported by most studies.

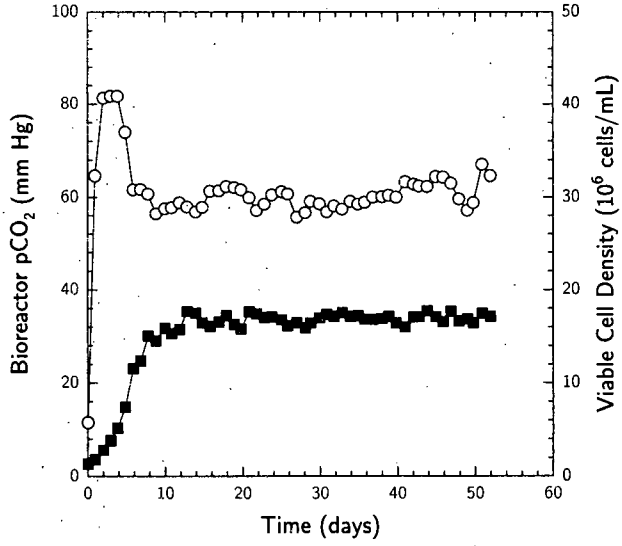

Figure 4.11: Time profiles of pCO_2 (○) and viable cell density (■) for BHK cells in a manufacturing-scale perfusion bioreactor when medium containing MOPS-histidine buffer ($NaHCO_3$-free) was used along with 0.57 M Na_2CO_3 as the base for pH control and oxygen sparged at 0.015 vessel volumes/minute. These pCO_2 values can be directly compared with those in Figure 4.7 despite differences in cell density since both reactors were operated at identical cell specific perfusion rates.

4.5.4 Closed-loop pCO_2 Control

Figures 4.6 and 4.7 show pCO_2 spikes in the beginning of the experiments when cell concentrations were increasing from initial cell densities. Use of $NaHCO_3$-free medium results

in low bioreactor pCO_2 values, often less than 15 mm Hg. This will severely inhibit cell growth unless CO_2 is added to increase bioreactor pCO_2 to 40 mm Hg or higher. Since closed loop pCO_2 control was not employed, manual CO_2 addition was responsible for the variability in bioreactor pCO_2 during the cell scale-up phase. Closed loop pCO_2 control is currently being tested.

Despite ~70% reduction in bioreactor pCO_2 after medium and base changes (Figures 4.6 and 4.7), the average values ranged from 68 to 85 mm Hg, still higher than the physiological range (30 – 50 mm Hg). While additional reduction is possible through NaOH pH control, medium precipitation and cell death associated with its use do not make this an attractive option for long-term cultivation. Stripping CO_2 with macrosparging reduced pCO_2 in a manufacturing-scale bioreactor to 60 mm Hg (Figure 4.11), a 29% reduction when compared to non-sparged conditions (84 mm Hg in Figure 4.7). Thus, additional pCO_2 reduction is possible with macrosparging and this approach is being investigated with the closed-loop bioreactor pCO_2 control

4.6 Conclusions

We have presented a practical strategy for pCO_2 reduction in high-density perfusion bioreactors by eliminating $NaHCO_3$ from the medium and base used for pH control. This method reduces pCO_2 at the source in contrast to stripping techniques that rely on CO_2 removal after it has been produced. By minimizing the indirect contributions to bioreactor pCO_2, a 63 – 70% pCO_2 reduction was achieved in laboratory-scale bioreactors and the results were reproduced at manufacturing-scale. Significant increases in cell growth, metabolism and protein productivity were obtained upon pCO_2 reduction and these trends were consistent with other published studies. This approach can be readily implemented in established manufacturing processes since no changes to the bioreactor physical configuration or operational parameters are necessary. It is robust because pCO_2 reductions are guaranteed once medium and base changes are made. The general nature of this approach makes it an attractive option for pCO_2 reduction in fed-batch cultivations as well.

Bibliography

[1] Chuppa, S.; Tsai, S.; Yoon, S.; Shackelford, S.; Rozales, C.; Bhat, R.; Tsay, G.; Matanguihan, R.; Konstantinov, K.; Naveh, D. Fermentor temperature as a tool for control of high-density perfusion cultures of mammalian cells. *Biotechnol. Bioeng.*, **1997**, *55*, 328–338.

[2] Konstantinov, K. B.; Tsai, Y.; Moles, D.; Matanguihan, R. Control of long-term perfusion Chinese hamster ovary cell culture by glucose auxostat. *Biotechnol Prog*, **1996**, *12*(1), 100–109.

[3] Gray, D.; Chen, S.; Howarth, W.; Inlow, D.; Maiorella, B. CO2 in large-scale and high-density CHO cell perfusion culture. *Cytotechnology*, **1996**, *22*, 65–78.

[4] Taticek, R.; Petersen, S.; Konstantinov, K.; Naveh, D. Effect of dissolved carbon dioxide and bicarbonate on mammalian cell metabolism and recombinant protein productivity in high density perfusion culture. in *Cell Culture Engineering VI*, San Diego, CA, 1998.

[5] Anderson, D.; Goochee, C. The effect of cell culture conditions on the oligosaccharide structures of secreted glycoproteins. *Curr. Opin. Biotechnol.*, **1994**, *5*, 546–549.

[6] Aunins, J.; Henzler, H.-J. in *Biotechnology: A multi-volume comprehensive treatise*, Stephanopoulos, G.; Rehm, H.-J.; Reed, G.; Puhler, A.; Stadler, P., Eds., volume 3, p 817p. VCH Verlag, Weinheim, 1993.

[7] deZengotita, V.; Kimura, G.; Miller, W. Effects of CO2 and osmolality on hybridoma cells: Growth, metabolism and monoclonal antibody production. *Cytotechnology*, **1998**, *28*, 213–227.

[8] deZengotita, V.; Schmeizer, A.; Miller, W. Characterization of hybridoma cell response to elevated pCO2 and osmolality: Intracellular pH, cell size, apoptosis, and metabolism. *Biotechnol. Bioeng.*, **2002**, *77*, 369–380.

[9] Garnier, A.; Voyer, R.; Tom, R.; Perret, S.; Jardin, B.; Kamen, A. Dissolved carbon dioxide accumulation in a large scale and high density production ot TGFb receptor with baculovirus infected Sf-9 cells. *Cytotechnology*, **1996**, *22*, 53–63.

[10] Kimura, R.; Miller, W. Effects of elevated pCO2 and/or osmolality on the growth and recombinant tPA production of CHO cells. *Biotechnol. Bioeng.*, **1996**, *52*, 152–160.

[11] Kimura, R.; Miller, W. Glycosylation of CHO-derived recombinant tPA produced under elevated pCO2. *Biotechnol. Prog.*, **1997**, *13*, 311–317.

[12] Matanguihan, R.; Sajan, E.; Zachariou, M.; Olson, C.; Michaels, J.; Thrift, J.; Konstantinov, K. Solution to the high dissolved DCO2 problem in high-density perfusion culture of mammalian cells. in *Animal Cell Technology: From Target to Market, 17th ESACT Meeting, Tylosand, Sweden*, pp 399–402. Kluwer, 2001.

[13] Mostafa, S.; Gu, X. Strategies for improved dCO2 removal in large-scale fed-batch cultures. *Biotechnol. Prog.*, **2003**, *19*, 45–51.

[14] Zanghi, J.; Schmelzer, A.; Mendoza, T.; Knop, R.; Miller, W. Bicarbonate concentration and osmolality are key determinants in the inhibition of CHO cell polysialylation under elevated pCO2 or pH. *Biotechnol. Bioeng.*, **1999**, *65*, 182–191.

[15] Zhou, W. C.; Rehm, J.; Hu, W. S. High viable cell concentration fed-batch cultures of hybridoma cells through on-line nutrient feeding. *Biotechnol. Bioeng.*, **1995**, *46*, 579–587.

[16] Kim, N.; Lee, G. Response of recombinant Chinese hamster ovary cells to hyperosmotic pressure: effect of Bcl-2 overexpression. *J. Biotechnol.*, **2002**, *95*, 237–248.

[17] Oh, S.; Rheem, S.; Sim, J.; Kim, S.; Baek, Y. Optimizing conditions for the growth of Lactobacillus casei YIT 9018 in tryptone-yeast extract-glucose medium by using response surface methodology. *Appl. Environ. Microbiol.*, **1995**, *61*(11), 3809–3814.

[18] Øyaas, K.; Ellingsen, T.; Dyrset, N.; Levine, D. Hyperosmotic hybridoma cultures: increased monoclonal antibody production with addition of glycine betaine. *Biotechnol. Bioeng.*, **1994**, *44*, 991–998.

[19] Ryu, J.; Lee, G. Effect of hyperosmotic stress on hybridoma cell growth and antibody production. *Biotechnol. Bioeng.*, **1997**, *55*, 565–570.

[20] Ryu, J.; Lee, G. Application of hypoosmolar medium to fed-batch culture of hybridoma cells for improvement of culture longevity. *Biotechnol. Bioeng.*, **1999**, *62*, 120–123.

[21] Zhu, M.; Goyal, A.; Rank, D.; Gupta, S.; Vanden Boom, T.; Lee, S. Effects of elevated pCO2 and osmolality on growth of CHO cells and production od antibody-fusion protein B1: A case study. *Biotechnol. Prog.*, **2005**, *21*, 70–77.

[22] Michaels, J.; Nowak, J. E.; Mallik, A. K.; Koczo, K.; Wasan, D. T.; Papoutsakis, E. Analysis of cell-to-bubble attachment in sparged bioreactors in the presence of cell-protecting additives. *Biotechnol. Bioeng.*, **1995**, *47*, 407–419.

[23] Michaels, J.; Nowak, J.; Mallik, A.; Koczo, K.; Wasan, D. T.; Papoutsakis, E. Interfacial properties of cell culture media with cell-protecting additives. *Biotechnol. Bioeng.*, **1995**, *47*, 420–430.

[24] Barngrover, D.; Thilly, T. High density mammalian cell growth in Leibovitz bicarbonate-free medium: effects of fructose and galactose on culture biochemistry. *J. Cell Sci.*, **1985**, *78*, 173–189.

[25] Bertheussen, K. Growth of cells in a new defined protein-free medium. *Cytotechnology*, **1993**, *11*, 219–231.

[26] Itagaki, A.; Kimura, G. TES and HEPES buffers in mammalian cell cultures and viral studies: problem of carbon dioxide requirement. *Exp. Cell Res.*, **1974**, *83*, 351–361.

[27] Leibovitz, A. The growth and maintenance of tissue-cell cultures in free gas exchange with the atmosphere. *Am. J. Hyg.*, **1963**, *78*, 173–180.

[28] Schmid, G.; Blanch, H.; Wilke, C. Hybridoma growth, metabolism and product formation in HEPES-buffered medium: Effect of pH. *Biotechnol. Lett.*, **1990**, *12*, 633–638.

[29] Swim, H.; Parker, R. Nonbicarbonate buffers in cell culture media. *Science*, **1955**, *122*, 466.

[30] Morel, F.; Hering, J. *Principles and Applications of Aquatic Chemistry.* John Wiley and Sons, New York, 1993.

[31] Goudar, C.; Nanny, M. A MATLAB toolbox for solving acid-base chemistry problems in Environmental Engineering Applications. *Computer Applications in Engineering Education*, **2005**, *13*, 257–265.

[32] Stumm, W.; Morgan, J. *Aquatic Chemistry.* John Wiley and Sons, New York, 3rd edition edition, 1996.

[33] Ozturk, S.; Palsson, B. Chemical decomposition of glutamine in cell culture media: Effect of media type, pH, and serum concentration. *Biotechnol. Prog.*, **1990**, *6*, 121–128.

[34] Matanguihan, R.; Sajan, E.; Konstantinov, K.; Zachariou, M.; Olson, C. Process and medium for mammalian cell culture under low dissolved carbon dioxide concentration, 2002.

[35] Ozturk, S. Engineering challenges in high density cell culture systems. *Cytotechnology*, **1996**, *22*(1-3), 3–16.

[36] Carrera, F.; Marcos, E.; Merkling, P.; Chaboy, J.; Munoz-Paez, A. Nature of metal binding sites in Cu(II) comples with histidine and related N-coordinating ligands, as studied by EXAFS. *Inorg. Chem.*, **2004**, *18*, 6674–6683.

[37] Strange, R.; Blackburn, N.; Knowles, P.; Hasnain, S. X-ray absorption spectroscopy of metal-histidine coordination in metalloproteins. Exact simulation of the EXAFS of tetrakis(imidazole) copper(II) nitrate and other other copper-imidazole complexes by the used of a multiple-scattering treatment. *J. Am. Chem. Soc.*, **1987**, *109*, 7157–7162.

[38] Balcarcel, R. R.; Clark, L. Metabolic screening of mammalian cell cultures using well-plates. *Biotechnol. Prog.*, **2003**, *19*, 98–108.

[39] Takuma, S.; Hirashima, C.; Piret, J. in *Animal Cell Technology: Basic and Applied Aspects*, Yagasaki, K.; Miura, Y.; Hatori, M.; Nomura, Y., Eds., pp 99–103. Kluwer Academic Publishers, Netherlands, 2004.

[40] Gillies, R.; Martinez-Zaguilan, R.; Peterson, E.; Perona, R. Role of intracellular pH in mammalian cell proliferation. *Cell Physiol. Biochem.*, **1992**, *2*, 159–179.

[41] Roos, A.; Boron, W. Intracellular pH. *Physiol. Rev.*, **1981**, *61*, 296–434.

[42] Busa, W. in *Na+/H+-exchange, intracellular pH and cell function*, Aronson, P.; Boron, W., Eds., p 291. Academic Press, New York, 1986.

[43] Fidelman, M.; Seeholzer, S.; Walsh, K.; Moore, R. Intracellular pH mediates action of insulin on glycosysis in frog skeletal muscle. *Am. J. Physiol.*, **1982**, *242*, C87–C93.

[44] McQueen, A.; Bailey, J. E. Effect of ammonium ion and extracellular pH on hybridoma cell metabolism amd antibody production. *Biotechnol. Bioeng.*, **1990**, *35*, 1067–1077.

[45] Moore, R.; Fidelman, M.; Hansen, J.; Otis, J. in *Intracellular pH: Its measurement, regulation and utilization in cellular function*, Nuccitelli, R.; Deamer, D., Eds., p 385. John Wiley and Sons Inc., New York, 1982.

[46] Stryer, L. *Biochemistry*. W. H. Freeman and Company, San Francisco, 4th edition, 1995.

[47] Boron, W. Regulation of intracellular pH. *Adv. Physiol. Educ.*, **2004**, *28*, 160–179.

[48] Madshus, H. Regulation of intracellular pH in eukaryotic cells. *Biochem. J.*, **1988**, *250*, 1–8.

[49] Bouyer, P.; Bradley, S.; Zhao, J.; Wang, W.; Richerson, G.; Boron, W. Effect of extracellular acid-base disturbances on the intracellular pH of neurones cultured from rat medullary raphe or hippocampus. *J. Physiol. (Lond).*, **2004**, *559*, 85–101.

[50] Buckler, K.; Vaughan-Jones, R.; Peers, C.; Lagadic-Gossmann, D.; Nye, P. Effects of extracellular pH, pCO2 and HCO3- on intracellular pH in isolated type-1 cells of the neonatal rat carotid body. *J. Physiol. (Lond).*, **1991**, *444*, 703–721.

[51] Thomas, R. The role of bicarbonate, chloride and sodium ions in the regulation of intracellular pH in snail neurones. *J. Physiol. (Lond).*, **1977**, *273*, 317–338.

[52] Murer, H.; Hopfer, U.; Kinne, R. Sodium/proton antiport in brush-border-membrane vesicles isolated from rat small intestine and kidney. *Biochem. J.*, **1976**, *154*, 597–604.

[53] Boron, W.; Boulpaep, E. Intracellular pH regulation in the renal proximal tubule of the salamander: basolateral HCO3- transport. *J. Gen. Physiol.*, **1983**, *81*, 53–94.

Chapter 5

OUR and CER Estimation in Perfusion Systems[1]

5.1 Introduction

Oxygen uptake and carbon dioxide evolution rates (OUR and CER, respectively) provide useful information on cell metabolism and physiology. Reliable estimation of these rates is desirable as they are indicators of changes in cellular metabolic activity [1–8]. Oxygen uptake data are an indicator of cell density and metabolic rates such as glucose consumption and on-line OUR measurements have been used to design feeding strategies and control bioreactor operation [9, 10]. OUR information is also necessary for bioreactor design and scale-up given the low solubility of oxygen. This is especially important for high density perfusion cultivations that have high oxygen transfer requirements. Moreover, OUR and CER are required for metabolic flux analysis even in the simplest of mammalian cell bioreaction networks [11]. Robust OUR and CER estimation is thus critical for bioprocess development and is also important for monitoring and diagnosing manufacturing bioreactors.

The primary approaches that have been used for in-situ OUR estimation in mammalian cell cultures include the stationary liquid phase balance approach, the dynamic method, and the global mass balance (GMB) approach [6]. The stationary liquid phase balance approach requires knowledge of the volumetric oxygen transfer coefficient, k_La, for OUR estimation [1, 2]. However, for both sparged and membrane aerated bioreactors, k_La can change over time making the stationary liquid phase balance approach unsuitable for long

[1] A version of this chapter will be submitted for publication. Goudar, C.T., Piret, J.M. and Konstantinov, K.B. (2006). Estimating OUR and CER in perfusion systems using global mass balances and novel off-gas analyzers.

term perfusion cultivations. The dynamic method is the simplest and perhaps the most widely used method for estimating oxygen uptake rates [10, 12, 13]. This approach typically involves increasing the DO concentration in the bioreactor to 60% saturation and turning off the oxygen supply. The subsequent rate of DO decrease is a consequence of cellular consumption and provides the OUR estimate. Despite its simplicity, this method involves a perturbation that is undesirable. Moreover, for high cell density perfusion cultures, rapid oxygen consumption complicates application of this method. For BHK cells at densities of 20 x 10^6 cells/mL, the time required for complete oxygen depletion when all supplies are cut off is on the order of 40 seconds resulting in unreliable OUR estimates from the dynamic method (DO probe response times are typically greater than 40 seconds).

To overcome these limitations, an alternate OUR estimation approach was proposed where reactor contents were continuously drawn into an external loop and DO measurements were made at the outlet of the loop [14]. The difference between the DO levels in the reactor and at the outlet of the external loop helped determine OUR. This method required only a single additional DO measurement while no gas phase oxygen measurements were necessary making the process simple and robust. The GMB approach becomes attractive for OUR estimation when reliable gas phase oxygen measurements can be made as it does not require k_La determination and bioreactor perturbation. Information on the gas flow rates and oxygen concentrations in the inlet and outlet streams is adequate for OUR estimation..

CER estimation is more difficult than OUR because of the reversible dissociation of CO_2 into $H_2CO_3^*$, HCO_3^- and CO_3^{2-} in solution. The equilibria of these dissociation reactions are strong functions of pH, temperature and ionic strength that must be accounted for during CER estimation. While there are several reports on CER estimation in microbial systems [15–20], there are only a few in mammalian cell chemostat and batch studies [1, 21, 22] and none in perfusion systems. The use of bicarbonate buffered medium in mammalian cells further complicates CER estimation because this is a major additional abiotic CO_2 component.

In this study, we present methods to estimate OUR and CER in mammalian cell perfusion cultures using global mass balances. While measurement of oxygen and carbon dioxide concentrations in the inlet and outlet gas streams is necessary, k_La data are not required and no reactor perturbations are necessary. Our approach allows real-time OUR and CER estimation that can also serve as indicators of cell density and nutrient consumption rates. Moreover, these data enable real-time estimation of metabolic fluxes providing useful insights into cell metabolism and physiology that can be used in advanced control strategies for optimal bioreactor operation.

5.2 Theory

5.2.1 OUR Estimation

Under ideal conditions, both liquid and gas stream oxygen flows must be taken into account in the generalized mass balance approach. However, a combination of low oxygen solubility and high cell density make liquid stream oxygen contributions negligible (usually less than 1%; Appendix E) and only gas phase oxygen balance equations are necessary for OUR estimation. Under steady-state conditions, there is no accumulation of oxygen in the bioreactor and oxygen uptake by the cells is the difference between the oxygen concentrations in the inlet and outlet streams

$$\text{OUR} = \frac{F_{total}}{X_V^B V}(O_2^{in} - O_2^{out})10^3 \tag{5.1}$$

where OUR is the cell specific oxygen uptake rate (pmol/cell-d), F_{total} is the total gas flow rate (L/d), X_V^B the bioreactor viable cell density (10^9 cells/L), V the bioreactor volume (L) and O_2^{in} and O_2^{out} the inlet and outlet oxygen concentrations (mol/L), respectively.

5.2.2 CER Estimation

5.2.2.1 Bicarbonate System Dynamics in a Mammalian Cell Bioreactor

Carbon dioxide sources in a perfusion system include cellular respiration, bicarbonate buffered medium and sodium bicarbonate when used as a base for pH control. Carbon dioxide produced by the cells dissolves in water to form carbonic acid

$$\mathrm{CO_{2(g)}} \leftrightarrow \mathrm{CO_{2(aq)}} \tag{5.2}$$

$$\mathrm{CO_{2(aq)}} + \mathrm{H_2O} \leftrightarrow \mathrm{H_2CO_3} \tag{5.3}$$

It is common practice in solution chemistry to combine the aqueous concentration of carbon dioxide and carbonic acid such that the above equations can be replaced by a single expression

$$\mathrm{CO_{2(g)}} + \mathrm{H_2O} \leftrightarrow \mathrm{H_2CO_3}^*; \quad K_g = 10^{-1.47} \tag{5.4}$$

where $\mathrm{H_2CO_3}^* = \mathrm{CO_{2(aq)}} + \mathrm{H_2CO_3}$ and K_g is the equilibrium constant under standard conditions (T = 25 °C and ionic strength (I) = 0). Further dissociation of $\mathrm{H_2CO_3}^*$ to $\mathrm{HCO_3^-}$ and subsequently to $\mathrm{CO_3^{2-}}$ can be described as

$$\mathrm{H_2CO_3}^* \leftrightarrow \mathrm{HCO_3^-} + \mathrm{H^+}; \quad K_1 = 10^{-6.35} \tag{5.5}$$

$$HCO_3^- \leftrightarrow CO_3^{2-} + H^+; \qquad K_2 = 10^{-10.33} \tag{5.6}$$

where K_1 and K_2 are the equilibrium constants under standard conditions.

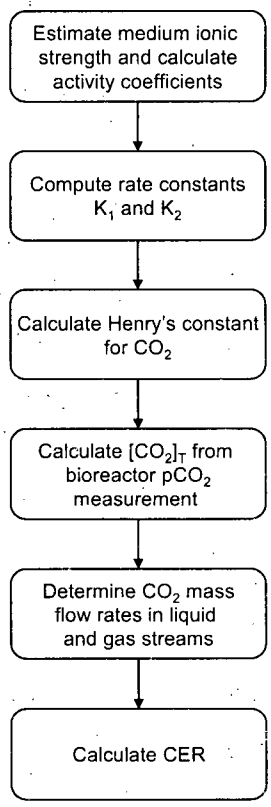

Figure 5.1: The steps involved in perfusion system CER estimation.

For typical mammalian cell cultivations, however, the temperature is close to 37 °C and the ionic strength is ~0.1 M depending upon the composition of the medium. The rate constants must hence be corrected to reflect experimental conditions. The rate constants can be corrected for temperature using the Van't Hoff equation [23]

$$K = K_{ref} \exp\left\{\left(\frac{\Delta H^0}{R}\right)\left(\frac{1}{T_{ref}} - \frac{1}{T}\right)\right\} \tag{5.7}$$

where K and K_{ref} are the corrected and reference rate constants, respectively at temperatures T and T_{ref}, ΔH^0 the standard enthalpy change for the reaction, and R, the gas constant. The corrected equilibrium constants K_g, K_1 and K_2 were $10^{-6.30}$ and $10^{-10.48}$, respectively, at 37 °C and calculation details have been presented in Appendix B.

To account for ionic strength effects, the activity coefficients were calculated using the

Davies equation which is valid for ionic strengths < 0.5 M

$$\log\gamma = -Az^2\left\{\frac{\sqrt{I}}{1+\sqrt{I}} - 0.2I\right\} \tag{5.8}$$

where γ is the activity coefficient, $A = 1.825 \text{ x } 10^6\,(\epsilon T)^{-3/2}$ is a constant ($\epsilon = 78.38$ is the dielectric constant for water, T is the absolute temperature) and I the ionic strength. The ionic strength of the medium used in this study was calculated as 0.115 M from the Debye-Hückel theory [24]

$$I = \frac{1}{2}\sum C_i z_i^2 \tag{5.9}$$

where C_i and z_i are charge and concentration of species i, respectively. The activity coefficients for $I = 0.115$ M were estimated from Eq.(5.8) as 0.7747 and 0.3602, respectively, for species with charges 1 and 2. Incorporating the temperature corrected values of the equilibrium constants, Eqs.(5.4) – (5.6) can be rewritten in terms of the species concentrations and activity coefficients as

$$K_g = \frac{[H_2CO_3{}^*]\,\gamma_{H_2CO_3{}^*}}{[CO_{2(g)}]\,\gamma_{CO_{2(g)}}} = K_g^c\frac{\gamma_{H_2CO_3{}^*}}{\gamma_{CO_{2(g)}}} = 10^{-1.60} \tag{5.10}$$

$$K_1 = \frac{[H^+]\,\gamma_{H^+}\,[HCO_3^-]\,\gamma_{HCO_3^-}}{[H_2CO_3{}^*]\,\gamma_{H_2CO_3{}^*}} = K_1^c\frac{\gamma_{H^+}\gamma_{HCO_3^-}}{\gamma_{H_2CO_3{}^*}} = 10^{-6.30} \tag{5.11}$$

$$K_2 = \frac{[H^+]\,\gamma_{H^+}\,[CO_3^{2-}]\,\gamma_{CO_3^{2-}}}{[HCO_3^-]\,\gamma_{HCO_3^-}} = K_2^c\frac{\gamma_{H^+}\gamma_{CO_3^{2-}}}{\gamma_{HCO_3^-}} = 10^{-10.48} \tag{5.12}$$

where K_g^c, K_1^c and K_2^c are the concentration based equilibrium constants and γ the activity coefficients of the various species. Activity coefficients for the charged species were calculated from the Davies equation ($\gamma_{H^+} = \gamma_{HCO3^-} = 0.7746$, $\gamma_{CO3^{2-}} = 0.3602$) and $\gamma_{CO_{2(g)}} = \gamma_{H_2CO_3{}^*}$ was estimated as 1.03 as described in [25]. Substituting these values in Eqs.(5.10) – (5.12), the concentration based equilibrium constants K_g^c, K_1^c and K_2^c were calculated as $10^{-1.60}$, $10^{-6.07}$ and $10^{-10.04}$, respectively. These values now incorporate both temperature and ionic strength corrections and are representative of the system at 37 °C and 0.115 M ionic strength. Temperature corrections alone resulted in -25.8, 12.2 and -29.2% change in K_g^c, K_1^c and K_2^c, respectively, while the combined effect of temperature and ionic strength were -25.8, 90.5 and 96.8%, respectively (K_g^c was not affected by ionic strength as seen from Eq.5.10).

It follows from the above discussion that the carbon dioxide produced by the cells does not exist just as a gas but also as $H_2CO_3{}^*$, HCO_3^- and CO_3^{2-}. The relative concentrations

of these species are influenced primarily by bioreactor pH while temperature and medium ionic strength have minor effects as seen from the ionization fraction expressions

$$\% \text{ of } H_2CO_3^* = \left(\frac{[H^+]^2}{[H^+]^2 + [H^+]\ K_1^c + K_1^c K_2^c} \right) \text{ x } 100 \tag{5.13}$$

$$\% \text{ of } HCO_3^- = \left(\frac{[H^+]\ K_1^c}{[H^+]^2 + [H^+] K_1^c + K_1^c K_2^c} \right) \text{ x } 100 \tag{5.14}$$

$$\% \text{ of } CO_3^{2-} = \left(\frac{K_1^c K_2^c}{[H^+]^2 + [H^+] K_1^c + K_1^c K_2^c} \right) \text{ x } 100 \tag{5.15}$$

At pH = 6.8, the cultivation pH in this study, the relative amounts of $H_2CO_3^*$, HCO_3^- and CO_3^{2-} in the medium were 15.69, 84.26 and 5 x 10^{-4}%, respectively. Thus HCO_3^- is the dominant species followed by $H_2CO_3^*$ while CO_3^{2-} can be neglected.

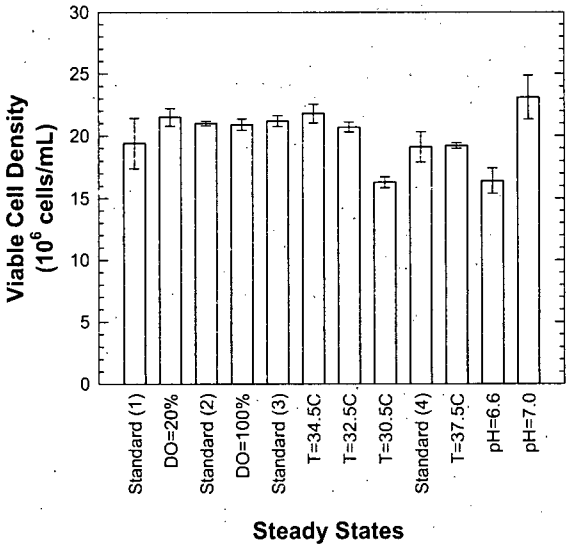

Figure 5.2: Cell density averages for the different experimental conditions during the course of the perfusion cultivation. For standard conditions, DO = 50%, T = 36.5 °C and pH = 6.8.

5.2.2.2 CO_2 Mass Balance Equations

In a perfusion system, bioreactor pCO_2 is relatively constant suggesting no CO_2 accumulation. The CO_2 produced by the cells is then simply the difference between the CO_2 leaving

and entering the system.

$$\text{CO}_2 \text{ produced by cells} = \text{CO}_2 \text{ leaving the System - CO}_2 \text{ entering the System} \quad (5.16)$$

with units of mol/d. Recognizing that CO_2 produced by the cells can exist as both $H_2CO_3{}^*$ and HCO_3^-, it is convenient to combine them while deriving mass balance expressions. The total CO_2 concentration, $[CO_2]_T$, is thus defined as $[CO_2]_T = [H_2CO_3{}^*] + [HCO_3^-]$. Sources of $[CO_2]_T$ include bicarbonate-containing cultivation medium, base ($NaHCO_3$ or Na_2CO_3) or CO_2 gas used for bioreactor pH control, and cellular metabolism. Removal mechanisms for $[CO_2]_T$ include the harvest and cell bleed streams along with gaseous CO_2 stripping, either through sparging or membrane aeration. Eq.(5.16) can be rewritten to include contributions of the individual components to the inlet and outlet streams

$$\begin{aligned} CER &= \left\{\frac{10^3}{VX_V^B}\right\}\left\{F_M[\text{CO}_2]_\text{T}^\text{M} + F_{base}[\text{CO}_2]_\text{T}^\text{base} + F_{CO_{2(in)}}\right\} \\ &\quad -\left\{F_H[\text{CO}_2]_\text{T}^\text{H} + F_{bleed}[\text{CO}_2]_\text{T}^\text{bleed} + F_{CO_{2(out)}}\right\} \end{aligned} \quad (5.17)$$

where CER is the carbon dioxide evolution rate (pmol/cell-d), V the reactor volume (L), X_V^B the viable cell density in the bioreactor (10^9 cells/L), F_M, F_{base}, F_H, F_{bleed} the medium, base, harvest and bleed flow rates (L/d), respectively, $[CO_2]_T^M$, $[CO_2]_T^{base}$, $[CO_2]_T^H$ and $[CO_2]_T^{bleed}$ the total CO_2 concentration (mol/L) in the medium, base, harvest and bleed streams, respectively, and $F_{CO_{2(in)}}$ and $F_{CO_{2(out)}}$ the molar flow rates of CO_2 (mol/d) in the inlet and outlet steams, respectively.

Quantifying contributions from the medium and base on a mol/day basis is straightforward as their carbonate concentrations and flow rates are known. The flow rate of CO_2 gas into the reactor will help determine the amount of CO_2 gas added to the reactor (this is seldom done when bicarbonate-containing medium is used). To determine $[CO_2]_T$ removal from the harvest and cell bleed streams, the total CO_2 concentration in the bioreactor must be known because CO_2 concentrations in the harvest and bleed streams are similar to those in the bioreactor. Bioreactor CO_2 concentration can be estimated from pCO_2 measurements that are typically made using a blood gas analyzer

$$[\text{CO}_2]_\text{T}^\text{bioreactor} = \left\{1 + \frac{K_1^c}{[\text{H}^+]} + \frac{K_1^c K_2^c}{[\text{H}^+]^2}\right\}\left\{\frac{pCO_{2_{bioreactor}}}{h_{CO_2}}\right\} \quad (5.18)$$

where $[CO_2]_T^{bioreactor}$ is the total CO_2 concentration in the bioreactor (mol/L), $pCO_{2_{bioreactor}}$ the bioreactor pCO_2 (mm Hg) and h_{CO_2} is the Henry's constant for CO_2 (mm Hg-L/mol)

determined as

$$h_{CO_2} = \left(\frac{101.3 * 22.395}{\alpha}\right) 7.500617 \quad (5.19)$$

$$\alpha = a + bT + cT^2 + dT^3 + eT^4 \quad (5.20)$$

with a = 1.72, b = -6.689 x 10^{-2}, c = 1.618 x 10^{-3}, d = -2.284 x 10^{-5} and e = 1.394 x 10^{-7} [26]. Once $[CO_2]_T^{bioreactor}$ is determined, the harvest and cell discard flow rates can be used to determine $[CO_2]_T$ removal on a mol/day basis. Finally, measuring CO_2 gas concentration in the outlet gas will help determine $[CO_2]_T$ removal by stripping. The CER is then estimated by substituting these values in Eq.(5.17). This CER estimation procedure is summarized in Figure 5.1.

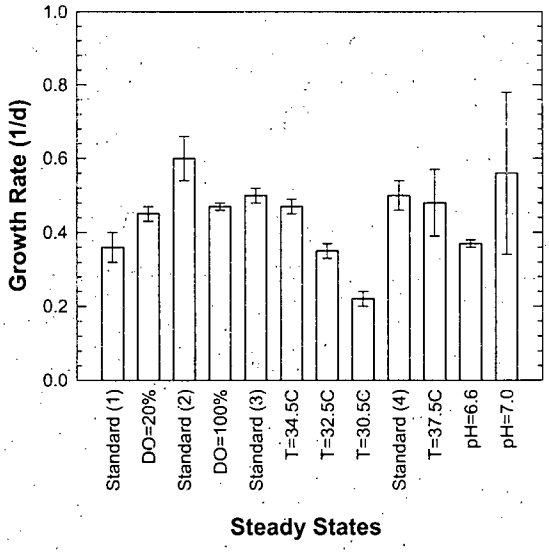

Figure 5.3: Growth rate averages for the different experimental conditions during the course of the perfusion cultivation. For standard conditions, DO = 50%, T = 36.5 °C and pH = 6.8.

5.3 Materials and Methods

5.3.1 Cell Line, Medium and Cell Culture System

CHO cells were cultivated in perfusion mode with glucose and glutamine as the main carbon and energy sources. Experiments were conducted in a 15 L bioreactor (Applikon, Foster City, CA) with a 12 L working volume. The temperature was maintained at 36.5 °C and

the agitation at 40 RPM. Under standard conditions, the dissolved oxygen (DO) concentration was maintained at 50% air saturation by sparging a mixture of oxygen and nitrogen (100 – 150 mL/min) through 0.5 μm spargers and the pH was maintained at 6.8 by the automatic addition of 0.3 M NaOH. The bioreactor was inoculated at an initial cell density of approximately 1.0 x 10^6 cells/mL and cells were allowed to accumulate to a steady-state concentration of 20 x 10^6 cells/mL. The steady-state cell density was maintained by automatic cell bleed from the bioreactor.

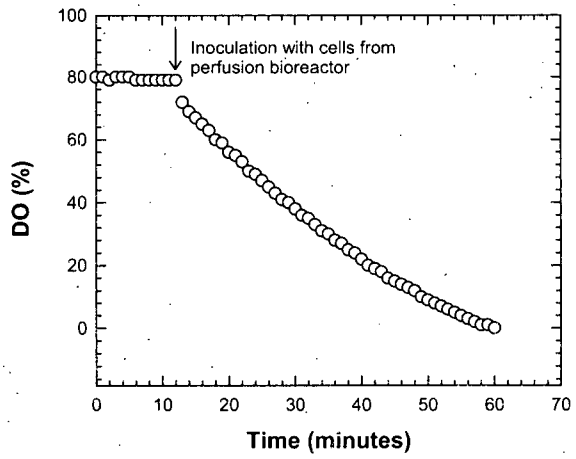

Figure 5.4: OUR estimation in the 2 L reactor by the dynamic method. DO data following inoculation with cells from the 15 L perfusion bioreactor were used for OUR estimation by the dynamic method.

Bioreactor DO, temperature and pH were varied during the course of the cultivation to determine the operating ranges for these variables. The low and high values for DO were 20% and 100%, respectively (set point = 50%) while those for pH were 6.6 and 7.0, respectively. The temperature set point was 36.5 °C and was varied between 30.5 – 37.5 °C during the course of the experiment. Bioreactor conditions were maintained at each of these altered conditions for 10 days and data from the last 4 days were considered representative of each experimental condition. OUR and CER data presented in later sections are averages of these 4 days for each experimental condition.

In addition to the above perfusion cultivation, a 2 L bioreactor was used for OUR estimation by the dynamic method. The reactor was initially filled with 1.9 L of fresh medium and was maintained at 36.5 °C, pH = 6.8, and DO concentration in the 75 – 85% range. The gas supply to the bioreactor was shut off and a 100 mL sample from the 15 L perfusion bioreactor (steady-state cell density of 20 x 10^6 cells/mL) was used to

inoculate the 2 L bioreactor at a cell density of ~1 x 10^6 cells/mL. The resulting decrease in DO concentration was monitored and this information was used to compute the OUR. A comparison was then made between OUR estimates from the mass balance method (*in-situ* estimation in the perfusion bioreactor) and the dynamic method (in the external 2 L bioreactor). The headspace volume was 100 mL such that surface aeration effects were minimal.

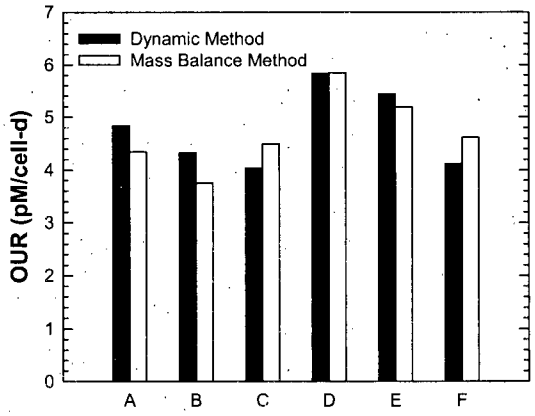

Figure 5.5: Comparison of OUR estimates from the dynamic method (external 2 L bioreactor) with those from the global mass balance method (*in-situ* estimation in the 15 L perfusion bioreactor).

5.3.2 Analytical Methods

Samples from the bioreactor were taken daily for cell density and viability analysis using the CEDEX system (Innovatis, Bielefeld, Germany). The samples were subsequently centrifuged (Beckman Coulter, Fullerton, CA) and the supernatants were analyzed for nutrient and metabolite concentrations. Glucose, lactate, glutamine and glutamate concentrations were determined using a YSI Model 2700 analyzer (Yellow Springs Instruments, Yellow Springs, OH) while ammonium was measured by an Ektachem DT60 analyzer (Eastman Kodak, Rochester, NY). The pH and DO were measured online using retractable electrodes (Mettler-Toledo Inc., Columbus, OH) and their measurement accuracy was verified through off-line analysis in a Stat Profile 9 blood gas analyzer (Nova Biomedical, Waltham, MA). The same instrument also measured the dissolved CO_2 concentration. On-line measurements of cell density were made with a retractable optical density probe (Aquasant Messtechnik, Bubendorf, Switzerland), calibrated with CEDEX cell density measurements. Concentra-

tions of oxygen and carbon-dioxide in the exit gas were measured using a MGA-1200 Mass Spectrometer (Applied Instrument Technologies, Pomona, CA).

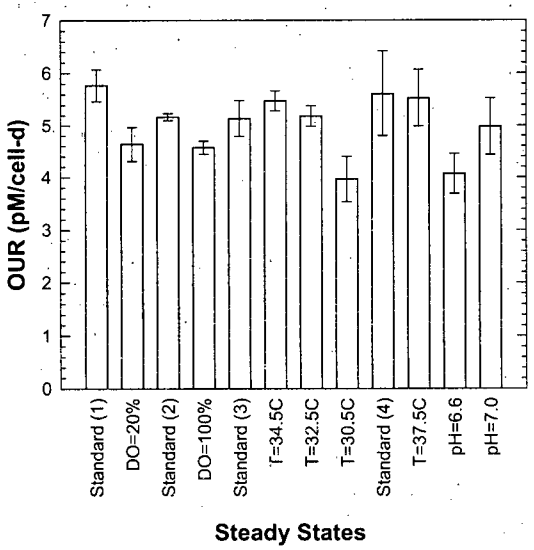

Figure 5.6: Average OUR estimates from the mass balance method for the 12 experimental conditions in the perfusion cultivation.

5.4 Results

5.4.1 Cell Density and Growth Rate

The perfusion cultivation comprised of 12 experimental conditions each of 10 day duration and average cell densities for each of these steady states are shown in Figure 5.2. The target cell density was 20 x 10^6 cells/mL with most values very close to the target. The exceptions were the T = 30.5 °C and pH = 6.6 steady states where growth rates were much lower than at the other conditions (Figure 5.3). Temperature reduction caused an expected decline in growth rate as did pH reduction. No change in growth rate was seen when the DO was varied between 20 and 100%. Cell viability was greater than 95% in all cases (not shown).

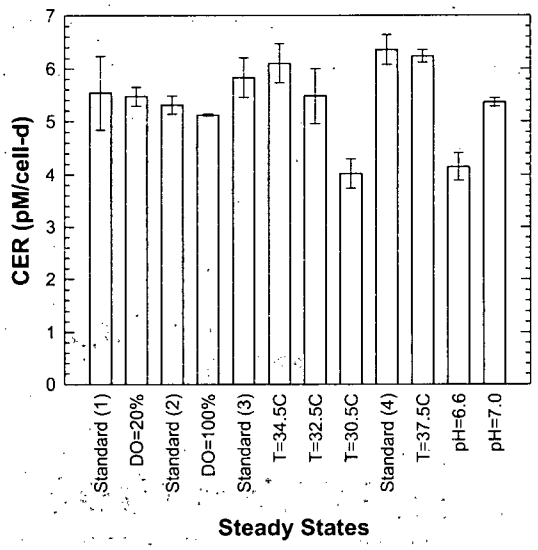

Figure 5.7: Average CER estimates for the 12 experimental conditions in the perfusion cultivation.

5.4.2 OUR and CER Estimation

5.4.2.1 Comparison of Mass Balance and Dynamic OUR Estimates

Two independent techniques were used for OUR estimation. In the MB approach, OUR was determined using Eq.(5.1) from the inlet and outlet gas stream oxygen concentrations. OUR estimation by the dynamic method was done off-line in a 2 L batch bioreactor using a sample from the perfusion bioreactor. A representative DO time profile in the 2 L batch reactor is shown in Figure 5.4 and DO data in the 60 – 30% range were used for OUR estimation.

A comparison of OUR estimates from these two methods for six different samples is shown in Figure 5.5. OUR estimates from both methods were comparable with the maximum difference being 13.4%. Percentage differences in OUR estimates from these methods were computed based on the assumption that dynamic method estimates were accurate while those from the GMB were in error. This is a reasonable assumption given the simplicity of the dynamic method. The mass balance approach requires accurate measurement of gas flow rates and gas phase oxygen concentrations that can introduce error in the OUR estimation process. However, despite these limitations, OUR estimates from the mass balance method were in close agreement with those from the dynamic method.

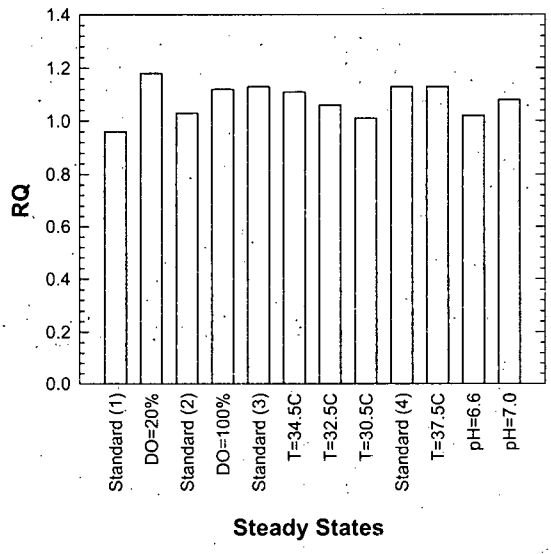

Figure 5.8: Respiratory quotient (RQ) estimates for the 12 experimental conditions in the perfusion cultivation.

5.4.2.2 OUR, CER and RQ at Varying Operating Conditions

OUR values at different DO, temperature and pH set points are shown in Figure 5.6. The values are averages over their respective experimental conditions along with their associated standard deviations. While OUR values were mostly unchanged across most experimental conditions, they were lower at T = 30.5 °C and pH = 6.6 where an overall reduction in growth (Figure 5.3) and metabolism (not shown) were observed. The lowest CER values of 4.02 and 4.15 pmol/cell-d were also observed at T = 30.5 °C and pH = 6.6, respectively, while those at other set points were relatively similar (Figure 5.7). RQ values estimated from the average OUR and CER values ranged from 0.96 - 1.18 (Figure 5.8) suggesting minimal impact of DO, temperature and pH set point changes on RQ.

5.5 Discussion

5.5.1 OUR, CER and RQ Estimation

We have presented methods to estimate OUR and CER in mammalian cell perfusion systems using the global mass balance method. This approach does not require k_La data and no reactor perturbations are necessary. Composition and flow rates of the inlet and exit gas streams along with other routinely measured quantities are adequate for OUR and CER

Table 5.1: Published OUR values for mammalian cells

OUR (pmol/cell-d)	Cell Line	Reference
3.6 – 8.64	Hybridoma	[27]
5.62	Hybridoma	[28]
1.2	Human diploid cells	[29]
4.56 – 9.6	Hybridoma	[2, 30–32]
0.55 – 2.09	Hybridoma	[4]
7.92 – 8.88	Hybridoma	[33]
3.6	Hybridoma	[13]
5.26 – 9.74	Myeloma	[14]
11.04	Hybridoma	[10]
5.52 – 10.08	Hybridoma	[34]
10.1 – 10.7	Hybridoma	[1]
3.97 – 5.77	CHO	This Study

estimation. Real-time OUR, CER and RQ estimations are possible (data could be generated every second if desired) because the required measurements and calculations can be rapidly performed. In addition to providing valuable information on cell metabolism, this enables real-time determination of metabolic fluxes providing additional insights into cell physiology.

5.5.2 Comparison with Literature Data

Changes to temperature and pH had the most effect on OUR and CER while DO in the 20 – 100% range had minimal effect (Figures 5.6 and 5.7). OUR values ranged from 3.97 – 5.77 pmol/cell-d and the low values of 3.97 and 4.07 were at T = 30.5 °C and pH = 6.6, respectively. Similar CER trends were seen with values of 4.02 and 4.15 pmol/cell-d at T = 30.5 °C and pH = 6.6, respectively (CER range was 4.02 – 6.36 pmol/cell-d). Published OUR values for mammalian cells are shown in Table 5.1 and are in the 0.55 – 10.7 pmol/cell-d range. Values for CHO cells obtained in this study were clustered in the middle of this range. CER values for hybridoma cells in chemostat culture were in the 9.9 – 11.1 pmol/cell-d range [1] while those in batch culture varied between 1.2 and 8.4 pmol/cell-d [21]. Our values for CHO cells were lower than the hybridoma chemostat data and closer to those observed in the batch hybridoma cultivations.

Despite significant changes to OUR and CER at low temperature and pH, they were correlated such that RQ values were relatively unchanged. RQ values were close to unity (0.96 - 1.18, Figure 5.8) under all experimental conditions and part of the variation was likely due to error in OUR and CER estimates. For instance, a 10% error in OUR can cause

RQ to vary between 0.9 and 1.1 (neglecting CER error). The maximum difference between mass balance and dynamic OUR estimates was 13.4% (Figure 5.5) indicating that OUR estimates could be associated with ~10% error. It is likely that errors of similar magnitude were associated with the CER values and a combination of these errors could be responsible for RQ variation in the 0.96 - 1.18 range. It is unlikely that cell metabolism was responsible for RQ changes because 1 mol of NADH accompanies 0.5 mol of CO_2 production and this NADH is oxidized by 0.5 mol of oxygen. While fatty acid synthesis can result in RQ values greater than unity [1], it is unlikely that fluxes through these reactions are significant enough to cause an RQ increase on the order of 20%.

5.6 Conclusions

We have presented methods to estimate OUR, CER and RQ from mammalian cells in perfusion culture. These are based on global mass balance expressions and do not require k_La information and bioreactor perturbations. They are especially suited for perfusion systems where k_La values change over the course of the cultivation and the dynamic method is not applicable. OUR estimates from the global mass balance method were in good agreement with estimates from the dynamic method and the maximum difference was 13.4%. Accurate CER estimation was possible by accounting for the dissociation of cellular CO_2 into $H_2CO_3^*$, HCO_3^- and CO_3^{2-} and the effect of temperature and ionic strength on the equilibria of the dissociation reactions. This CER estimation method is general and works when bicarbonate is present both in the medium and base. Since all necessary measurements can be made on-line, real time OUR and CER estimation is possible. In addition to providing information on cell physiology, these data can be used for real-time metabolic flux estimation resulting in improved understanding of cell metabolism. Since these advantages come at the expense of minimal analytical and computational effort, the OUR and CER estimation strategies presented in this study should be useful both for bioprocess development and monitoring of manufacturing bioreactors producing licensed biotherapeutics.

Bibliography

[1] Bonarius, H.; de Gooijer, C.; Tramper, J.; Schmid, G. Determination of the respiration quotient in mammalian cell culture in bicarbonate buffered media. *Biotechnol. Bioeng.*, **1995**, *45*, 524–535.

[2] Miller, W.; Wilke, C.; Blanch, H. Effects of dissolved oxygen concentration on hy-

bridoma growth and metabolism in continuous cultures. *J. Cell. Physiol.*, **1987**, *132*, 524–530.

[3] Ogawa, T.; Kamihira, M.; Yoshida, H.; Iijima, H.; Kobayashi, T. Effect of dissolved oxygen concentration on monoclonal antibody production in hybridoma cell cultures. *J. Ferment. Bioeng.*, **1992**, *74*, 372–378.

[4] Ozturk, S.; Palsson, B. Effects of dissolved oxygen on hybridoma cell growth, metabolism, and antibody production kinetics in continuous culture. *Biotechnol. Prog.*, **1990**, *6*, 437–446.

[5] Philips, H.; Scharer, J.; Bols, N.; Moo-Young, M. Effect of oxygen on antibody production in hybridoma culture. *Biotechnol. Lett.*, **1987**, *9*, 745–750.

[6] Ruffieux, P.; Stockar, U.; Marison, I. Measurement of volumetric (OUR) and determination of specific (qO2) oxygen uptake rates in animal cell cultures. *J. Biotechnol.*, **1998**, *63*, 85–95.

[7] Shi, Y.; Ryu, D.; Park, S. Monoclonal-antibody productivity and the metabolic pattern of perfusion cultures under varying oxygen-tensions. *Biotechnol. Bioeng.*, **1993**, *42*, 430–439.

[8] Yamada, K.; Furushou, S.; Sugahara, T.; Shirahata, S.; Murakami, H. Relationship between oxygen consumption rate and cellular activity of mammalian cells cultured in serum-free media. *Biotechnol. Bioeng.*, **1990**, *36*, 759–762.

[9] Kyung, Y.-S.; Peshwa, M. V.; Gryte, D.; Hu, W. S. High density culture of mammalian cells with dynamic perfusion based on on-line oxygen uptake measurements. *Cytotechnology*, **1994**, *14*, 183:190.

[10] Zhou, W. C.; Hu, W. S. On-line characterization of a hybridoma cell culture process. *Biotechnol. Bioeng.*, **1994**, *44*, 170–177.

[11] Balcarcel, R. R.; Clark, L. Metabolic screening of mammalian cell cultures using well-plates. *Biotechnol. Prog.*, **2003**, *19*, 98–108.

[12] Eyer, K.; Oeggerli, A.; Heinzle, E. On-line gas analysis in animal cell cultivation: II. Methods for oxygen uptake rate estimation and its application to controlled feeding of glutamine. *Biotechnol. Bioeng.*, **1995**, *45*, 54–62.

[13] Singh, V. On-line measurement of oxygen uptake in cell culture using the dynamic method. *Biotechnol. Bioeng.*, **1996**, *52*, 443–448.

[14] Yoon, S.; Konstantinov, K. Continuous, real-time monitoring of the oxygen uptake rate (OUR) in animal cell bioreactors. *Biotechnol. Bioeng.*, **1994**, *44*, 983–990.

[15] Aiba, S.; Furuse, H. Some comments on respiratory quotient (RQ) determination from the analysis of exit gas from a fermentor. *Biotechnol. Bioeng.*, **1990**, *36*, 534–538.

[16] Ho, C.; Smith, M.; Shanahan, J. Carbon dioxide transfer in biochemical reactors. *Advances in Biochemical Engineering*, **1987**, *35*, 83–125.

[17] Minkevich, I.; Neubert, M. Influence of carbon dioxide solubility on the acuracy of measurements of carbon dioxide production rate by gas balance technique. *Acta Biotechnology*, **1985**, *5*, 137–143.

[18] Royce, P. Effect of changes in the pH and carbon dioxide evolution rate on the measured respiratory quotient of fermentations. *Biotechnol. Bioeng.*, **1992**, *40*, 1129–1138.

[19] Royce, P.; Thornhill, N. Estimation of dissolved carbon dioxide concentrations in aerobic fermentations. *AIChE J.*, **1991**, *37*, 1680–1685.

[20] Zeng, A. P. Effect of CO2 absorption on the measurement of CO2 evolution rate in aerobic and anerobic continuous cultures. *Appl. Microbiol. Biotechnol.*, **1995**, *42*, 688–691.

[21] Frahm, B.; Blank, H.-C.; Cornand, P.; Oelbner, W.; Guth, U.; Lane, P.; Munack, A.; Johannsen, K.; Pörtner, R. Determination of dissolved CO2 concentration and CO2 production rate of mammalian cell suspension culture based on off-gas measurement. *J. Biotechnol.*, **2002**, *99*, 133–148.

[22] Lovrecz, G.; Gray, P. Use of on-line gas analysis to monitor recombinant mammalian cell cultures. *Cytotechnology*, **1994**, *14*, 167–175.

[23] Snoeyink, V.; Jenkins, D. *Water Chemistry.* John Wiley and Sons, New York, 1980.

[24] Morel, F.; Hering, J. *Principles and Applications of Aquatic Chemistry.* John Wiley and Sons, New York, 1993.

[25] Butler, J. *Ionic Equilibrium: Solubility and pH Calculations.* John Wiley and Sons, New York, 1998.

[26] Schumpe, A.; Quicker, G.; Deckwer, W. D. Gas solubilities in microbial culture media. *Adv. Biochem. Eng. Biotechnol.*, **1982**, *24*, 1–38.

[27] Backer, M.; Metzger, L.; Slaber, P.; Nevitt, K.; Boder, G. Large-scale production of monoclonal antibodies in suspension culture. *Biotechnol. Bioeng.*, **1988**, *32*, 993–1000.

[28] Dorresteijn, R. C.; Numan, K. H.; D., d. G. C.; Tramper, J.; Beuvery, E. C. On-line estimation of the biomass activity during animal-cell cultivations. *Biotechnol. Bioeng.*, **1996**, *50*, 206–214.

[29] Fleischaker, R.; Sinskey, A. J. Oxygen demand and supply in cell culture. *Appl. Microbiol. Biotechnol.*, **1981**, *12*, 193–197.

[30] Miller, W.; Blanch, H.; Wilke, C. A kinetic analysis of hybridoma growth and metabolism in batch and continuous suspension culture: Effect of nutrient concentration, dilution rate and pH. *Biotechnol. Bioeng.*, **1987**, *32*, 947–965.

[31] Miller, W.; Wilke, C.; Blanch, H. Transient responses of hybridoma cells to nutrient additions in continuous culture: I. Glucose pulse and step changes. *Biotechnol. Bioeng.*, **1989**, *33*, 477–486.

[32] Miller, W.; Wilke, C.; Blanch, H. Transient responses of hybridoma cells to nutrient additions in continuous culture: II. Glutamine pulse and step changes. *Biotechnol. Bioeng.*, **1989**, *33*, 487–499.

[33] Ramirez, O.; Mutharasan, R. Cell cycle and growth phase dependent variations in size distribution, antibody productivity, and oxygen demand in hybridoma cultures. *Biotechnol. Bioeng.*, **1990**, *36*, 839–848.

[34] Hiller, G.; Aeschlimann, A.; Clark, D.; Blanch, H. A kinetic analysis of hybridoma growth and metabolism in continuous suspension cultures on serum free medium. *Biotechnol. Bioeng.*, **1991**, *38*, 733–741.

Part III

Robust Specific Rate and Metabolic Flux Estimation

Chapter 6

Logistic Modeling of Batch and Fed-batch Kinetics[1]

6.1 Introduction

There has been an increasing use of mammalian cell cultures for the manufacture of complex therapeutic proteins. However, protein yields from mammalian culture are relatively low, requiring the optimization of cell lines, medium formulations and bioprocesses. These optimization efforts typically first involve evaluating non-instrumented batch cultivations (typically <100 mL working volume) in T-flasks, spinners or roller bottles where cell growth, metabolism and protein productivity are monitored over the course of the experiment. This provides information used to select the cell lines and medium components that maximize protein yields. Further bioprocess optimization, in either fed-batch or continuous perfusion cultivations, is mainly performed using laboratory-scale (>1 L) bioreactors. While maximizing specific protein productivity is often the primary objective in laboratory-scale experiments, ensuring robust cell growth and metabolism are also important. All these variables of interest are quantified using cell specific rates that enable comparison of cell lines and cultivation conditions. Accurate estimation of specific rates is thus vital to meaningfully interpret results from bioprocess optimization experiments.

While specific rates for steady-state perfusion cultures are readily computed because of their relatively time-invariant nature, analyzing the dynamic kinetics of batch and fed-batch cultures is more challenging. A conventional approach to model mammalian cells in

[1] A version of this chapter has been published: Goudar, C.T., Joeris, K., Konstantinov, K. and Piret, J.M. (2005) Logistic equations effectively model mammalian cell batch and fed-batch kinetics by logically constraining the fit. *Biotechnology Progress*, **21**, 1109-1118.

batch and fed-batch cultures has been through the use of unstructured kinetic models or variations of the classical Monod equation [1–5], and reviews of these models are available [6, 7]. While unstructured kinetic models have adequately described experimental data, they are computationally not practical to implement as they involve nonlinear estimation of a large number of kinetic parameters from a system of differential equations. Unique estimation of the kinetic parameters in such systems is not always possible. Moreover, given the variety of unstructured kinetic models that have been used to describe mammalian cell cultures, comparisons between studies is complicated. Analytical solutions of the differential equations describing the state variables have also been used to estimate specific rates [8–11]. These solutions, however, are derived under the assumption that the specific rates are constant as can be expected during the exponential growth phase. These have limited applicability to the other phases of batch and fed-batch cultures where specific rates are not constant. Specific rates in fed-batch cultures have also been estimated from the slope on plots of cumulative state variables (nutrient, metabolite or product) versus integral viable cell density [12, 13]. This approach provides an average estimate of the specific rate of interest over the exponential growth phase but additional linear or nonlinear fits need to be used for other cultivation phases. This need for multiple fits to describe the time course of a single variable makes this approach cumbersome and prone to error.

A general approach that is applicable over the entire time course of cultures, is fitting polynomials to the data [14, 15]. This approach has been used both for batch and fed-batch cultivations and is attractive because it allows simplified computation of the time derivatives necessary to estimate cell specific rates. However, as time profiles of cellular, nutrient and product concentrations exhibit exponential behavior, they are difficult to describe by polynomials [16]. For instance, two polynomial functions were necessary to describe the time course of some state variables [14]. Moreover, polynomial fits are known to yield unrealistic trends, especially when the data include even a few outliers.

Logistic equations have been successfully used to describe population dynamics in a variety of applications [17–23] but have not been reported to model experimental data from mammalian cell batch or fed-batch cultures. Most reported applications involve bacterial growth curves characterized by lag, exponential and stationary phases that are adequately described by the logistic growth equation. Mammalian cells in batch and fed-batch cultivations also exhibit a sharp decline in cell density following the stationary phase, a behavior that cannot be described by the standard logistic growth equation. In addition, a decline in lactate concentration during later stages of fed-batch cultivation is also frequently observed [13, 24]. Alternate logistic formulations that incorporate both the ascending and descending components of cell growth are available [25].

This study presents a method for modeling batch and fed-batch mammalian cell culture data using logistic equations. An alternate logistic formulation was applied to cases where variables had both increasing and decreasing phases. Cell specific rates were readily obtained from the analytically differentiable logistic equations. A comparison was made between this logistic modeling approach and the polynomial fitting or the unstructured kinetic modeling approaches that are commonly used to describe batch and fed-batch data.

6.2 Theory

6.2.1 Calculation of Batch Culture Specific Rates

Most batch kinetic studies have used discrete forms to compute specific rates. The widespread use of this approach is primarily due to its simplicity as seen from the specific growth rate expression

$$\mu' = (\mu - k_D) = \frac{\Delta X_v}{\bar{X}_v \Delta t} \tag{6.1}$$

where μ' is the apparent specific growth rate (1/day) over an interval from t_1 to t_2, μ the actual specific growth rate (1/day), k_D the specific death rate (1/day), X_v the viable cell density (x 10^6 cells/mL), $\Delta X_v = X_{v_2} - X_{v_1}$, t is time (day), $\Delta t = t_2 - t_1$ and $\bar{X}_v = \frac{X_{v_2} + X_{v_1}}{2}$. Thus ΔX_v and Δt represent the difference between successive viable cell density and time points, respectively, while $\bar{X}_v$ is the arithmetic average of the consecutive cell density data points. A log-normal average can also be used for $\bar{X}_v$ during the exponential growth phase but this provides a poor estimate for the average X_v in the decline phase. For intervals of constant apparent growth rate, a more accurate estimate of μ' can be obtained by combining multiple data points. However, when this constant growth rate ends and how the growth rate changes beyond that point remain difficult to accurately compute.

The primary sources of carbon and energy in a typical mammalian cell culture medium are glucose and glutamine. The specific consumption rate of glucose can be calculated from

$$q_G = -\frac{\Delta G}{\bar{X}_v \Delta t} \tag{6.2}$$

where q_G is the specific glucose consumption rate (pmol/cell-day) and $\Delta G = G_2 - G_1$ is the difference in glucose concentration over consecutive data points (mol/L). The primary known toxic metabolites of glucose and glutamine metabolism are lactate and ammonium,

respectively. These metabolite as well as protein production rates can be calculated from

$$q_P = \frac{\Delta P}{\bar{X}_v \Delta t} \tag{6.3}$$

where q_P is the specific production rate (pg/cell-day) and $\Delta P = P_2 - P_1$ is the change in metabolite/product concentration over consecutive data points (g/L).

6.2.2 Calculation of Fed-batch Culture Specific Rates

Fed-batch cultivations typically involve the periodic feeding of glucose, glutamine and other medium components. Hence nutrient mass balance expressions are modified to take the feeding into account while the expressions for cell density, metabolites and products are essentially identical to those in a simple batch cultivation (when dilution effects can be neglected). For example, specific glutamine uptake rate in a continuously fed batch reactor can be described by

$$q_{Gln} = -\frac{\Delta Gln}{\bar{X}_v \Delta t} + \frac{F}{V}\frac{Gln_f}{\bar{X}_v} - k_{Gln}\frac{Gln}{\bar{X}_v} \tag{6.4}$$

where q_{Gln} is the specific glutamine uptake rate (pmol/cell-day), $\Delta Gln = Gln_2 - Gln_1$ the change in glutamine concentration over consecutive data points (mol/L), F the glutamine feed rate (L/day), V the bioreactor working volume (L), Gln_f the glutamine concentration in the feed (mol/L) and k_{Gln} the first-order abiotic degradation constant for glutamine with values depending on the medium composition, temperature and culture pH [26]. The last term in the right hand side of Eq.(6.4) accounts for abiotic glutamine degradation at cultivation temperature.

6.2.3 A General Equation Describing the Dynamics of Batch and Fed-batch Cultures

The selection of final process parameters from optimization experiments is derived mainly from comparisons of cell specific productivity and growth rate. Therefore, it is important to reliably estimate these rates from sequential data points and Eqs.(6.1) – (6.4). However, this typically yields erratic time profiles since this method is sensitive to the measurement errors common in biological systems. Mathematical models that describe the dynamics of cellular growth and protein production according to expected trends can provide more robust estimates of the cell specific variables of interest. Such models should more smoothly and logically fit the experimental data. For instance, to describe viable cell density (X) in batch and fed-batch systems requires initially increasing and subsequently decreasing levels.

This cannot be fit by a simple exponential growth model (Eq.6.1) or by the commonly used logistic growth equation. It is proposed that a four-parameter generalized logistic equation (GLE) should be used to describe viable cell concentration [25].

$$X = \frac{A}{\exp(Bt) + C\exp(-Dt)} \tag{6.5}$$

where A, B, C and D are non-negative model parameters that are specific to the data set being modeled. It is informative to relate the logistic equation parameters to corresponding biological process parameters. The contribution of $\exp(Bt)$ is minimal in the growth phase and when set to zero, Eq.(6.5) reduces to an exponential growth equation with D as the specific growth rate. Similarly, neglecting contributions of $C\exp(-Dt)$ during the cell death phase reduces Eq.(6.5) to an exponential decay expression with B as the death rate. The parameters D and B thus represent the maximum growth rate, $\mu_{\max}$, and the maximum death rate, $k_{d_{\max}}$, respectively. These would be constant in the exponential growth and corresponding decline phases, respectively. Simulations were performed to test this hypothesis and Figure 6.1 illustrates sensitivity of the cell density curve to D and B and hence $\mu_{\max}$ and $k_{d_{\max}}$ values. As expected, changes to $\mu_{\max}$ affect the exponential growth phase while the influence is negligible in the decay phase, especially for $t > 1.5t_{\max}$ (Figure 6.1a). Sensitivity to $k_{d_{\max}}$ is minimal for $t < 0.5t_{\max}$ while later portions of the cell density curve are significantly affected (Figure 6.1b). Eq.(6.5) can thus be written in terms of $\mu_{\max}$ and $k_{d_{\max}}$ as

$$X = \frac{A}{\exp(k_{d_{\max}}t) + C\exp(-\mu_{\max}t)} \tag{6.6}$$

The initial cell density, X_0, can be expressed in terms of A and C by setting $t = 0$ in Eq.(6.6)

$$X_0 = \frac{A}{1+C} \tag{6.7}$$

Setting the derivative of Eq.(6.6), $\frac{dX}{dt} = 0$ provides an equation for $t_{\max}$, the time corresponding to the maximum cell density

$$t_{\max} = \frac{1}{k_{d_{\max}} + \mu_{\max}} \ln\left(\frac{C\mu_{\max}}{k_{d_{\max}}}\right) \tag{6.8}$$

An estimate for $X_{\max}$, the maximum cell density attained during the cultivation, can be obtained from substituting Eq.(6.8) into Eq.(6.6)

It must be noted that Eq.(6.5) could also fit the successive ascending and descending

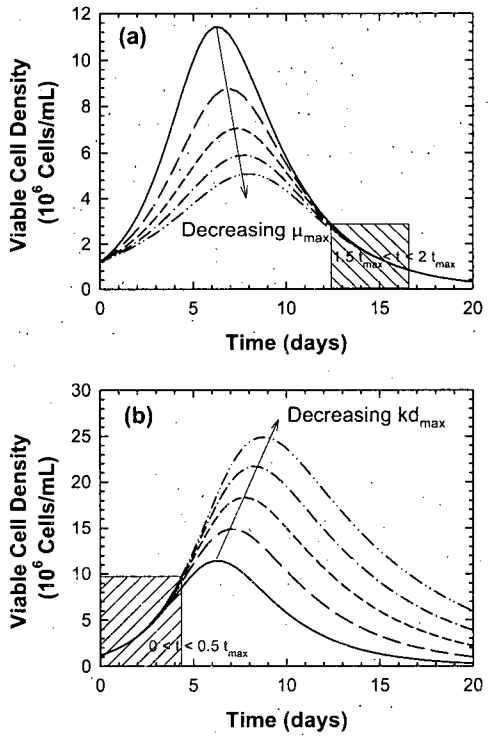

Figure 6.1: Sensitivity of the viable cell density curve to the logistic parameters $D\,(\mu_{\max})$ and $B\,(k_{d_{\max}})$. Successive curves are for 25% decreased parameters compared to the previous curve.

lactate concentrations often observed in fed-batch culture. Most other product and nutrient concentrations can be expected to monotonically increase or decrease, respectively, over the whole duration of the run (expect at times of fed-batch additions). This suggests that simplified forms of Eq.(6.5) could effectively describe the concentrations of nutrients and products in batch or fed-batch cultivations. Setting $B \rightarrow 0$ in Eq.(6.5) results in the logistic growth equation (LGE) that can be used to describe a monotonically increasing product concentration, P:

$$P = \frac{A}{1 + C\exp\left(-Dt\right)} \tag{6.9}$$

The parameter D is a rate constant for concentration increase and definitions of A and C can be obtained by setting $\frac{dP}{dt} = 0$ and $t = 0$ in Eq.(6.9), respectively

$$A = P_{\max}; \qquad C = \frac{P_{\max} - P_0}{P_0} \tag{6.10}$$

where P_{max} is the maximum value of P and P_0 the initial value at $t = 0$. Using these definitions, the LGE can be rewritten to be consistent with other presentations in the literature [27]

$$P = \frac{P_0 P_{max}}{P_0 + (P_{max} - P_0)\exp(-Dt)} \tag{6.11}$$

Setting $D \to 0$ in Eq.(6.5) results in the logistic decline equation (LDE) that can be used to describe any monotonically decreasing nutrient concentration, N:

$$N = \frac{A}{\exp(Bt) + C} \tag{6.12}$$

where B is a rate constant for concentration decrease and A and C are related to the initial nutrient concentration, N_0, as:

$$N_0 = \frac{A}{1 + C} \tag{6.13}$$

Specific rates could be readily estimated from the logistic models as Eqs.(6.5), (6.9) and (6.12) are analytically differentiable:

$$\frac{dX}{dt} = X\left\{\frac{DC\exp(-Dt) - B\exp(Bt)}{\exp(Bt) + C\exp(-Dt)}\right\} \tag{6.14}$$

$$\frac{dP}{dt} = PD\left(1 - \frac{P}{A}\right) \tag{6.15}$$

$$\frac{dN}{dt} = -NB\left(1 - \frac{C}{A}N\right) \tag{6.16}$$

6.3 Materials and Methods

6.3.1 Cell Line, Medium and Cell Culture System

CHO cells were cultivated in batch mode with glucose and glutamine as the main carbon and energy sources in a proprietary medium formulation. Experiments were conducted in three 15 L bioreactors (Applikon, Foster City, CA) with a 10 L working volume. The temperature was maintained at 36.5 °C and the agitation at 40 RPM. The dissolved oxygen (DO) concentration was maintained at 50% air saturation by sparging a mixture of oxygen and nitrogen (100 - 150 mL/min) through 0.5 μm spargers. The bioreactor was inoculated at an initial cell density of approximately 1.0 x 10^6 cells/mL and the pH was maintained at 6.8 by the automatic addition of 0.3 M NaOH.

6.3.2 Analytical Methods

Samples from the bioreactor were taken daily for cell density and viability analyses using the CEDEX system (Innovatis, Bielefeld, Germany). The samples were subsequently centrifuged (Beckman Coulter, Fullerton, CA) and the supernatants were analyzed for nutrient and metabolite concentrations. Glucose, lactate, glutamine and glutamate concentrations were determined using a YSI Model 2700 analyzer (Yellow Springs Instruments, Yellow Springs, OH) while ammonium was measured by an Ektachem DT60 analyzer (Eastman Kodak, Rochester, NY). The pH and DO were measured online using retractable electrodes (Mettler-Toledo Inc., Columbus, OH) and their measurement accuracy was verified through off-line analysis in a Stat Profile 9 blood gas analyzer (Nova Biomedical, Waltham, MA). The same instrument also measured the dissolved CO_2 concentration. On-line measurements of cell density were made with a retractable optical density probe (Aquasant Messtechnik, Bubendorf, Switzerland), calibrated with heamocytometer counts of cell concentrations.

6.3.3 Nonlinear Parameter Estimation

The parameters A, B, C and D in Eqs.(6.5), (6.9) and (6.12) were estimated by minimizing the sum of squares error (SSE) between the experimental and model fit data.

$$\mathbf{SSE} = \sum_{i=1}^{j} \left\{ (x_{meas})_i - (x_{fit})_i \right\}^2 \tag{6.17}$$

where $(x_{meas})_i$ is the i^{th} experimental x value and $(x_{fit})_i$ is the i^{th} model fitted x value in a total of j observations. Eq.(6.5) involved the sum of exponentials and was inherently unstable. Hence three different algorithms were used for nonlinear parameter estimation: the Levenberg-Marquardt method [28], the simplex approach [29] and the generalized reduced gradient method [30, 31]. The parameters used were those that resulted in the lowest values of the SSE defined in Eq.(6.17). The parameter standard errors and the correlation between parameters were estimated from the covariance matrix to help evaluate the quality of the model fit to the experimental data. When multiple models with different degrees of freedom were fitted to the same data set, the F test [32] was used to discriminate among the models. Computer programs for logistic modeling are presented in Appendix F and nonlinear parameter estimation details are provided in Appendix G.

6.4 Results and Discussion

6.4.1 Biological Significance of the Logistic Parameters

The exponential growth and death phases were defined as $0 < t < 0.5t_{\max}$ and $1.5t_{\max} < t < 2t_{\max}$, respectively, based on an examination of the cell density profiles from Figure 6.1. To verify these definitions, $\mu_{\max}$ and $k_{d_{\max}}$ were computed from all the cell concentration data analyzed in this work and compared with the logistic parameters D and B. Excellent agreement between the maximum rates and the logistic parameters was seen in all cases (Figure 6.2a, 6.2b) supporting the reformulation of Eq.(6.5) as Eq.(6.6). The utility of Eqs.(6.6) and (6.8) to predict the maximum cell density in batch and fed-batch cultures was verified by comparing $X_{\max}$ values calculated from these equations with experimental data (Figure 6.2c). For all 15 data sets, experimentally observed maximum cell densities were accurately predicted by Eqs.(6.6) and (6.8) and the fitted logistic parameters.

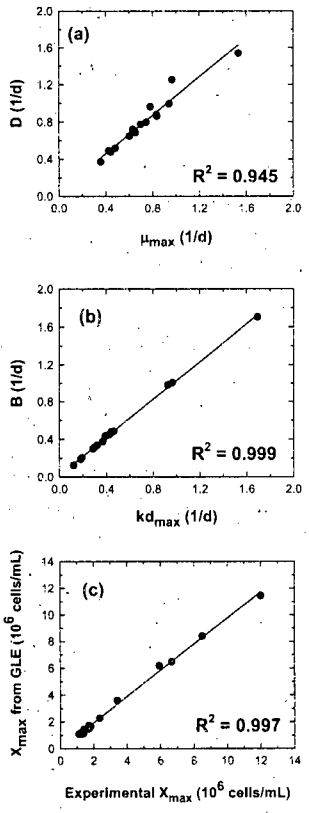

Figure 6.2: Illustration of the biological significance of the logistic parameters using 8 batch and 7 fed-batch cell density data sets [1, 14, 33, 34].

6.4.2 Description of Experimental Data from Batch Cultures

The time profiles of CHO cell density, nutrient and metabolite concentrations along with the logistic model fits are shown in Figure 6.3. The GLE was first used to describe all the state variables measured in this experiment. Subsequently, the LDE was used to describe the monotonically decreasing glucose and glutamine concentrations while the LGE was used to describe the increasing lactate and ammonium concentrations. Model discrimination using the F test indicated that the LDE and LGE fits were statistically superior to the GLE at the 95% confidence level for the nutrient and metabolite concentrations, respectively, and hence results from these equations are presented in Figure 6.3. The experimental data were well fitted by the models and the corresponding specific rates were calculated from Eqs.(6.1) – (6.3) using analytical derivatives of the logistic equations (Eqs.6.14 – 6.16).

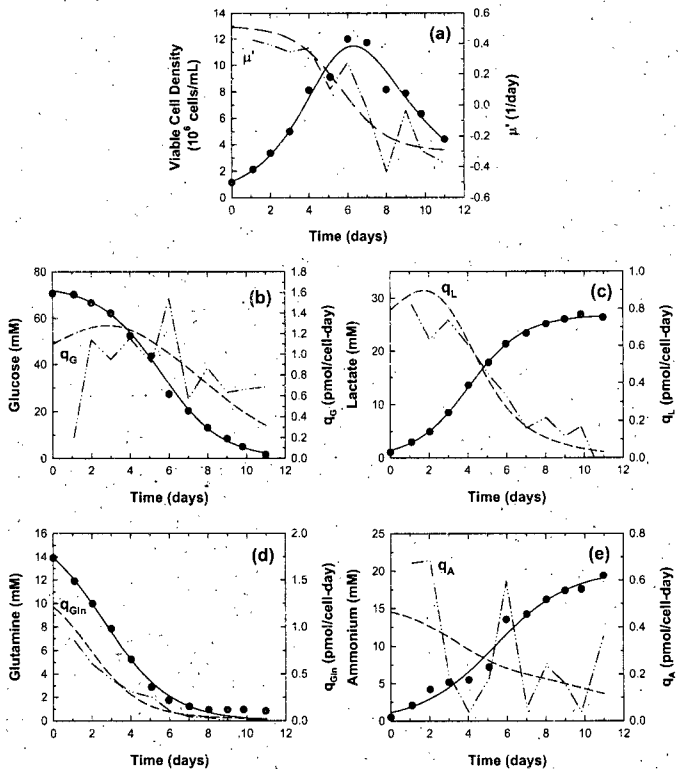

Figure 6.3: Time profiles of cell density, nutrient and metabolite concentrations for CHO cells in 15 L batch culture. Experimental data (●●●●●); Logistic (GLE for cell density, LDE for glucose and glutamine and LGE for lactate and ammonium) fit (———); Logistic specific rate (– – – – –); Discrete derivative specific rate (– · · – · ·).

It is remarkable that the model fit the data so well even though logistic models do not include independent terms for growth-related and maintenance-related metabolism. This could be in part due to the predominant effect of exponential cell growth compared to relatively gradual shifts over a batch culture of growth- or maintenance-related metabolic rates. From a practical standpoint, the use of a single equation and its reduced forms to describe all experimental measurements in batch (or fed-batch) cultivations adds to the simplicity of the proposed logistic approach.

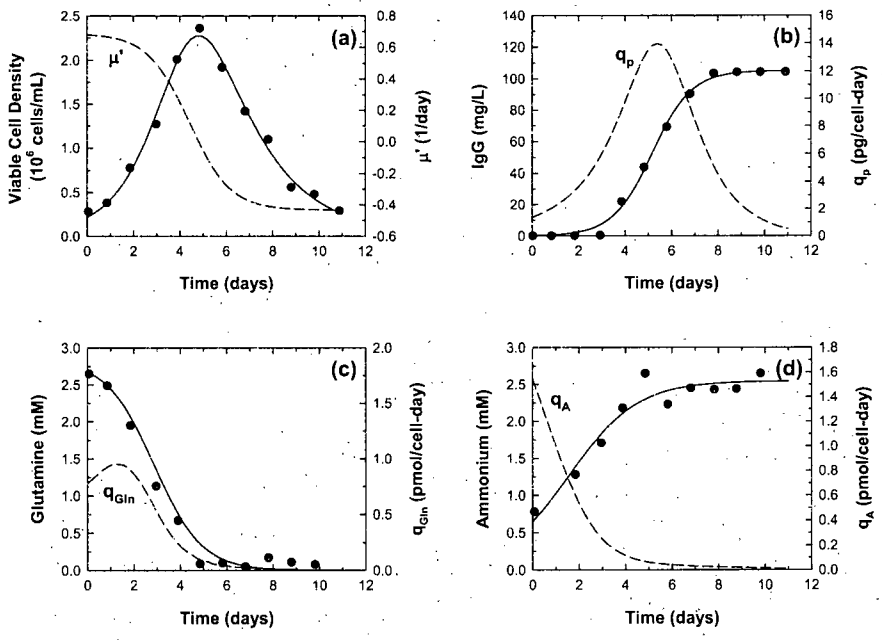

Figure 6.4: Viable cell density, IgG, glutamine and ammonium concentrations for hybridoma cells in 300 L batch culture [1]. The points are experimental data and the solid lines are fits by the logistic equations (GLE for cell density, LDE for glutamine and LGE for IgG and ammonium). Specific rates calculated from the logistic fits are shown as dashed lines.

Experimental data from batch cultivations are obtained from periodic samples whose concentrations are analyzed and then the data are converted to the corresponding derivatives to obtain specific rates. The logistic equations provided smooth and close fits to all of the concentration data, thereby yielding smooth logistic specific rate profiles (Figure 6.3). In contrast, specific rates obtained using discrete derivatives of the state variables were not smooth and were highly sensitive to outliers in experimental measurements. Though the discretely derived q_{Gln} values were acceptable, those for glucose and ammonium were in

gross error, primarily due to outliers in the experimental data. The μ' and specific lactate production rate, q_L, profiles were similar to those from the logistic fits, albeit not as smooth. In all cases besides q_{Gln}, physiologically implausible oscillations were introduced by the discrete fit and not by the logistic fit.

Table 6.1: Previously-published batch and fed-batch studies used to test the logistic modeling approach presented in this study

Reference	Cell Line	Bioreactor Type	Modeling Approach
[1]	Hybridoma	Stirred tank (300 L batch)	Kinetic modeling
[33]	Hybridoma	T-flask (100 mL batch)	Kinetic modeling
[14]	BHK	Spinner (500 mL batch)	Polynomial fitting
[15]	Hybridoma	Bench-top (2.4 L fed-batch)	Polynomial fitting
[34]	CHO, Hybridoma	Bench-top (0.7 L fed-batch)	Discrete derivatives

The more general utility of this logistic approach was further evaluated using data from published batch studies that investigated different cell lines (hybridoma and Baby Hamster Kidney) in bioreactors ranging from 150 cm^2 T-flasks to 300 L stirred tanks (Table 6.1). Two of these studies [1, 33] used Monod-type kinetics to describe the experimental data while experimental data were fitted by polynomial functions in the third [14]. Results from using the logistic equations to describe the data from two of these experiments are shown in Figures 6.4 and 6.5. The nutrient, metabolite and product concentrations were fit by the LDE and LGE models while the four-parameter GLE was necessary to describe the dynamics of viable cell concentration. In all cases, the experimental data were well described by the logistic equations and similar good fits were obtained for data from the third study (not shown). These results clearly indicate the applicability of the logistic models to describe experimental data obtained by multiple groups from batch reactors of varying sizes and cell types.

6.4.3 Description of Experimental Data from Fed-Batch Cultures

These logistic methods would be much more useful if they could be applied to fed-batch cultures that become the focus of later stages of development and manufacturing. However, it was a concern that periodic feeding of nutrients would distort the resulting profiles so that the logistic approach might not be suitable. Fed-batch data from two studies [15, 34] (Table 6.1) were analyzed using the logistic equations. In the first study [15], hybridoma cells were cultivated in a 2.4 L bioreactor with the feeding of glucose or glutamine or both. The second involved cultivation of tissue plasminogen activator (t-PA) producing CHO cells

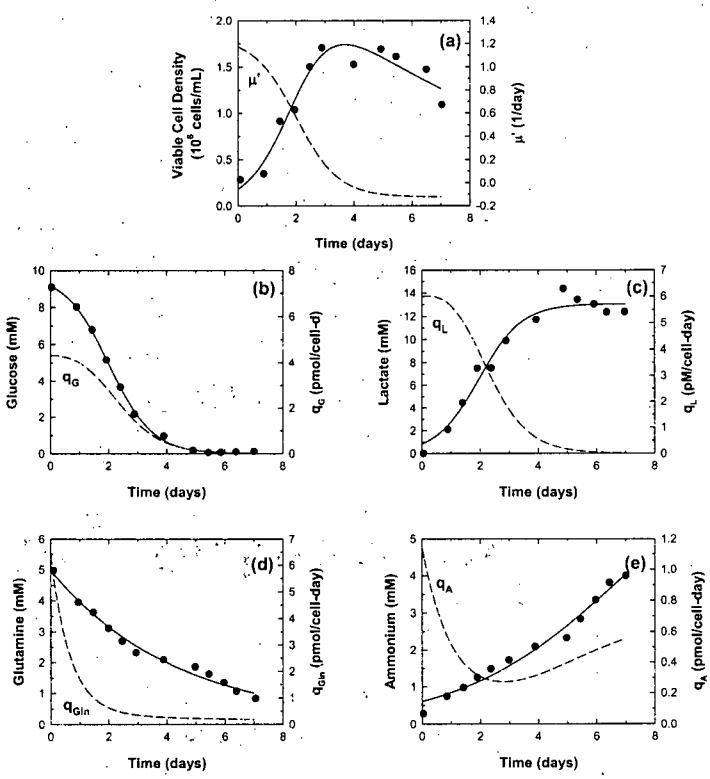

Figure 6.5: Viable cell density, nutrient and metabolite concentrations for BHK cells in 500 mL batch culture [14]. The points are experimental data and the solid lines are fits by the logistic equations (GLE for cell density, LDE for glucose and glutamine and LGE for lactate and ammonium). Specific rates calculated from the logistic fits are shown as dashed lines.

in a 0.7 L bioreactor with glucose or amino acid feeding.

Data from glutamine limited fed-batch hybridoma cultures are shown in Figure 6.6 along with corresponding logistic fits. All variables except glutamine (the nutrient that was fed) were fit well by the logistic equations. Time profiles of the fed nutrient will depend strongly on the feeding strategy, often with concentrations at low values to minimize the production of metabolites [13, 35]. The logistic equations cannot be expected to effectively fit such fed-nutrient profiles. A total of 20 data sets were analyzed from the CHO fed-batch cultivations [34] and representative cell density and t-PA concentration data under two different feeding conditions are shown in Figure 6.7. The logistic equations fit the data well as was true for the remaining 16 data sets (not shown). It should be noted that the 4-parameter GLE was used to describe t-PA concentration due to the declining trend later in the culture. Similar

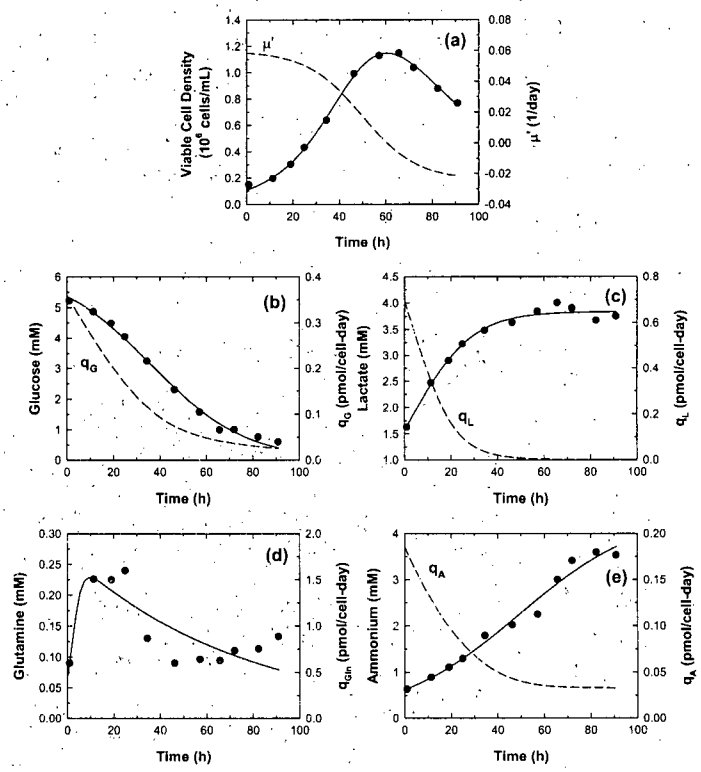

Figure 6.6: Viable cell density, nutrient and metabolite concentrations for hybridoma cells in glutamine limited 2.4 L fed-batch culture [15]. The points are experimental data and the solid lines are fits by the logistic equations (GLE for cell density, LDE for glucose and glutamine and LGE for lactate and ammonium). Specific rates calculated from the logistic fits are shown as dashed lines.

declines have been observed for lactate concentration in fed-batch cultures [24] and in such instances, the GLE (as opposed to the LGE) more effectively fits those experimental data.

6.4.4 Comparison with Other Modeling Approaches

Polynomial approximation and unstructured kinetic modeling are the primary methods currently used to fit data from batch and fed-batch experiments. Given the conceptual similarity between the logistic modeling approach presented in this study and polynomial approximation, it is important to compare their ability to describe mammalian cell culture data. Polynomial approximation has limitations because exponential state variable time profiles are difficult to describe with polynomial functions [16]. The same 30 data sets from batch cultures were also analyzed using polynomial fitting and the inability to describe the

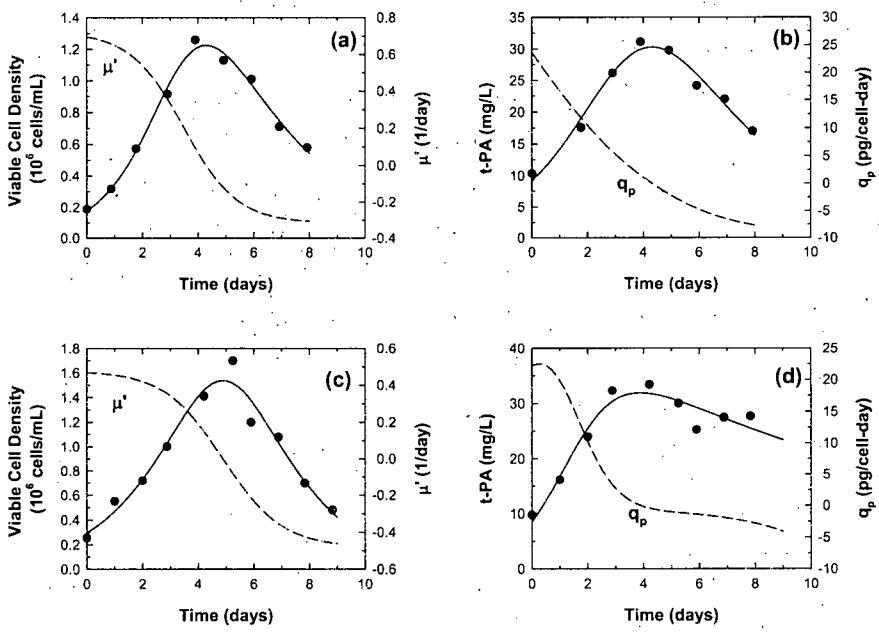

Figure 6.7: Viable cell density and t-PA concentration for CHO cells in 0.7 L fed-batch culture under two different feeding conditions [34]. Glucose was fed at 4 pmol/cell-day for panels a and b while amino acids were also fed for panels c and d. The points are experimental data and the solid lines are fits by the logistic equations (GLE for both cell density and t-PA). Specific rates calculated from the logistic fits are shown as dashed lines.

experimental data was quantified by the Eq.(6.17) sum of squares errors to compare with logistic fitting. Since increasing the order of a polynomial function could result in a better fit to experimental data, polynomial functions with one additional parameter than the corresponding logistic equation were also evaluated. For instance, the viable cell density description using Eq.(6.5) has 4 parameters and this was compared with polynomials of orders 3 (4 parameters) and 4 (5 parameters). Comparisons between logistic equations and polynomials of the same order used the SSE values while comparisons between logistic equations and higher order polynomials were done using the F-test. The F-test determined if the higher order polynomial fit was indeed a closer representation at the 95 % confidence level.

Of the 30 batch data sets examined using both the logistic and polynomial approaches, the polynomial approach was statistically superior in only 3 instances. It is important to note that even in the few cases of statistical superiority for the polynomial fit, these did

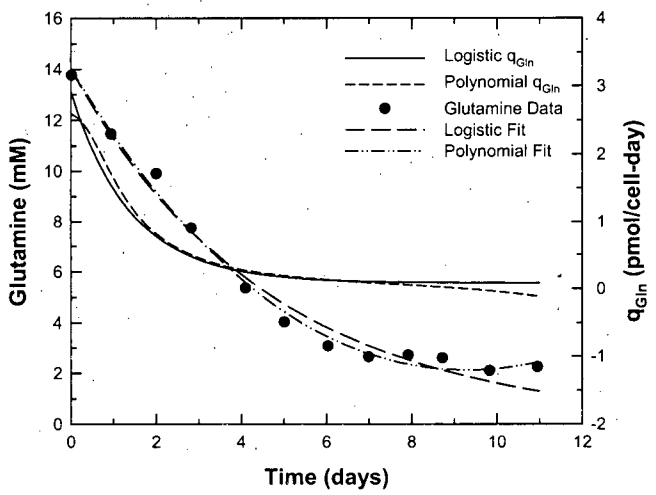

Figure 6.8: Comparison of q_{Gln} values from logistic (LDE) and polynomial fits for CHO cells in 15 L batch culture. The polynomial fit to glutamine depletion data was statistically superior than the logistic fit for this data set.

not necessarily yield improved specific rate estimates. Figure 6.8 shows specific glutamine consumption rates for CHO cells that was one of the above mentioned 3 cases where the polynomial fit was statistically superior to the logistic fit. An examination of the specific rate data from the polynomial fit indicates that data after $t = 9$ days were negative, suggesting net glutamine production. This is not reflective of the biology and is an artifact due to an inflexion in the polynomial fit to the data at $t = 9$ days and beyond. The logistic modeling approach does not suffer from such errors. Instead the fits are constrained to the expected trends, monotonic in this case.

Logistic and polynomial fits to the data from Dalili et al. [33] are shown in Figure 6.9 as examples of the data sets where the logistic approach was statistically superior. Both polynomials grossly misrepresented the time course of viable cell density and no improvement was obtained by increasing the order of the polynomial. Computation of growth rates from either of the polynomial fits would not be acceptable. Similar limitations, albeit to a lesser extent, were seen for the IgG and glutamine data sets in Figure 6.9. The polynomial approach thus lacks generality and cannot be relied upon as a robust tool for specific rate estimation in batch cultures.

Unstructured kinetic modeling involves the use of Monod-type equations and estimating a large number of kinetic parameters by nonlinear optimization in the system of differential equations. Two batch studies [1, 33], whose data were used in this study for verification

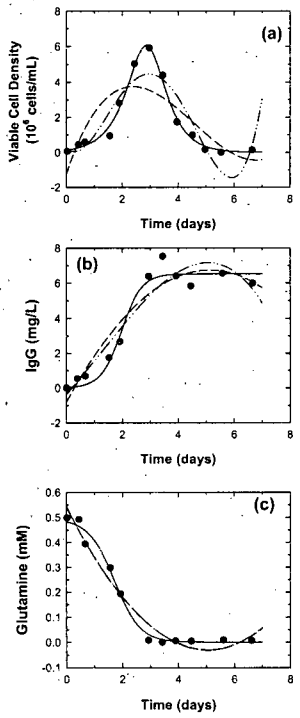

Figure 6.9: Comparison of logistic (GLE for cell density, LGE for IgG and LDE for glutamine) and polynomial fits for batch cultivation of hybridoma cells in 100 mL T-flasks [33]. (———) logistic fit; (– – – – –) polynomial fit with the same number of parameters as the logistic fit; (– · · – · ·) polynomial fit with one additional parameter (The two polynomial fits in panel c overlap).

of the logistic approach, employed modified forms of the Monod equation in kinetic expressions to describe their experimental data. One used simpler kinetic expressions for glutamine limited cultures [33], requiring 8 parameters to be estimated while 13 parameters were required for a more comprehensive kinetic model [1]. Estimating such a large number of kinetic parameters through nonlinear least squares from a system of nonlinear differential equations is not trivial and is unlikely to provide robust parameter estimates due to the strong correlation among the kinetic parameters. Moreover, the large variability in the kinetic models used [6, 7] makes it difficult to compare results from different studies employing this approach.

6.4.5 Computation of Integral Quantities

The integral viable cell density is an important parameter for the characterization of batch and fed-batch cultures [36]. Since it corresponds to the area under the curve in a plot of viable cell density versus time, it can be computed by integrating Eq.(6.5). However, Eq.(6.5) cannot be analytically integrated because of the sum of exponential terms in the denominator and an approximation to this integral is presented in Appendix F. Alternatively, a simple numerical technique, such as the trapezoidal or any higher-order quadrature rule [37], can be used to estimate the integral viable cell density from Eq.(6.5).

6.4.6 Data for Estimation of Metabolic Fluxes

An original motivation for this work was in the context of metabolic flux analysis that is increasingly used to characterize cellular metabolism and physiology by estimating fluxes through the pathways of central carbon metabolism [38]. Input data for metabolic flux analysis include specific uptake and production rates in addition to cellular growth rate. The logistic equations presented in this study provide a practical means of more reliable specific rate estimation that should enable more robust metabolic flux computation in batch and fed-batch cultures.

6.5 Conclusions

The application of logistic equations for analyzing mammalian cell batch and fed-batch data has been illustrated. Though non-mechanistic in nature, these equations did provide a means to impose logical general constraints on the fitted profiles. Simplified logistic equation forms were selected based on expected monotonic or increasing followed by decreasing trends. Time profiles of cell density, nutrients and metabolites were well fitted by the logistic equations and time derivatives of these variables were readily computed, resulting in rapid estimation of specific rates. Besides providing valuable information on cellular physiology and metabolism, specific rates are precursors for metabolic flux estimation, thereby allowing improved use of information collected in batch and fed-batch cultivations. This functional representation also allowed for computation of integral viable cell density, an indicator of batch and fed-batch process performance. Another advantage of the logistic approach is its general nature thereby increasing its applicability to a wide variety of experimental systems as shown in this study. This general nature coupled with the ability to rapidly obtain more robust specific rate estimates should make it an attractive alternative for describing the dynamics of mammalian cell growth and protein production in batch and fed-batch culture.

This philosophy of empirical modeling based on constraining fits to expected trends could be extended to the derivation of other useful models where the complexity of systems makes mechanistic models impractical.

Bibliography

[1] Bree, M.; Dhurjati, P.; Geoghegan, R.; Robnett, B. Kinetic modeling of hybridoma cell growth and immunoglobulin production in a large-scale suspension culture. *Biotechnol. Bioeng.*, **1988**, *32*, 1067–1072.

[2] Dhir, S.; Morrow, K.; Rhinehart, R.; Wiesner, T. Dynamic optimization of hybridoma growth in a fed-batch bioreactor. *Biotechnol. Bioeng.*, **2000**, *67*, 197–205.

[3] Gaertner, J.; Dhurjati, P. Fractional factorial study of hybridoma behavior. 1. Kinetics of growth and antibody production. *Biotechnol. Prog.*, **1993**, *9*, 298–308.

[4] Gaertner, J.; Dhurjati, P. Fractional factorial study of hybridoma behavior. 2. Kinstics of nutrient uptake and waste production. *Biotechnol. Prog.*, **1993**, *9*, 309–316.

[5] Kurokawa, H.; Park, Y.; Iilima, S.; Kobayashi, T. Growth characteristics in fed-batch culture of hybridoma cells with control of glucose and glutamine concentrations. *Biotechnol. Bioeng.*, **1994**, *44*, 95–103.

[6] Pörtner, R.; Schäfer, T. Modelling hybridoma cell growth and metabolism - A comparison of selected models and data. *J. Biotechnol.*, **1996**, *49*, 119–135.

[7] Tziampazis, E.; Sambanis, A. Modeling of cell culture processes. *Cytotechnology*, **1994**, *14*, 191–204.

[8] Altamirano, C.; Paredes, C.; Cairo, J.; Gòdia, C. Improvement of CHO cell culture medium formulation: Simultaneous substitution of glucose and glutamine. *Biotechnol. Prog.*, **2000**, *16*, 69–75.

[9] Glacken, M.; Adams, E.; Sinskey, A. J. Mathematical description of hybridoma culture kinetics: I. Initial metabolic rates. *Biotechnol. Bioeng.*, **1988**, *32*, 491–506.

[10] Ozturk, S.; Palsson, B. Effects of dissolved oxygen on hybridoma cell growth, metabolism, and antibody production kinetics in continuous culture. *Biotechnol. Prog.*, **1990**, *6*, 437–446.

[11] Zupke, C.; Sinskey, A. J.; Stephanopoulos, G. Intracellular flux analysis applied to the effect of dissolved oxygen on hybridomas. *Appl. Microbiol. Biotechnol.*, **1995**, *44*(1-2), 27–36.

[12] Sauer, P.; Burky, J.; Wesson, M.; Sternard, H.; Qu, L. A high-yielding, generic fed-batch cell culture process for production of recombinant antibodies. *Biotechnol. Bioeng.*, **2000**, *67*, 585–597.

[13] Zhou, W. C.; Chen, C.-C.; Buckland, B.; Aunins, J. Fed-batch culture of recombinant NSO myeloma cells with high monoclonal antibody production. *Biotechnol. Bioeng.*, **1997**, *55*, 783–792.

[14] Linz, M.; Zeng, A. P.; Wagner, R.; Deckwer, W. D. Stoichiometry, kinetics and regulation of glucose and amino acid metabolism of a recombinant BHK cell line in batch and continuous culture. *Biotechnol. Prog.*, **1997**, *13*, 453–463.

[15] Ljumggren, J.; Häggström, L. Catabolic control of hybridoma cells by glucose and glutamine limited fed batch cultures. *Biotechnol. Bioeng.*, **1994**, *44*, 808–818.

[16] Stephanopoulos, G.; Aristodou, A.; Nielsen, J. *Metabolic Engineering. Principles and Methodologies.* Academic Press, San Diego, 1998.

[17] Gibson, A.; Bratchell, N.; Roberts, T. The effect of sodium chloride and temperature on the rate and extent of growth of Clostridium botulinium type A in pasteurized prok slurry. *J. Appl. Bacteriol.*, **1987**, *62*, 479–490.

[18] Jason, A. A deterministic model for monophasic growth of batch cultures of bacteria. *Antonie Van Leeuwenhoek*, **1983**, *49*, 513–536.

[19] Sangsuurasak, P.; Mitchell, D. Incorporation of death kinetics into a 2-dimensional dynamic heat transfer model for solid state fermentation. *J. Chem. Technol. Biotechnol.*, **1995**, *64*, 253–260.

[20] Szewczyk, K.; Myszka, L. The effect of temperature on the growth of A. niger in solid state fermentation. *Bioprocess Engineering*, **1994**, *10*, 123–126.

[21] Tsoularis, A.; Wallace, J. Analysis of logistic growth models. *Math. Biosci.*, **2002**, *179*, 21–55.

[22] Viniegra-Gonzalez, G.; Larralde-Corona, C.; Lopez-Isunza, F.; Favela-Torres, E. Symmetric branching model for the kinetics of mycelial growth. *Biotechnol. Bioeng.*, **1993**, *42*, 1–10.

[23] Zwietering, M.; Jongenburger, I.; Rombouts, F.; van't Riet, K. Modeling of the bacterial growth curve. *Appl. Environ. Microbiol.*, **1990**, *56*(6), 1875–1881.

[24] Altamirano, C.; Paredes, C.; Illanes, A.; Cairó, J.; Gòdia, C. Strategies for fed-batch cultivation of t-PA producing CHO cells: substitution of glucose and glutamine and rational design of culture medium. *J. Biotechnol.*, **2004**, *110*, 171–179.

[25] Jolicoeur, P.; Pontier, J. Population growth and decline: A four-parameter generalization of the logistic curve. *J. Theor. Biol.*, **1989**, *141*, 563–571.

[26] Ozturk, S.; Palsson, B. Chemical decomposition of glutamine in cell culture media: Effect of media type, pH, and serum concentration. *Biotechnol. Prog.*, **1990**, *6*, 121–128.

[27] Schuler, M.; Kargi, F. *Bioprocess Engineering.* Prentice Hall, Upper Saddle River, NJ, 2nd edition, 2002.

[28] Marquardt, D. An Algorithm for Least-Squares Estimation of Nonlinear Parameters. *SIAM J. Appl. Math.*, **1963**, *11*, 431–441.

[29] Nelder, J.; Mead, R. A simplex method for function minimization. *Comput. J.*, **1965**, *7*, 308–313.

[30] Lasdon, L.; Smith, S. Solving large spare nonlinear programs using GRG. *ORSA J. Comput.*, **1992**, *4*(1), 2–15.

[31] Lasdon, L.; Waren, A.; Jain, A.; Ratner, M. Design and testing of a generalized reduced gradient code for nonlinear programming. *ACM Trans. Math. Softw.*, **1978**, *4*(1), 34–50.

[32] Robinson, J. Determining microbial kinetic parameters using nonlinear regression analysis. Advantages and limitations in microbial ecology. *Adv. Microb. Ecol.*, **1985**, *8*, 61–110.

[33] Dalili, M.; Sayles, G.; Ollis, D. Glutamine-limited batch hybridoma growth and antibody production: Experiment and model. *Biotechnol. Bioeng.*, **1990**, *36*, 74–82.

[34] Dowd, J.; Kwok, K.; Piret, J. Increased t-PA yields using ultrafiltration of an inhibitory product fron CHO fed-batch culture. *Biotechnol. Prog.*, **2000**, *16*, 786–794.

[35] Zhou, W. C.; Rehm, J.; Hu, W. S. High viable cell concentration fed-batch cultures of hybridoma cells through on-line nutrient feeding. *Biotechnol. Bioeng.*, **1995**, *46*, 579–587.

[36] Luan, Y.; Mutharasan, R.; Magee, W. Effect of various glucose/glutamine ratios on hybridoma growth, viability and monoclonal antibody production. *Biotechnol. Lett.*, **1987**, *9*(8), 691–696.

[37] Press, W.; Teukolsky, S.; Vellerling, W.; Flannery, B. *Numerical Recipies in FORTRAN. The art of scientific computing.* Cambridge University Press, Cambridge, 2nd edition, 1992.

[38] Stephanopoulos, G.; Stafford, D. Metabolic Engineering: a new frontier of chemical reaction engineering. *Chem. Eng. Sci.*, **2002**, *57*, 2595–2602.

Chapter 7

Error in Specific Rates and Metabolic Fluxes[1]

7.1 Introduction

Metabolic fluxes are considered a fundamental determinant of cell physiology [1] and metabolic flux analysis has been increasingly used to characterize the metabolism of mammalian cell cultures [2–8]. Flux data provide a quantitative description of the cellular response to changing environmental conditions, such as those encountered during bioprocess development, and are hence useful for bioprocess optimization. The first step in metabolic flux estimation is the construction of a bioreaction network that describes the conversion of substrates to metabolites and biomass. These bioreaction networks are typically simplified to enable flux estimation from available experimental data. For mammalian cells, these include the main reactions of central carbon and amino acid metabolism [5, 6, 9]. The unknown fluxes in the bioreaction network are subsequently estimated either using metabolite balancing [2, 3, 6, 8, 10–13] or isotope tracer techniques [9, 14–19]. In the metabolite balancing approach, fluxes are estimated by applying mass balances around the intracellular metabolites using the measured extracellular rates as input data. The analytical and computational techniques associated with the metabolite balancing approach are relatively simple [1] and can be readily applied to most experimental systems. This approach, however, cannot determine fluxes in cyclic and bidirectional reactions. Additional shortcomings and approaches to overcome them have been discussed in detail [10, 20]. Despite these limitations, metabolite

[1] A version of this chapter will be submitted for publication. Goudar, C.T., Biener, R., Konstantinov, K.B. and Piret, J.M. (2006). Error propagation from prime variables into specific rates and metabolic fluxes for mammalian cells in perfusion culture.

balancing remains the method of choice for a majority of process development experiments and for all pilot and manufacturing-scale studies given the expense of the isotope tracing alternative.

Information on the error associated with metabolic flux values obtained by the metabolite balancing approach is critical to meaningfully interpret changes in cellular metabolism. As cell specific rates including growth, nutrient consumption and metabolite production comprise the input data for flux estimation, flux values can be strongly influenced by specific rate errors. Cell specific rates, however, are not experimentally measured but are calculated from measured prime variables including cell, nutrient, metabolite and product concentrations. Information on prime variable error is thus necessary to characterize their influence on specific rate error and ultimately on flux values.

The need to have specific rate data with no gross measurement error has been long recognized and a framework has been proposed to check for the presence of gross errors [19, 21, 22]. However, error propagation from prime variables into metabolic fluxes has not been reported. This study is aimed at systematically characterizing error propagation from prime variables to metabolic fluxes for mammalian cells. Prime variable errors were first estimated and their propagation into specific rates and metabolic fluxes was quantified using a combination of experimental data and Monte-Carlo analysis. An operating flux error region could be identified allowing more reliable interpretation of the calculated fluxes.

7.2 Materials and Methods

7.2.1 Cell Line, Medium and Cell Culture System

CHO cells were cultivated in perfusion mode with glucose and glutamine as the main carbon and energy sources in a proprietary medium formulation. The bioreactor was inoculated at 0.92 x 10^6 cells/mL and cells were accumulated until the bioreactor reached 20 x 10^6 cells/mL at which point the cell concentration was maintained constant by controlling the bleed stream from the bioreactor. Experiments were conducted in a 15 L bioreactor (Applikon, Foster City, CA) with a 10 L working volume. Under standard operating conditions, the temperature was maintained at 36.5 °C and the agitation at 40 rpm. The dissolved oxygen (DO) concentration was maintained at 50% air saturation by sparging a mixture of oxygen and nitrogen through 0.5 μm spargers. The bioreactor pH was maintained at 6.8 by the addition of 0.3 M NaOH. Temperature, DO and pH were varied during the course of the cultivation resulting in a total of 12 experimental conditions, each of 10 day duration to identify valid operating ranges for these variables. Data from the last 4 days of each ex-

perimental condition were considered representative (variation < 15%) and used for specific rate and metabolic flux calculations.

7.2.2 Analytical Methods

Samples from the bioreactor were analyzed daily for cell concentration and viability using the Cedex system (Innovatis, Bielefeld, Germany). The samples were subsequently centrifuged (Beckman Coulter, Fullerton, CA) and the supernatant was analyzed for nutrient and metabolite concentrations. Glucose, lactate, glutamine and glutamate concentrations were determined using a YSI Model 2700 analyzer (Yellow Springs Instruments, Yellow Springs, OH) while ammonium was measured using an Ektachem DT60 analyzer (Eastman Kodak, Rochester, NY). The pH and DO were measured online using retractable electrodes (Mettler-Toledo Inc., Columbus, OH) and their measurement accuracy was verified through off-line analysis in a Stat Profile 9 blood gas analyzer (Nova Biomedical, Waltham, MA). The same instrument also measured the dissolved CO_2 concentration. On-line measurements of cell concentration were made with a retractable optical density probe (Aquasant Messtechnik, Bubendorf, Switzerland) that was calibrated with cell concentrations estimated using the Cedex system. Oxygen and carbon-dioxide concentrations in the exit gas were determined using a MGA-1200 Mass Spectrometer (Applied Instrument Technologies, Pomona, CA)

7.2.3 Prime Variables and Specific Rates

Errors in prime variable (cell concentration, product, glucose, glutamine, lactate, ammonium and oxygen) measurements were estimated by analyzing multiple bioreactor samples with replicate numbers determined by power analysis A significance level of 0.05 was assumed and the detectable difference was set equal to the assumed experimental error. The sample size was determined at a power value of 0.95. A total of 32 samples from 2 bioreactors (16/bioreactor) were used for error estimation from the mean and standard deviation of the 16 measurements.

Specific rate expressions were derived from mass balance equations for all prime variables of interest. Error in specific rates calculated from these equations were determined using the Gaussian approach [23] retaining only the first-order term in the Taylor series expansion

$$\Delta f\left(x_1, x_2, \ldots x_n\right) \cong \left|\frac{\partial f}{dx_1}\right| \Delta \bar{x}_1 + \left|\frac{\partial f}{dx_2}\right| \Delta \bar{x}_2 + \ldots \left|\frac{\partial f}{dx_n}\right| \Delta \bar{x}_n \tag{7.1}$$

where $\Delta f\left(x_1, x_2, \ldots x_n\right)$ is the error in the function f, $x_1, x_2, \ldots x_n$ are the true values of the

prime variables and $\Delta\bar{x}_1, \Delta\bar{x}_2, ...\Delta\bar{x}_n$ the measurement errors. Recognizing the truncation associated limitation of the Gaussian approach at high prime variable errors, a Monte-Carlo approach was also used for specific rate error estimation. Normally distributed noise with mean=0 and desired standard deviation was introduced in the prime variables and specific rates were computed. As most specific rates were functions of multiple prime variables, errors in each prime variable were changed one at a time to calculate the corresponding specific rate errors. This allowed comprehensive specific rate error characterization in a multidimensional grid over the desired range of prime variable errors. For each prime variable error value, 10,000 normally distributed random error values were generated and 10,000 specific rates calculated. Thus the specific rate data reported from Monte-Carlo analysis are an average of 10,000 estimates. This procedure was repeated when all associated prime variables were in error. Additional details and computer programs are presented in Appendix G.

7.2.4 Metabolic Fluxes

A biochemical network previously developed for CHO cells [8] was used in this study. This includes the major reactions of central carbon metabolism along with reactions for amino acid metabolism by an approach previously described in more detail [6, 8]. The stoichiometric matrix for this reaction network was of full rank and had a low condition number (69) indicating that flux estimates were not overly sensitive to specific rate variations. Metabolic fluxes were estimated using weighted least squares

$$\mathbf{x} = \left(\mathbf{A}^{\mathrm{T}}\psi^{-1}\mathbf{A}\right)^{-1}\mathbf{A}^{\mathrm{T}}\psi^{-1}\mathbf{r} \tag{7.2}$$

where $\mathbf{x}$ is the flux vector, $\mathbf{A}$ the stoichiometric matrix, $\mathbf{r}$ the rate vector and ψ the variance-covariance matrix of $\mathbf{r}$. The bioreaction network was characterized by two degrees of freedom and the two redundant measurements were used to test the consistency of the experimental data and the assumed biochemistry. The consistency index, h, was calculated for each of the 12 experimental conditions according to methods previously described [19, 21, 22] and was compared with $\chi^2 = 5.99$ (95% confidence level for 2 degrees of freedom).

To characterize error propagation from specific rates into metabolic fluxes, an initial metabolic flux vector was assumed and the corresponding specific rate vector was determined as $\mathbf{r} = \mathbf{A}\mathbf{x}$. Subsequently, error was introduced in $\mathbf{r}$ using normally distributed noise with zero mean and standard deviation corresponding to the desired error level (0 – 25%). Initially, error was separately added to each element in $\mathbf{r}$ (10,000 points at each error magnitude) and the resulting flux vector was computed. The flux data were averaged

and compared with the error-free flux vector. The difference between these flux values was caused by the specific rate error and helped quantify error propagation from the specific rates into the metabolic fluxes. For a more realistic representation of experimental conditions, this procedure was repeated with all elements of the specific rate vector simultaneously in error.

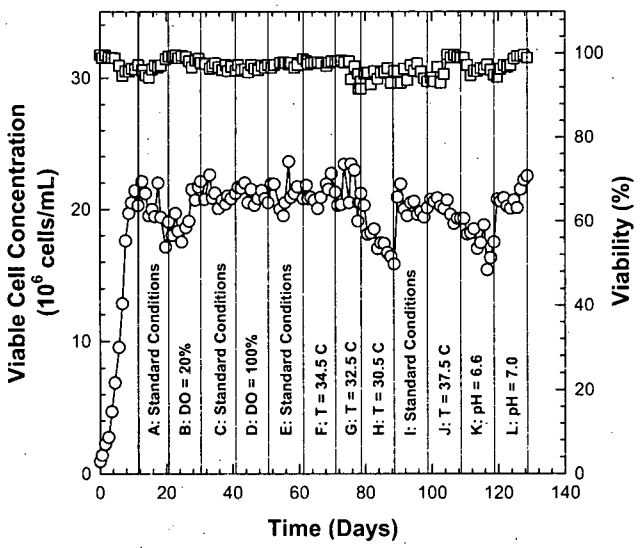

Figure 7.1: Viable cell concentration (○) and viability (□) time profiles over the 12 conditions examined in this study. Under standard conditions, DO = 50%, T = 36.5 °C, pH = 6.8 and the target cell concentration was 20 x 10^6 cells/mL for all conditions.

7.3 Results and Discussion

7.3.1 Perfusion Cultivation

DO, temperature and pH set points were varied during the course of the cultivation resulting in a total of 12 experimental phases, each of 10 day duration. Time courses of viable cell concentration and cell viability are shown in Figure 7.1. While the target cell concentration throughout the cultivation was 20 x 10^6 cells/mL, cell concentrations for T = 30.5 °C and pH = 6.6 were significantly lower due to reduced growth rates. Cell viability was greater than 90% throughout the experiment. Specific rates including growth, nutrient consumption and metabolite/product formation were calculated using the Table 7.1 equations. The average specific glucose consumption rates are shown in Figure 7.2. Changes to DO had no effect

on glucose consumption while temperature and pH reduction significantly lowered the cell specific glucose consumption rate. Glucose consumption increased at higher temperatures and pH = 7.

Table 7.1: Expressions for growth rate, specific productivity and specific uptake/production rates of key nutrients and metabolites in a perfusion system

Specific Rate	Expression
specific growth rate	$\mu = \frac{F_b}{V} + \frac{F_b}{V}\left(\frac{X_V^H}{X_V^B}\right) + \frac{1}{X_V^B}\left(\frac{dX_V^B}{dt}\right)$
specific productivity	$q_p = \frac{1}{X_V^B}\left(\frac{F_m P}{V} + \frac{dP}{dt}\right)$
specific glucose consumption rate	$q_G = \frac{1}{X_V^B}\left(\frac{F_m(G_m - G)}{V} - \frac{dG}{dt}\right)$
specific glutamine consumption rate	$q_{Gln} = \frac{1}{X_V^B}\left(\frac{F_m(Gln_m - Gln)}{V} - \frac{dGln}{dt} - k_{Gln}\,Gln\right)$
specific lactate production rate	$q_L = \frac{1}{X_V^B}\left(\frac{F_m L}{V} + \frac{dL}{dt}\right)$
specific ammonium production rate	$q_A = \frac{1}{X_V^B}\left(\frac{F_m A}{V} + \frac{dA}{dt} + k_{Gln}\,Gln\right)$
specific oxygen uptake rate	$q_{O_2} = \frac{1}{X_V^B}\left(\frac{F_{gas}(O_{2_{in}} - O_{2_{out}})}{V}\right)$

Metabolic fluxes were computed using the average specific rates as inputs from the steady-state portion of each of the 12 experimental conditions. and are shown in Figure 7.3 for experimental phase E (standard bioreactor conditions). The fluxes through glycolysis, the TCA cycle and oxidative phosphorylation were one to three orders of magnitude higher than those for amino acid biosynthesis and catabolism as were some fluxes for biomass synthesis. Similar observations on relative flux magnitudes were made for the 11 other experimental conditions (not shown). The actual flux values, however, did change between different experimental phases, especially when temperature and pH were varied.

7.3.2 Prime Variable Error

Errors in prime variable measurements were determined by analyzing multiple samples and the results are shown in Table 7.2. Glucose, lactate and glutamine measurements had errors close to 5% of the measured value, among the lowest. The highest errors were 12.2 and 10.4%, respectively, for ammonium and oxygen. Errors in the bioreactor volume and the harvest, cell discard and gas flow rates were assumed to be 5% based on manufacturer specifications.

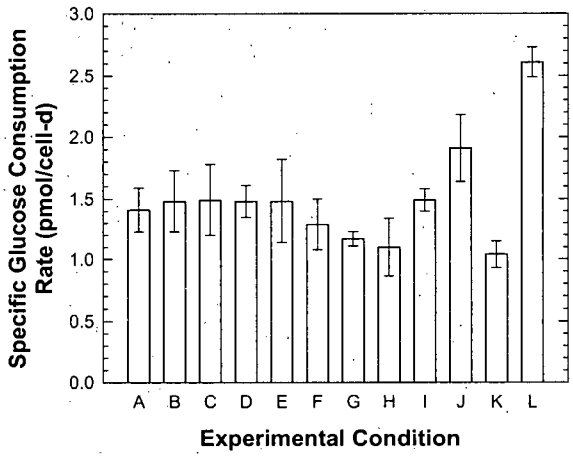

Figure 7.2: Average specific glucose consumption rates (mean ± standard deviation) for the 12 experimental conditions in this study. More information about conditions A – L is in Figure 7.1.

7.3.3 Specific Rate Error

Mass balances around the bioreactor and cell retention device were used to obtain expressions for growth rate, specific productivity and specific uptake/consumption rates for nutrients and metabolites (Table 7.1). Since perfusion systems are typically operated at constant cell concentration and perfusion rates, the prime variables would ideally be time invariant. However, imperfect cell concentration control and shifts in cellular metabolism require retention of the accumulation terms in the mass balance expressions.

Table 7.2: Error in Prime Variable Measurements

Prime Variable	Error (%)
Bioreactor viable cell concentration (X_V^B)	8.9
Harvest viable cell concentration (X_V^H)	7.9
Product concentration (P)	8
Glucose concentration (G)	4.9
Glutamine concentration (Gln)	5.1
Lactate concentration (L)	4.8
Ammonium concentration (A)	12.2
Oxygen concentration (O_2)	10.4

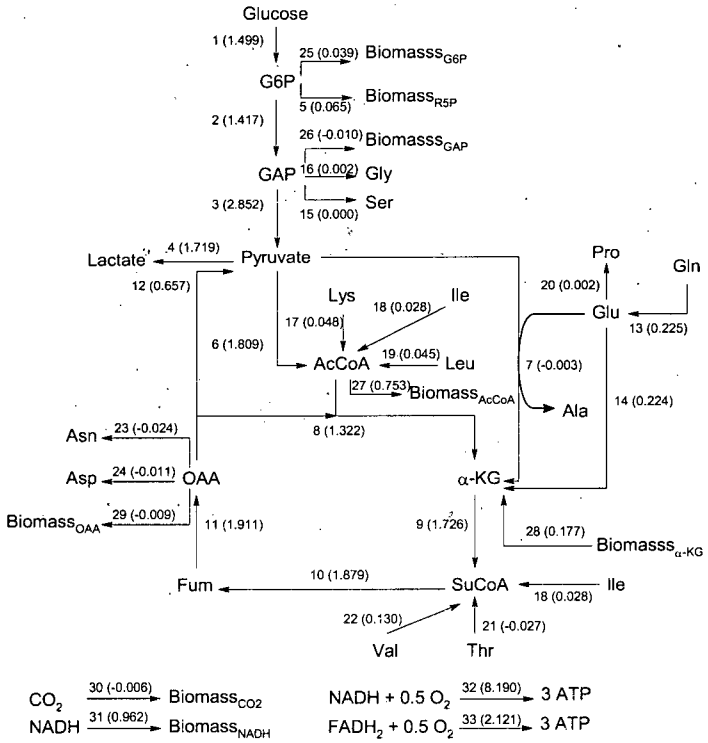

Figure 7.3: Flux map for experimental condition E using the network of Nyberg et al [8]. Reaction numbers (1 — 33) and flux values (in parenthesis as pmol/cell-d) are also shown.

7.3.3.1 Gaussian Error Estimation vs. Monte-Carlo Analysis

Specific glucose consumption rate, q_G, was used to compare the Gaussian and Monte-Carlo approaches for specific rate error estimation. The specific glucose consumption rate is a function of five prime variables, V, F_h, G_m, G, and X_V^B (Table 7.1) and is thus affected by error in all of them. For simplicity, however, the bioreactor volume, V, the harvest flow rate, F_h, and the glucose concentration in the medium, G_m, were assumed to be error-free for this comparison. The error in bioreactor glucose concentration was varied from 0 – 10% while that in bioreactor viable cell concentration, was varied from 0 – 20%. For each pair of G and X_V^B errors, the corresponding error in q_G was calculated using both the Gaussian and Monte-Carlo approaches (Figure 7.4). For X_V^B error <8%, both the Gaussian and Monte-Carlo approaches resulted in similar q_G errors while the Gaussian approach underpredicted q_G error at X_V^B error >8% for all G errors (Error estimates from the Monte-Carlo method are representative since no assumptions and approximations are made). Since X_V^B errors of 8.9% (Table 7.2) and higher are commonly observed in practice, the Gaussian approach as

defined in Eq.(7.1) has limited utility.

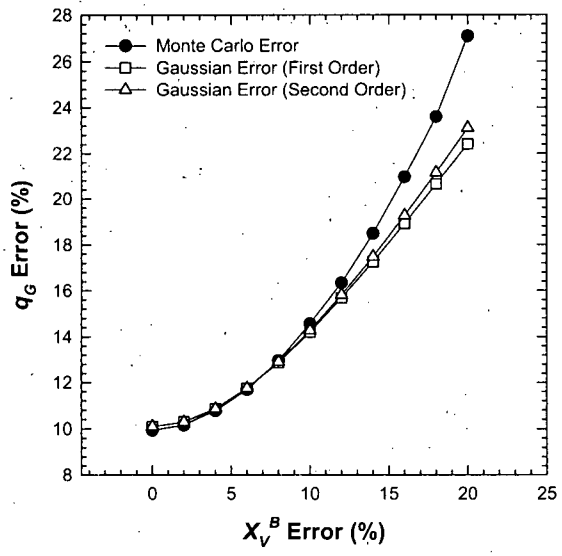

Figure 7.4: Comparison of Gaussian and Monte-Carlo q_G error estimates at 10% glucose error and 0 –20% X_V^B error. Both the first and second order Gaussian q_G errror estimates were lower than the Monte-Carlo error at higher X_V^B errors.

This limitation of the Gaussian approach is due the lack of higher-order terms in Eq.(7.1) Inclusion of the second-order term considerably increased the complexity of the Gaussian error expression with only a minor improvement in error prediction (Figure 7.4). For example, a 10% error in G and a 20% error in X_V^B resulted in a 26.9% q_G error by the Monte-Carlo method while the corresponding Gaussian error estimates were 22.4 and 23.1%, respectively, using the first and second-order terms. While addition of third and higher order terms can further increase the accuracy of Gaussian error estimates, the resulting expressions are quite complex. The Monte-Carlo approach with its ability to accurately estimate error over any desired range without derivative computation is superior to the Gaussian approach and has been used to obtain the data presented in subsequent sections.

7.3.3.2 Error in Specific Growth Rate

The apparent specific growth rate, μ, is a function of five prime variables (Table 7.1) and using values from Condition E, the dominant contributor is the cell bleed stream, followed

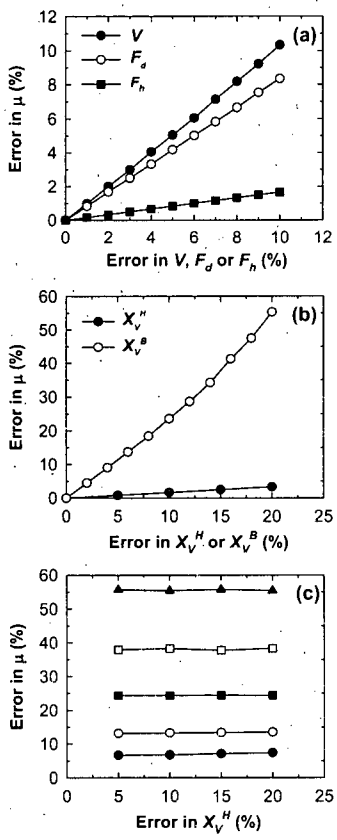

Figure 7.5: Error in μ as a function of error in the 5 associated prime variables. Panel (a) is for V, F_d and F_h while panel (b) is for X_V^H and X_V^B. Panel (c) is when all prime variables are simultaneously in error (V, F_d and F_h at 5%; X_V^H = 5 - 20 %; X_V^B = 0 - 20 %). X_V^B error legend for panel c: (•) 0 %; (○) 5 %; (■) 10 %; (□) 15 %; (▲) 20 %.

by the cell loss in the harvest

$$\mu = \frac{4.9}{10} + \frac{100}{10}\left(\frac{0.21}{20}\right) + \frac{1}{20}\left(\frac{0}{1}\right) \tag{7.3}$$

$$0.60 = 0.49 + 0.11 + 0.0 \tag{7.4}$$

The bleed stream term makes up 82% of the growth rate while the remaining 18% is from the harvest stream term. The dX_V^B has been set to zero to reflect an ideal steady-state with perfect cell concentration control. It is common to observe ~10% variation in cell density that can be more due to sampling and instrument error than a true change in cell density. Including this variation in the above expression will misrepresent contributions of the cell

bleed and harvest streams to growth rate. It is the $\frac{dX_V^B}{dt}$ term, however, that largely affects growth rate error as will be shown below.

Figure 7.5 shows the error in μ as a function of errors in the 5 prime variables that make up the specific growth rate expression. The impacts of 0 – 10% error in V, F_b, and F_h are shown in Figure 7.5a (X_V^B and X_V^H were assumed error free) where the μ errors increased monotonically with those in V, F_b, or F_h. Errors in V had the highest impact on μ and the average $\frac{\mu}{V}$ error ratio was 1.03 (standard deviation of 0.01) suggesting a one-to-one relationship. The $\frac{\mu}{F_b}$ and $\frac{\mu}{F_h}$ error ratios were 0.83 (SD = 3.3 x 10^{-3}) and 0.17 (SD = 6.4 x 10^{-4}), respectively, indicating lower sensitivity of μ to F_b and F_h errors. This difference in error sensitivity is consistent with the relative prime variable contributions to the μ value. The fermentor volume, V, is in both the terms that contribute to μ in Eq.(7.3) resulting in the one-to-one error dependence. The bleed rate is present only in the first term that contributes 82% to the μ value, consistent with the $\frac{\mu}{F_b}$ error ratio of 0.83. Errors in the harvest flow rate have the least impact because F_h is present only in the second term with a 18% contribution to μ, consistent with the $\frac{\mu}{F_h}$ error ratio of 0.17.

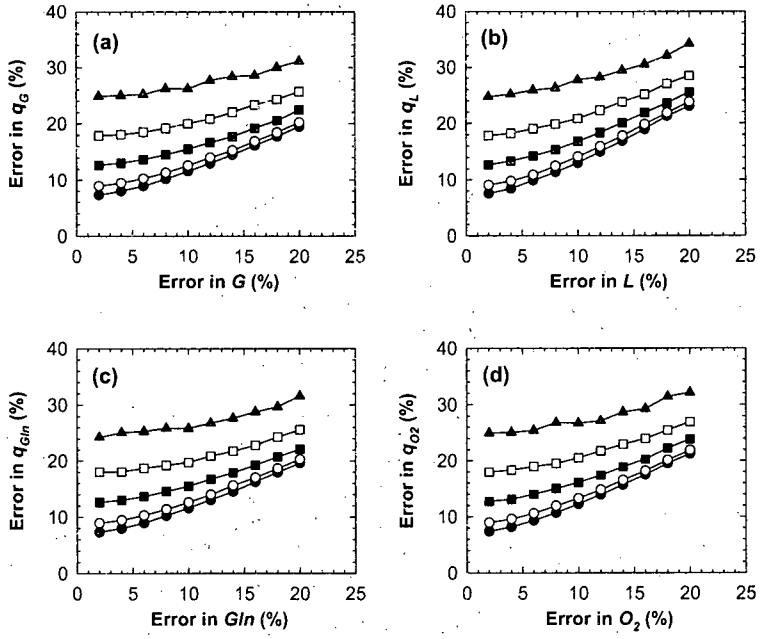

Figure 7.6: Errors in q_G, q_L, q_{Gln} and q_{O_2} as functions of error in X_V^B and the corresponding prime variable. X_V^B error Legend: (•) 0 %; (○)5 %; (■) 10 %; (□) 15 %; (▲) 20 %.

Impacts on μ errors from errors in bioreactor and harvest cell concentrations are shown

in Figure 7.5b (V, F_b, and F_h were assumed to be error free). Cell concentration estimates are more prone to error as manual cell counting techniques continue to be widespread. While this has been alleviated with the advent of reliable automated cell concentration estimators, viable cell concentration in the harvest stream, X_V^H, is especially susceptible to experimental error as there are relatively few cells. However, given the minor contribution of the harvest stream term to the growth rate, a 20% error in X_V^H results in only 3.3% error in the corresponding μ estimate (Figure 7.5b). Errors in X_V^B however have a dramatic effect on the error in μ with the third term in Eq.(7.3) largely responsible for the strong influence of X_V^B error on μ. This was primarily due to the error associated with derivative estimation that is typically done by finite forward differences using X_V^B values from two consecutive days. More accurate derivative estimation approaches should be used to minimize the error in μ. Derivative computation using central differences resulted in a 50% reduction in μ errors (data not shown) and techniques such a splining could provide improved derivative estimates as well.

Figure 7.5c shows the calculated error in μ when all the five prime variables are in error, reflective of experimental conditions. For a 5% error in V, F_b, and F_h and a 10% error in X_V^B and X_V^H (approximate conditions in this study), the corresponding μ error was 24.4%, emphasizing the need for accurate cell concentration determination and subsequent derivative estimation.

7.3.3.3 Error in Specific Uptake and Production Rates

The Monte-Carlo approach was used to estimate error in nutrient consumption and metabolite production rates from the Table 7.1 expressions. With the exception of oxygen, these specific rates were functions of V, F_h, X_V^B and the corresponding nutrient/metabolite concentration while the oxygen uptake rate expression had F_{O_2} in place of F_h. A 5% error was assumed for V, F_h and F_{O_2} while X_V^B and the nutrient/metabolite concentration were evaluated over a $2-20$ % error range. For each combination of X_V^B and nutrient/metabolite error, 10,000 specific rates were calculated and average error values are shown in Figure 7.6. For 0% error in X_V^B, error in all specific rates increased monotonically with error in the corresponding prime variable. For instance, the q_G error was 7.3% at a 2% G error (V and F_h error = 5%, X_V^B error = 0%) and this value increased to 19.5% at a 20% G error. Increases in the X_V^B error caused an upward shift in the error profile while maintaining the monotonic dependence on the corresponding prime variable error. There were slight differences in the specific rate errors for their corresponding prime variables and this is due to differences in the specific rate expressions (Table 7.1). Error profiles for q_P and q_A were

identical to those for q_L.

Table 7.3: Consistency index values for the 12 experimental conditions examined in this study

Experimental Condition	Bioreactor Set Points	h
A	Standard	5.93
B	DO = 20%	2.54
C	Standard	4.64
D	DO = 100%	3.08
E	Standard	1.59
F	T = 34.5°C	0.95
G	T = 32.5°C	0.80
H	T = 30.5°C	4.28
I	Standard	0.89
J	T = 37.5°C	0.26
K	pH = 6.6	4.84
L	pH = 7.0	3.56

Of all specific rates for the approximate conditions in this study (Table 7.2), the specific growth rate was characterized by the highest error with 5% errors in V, F_d and F_h and 10% errors in X_V^H and X_V^B resulting in a 24.4% error in μ (Figure 7.5). For a 5% measurement errors in glucose, lactate and glutamine concentrations, errors in their respective specific rates at a 10% X_V^B error were in the 12 – 14% range (Figure 7.6). The estimated error in oxygen uptake rate at a 10% X_V^B and oxygen errors was 16.1% (Figure 7.6). Overall, specific rate errors are ~10% with 5% errors in prime variables and 20 – 25% with 15% prime variable errors. (Figure 7.6). Thus the specific rate errors in a perfusion system can be expected to span a 10 – 25% range depending upon the accuracy of prime variable measurements.

7.3.4 Error in Metabolic Fluxes

Metabolic fluxes were computed for all 12 experimental conditions and the consistency of the experimental data was verified by calculating the consistency index (h) values (Table 7.3) using methods described earlier [6, 21]. The h values for all steady states passed the χ^2 distribution test with a 95% confidence level ($h < 5.99$ for 2 degrees of freedom) indicating that the experimental data for all experimental conditions were consistent and unlikely to contain gross measurement errors. This observation coupled with the stoichiometirc matrix, $\mathbf{A}$, being of full rank and having a low condition number clearly attest to the robustness of the bioreaction network and the quality of the experimental data. Experimental condition

E, where the bioreactor was operated under standard conditions (Table 7.3) was arbitrarily chosen to quantify the effect of specific rate errors on those in the metabolic fluxes.

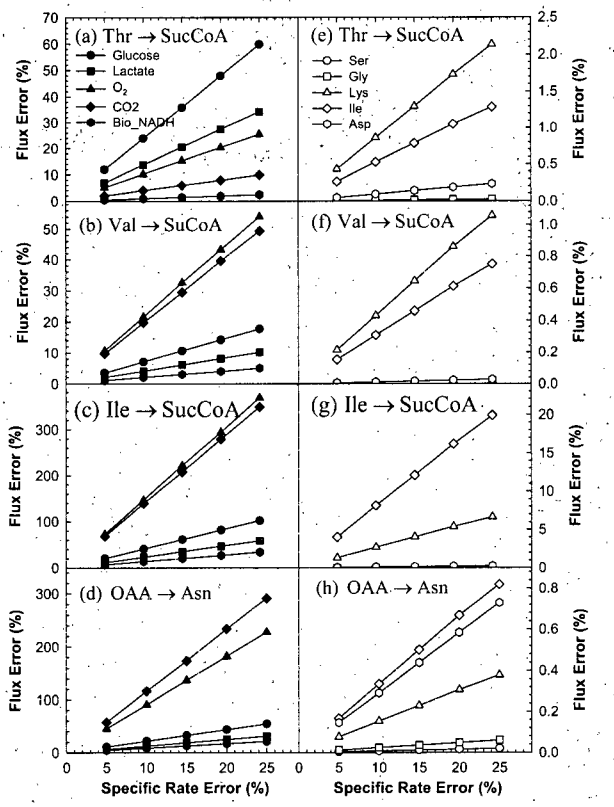

Figure 7.7: Effect of specific rate error on the error in lower metabolic fluxes. Panels (a)-(d) are for errors in the 5 greater specific rates while (e)-(h) are for errors in lower specific rates (amino acid metabolism).

7.3.4.1 Lower Metabolic Fluxes

The effect of specific rate errors on the lower metabolic fluxes is shown in Figure 7.7. Panels a-d are for relatively greater specific rates while e-h are for amino acid metabolism (lower specific rates). Despite all 4 metabolic fluxes in Figure 7.7 being associated with the TCA cycle (Figure 7.3: threonine, valine and isoleucine are catabolized to SuCoA, asparagine is produced from oxaloacetate), they were greatly affected by the glucose uptake rate error. A 25% error in glucose uptake rate resulted in 60, 18, 103 and 54% errors, respectively (Figure 7.7a-d). The lactate production rate had a similar effect resulting in errors of 34,

10, 59 and 31%, respectively, (Figure 7.7a-d) for a 25% lactate production rate error. As expected, the Figure 7.7a-d fluxes were affected by errors in the oxygen uptake and carbon dioxide production rates given their close relation to the TCA cycle (threonine catabolism was less affected since this reaction does not directly involve O_2 or CO_2). A 25% error in the oxygen uptake rate resulted in respective errors of 26, 54, 387 and 228% while that in the CO_2 production rate caused 10, 49, 349 and 291% errors, respectively, in the Figure 7.7a-d fluxes. Thus errors in the greater specific rates very substantially influence the lower metabolic fluxes to the extent that the values are far from accurately representing cellular metabolism.

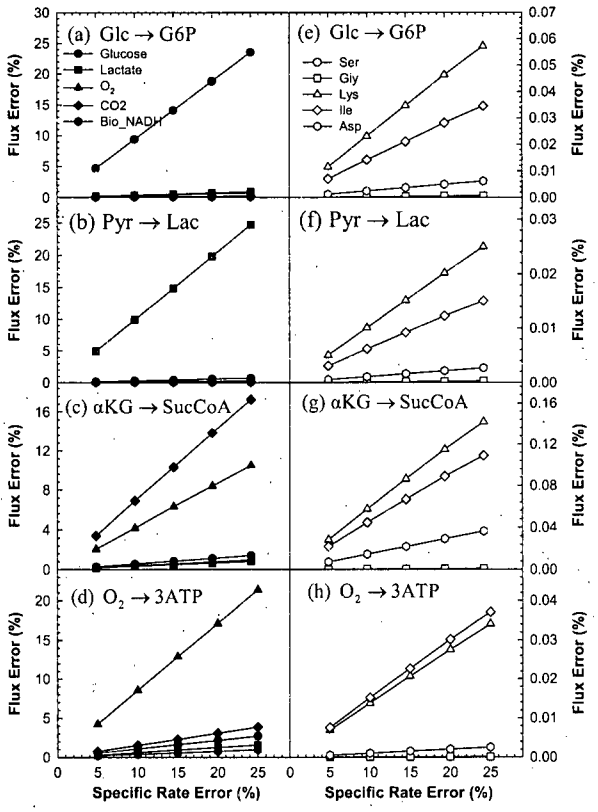

Figure 7.8: Effect of specific rate error (shown in each frame) on the error in 4 greater metabolic fluxes. Panels (a)-(d) are for errors in 5 larger specific rates while (e)-(h) are for errors in lower specific rates (amino acid metabolism).

With the exception of the Ile → SucCoA flux, errors in amino acid metabolic rates did not significantly affect the metabolic fluxes. Overall, the maximum flux error was less than 2.5% even when the specific rate error was 25% (Figure 7.7e,f,h). As expected, the Ile →

SucCoA flux was influenced by errors in isoleucine catabolism with a 25% error resulting in a 20% error in the flux (Figure 7.7g) and this dependence was true in all instances where the specific rate and flux were closely related.

7.3.4.2 Greater Metabolic Fluxes

The effect of specific rate errors in the 5 – 25% range on the greater metabolic flux errors was examined for experimental condition E and data for four fluxes representing glycolysis, lactate production, the TCA cycle and oxidative phosphorylation are shown in Figure 7.8. While the influence of all 35 specific rates in the bioreaction network were examined, Figure 7.8 shows representative results for the 5 greater specific rates (glucose, lactate, oxygen, carbon dioxide, Bio_NADH; panels a-d) and 5 lower specific rates representing amino acid metabolism (serine, glycine, lysine, isoleucine, aspartate; panels e-h). As expected, specific rates that were not closely related to the flux had a lower impact on the flux error. For instance, a 25% error in glucose uptake rate caused 0.7, 1.4 and 2.7% errors, respectively, in Figures 7.8b-c while the error in Figure 7.8a was 23.6%. Similarly, a 25% error in lactate production rate caused errors of 0.92, 0.81 and 1.54%, respectively, in Figure 7.8a,c,d while that in Figure 7.8b was 24.8%.

Thus, errors in the greater specific rates had a significant effect on the errors in the most closely related fluxes. For instance, a 25% error in glucose uptake resulted in a 23.6% error in the Glc $\rightarrow$ GCP flux (Figure 7.8a) and a similar dependence was seen between the error in the lactate production rate and the Pyr $\rightarrow$ Lac flux (Figure 7.8b). The error in the TCA cycle flux, αKG $\rightarrow$ SuCoA, was most influenced by error in CO_2 production and oxygen uptake (Figure 7.8c) while that for oxidative phosphorylation was primarily affected by error in the oxygen uptake rate (Figure 7.8d).

Errors in the amino acid metabolic rates, however, had minimal impact on the flux errors even when they were related to the flux. For instance, the specific production rates of serine and glycine (both synthesized from GAP (Figure 7.3)), had a negligible impact on the glycolytic fluxes. A 25% error in serine or glycine production rates resulted in 2.34 x 10^{-4} or 7.02 x 10^{-4}% error, respectively, in the Glc $\rightarrow$ GCP flux (Figure 7.8e). While lysine and isoleucine are catabolized to form AcCoA which enters the TCA cycle, their rate errors had little impact on the TCA cycle flux (αKG $\rightarrow$ SucCoA). A 25% error in their catabolic rates resulted in respective flux errors of 0.14 or 0.12% (Figure 7.8g). Aspartate is formed in the TCA cycle from oxaloacetate and a 25% error in aspartate production rate caused a 3.67 x 10^{-2}% error in the αKG $\rightarrow$ SucCoA flux. Thus, errors from lower magnitude specific rates have negligible impact on the error in the greater metabolic fluxes even when

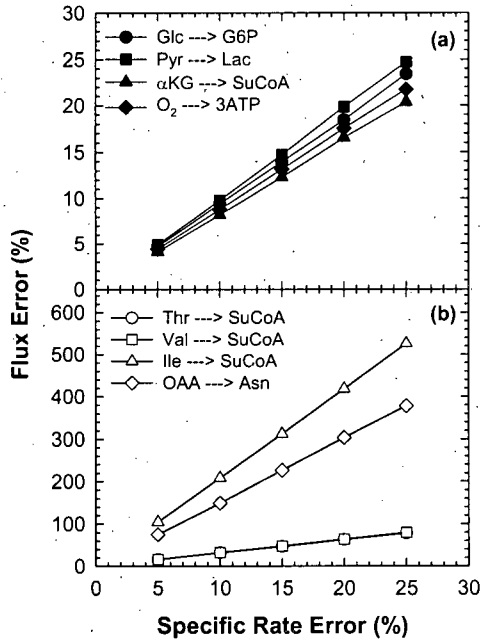

Figure 7.9: Flux error for greater (panel a) and lesser (panel b) fluxes when all specific rates in the bioreaction network have errors in the 5 – 25% range. The Thr → SuCoA and Val → SuCoA error profiles overlap in panel b.

the specific rates and metabolic fluxes are related.

7.3.4.3 Overall Flux Errors in Perfusion Cultivation

Figures 7.7 and 7.8 and show flux error data when only one specific rate is in error. In a typical experiment, all specific rates have error and their combined influences on the flux error are shown in Figure 7.9. Specific rate errors in the 5 – 25% range were examined and when all specific rate errors were 15%, the greater flux errors ranged from 12.3% for αKG → SuCoA to 14.7% for Pyr → Lac (Figure 7.9a). For the lesser fluxes, when the specific rate errors were 15%, the flux errors were between 46.9% (Thr → SuCoA) and 312.5% (Ile → SuCoA) (Figure 7.9b). Hence lesser flux values can be extremely sensitive to specific rate errors making their accurate determination difficult even at relatively low prime variable and specific rate errors. This was despite using a robust bioreaction network with a stoichiometric matrix of full rank and low condition number.

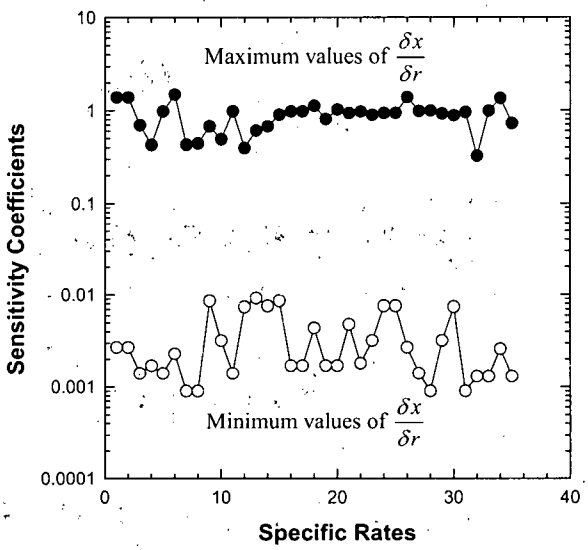

Figure 7.10: Absolute values of the maximum and minimum sensitivity coefficients for the metabolic model used in this study. For each of the 35 specific rates, there were 33 sensitivity coefficients corresponding to the 33 fluxes (Figure 7.3) in the bioreaction network.

7.3.4.4 Normalized Sensitivity Coefficients for Analysis of Metabolic Flux Errors

The flux error data in Figures 7.7 and 7.8 were obtained from multiple simulations using the Monte-Carlo method. Although comprehensive, this approach is cumbersome to apply to new metabolic models and a generalized approach to quantify the relationship between specific rate and metabolic flux errors is desirable. The sensitivity matrix, **S**, provides a framework for such quantification and can be readily estimated from the stoichiometric matrix of the metabolic network [1] as

$$\mathbf{S} = \left(\mathbf{A}^{\mathbf{T}}\mathbf{A}\right)^{-1}\mathbf{A}^{\mathbf{T}} \tag{7.5}$$

and the individual elements of **S** can be written as

$$s_{i,j} = \left(\frac{\partial x_i}{dr_j}\right) \tag{7.6}$$

where $s_{i,j}$ is the sensitivity of the i^{th} flux with respect to the j^{th} rate. For the metabolic network examined in this study, **S** is a 33 x 35 matrix where the j^{th} column contains

the sensitivities of the 33 fluxes to the j^{th} rate. Figure 7.10 shows absolute values of the minimum and maximum flux sensitivities for each of the 35 specific rates. The minimum sensitivities ranged from 0.0009 – 0.0092 while the maximum values were in the 0.32 – 1.50 range. Low sensitivity coefficients are favorable from an error analysis standpoint as the influence of specific rate errors on flux estimates is minimal. Even the maximum sensitivities obtained were quite low, consistent with the low condition number (69) of the stoichiometric matrix, **A**.

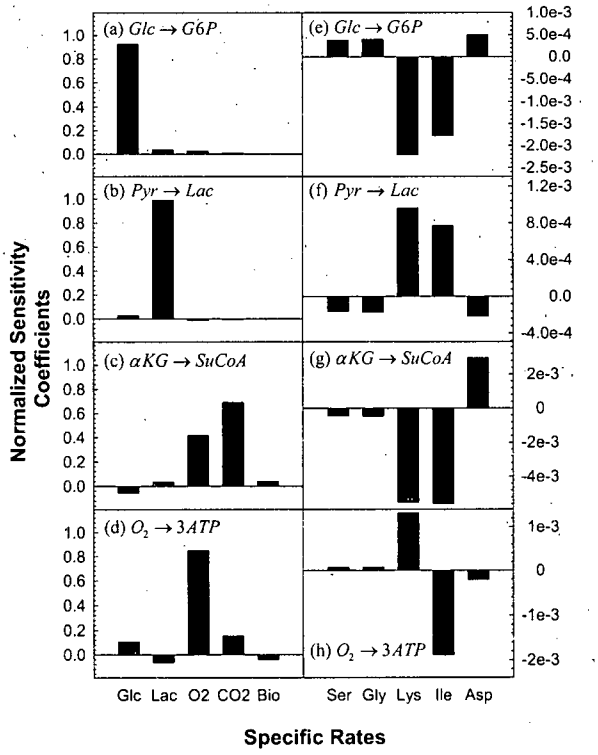

Figure 7.11: Normalized sensitivity coefficients for the greater fluxes in the bioreaction network for both greater (panels a-d) and lesser (panels e-h) specific rates.

However, sensitivity coefficients as defined in Eq.(7.5) do not completely explain the relationship between specific rate and flux error. For instance, sensitivity coefficients for the $O_2 \rightarrow$ 3ATP flux are -1.354 and -0.587 for the oxygen uptake and glucose uptake rates,

respectively, a ratio of 2.3. Errors in the $O_2 \rightarrow$ 3ATP flux, however, are scaled differently since 25% errors in glucose and oxygen uptake rates result in flux errors of 21.39 and 2.7%, respectively, a ratio of 7.9. This discrepancy is due to the difference in the magnitudes of the oxygen and glucose uptake rates (-5.14 and -1.48 pmol/cell-d, respectively) which is not accounted for in Eq.(7.6). If the sensitivity coefficients -1.35 and -0.59 are multiplied by their respective specific rates of -5.14 and -1.48, the resulting values are 6.94 and 0.87 with a ratio of 7.9 that is consistent with the flux error ratio and the results of Monte-Carlo analysis (Figure 7.8).

A normalization of the Eq.(7.6) sensitivity coefficients is thus necessary for the resulting value to be representative of the error relationship between the specific rate and metabolic flux pair. This can be done by multiplying the right hand side of Eq.(7.6) with a ratio of the specific rate and metabolic flux

$$s_{i,j}^N = \left(\frac{\partial x_i}{dr_j}\right)\frac{r_j}{x_i} \tag{7.7}$$

where $s_{i,j}^N$ is the normalized sensitivity coefficient (NSC) for flux x_i with respect to rate r_j (A similar approach is used to define the flux control coefficients in metabolic control analysis that describe the change in steady-state flux due to a change in enzyme activity [24]). For the $O_2 \rightarrow$ 3ATP flux, the normalized sensitivity coefficients from Eq.(7.7) were 0.849 and 0.106 for oxygen uptake and glucose uptake, respectively. The ratio of these normalized sensitivity coefficients is 8 which is similar to the flux error ratio of 7.9 from Monte-Carlo analysis with a small difference due to round-off errors. Normalized sensitivity coefficients as defined in Eq.(7.7) thus provide accurate quantification of the dependence of metabolic flux error on specific rate error (this was verified for other flux-specific rate combinations).

NSCs for the greater fluxes are shown for both greater and lesser specific rates in Figure 7.11. For the Glc $\rightarrow$ G6P flux, the NSC with respect to the glucose uptake rate from Eq.(7.7) was 0.923 indicating that a 1% error in glucose uptake rate would result in a 0.923% error in the Glc $\rightarrow$ G6P flux (Figure 7.11a). The flux to specific rate error ratio from Figure 7.8a was $0.940 \pm 1.7 \times 10^{-3}$ (average of 5 data points for the glucose uptake rate) verifying the ability of the NSC to accurately describe the specific rate and flux error relationship. NSCs for lactate, oxygen, CO_2 and biomass from Eq.(7.7) were 0.037, 0.027, 0.011 and 0.003, respectively (error ratios from Figure 7.8b-d were identical), suggestive of their much lower impact on the Glc $\rightarrow$ G6P flux. The highest NSC for the Pyr $\rightarrow$ Lac flux was for lactate (0.99) while both oxygen and CO_2 were characterized by high NSCs for the αKG $\rightarrow$ SucCoA flux (0.416 and 0.691, respectively). The $O_2 \rightarrow$ 3ATP flux was most affected by errors in the oxygen uptake rate and this dependence was characterized by a

normalized sensitivity coefficient of 0.849 (Figure 7.11d). Normalized sensitivity coefficients with respect to amino acid metabolism were much smaller (Figure 7.11e-h) reflecting their minimal impact on the greater flux errors.

While both Figures 7.8 and 7.11 provide very similar information on the specific rate and flux error relationship, Figure 7.11 data are easier to generate and are a more compact representation of error dependence. The sensitivity matrix can be readily estimated from the stoichiometric matrix using Eq.(7.5) and once metabolic fluxes are calculated using the experimentally measured specific rates (Eq.7.2), NSCs can be determined from Eq.(7.7). Moreover, a single number completely characterizes the specific rate and flux error relationship.

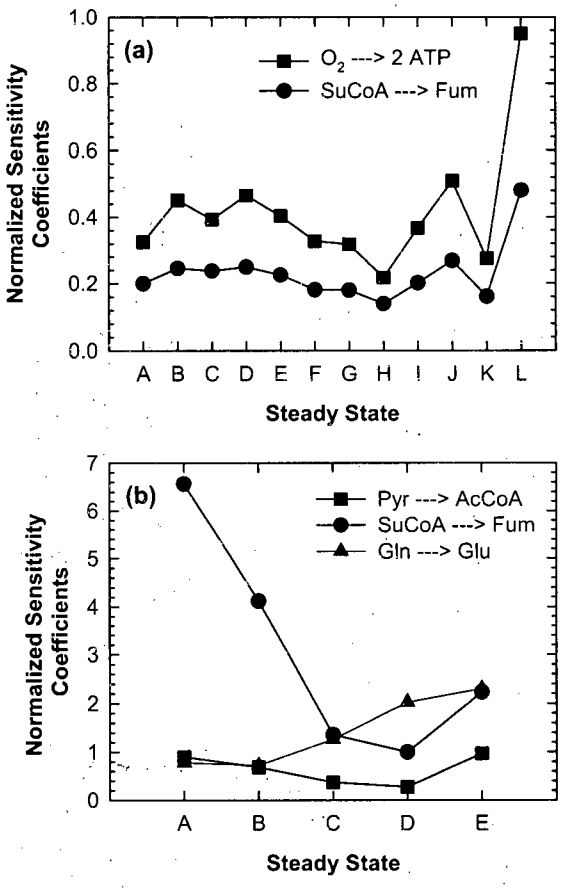

Figure 7.12: NSC variation with respect to glucose uptake rate during the course of an experiment. Data from this study are shown in panel a and those from Follstad et al. [6] in panel b.

7.3.4.5 Variation in Normalized Sensitivity Coefficients

It must be recognized that NSCs and hence specific rate-flux error relationships can change during the course of an experiment if either the specific rate or metabolic flux changes. This is not true of the conventional sensitivity coefficients that depend only upon the stoichiometry of the bioreaction network (Eq.7.6). Figure 7.12a shows variation in the normalized sensitivity coefficients for the $O_2 \rightarrow$ 2ATP and SuCoA $\rightarrow$ Fum fluxes with respect to glucose uptake rate for the 12 experimental conditions in this study. For both fluxes, the lowest values of the normalized sensitivity coefficients (0.218 and 0.139, respectively) were at T = 30.5 °C (condition H), where the flux values were the highest and the rate values were among the lowest. The opposite was true at pH = 7 (condition L) where flux values were the lowest and rate values were the highest (NSCs of 0.949 and 0.481). Thus during the course of a single experiment, the NSC for the $O_2 \rightarrow$ 2ATP flux with respect to glucose uptake rate ranged from 0.218 – 0.949, a 4.4-fold variation while a 3.4 increase was observed for the SuCoA $\rightarrow$ Fum flux. The value of the $O_2 \rightarrow$ 2ATP flux was 4.4 times more affected by errors in glucose uptake rate at pH = 7 than at T = 30.5 °C while the SuCoA $\rightarrow$ Fum flux was 3.4 more affected.

Eq.(7.7) was also used to calculate NSCs for hybridoma cell cultivation in chemostat culture reported by Follstad et al, [6] at different dilution rates (Figure 7.12b). The dilution rates corresponding to steady states A – E were 0.04, 0.03, 0.02, 0.01 and 0.04 hr^{-1}, respectively, and significant changes in cellular metabolism were observed over the course of the experiment. The sensitivity coefficient for the Pyr $\rightarrow$ AcCoA flux was 0.67 and the normalized sensitivity coefficient for steady state A was 6.57 reflecting the 10-fold higher value of glucose uptake when compared to this flux. For steady states B – D, the Pyr $\rightarrow$ AcCoA flux increased while the glucose uptake rate decreased resulting in significant reduction in the NSC. An increase in the glucose uptake rate for steady state E was responsible for the slight increase in the NSC. Thus the Pyr $\rightarrow$ AcCoA flux was most sensitive to glucose uptake rate errors in steady state A and this decreased by 6.5-fold for steady state D. Variations in the SuCoA $\rightarrow$ Fum flux were primarily due to changes in the glucose uptake rate since the SuCoA $\rightarrow$ Fum flux did not change much over the course of the cultivation while those for the Gln $\rightarrow$ Glu flux were due to changes in both the flux and glucose uptake rate. Thus the flux and specific rate error relationship can change during the course of an experiment and NSCs under all experimental conditions must be calculated to rationally interpret the metabolic flux data.

7.4 Conclusions

We have characterized error propagation from prime variables into specific rates and subsequently into metabolic fluxes for mammalian cells in high cell concentration perfusion culture. Prime variable errors were in the 5 – 15% range resulting in a 10 – 25% error in specific rates. The effect of specific rate error on the flux error was a function of both the sensitivity of the flux with respect to the specific rate and relative magnitudes of the flux and the specific rate. The greater fluxes in the bioreaction network had errors that were comparable in magnitude to the related greater specific rate errors and were virtually unaffected by errors in the lower specific rates. Greater flux errors ranged from 12 – 15% for 15% error in the greater specific rates suggesting that the 30% increase in TCA cycle fluxes reported in Chapter 9 are indeed representative of changes in cell metabolism. The lower fluxes, however, were extremely sensitive to errors in the greater specific rates making their accurate estimation difficult given analytical limitations in prime variable measurements. Often, errors were so large that the flux values grossly misrepresented cellular metabolism. The relationship between specific rate and flux error was accurately described by the normalized sensitivity coefficient that could be readily calculated once the metabolic fluxes were estimated. We recommend normalized sensitivity coefficient calculation be an integral part of metabolic flux analysis as it describes the relationship between flux and specific rate error through a single numeric value.

Bibliography

[1] Stephanopoulos, G.; Aristodou, A.; Nielsen, J. *Metabolic Engineering. Principles and Methodologies.* Academic Press, San Diego, 1998.

[2] Balcarcel, R. R.; Clark, L. Metabolic screening of mammalian cell cultures using well-plates. *Biotechnol. Prog.*, **2003**, *19*, 98–108.

[3] Bonarius, H.; Hatzimanikatis, V.; Meesters, K.; de Gooijer, C. D.; Schmid, G.; Tramper, J. Metabolic flux analysis of hybridoma cells in different culture media using mass balances. *Biotechnol. Bioeng.*, **1996**, *50*, 229–318.

[4] Bonarius, H.; Houtman, J.; Schmid, G.; C.D., d. G.; Tramper, J. Metabolic-flux analysis of hybridoma cells under oxidative and reductive stress using mass balance. *Cytotechnology*, **2000**, *32*, 97–107.

[5] Europa, A. F.; Gambhir, A.; Fu, P. C.; Hu, W. S. Multiple steady states with distinct

cellular metabolism in continuous culture of mammalian cells. *Biotechnol Bioeng*, **2000**, *67*(1), 25–34.

[6] Follstad, B. D.; Balcarcel, R. R.; Stephanopoulos, G.; Wang, D. I. Metabolic flux analysis of hybridoma continuous culture steady state multiplicity. *Biotechnol Bioeng*, **1999**, *63*(6), 675–83.

[7] Gòdia, C.; Cairó, J. Metabolic engineering of animal cells. *Bioprocess Engineering*, **2002**, *24*, 289–298.

[8] Nyberg, G. B.; Balcarcel, R. R.; Follstad, B. D.; Stephanopoulos, G.; Wang, D. I. Metabolism of peptide amino acids by Chinese hamster ovary cells grown in a complex medium. *Biotechnol Bioeng*, **1999**, *62*(3), 324–35.

[9] Bonarius, H.; Timmerarends, B.; de Gooijer, C.; Tramper, J. Metabolite-balancing techniques vs. 13C tracer experiments to determine metabolic fluxes in hybridoma cells. *Biotechnol Bioeng*, **1998**, *58*(2-3), 258–262.

[10] Bonarius, H.; Schmid, G.; Tramper, J. Flux analysis of underdetermined metabolic networks: the quest for the missing constraints. *Trends Biotechnol.*, **1997**, *15*, 308–314.

[11] Nadeau, I.; Sabatié, J.; Koehl, M.; Perrier, M.; Kamen, A. Human 293 cell metabolism in low glutamine-supplied culture: Interpretation of metabolic changes through metabolic flux analysis. *Metab. Eng.*, **2000**, *2*, 277–292.

[12] Xie, L.; Wang, D. Material balance studies on animal cell metabolism using a stoichiometrically based reaction network. *Biotechnol. Bioeng.*, **1996**, *52*, 579–590.

[13] Zupke, C.; Sinskey, A. J.; Stephanopoulos, G. Intracellular flux analysis applied to the effect of dissolved oxygen on hybridomas. *Appl. Microbiol. Biotechnol.*, **1995**, *44*(1-2), 27–36.

[14] Bonarius, H.; Ozemere, A.; B, T.; Skrabal, P.; Tramper, J.; Schmid, G.; Heinzle, E. Metabolic-flux analysis of continuously cultured hybridoma cells using 13CO2 mass spectrometry in combination with 13C-Lactate nuclear magnetic resonance spectroscopy and metabolite balancing. *Biotechnol. Bioeng.*, **2001**, *74*, 528–538.

[15] Forbes, N.; Clark, D.; Blanch, H. Using isotopomer path tracing to quantify metabolic fluxes in pathway models containing reversible reactions. *Biotechnol. Bioeng.*, **2001**, *74*, 196–211.

[16] Mancuso, A.; Sharfstein, S.; Tucker, S.; Clark, D.; Blanch, H. Examination of primary metabolic pathways in a murine hybridoma with carbon-13 nuclear magnetic resonance spectroscopy. *Biotechnol. Bioeng.*, **1994**, *44*, 563–585.

[17] Sharfstein, S.; Tucker, S.; Mancuso, A.; Blanch, H.; Clark, D. Quantitative in vivo nuclear magnetic resonance studies of hybridoma metabolism. *Biotechnol. Bioeng.*, **1994**, *43*, 1059–1074.

[18] Zupke, C.; Stephanopoulos, G. Modeling of isotope distributions and intrecellular fluxes in metabolic networks using atom mapping matrices. *Biotechnol. Prog.*, **1994**, *10*, 489–498.

[19] Zupke, C.; Stephanopoulos, G. Intracellular flux analysis in hybridomas using mass balances and In Vitro 13C NMR. *Biotechnol. Bioeng.*, **1995**, *45*, 292–303.

[20] Wiechert, W. 13C Metabolic flux analysis. *Metab. Eng.*, **2001**, *3*, 195–206.

[21] Wang, N. S.; Stephanopoulos, G. Application of macroscopic balances to the identification of gross measurement errors. *Biotechnol. Bioeng.*, **1983**, *25*, 2177–2208.

[22] van der Heijden, R.; Romein, B.; Heijnen, S.; Hellinga, C.; Luyben, K. Linear constraint relations in biochemical reaction systems: II. Diagnosis and estimation gross errors. *Biotechnol. Bioeng.*, **1994**, *43*, 11–20.

[23] Taylor, J. *An Introduction to Error Analysis: The Study of Uncertainties in Physical Measurements.* University Science Books, Sausalito, CA, 2nd edition, 1997.

[24] Fell, D.; Sauro, H. Metabolic control and its analysis. Additional relationships between elasticities and control coefficients. *Eur. J. Biochem.*, **1985**, *148*, 555–561.

Part IV

Metabolic Flux Analysis

Chapter 8

Metabolic Flux Analysis using Isotope Tracers[1]

8.1 Introduction

Metabolic flux analysis is being increasingly used to characterize the metabolism of mammalian cells [1–13]. While both metabolite balancing and isotope tracer analyses have been used for flux estimation, the metabolite balancing method is considerably simpler both from experimental and analytical approaches. Extracellular uptake/production rates constitute the input data from which intracellular fluxes are estimated by simple matrix algebra [14]. Thus very few additional measurements are necessary and the associated computations can be readily performed. This approach, however, has limitations because fluxes in cyclical pathways such as the pentose phosphate pathway and those in reversible reactions cannot be determined (only the net flux in a reversible reaction may be calculated).

These limitations can be overcome by isotope tracer studies using media containing a mixture of unlabeled and ^{13}C glucose and analyzing the isotope distribution in the metabolites by GC-MS or NMR. Isotope distribution in the metabolites is a direct consequence of cell metabolism and analysis of this data provides additional constraints that increase the observability of the fluxes in the bioreaction network. Substantial progress has been made in the experimental and computational approaches for applying NMR spectroscopy to metabolic flux analysis [9, 15–29] with 2D [^{13}C,^{1}H] correlation spectroscopy being the most widely adopted approach for isotope tracer experiments.

A major disadvantage of isotope tracer experiments is their cost since ^{13}C glucose makes

[1] A version of this chapter will be submitted for publication. Metabolic flux analysis of CHO cells in perfusion culture by metabolite balancing and 2D [^{13}C, ^{1}H] COSY NMR spectroscopy.

up a substantial portion of the medium glucose. They are seldom applied to laboratory-scale bioreactors and are typically performed at very small working volumes in environments that may not be representative of bioreactor conditions. While such studies do provide valuable insight into cellular metabolism, the metabolic profile may not be representative of that in a laboratory or manufacturing-scale bioreactor. Metabolism can be scale-dependent, especially if conditions such as shear and mixing do not scale linearly. The metabolite balancing method, however, is essentially scale-independent since it does not require ^{13}C glucose and extracellular rates are typically measured in both laboratory and manufacturing-scale systems.

For routine application of metabolite balancing to process development and manufacturing bioreactors, validation with results from isotope tracer experiments is necessary. Upon favorable comparison of flux estimates from these two methods, metabolite balancing can then almost exclusively be used for flux estimation. When significant process modifications such as medium composition and cell line changes are made, a revalidation of the metabolite balancing method may be necessary. Comparison of flux estimates from the metabolite balancing and isotope tracer method have been made for hybridoma cells in batch [15] and continuous culture [30] and for *Aspergillus oryzae* in a chemostat culture [21]. No such comparisons have been made for Chinese Hamster Ovary (CHO) cells in perfusion culture.

This study presents a comparison of metabolic fluxes from the metabolite balancing and isotope tracer methods for CHO cells in perfusion culture. CHO cells were initially cultivated in a medium containing unlabeled glucose which was subsequently switched to a mixture of unlabeled and ^{13}C glucose. Once isotopic steady state was reached, biomass samples from the bioreactor were used for flux estimation by 2D [^{13}C,^{1}H] NMR spectroscopy and these fluxes were compared with those obtained by the metabolite balancing method.

8.2 Materials and Methods

8.2.1 Cell Line Culture Medium and Bioreactor Operation

CHO cells were grown in perfusion culture using a medium with 7 g/L glucose and 7 mM glutamine as the primary carbon and energy sources. All experiments were conducted in a 2.5 L bioreactor (MBR Bioreactor AG, Switzerland) with a 2 L working volume and a heated water jacket. The bioreactor was maintained at 36.5 °C, with agitation constant at 70 rpm. Dissolved oxygen (DO) was maintained at 50% air saturation by sparging mixed oxygen and nitrogen. Bioreactor pH was maintained at 6.8 by the addition of 0.3 M NaOH. The bioreactor was inoculated at 8.53 x 10^6 cells/mL and cell concentrations during the

initial experimental phase (operation with unlabeled glucose) were maintained at 10 x 10^6 cells/mL by bleeding cells from the bioreactor. The perfusion rate during this phase was 1.5 bioreactor volumes/day. Subsequently, a medium containing ^{13}C glucose was used (10% uniformly labeled, 40% labeled in the 1 position and the remaining 50% unlabeled) for cell cultivation. In the 6 days following the switch to ^{13}C glucose, the target cell density was 10 x 10^6 cells/mL at a perfusion rate of 1.5 bioreactor volumes/day. Subsequently cell bleed was stopped and the cell density was allowed to reach ~20 x 10^6 cells/mL. Samples and measurements from the last 2 days of cultivation were used for metabolic flux analysis.

8.2.2 Analytical Methods

Samples from the bioreactor were taken for cell density and viability analyses using the CEDEX system (Innovatis, Bielefeld, Germany). The samples were subsequently centrifuged (Beckman Coulter, Fullerton, CA) and the supernatants were analyzed for nutrient and metabolite concentrations. Glucose, lactate, glutamine and glutamate concentrations were determined using a YSI Model 2700 analyzer (Yellow Springs Instruments, Yellow Springs, OH) while ammonium was measured by an Ektachem DT60 analyzer (Eastman Kodak, Rochester, NY). The pH and DO were measured online using retractable electrodes (Mettler-Toledo Inc., Columbus, OH) and their measurement accuracy was verified through off-line analysis in a Rapidlab® 248 blood gas analyzer (Bayer HealthCare, Tarrytown, NY). The same instrument also measured the dissolved CO_2 concentration. Concentrations of oxygen and carbon-dioxide in the exit gas were measured using a MGA-1200 Mass Spectrometer (Applied Instrument Technologies, Pomona, CA). Amino acids were analyzed on a HP 1090 HPLC (Hewlett Packard, CA) using the AminoQuant protocol with pre-column derivitization by ortho-phthalaldehyde and 9-fluorenylmethyl chloroformate for detection of primary and secondary amino acids, respectively.

8.2.3 Sample Preparation for NMR Analysis

The target biomass weight in samples for 2D-NMR analysis was 150 mg and appropriate amounts of cell culture fluid (~15 mL at 20 x 10^6 cell/mL; 30 mL at 10 x 10^6 cell/mL) were drawn from the bioreactor into a 50 mL polypropylene centrifuge tube and the sample was centrifuged at 5000 g and 4 °C for 5 minutes. The supernatant was discarded and the cell pellet was resuspended in 30 mL of PBS buffer. Following subsequent centrifugation and supernatant discard, the cell pellet was freeze-dried and stored at -80 °C. For biomass hydrolysis, 10 mL of 6N HCl was added to the freeze dried cells and the mixture was incubated at 105 °C for 24 hours. Following incubation, the mixture was filtered using a

0.45 μm syringe filter and the filtrate was evaporated under nitrogen flux until the residual volume was 200 μL. One mL of D_2O was added and the mixture was again evaporated to 200 μL. D_2O addition and evaporation was repeated two more times before the samples were analyzed by NMR.

8.2.4 2D-NMR Analysis

NMR measurements were performed at 500.16 MHz at 27 °C on a Bruker Avance 500 spectrometer (Bruker BioSpin GmbH, Silberstreifen, Germany). The [^{13}C, ^{1}H] COSY experiment was the Heteronuclear Single Quantum Correlation (HSQC) sequence with gradients for artifact suppression. Folding in F1 was used for reducing the sweepwidth. The carrier was set to 61 ppm for ^{13}C and 4.7 ppm for ^{1}H and the acquisition parameters were t_{1max} = 480 ms and t_{2max} = 221 ms. The window function used before Fourier transformation was a squared sine bell shifted by $\pi/2$ in F1 and in F2.

8.2.5 Biochemical Network

The biochemical network formulated in this study was based on mammalian cell metabolic models described in the literature [1, 11, 31, 32]. It includes glycolysis, pentose phosphate pathway (PPP), TCA cycle, amino acid catabolism and oxidative phosphorylation. Anabolic pathways include the biosynthesis of macromolecules (proteins, lipids, RNA, DNA and carbohydrates). The compartmentalization of animal cells is also considered in such a way that some processes occur only in the cytosol and mitochondria, respectively. The consequence of this is that some metabolites occur in the model in a mitochondrial state (subscript "_M") and a cytosolic state, e.g. acetyl-CoA, pyruvate, oxaloacetate, and malate.

The recycle rate of the pentose phosphate pathway cannot be uniquely identified by measuring extracellular uptake and production rates alone. This is because the portion of the flux leaving glycolysis at glucose-6-phosphate to enter the PPP is cycled back to glycolysis at fructose-6-phosphate and glyceraldehyde-3-phosphate. The PPP recycle rate, however, can be measured from isotope analysis and this value was used in the stoichiometric model. The same was true for the anaplerotic fluxes in the TCA cycle. In the metabolic balancing model both pyruvate carboxylase and malic enzyme were assumed to be active. However, if decarboxylation of oxaloacetate also occurs, only the net flux can be calculated via metabolite balancing while the isotope analysis can distinguish between these bidirectional fluxes. The pyruvate carboxylase flux obtained from NMR analysis was used in the metabolite balancing model.

Inputs for metabolite balancing were the extracellular uptake/production rates of glu-

cose, lactate, all amino acids, OUR, CER, and the specific growth rate. These coupled with the two fixed internal fluxes, PPP recycle rate and pyruvate carboxylase flux (obtained from isotope analysis by NMR) comprised the 27 input variables resulting in 2 redundant measurements that allowed calculation of the consistency index and gross error detection (The stoichiometric model consisted of 62 intracellular metabolites and 87 internal fluxes resulting in 25 degrees of freedom).

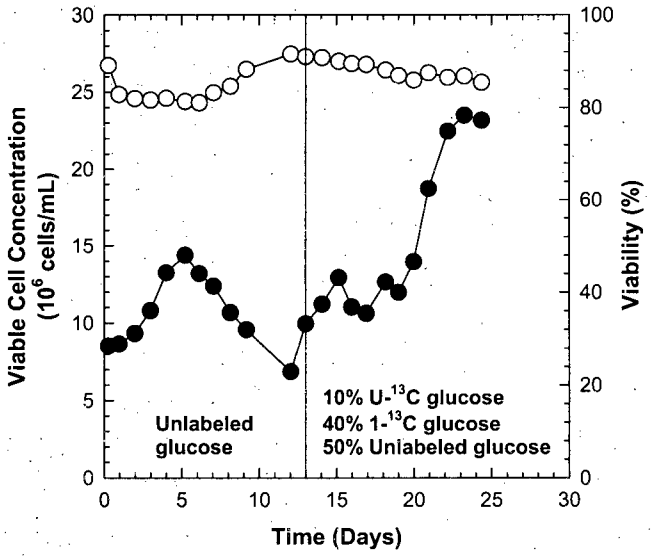

Figure 8.1: Time profiles of viable cell density (•) and viability (O) for CHO cells in perfusion culture

8.2.6 Metabolic Flux Analysis

Fluxes in the metabolite balancing method were determined using weighted least squares as described in Chapter 3. The consistency index was computed to ensure no gross experimental errors were present and since 2 redundant measurements were available, the impact of OUR and CER measurements on the consistency index was also analyzed. Estimating CER in a perfusion system is not trivial (Chapter 5) and the possibility of measurement error in CER was verified this way. Analysis of NMR data was based on the approach described in detail previously [18, 27–29].

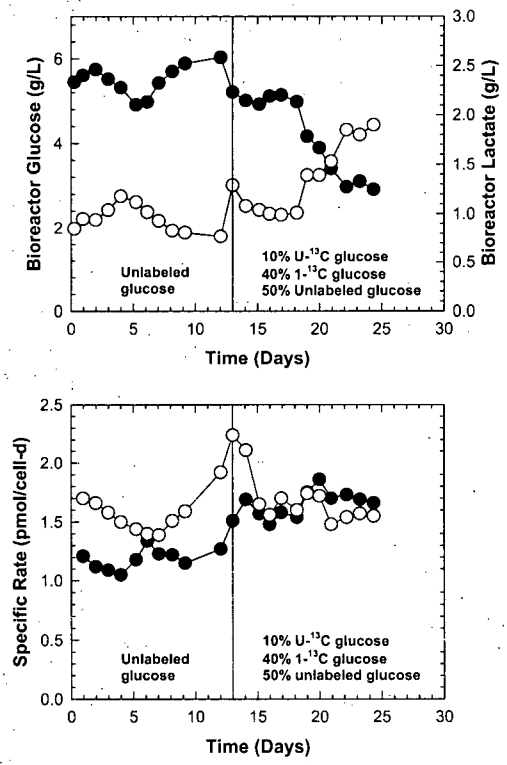

Figure 8.2: Time profiles of bioreactor glucose (•) and lactate (O) concentrations along with their respective specific uptake and production rates over the course of the perfusion cultivation.

8.3 Results

8.3.1 Cell Density and Viability

Time profiles of viable cell density and viability are shown in Figure 8.1. The bioreactor was inoculated at an initial cell density of 8.53 x 10^6 cells/mL and the target cell density was 10 x 10^6 cells/mL when the medium contained unlabeled glucose. While the average cell density with unlabeled glucose was 10.64 ± 2.26 x 10^6 cells/mL, the cell density control based on oxygen uptake rate was not very smooth in this initial portion of the experiment. Upon switching to a medium containing a mixture of unlabeled and ^{13}C glucose on day 13, cell density control improved and the average value from days 14 – 19 was 11.74 ± 0.93 x 10^6 cells/mL. Cell bleed was stopped on day 19 and the cell density was allowed to reach 20 x 10^6 cells/mL, reflective of conditions in a manufacturing bioreactor. The average cell density over the last 3 days of cultivation was 23.05 ± 0.52 x 10^6 cells/mL and data from

this time period were used for metabolic flux analysis. The fermentor viability ranged from 81 – 91.6% over the 25 day cultivation period (Figure 8.1)

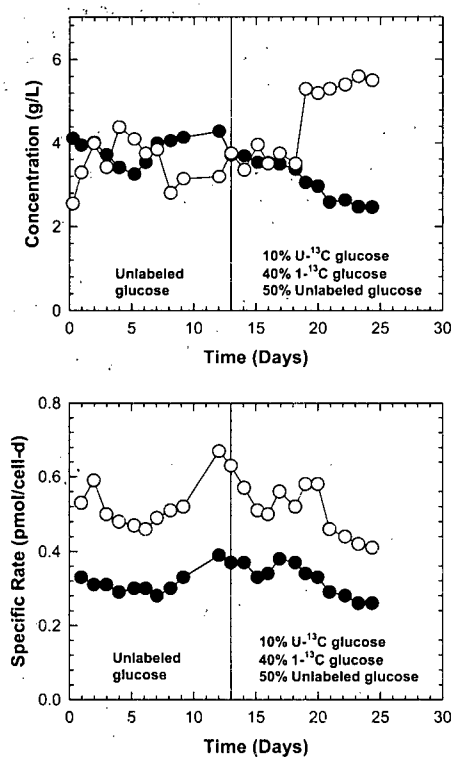

Figure 8.3: Time profiles of bioreactor glutamine (•) and ammonium (O) concentrations along with their respective specific uptake and production rates over the course of the perfusion cultivation.

8.3.2 Glucose and Lactate Metabolism

Bioreactor glucose and lactate concentrations along with their respective specific consumption and production rates are shown in Figure 8.2. Decreasing glucose and increasing lactate concentration trends from days 19 – 25 were due to cell density increase over that period (Figure 8.1), effectively reducing the cell specific perfusion rate and hence nutrient availability. The specific glucose consumption rate with unlabeled glucose was 1.22 ± 0.11 pmol/cell-d and increased to 1.66 ± 0.11 pmol/cell-d following the switch to labeled glucose. It is unlikely that this difference in glucose metabolism was due to the switch to labeled medium. In fact, the glucose uptake rate exhibited an increasing trend over the entire course of the experiment and is perhaps reflective of changing cell metabolism or

selection of cells with altered metabolic characteristics by the cell retention device. It must be recognized that these metabolic changes do not affect the flux comparisons presented in the subsequent sections because those calculations were performed on the same sample. No such changes were seen in lactate production with specific rates of 1.63 ± 0.25 and 1.66 ± 0.17 pmol/cell-d for unlabeled and labeled glucose, respectively.

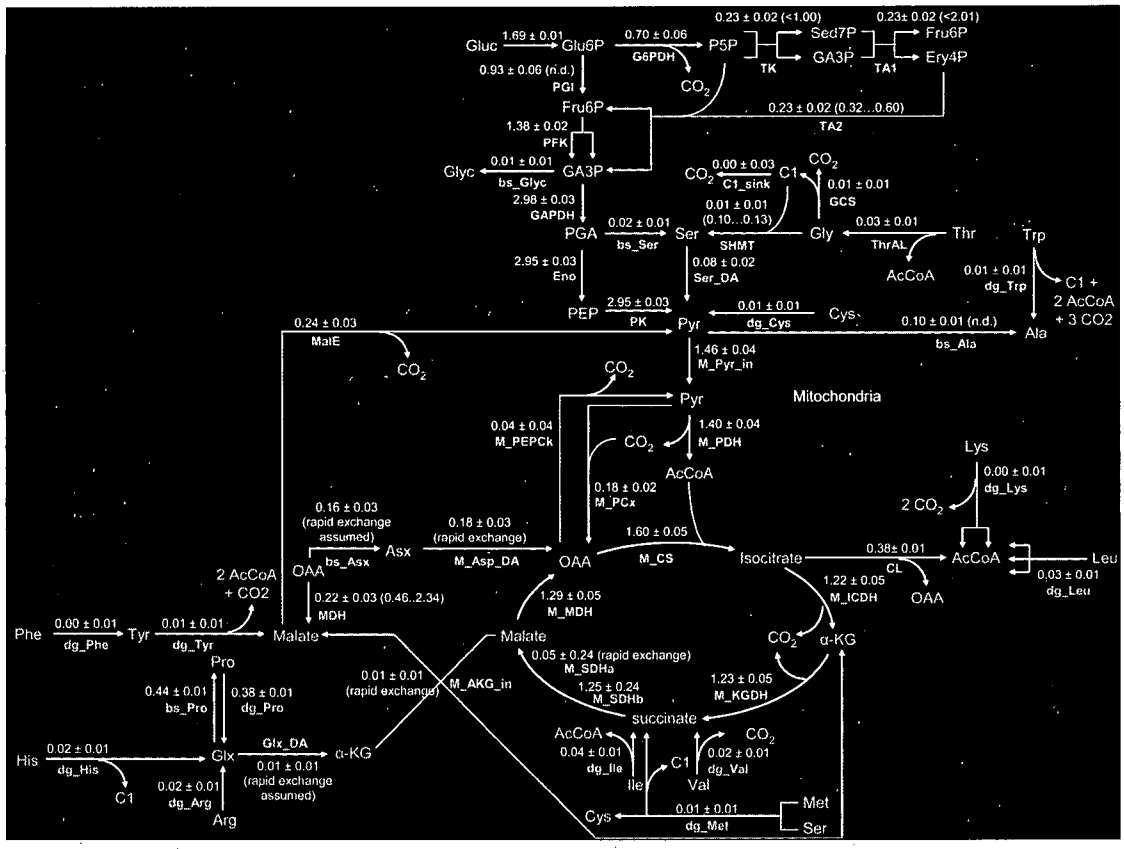

Figure 8.4: Metabolic fluxes estimated from analysis of NMR data.

8.3.3 Glutamine and Ammonium Metabolism

Time profiles of glutamine and ammonium concentrations along with their respective specific consumption and production rates are shown in Figure 8.3. Changes in their concentrations from days 19 – 25 are a result of cell density increase (Figure 8.1) and do not necessarily indicate a shift in glutamine metabolism. While both glutamine uptake and ammonium production rates were lower at the end of the cultivation, especially from days 21 – 25, the average specific rates across the unlabeled and labeled glucose phases were very similar

(0.32 ± 0.03 and 0.32 ± 0.04 pmol/cell-d for glutamine and 0.53 ± 0.07 and 0.50 ± 0.06 pmol/cell-d for ammonium).

Table 8.1: Comparison of Glycolytic Fluxes from the Isotope Tracer and Metabolite Balancing Methods

Reaction	Isotope Flux (pmol/cell-d)	Balancing Flux (pmol/cell-d)	Difference (%)
Glc → G6P	1.69	1.73	2.53
G6P → F6P	0.93	1.00	7.83
F6P → 2GAP	1.38	1.44	4.30
GAP → PG	2.98	3.07	2.86
PG → PEP	2.95	3.02	2.49
PEP → Pyr	2.95	3.02	2.49
Pyr → Pyr_M	1.46	1.83	25.2
Pyr → Lac	1.57	1.56	0.34

8.3.4 Metabolic Fluxes

The reactions in the bioreaction network along with metabolic fluxes estimated from NMR data analysis are shown in Figure 8.4. Metabolic fluxes were also calculated from the balancing method and the consistency index, h, associated with the flux estimates was 2.07 suggesting the assumed biochemistry was acceptable and that there were no gross experimental errors. A comparison of the flux estimates from the isotope tracer and metabolite balancing methods is made in Tables 8.1 – 8.4. The anaplerotic conversion of pyruvate to oxaloacetate in the mitochondria and the flux through the pentose phosphate pathway cannot be uniquely determined from the balancing method and their values (0.18 and 0.70 pmol/cell-d) were taken from the NMR analysis. Glycolytic fluxes are compared in Table 8.1 where there is close agreement (<8% absolute difference) between all fluxes except for Pyr → Pyr_M. Table 8.2 compares the TCA cycle fluxes where the maximum flux difference is 7.76% for the conversion of pyruvate to acetyl-CoA. Comparisons of fluxes in the pentose phosphate pathway and the oxidative phosphorylation reactions are shown in Table 8.3 where the maximum flux difference is 5.09%. Much higher differences are seen for the fluxes related to amino acid metabolism (Table 4) and these are primarily because these fluxes, in most cases, are two orders of magnitude smaller than those in glycolysis, PPP and the TCA cycle. Small differences in these fluxes translate into the high percentage differences shown in Table 8.4. Overall, there was excellent agreement in flux estimates from metabolite balancing and isotope tracer analysis.

Table 8.2: Comparison of TCA Cycle Fluxes from the Isotope Tracer and Metabolite Balancing Methods

Reaction	Isotope Flux (pmol/cell-d)	Balancing Flux (pmol/cell-d)	Difference (%)
Pyr_M + CO_2 → OAA_M	0.18	0.18	–
Pyr_M → AcCoA_M + CO_2	1.40	1.51	7.76
AcCoA_M + OAA_M → Icit_M	1.60	1.70	6.39
Icit_M → αKG_M + CO_2	1.22	1.19	2.25
αKG_M → SuCoA_M + CO_2	1.23	1.24	0.55
SuCoA_M → Suc_M	1.23	1.30	5.50
Suc_M → Fum_M	1.25	1.28	2.62
Fum_M → Mal_M	1.25	1.29	3.51
Mal_M → OAA_M	1.29	1.32	2.25

8.4 Discussion

8.4.1 Pentose Phosphate Pathway

The PPP flux could not be identified by the balancing method and was set to 0.7 pmol/cell-d from NMR analysis. Even if the PPP was neglected for flux estimation by metabolite balancing, the impact on glycolytic fluxes would be minimal. However, since 14.9% of the total CO_2 was produced in the PPP (Figure 8.4), it is likely that some of the CO_2 producing fluxes in the TCA cycle would be overestimated to compensate for that produced in the PPP. In our experiments, 41% of the glucose was metabolized through the PPP (Figure 8.4) and this number was 23% for hybridoma cells in chemostat culture [30]. For hybridoma cells in batch culture 9 - 10% of the glucose was metabolized in the PPP [15]. For astrocytes and granule cells, the PPP flux was determined as 11 and 29%, respectively [33]. In addition to providing ribose-5-phosphate for the synthesis of the nucleotides and nucleic acids, the pentose phosphate pathway also generates reducing equivalents in the form of NADPH for reductive biosynthesis reactions. It is possible that the high pentose phosphate flux observed in this study was to generate the NADPH necessary to support rapid cell growth during the perfusion cultivation.

The use of ^{13}C glucose provides evidence that the PPP is active for the CHO cells in this study. Alternatively, the feasibility of biochemical networks can be determined from the reaction free energies and an illustration of this approach for reactions in glycolysis is shown in Appendix I. However, intracellular concentrations of reactants and products are necessary to use this approach and this information is not readily available limiting its

applicability.

Table 8.3: Comparison of PPP, Lactate Production, Malic Enzyme and Oxidative Phosphorylation Fluxes from the Isotope Tracer and Metabolite Balancing Methods

Reaction	Isotope Flux (pmol/cell-d)	Balancing Flux (pmol/cell-d)	Difference (%)
G6P $\rightarrow$ Rib5P + CO_2	0.70	0.70	–
2Rib5P $\rightarrow$ F6P + E4P	0.23	0.22	5.09
Rib5P + E4P $\rightarrow$ F6P + GAP	0.23	0.22	5.09
3ADP+NADH+0.5O_2 $\rightarrow$ 3ATP+NAD^+	7.99	7.83	2.05
2ADP+$FADH_2$+0.5O_2 $\rightarrow$ 2ATP+FAD	1.41	1.38	2.45

8.4.2 Pyruvate Carboxylase Flux

Conversion of pyruvate to oxaloacetate by the action of pyruvate carboxylase is a major anaplerotic reaction. It helps replenish TCA cycle intermediates that are used for synthesis of fatty acids and non-essential amino acids. While this pathway can be ignored in non-growing cells [34], it can be expected to carry a substantial flux in actively growing cells. For the CHO cells in this study, the flux through this reaction was 12.8% of the pyruvate flux into the TCA cycle (Figure 8.4).

8.4.3 Implications for Bioprocess Development

We have seen good agreement in the metabolic fluxes calculated from metabolite balancing and isotope tracer analysis. They both indicated that ~50% of the glucose is converted to lactate with the remaining used for biomass synthesis and energy production. Fluxes through the PPP and the anaplerotic conversion of pyruvate to oxaloacetate could only be obtained by the isotope tracer method. However, eliminating them from the bioreaction network would have a low impact on the other fluxes (<10% change) in the bioreaction network. The metabolite balancing method thus provides a representative and accurate depiction of CHO cell metabolism. This is further confirmed by the low consistency index (2.07) associated with the calculated metabolic fluxes. The bioreaction network formulated in this study can thus be used for routine monitoring of development and manufacturing bioreactors without the need for frequent isotope labeling experiments.

Table 8.4: Comparison of Amino Acid fluxes from the Isotope Tracer and Metabolite Balancing Methods

Reaction	Isotope Flux (pmol/cell-d)	Balancing Flux (pmol/cell-d)	Difference (%)
Pyr + Glu → Ala + αKG_M	0.10	0.14	44.7
OAA_M + Glu → Asp + αKG_M	-0.18	-0.20	11.8
OAA_M + Gln → Asn + αKG_M	0.00	0.00	–
Glu → αKG + $NH4^+$	0.28	0.24	16.0
Glu → Pro	0.01	0.04	292
PG + Ala → Pyr + Ser	0.02	0.04	108
Ser → Gly	-0.01	-0.02	132
Val → SuCoA_M + CO_2	0.02	0.01	48.5
Leu → 3ACoA_M	0.03	0.04	16.7
Lys → 2ACoA_M + $2CO_2$	0.00	0.01	–
Met → Cys	0.01	0.02	50.0
Thr → ACoA + Gly	0.03	0.03	2.67
Ile → ACoA_M + SucCoA_M	0.04	0.04	11.0
His → Glu + $NH4^+$	0.02	0.01	31.0
Gln → Glu + $NH4^+$	0.16	0.14	9.81
Arg + αKG_M → 2Glu	0.02	0.03	43.5
Trp → Pyr_M + 2ACoA_M + $NH4^+$	0.01	0.00	67.0
Tyr → 2ACoA_M + Fum_M + CO_2	0.01	0.01	13.0
Phe → 2ACoA_M + Fum_M + CO_2	0.00	0.00	–
Cys → Pyr_M + $NH4^+$	0.01	0.03	199

8.5 Conclusions

We have compared flux estimates from the metabolite balancing and isotope tracer methods for CHO cells in high-density perfusion culture. There was good agreement in the glycolytic, TCA cycle and oxidative phosphorylation fluxes from these methods with <8% difference for most fluxes. The percentage differences in the amino acid fluxes were high, primarily because these fluxes were typically two orders of magnitude lower than those in glycolysis and the TCA cycle and thus sensitive to small variations in the larger fluxes. Fluxes through the PPP and anaplerotic conversion of pyruvate to oxaloacetate could only be estimated by the isotope tracer method. While inclusion of these fluxes makes the bioreaction network more representative of cell metabolism, their omission will have a limited impact on other fluxes in the network (perhaps <10%). The similarity in flux estimates from these two methods is confirmation that fluxes from the metabolite balancing method are a good representation of cellular metabolism and can be routinely used to characterize cellular metabolism in process

development and manufacturing bioreactors.

Bibliography

[1] Bonarius, H.; Hatzimanikatis, V.; Meesters, K.; de Gooijer, C. D.; Schmid, G.; Tramper, J. Metabolic flux analysis of hybridoma cells in different culture media using mass balances. *Biotechnol. Bioeng.*, **1996**, *50*, 229–318.

[2] Bonarius, H.; Houtman, J.; Schmid, G.; C.D., d. G.; Tramper, J. Metabolic-flux analysis of hybridoma cells under oxidative and reductive stress using mass balance. *Cytotechnology*, **2000**, *32*, 97–107.

[3] Europa, A. F.; Gambhir, A.; Fu, P. C.; Hu, W. S. Multiple steady states with distinct cellular metabolism in continuous culture of mammalian cells. *Biotechnol Bioeng*, **2000**, *67*(1), 25–34.

[4] Follstad, B. D.; Balcarcel, R. R.; Stephanopoulos, G.; Wang, D. I. Metabolic flux analysis of hybridoma continuous culture steady state multiplicity. *Biotechnol Bioeng*, **1999**, *63*(6), 675–83.

[5] Gòdia, C.; Cairó, J. Metabolic engineering of animal cells. *Bioprocess Engineering*, **2002**, *24*, 289–298.

[6] Nyberg, G. B.; Balcarcel, R. R.; Follstad, B. D.; Stephanopoulos, G.; Wang, D. I. Metabolism of peptide amino acids by Chinese hamster ovary cells grown in a complex medium. *Biotechnol Bioeng*, **1999**, *62*(3), 324–35.

[7] Nadeau, I.; Sabatié, J.; Koehl, M.; Perrier, M.; Kamen, A. Human 293 cell metabolism in low glutamine-supplied culture: Interpretation of metabolic changes through metabolic flux analysis. *Metab. Eng.*, **2000**, *2*, 277–292.

[8] Xie, L.; Wang, D. Material balance studies on animal cell metabolism using a stoichiometrically based reaction network. *Biotechnol. Bioeng.*, **1996**, *52*, 579–590.

[9] Forbes, N.; Clark, D.; Blanch, H. Using isotopomer path tracing to quantify metabolic fluxes in pathway models containing reversible reactions. *Biotechnol. Bioeng.*, **2001**, *74*, 196–211.

[10] Mancuso, A.; Sharfstein, S.; Tucker, S.; Clark, D.; Blanch, H. Examination of primary metabolic pathways in a murine hybridoma with carbon-13 nuclear magnetic resonance spectroscopy. *Biotechnol. Bioeng.*, **1994**, *44*, 563–585.

[11] Sharfstein, S.; Tucker, S.; Mancuso, A.; Blanch, H.; Clark, D. Quantitative in vivo nuclear magnetic resonance studies of hybridoma metabolism. *Biotechnol. Bioeng.*, **1994**, *43*, 1059–1074.

[12] Altamirano, C.; Illanes, A.; Casablancas, A.; Gámez, X.; Cairo, J.; Gòdia, C. Analysis of CHO cells metabolic redistribution in a glutamate-based defined medium in continuous culture. *Biotechnol. Prog.*, **2001**, *17*, 1032–1041.

[13] Xie, L.; Wang, D. Applications of improved stoichiometric model in medium design and fed-batch cultivation of animal cells in bioreactor. *Cytotechnology*, **1994**, *15*, 17–29.

[14] Stephanopoulos, G.; Aristodou, A.; Nielsen, J. *Metabolic Engineering. Principles and Methodologies.* Academic Press, San Diego, 1998.

[15] Zupke, C.; Stephanopoulos, G. Intracellular flux analysis in hybridomas using mass balances and In Vitro 13C NMR. *Biotechnol. Bioeng.*, **1995**, *45*, 292–303.

[16] de Graaf, A. A.; Mahle, M.; Möllney, M.; Wiechert, W.; Stahmann, P.; Sahm, H. Determination of full 13C isotopomer distributions for metabolic flux analysis using heteronuclear spin echo difference NMR spectroscopy. *J. Biotechnol.*, **2000**, *77*, 25–35.

[17] Klapa, M. I.; Park, S. M.; Sinskey, A. J.; Stephanopoulos, G. Metabolite and isotopomer balancing in the analysis of metabolic cycles: I. Theory. *Biotechnol Bioeng*, **1999**, *62*(4), 375–391.

[18] Möllney, M.; Wiechert, W.; Kowanatzki, D.; de Graaf, A. A. Bidirectional reaction steps in metabolic networks: IV. Optimal design of isotopomer labeling experiments. *Biotechnol. Bioeng.*, **1999**, *66*, 86–103.

[19] Park, S. M.; Klapa, M. I.; Sinskey, A. J.; Stephanopoulos, G. Metabolite and isotopomer balancing in the analysis of metabolic cycles: II. Applications. *Biotechnol Bioeng*, **1999**, *62*(4), 392–401.

[20] Schmidt, K.; Carlsen, M.; Nielsen, J.; Villadsen, J. Modeling isotopomer distributions in biochemical networks using isotopomer mapping matrices. *Biotechnol. Bioeng.*, **1997**, *56*, 831–840.

[21] Schmidt, K.; Marx, A.; de Graaf, A. A.; Wiechert, W.; Sahm, H.; Nielsen, J.; Villadsen, J. 13C tracer experiments and metabolite balancing for metabolic flux analysis: Comparing two approaches. *Biotechnol. Bioeng.*, **1998**, *58*, 254–257.

[22] Schmidt, K.; Nielsen, J.; Villadsen, J. Quantitative analysis of metabolic fluxes in Escherichia coli, using two-dimensional NMR spectroscopy and complete isotopomer models. *J. Biotechnol.*, **1999**, *71*, 715–190.

[23] Sriram, G.; Shanks, J. V. Improvements in metabolic flux analysis using carbon bond labeling experiments: bondomer balancing and Boolean function mapping. *Metab. Eng.*, **2004**, *6*, 116–132.

[24] Szyperski, T.; Bailey, J. E.; Wüthrich, K. Detecting and dissecting metabolic fluxes using biosynthetic fractional 13C labeling and two-dimensional NMR spectroscopy. *Trends Biotechnol.*, **1996**, *14*, 453–458.

[25] Szyperski, T.; Glaser, R.; Hochuli, M.; Fiaux, J.; Sauer, U.; Bailey, J. E.; Wüthrich, K. Bioreaction network topology and metabolic flux ration analysis by biosynthetic fractional 13C labeling and two-dimensional NMR spectrosopy. *Metab. Eng.*, **1999**, *1*, 189–197.

[26] van Winden, W.; Schipper, D.; Verheijen, P.; Heijnen, J. Innovations in generation and analysis of 2D [13C, 1H] COSY NMR spectra for metabolic flux analysis purposes. *Metab. Eng.*, **2001**, *3*, 322–343.

[27] Wiechert, W.; de Graaf, A. A. Bidirectional reaction steps in metabolic networks: I. Modeling and simulation of carbon isotope labeling experiments. *Biotechnol. Bioeng.*, **1997**, *55*, 101–117.

[28] Wiechert, W.; Siefke, C.; de Graaf, A. A.; Marx, A. Bidirectional reaction steps in metabolic networks: II. Flux estimation and stastical analysis. *Biotechnol. Bioeng.*, **1997**, *55*, 118–135.

[29] Wiechert, W.; Möllney, M.; Isermann, N.; Wurzel, M.; de Graaf, A. A. Bidirectional steps in metabolic networks: III. Explicit solution and analysis of isotopomer labeling systems. *Biotechnol. Bioeng.*, **1999**, *66*, 69–85.

[30] Bonarius, H.; Timmerarends, B.; de Gooijer, C.; Tramper, J. Metabolite-balancing techniques vs. 13C tracer experiments to determine metabolic fluxes in hybridoma cells. *Biotechnol Bioeng*, **1998**, *58*(2-3), 258–262.

[31] Zupke, C.; Stephanopoulos, G. Modeling of isotope distributions and intrecellular fluxes in metabolic networks using atom mapping matrices. *Biotechnol. Prog.*, **1994**, *10*, 489–498.

[32] Cruz, H. J.; Ferreira, A. S.; Freitas, C. M.; Moreira, J. L.; Carrondo, M. J. Metabolic responses to different glucose and glutamine levels in baby hamster kidney cell culture. *Appl. Microbiol. Biotechnol.*, **1999**, *51*(5), 579–585.

[33] Martin, M.; Portais, J.; Labouesse, J.; Canioni, P.; Merle, M. [1-13C]glucose metabolism in rat cerebellar granule cells and astrocytes in primary culture. Evaluation of flux parameters by 13C- and 1H-NMR spectroscopy. *Eur. J. Biochem.*, **1993**, *217*, 617–625.

[34] Hyder, F.; Chase, J.; Behar, K.; Mason, G.; Siddeek, M.; Rothman, D.; Shulman, R. Increased tricarboxylic acid cycle flux in rat brain during forepaw stimulation detected with 1H [13C] NMR. *Proc. Natl. Acad. Sci. U. S. A.*, **1996**, *93*, 7612–7617.

Chapter 9

Quasi Real Time Metabolic Flux Analysis[1]

9.1 Introduction

Mammalian cells are widely used for the production of therapeutic proteins that require their ability to effectively fold and glycosylate proteins. However, productivities from typical mammalian cell processes are low and a variety of approaches have been taken to overcome this limitation. These include bioprocess engineering of perfusion culture reactors to 20 x 10^6 cells/mL cell densities [1, 2], and developing improved feeding strategies to optimize cellular metabolism [3, 4]. Another tool for productivity engineering is metabolic flux analysis (MFA) which determines carbon fluxes in the central carbon metabolism and related pathways [5–8]. MFA provides insights into cellular metabolism, especially under varied environmental bioreactor conditions, rapidly clarifying cellular responses to culture conditions that can influence productivities.

Most studies on MFA use either the stoichiometric approach [9, 10] or the isotope tracer approach [11] to estimate intracellular fluxes. In these studies, metabolic fluxes are computed off-line after analysis of nutrient and metabolite levels or isotopic tracer concentrations (i.e. hours or days). While this approach allows for quantification of metabolic fluxes in the chosen reaction pathway and provides information on cellular physiology and metabolism, its off-line nature limits the MFA impact and can even slow down the rate of bioprocess diagnostics, decision-making and control. To fully realize the potential of MFA, real-time

[1] A version of this chapter has been accepted for publication. Goudar, C.T., Biener, R., Zhang, C., Michaels, J., Piret, J. and Konstantinov, K. (2006) Towards industrial application of real-time metabolic flux analysis for animal cell culture. *Advances in Biochemical Engineering and Biotechnology.*

metabolic flux information should be coupled with automated process control strategies to more rapidly optimize bioreactor operation.

Early applications of on-line data for process optimization include analysis of stoichiometry [12–14], heat balances [15], and respiratory quotient measurements [16]. It is now common practice to use information on stoichiometry as well as specific uptake and production rates for on-line identification and control of bioprocesses [17]. However, this approach has not been reported using real-time information on the network of intracellular fluxes.

In the present study, we present a framework for a quasi-real-time metabolic flux analysis system and illustrate its application studying the metabolism of CHO cells in high cell-density perfusion culture. This was achieved through seamless integration of LabVIEW (National Instruments, TX), the process monitoring and control environment, with MATLAB (Mathworks, MA) for metabolic flux computation. Metabolic fluxes were computed for a 15 L bioreactor where glucose and glutamine concentrations were varied during the course of the experiment. Sensitivity analysis was performed on key metabolic fluxes to provide the basis for a discussion of the need for accurate and reliable on-line sensors.

9.2 Framework for QRT-MFA

A schematic representation of the evolution of bioreactor monitoring and physiological state identification techniques is shown in Figure 9.1. The environment in the bioreactor is characterized by several key process variables including pH, temperature, dissolved oxygen concentration and the cell specific perfusion rate (CSPR) in addition to concentrations of carbon and energy sources such as glucose and glutamine and metabolites such as lactate and ammonia. Information on cellular physiology and metabolism is obtained in the physiological state identification step which can be further sub-divided into two categories which provide extracellular and intracellular information, respectively. Extracellular information includes specific nutrient uptake and metabolite production rates, and the specific growth rate of cells. This information comprises a portion of the state vector that describes the physiology of the cell and can be used to guide bioreactor operation [18]. However, the physiological state vector defined in this fashion is limited to extracellular information. The next logical step towards obtaining more information on cell physiology and metabolism is through the computation of intracellular fluxes. This upgrade of information content in the physiological state vector can help implement better control strategies that can result in improved bioreactor performance [19].

Our motivation for developing a framework that would enable metabolic flux calculation in quasi-real-time was to increase the quantitative information on cellular physiology and

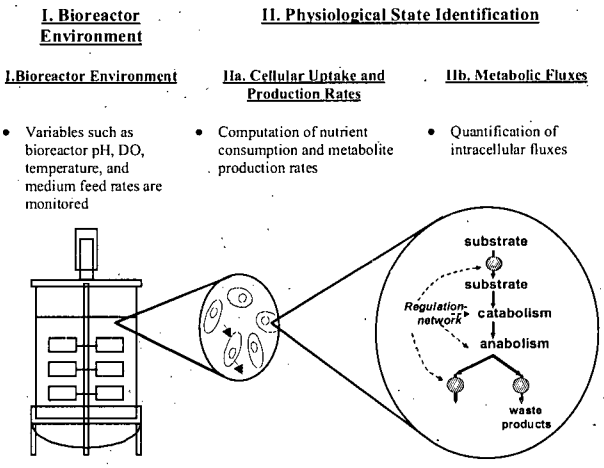

Figure 9.1: Evolution of bioreactor monitoring and physiological state identification strategies from environment to intracellular fluxes

metabolism to rapidly detect and understand shifts in cellular metabolism. There is a great deal of pressure in the biotechnology industry for rapid process development and optimization. To achieve this objective, bioprocess development efforts need to be supported with rapid and high-quality information. QRT-MFA should be one such source of information that could accelerate the development of diagnostic and process control strategies.

A variety of factors were taken into consideration during the formulation of this framework. Initial work was done with simple metabolic networks that were subsequently modified to incorporate additional reactions. This resulted in the development of a metabolic network model that could be readily modified and tested. Another important feature was the provision to include both on-line and off-line experimental data as inputs for the computation of metabolic fluxes. While input data for QRT-MFA would ideally be obtained on-line, this is difficult to achieve in practice, especially given the extensive number of analytical tests needed. With continued development of on-line analytical techniques [20], it should be possible in the future to obtain more analytical information in real-time. Given the large amount of metabolic flux data generated during long perfusion cultures (100 days or more), provisions were made to archive this information in a relational database management system. This facilitated mining for correlations between experimental variables and key metabolic fluxes as well as the comparison of results to archived cultures.

9.3 Materials and Methods

9.3.1 Cell Line, Culture Medium and Bioreactor Operation

Chinese hamster ovary cells were grown in perfusion culture using a medium with either 4.5 g/L glucose and 6 mM glutamine or with 6 g/L glucose and 8 mM glutamine (Table 9.1). All experiments were conducted in 15 L bioreactors (MBR Bioreactor AG, Switzerland) with a 12 L working volume and a heated water jacket. The bioreactor was maintained at 37 °C, with agitation constant at 40 rpm. Dissolved oxygen (DO) was maintained at 50 % air saturation by sparging mixed oxygen and nitrogen. Bioreactor pH was maintained at 6.8 by the addition of 0.3 M NaOH. The bioreactor was inoculated at ~1.0 x 10^6 cells/mL and cell concentrations during the experiment were maintained between 10 and 30 x 10^6 cells/mL by automatically bleeding cells from the bioreactor based on optical density measurements. The bioreactor was operated in perfusion mode by continuously withdrawing reactor fluid and passing it through a cell separation device. The cells were recycled back to the bioreactor while the clarified liquid was harvested for subsequent purification steps to isolate the protein of interest.

Table 9.1: Medium composition and dilution rate for the six operating conditions examined in this study

State	Glucose (g/L)	Glutamine (mM)	Dilution Rate (vol/d)
A	4.5	6	2
B	6	8	2
C	6	8	1.5
D	6	8	1
E	4.5	6	1
F	6	8	2

9.3.2 Analytical Methods

Samples from the bioreactor and the harvest stream were taken daily for cell density and viability analysis using a heamocytometer and the trypan blue dye-exclusion method, respectively. Cell sizes were determined using a particle counter (Casy, Schärfe Systems, Germany). These samples were then centrifuged in a Beckman CS-6 centrifuge (Beckman Coulter, CA) and the supernatant analyzed for nutrient and metabolite concentrations. Glucose, lactate, glutamine and glutamate concentrations were determined using a YSI Model 2700 analyzer (Yellow Springs Instruments, OH) while ammonia was measured using

an Ektachem DT60 analyzer (Eastman Kodak, NY). DO and pH were measured online using retractable Ingold electrodes (Ingold Electrodes, MA). The accuracy of these measurements was verified off-line using a Stat Profile 9 blood gas analyzer (Nova Biomedical, MA). The same instrument was also measured the dissolved CO_2 concentration. On-line measurements of cell density were made with a retractable optical density probe (Aquasant Messtechnik, Switzerland) calibrated with cell density estimated by the heamocytometer. Amino acids were analyzed on a HP 1090 HPLC (Hewlett Packard, CA) using the AminoQuant protocol (Series II Operator's Handbook) with pre-column derivitization by ortho-phthalaldehyde and 9-fluorenylmethyl chloroformate for detection of primary and secondary amino acids, respectively.

9.3.3 Estimation of Specific Rates

A mass balance on viable cells in the bioreactor and the cell bleed system results in

$$\mu' = \frac{F_b}{V} + \left(\frac{F_h}{V}\right)\frac{X_V^H}{X_V^B} + \frac{1}{X_V^B}\frac{dX_V^B}{dt} \tag{9.1}$$

where μ' is the apparent specific growth rate (1/day), F_b, the bleed rate (L/day), V, the bioreactor volume (L), F_h, the harvest flow rate (L/day), X_V^H, the viable cell density in the harvest stream (x 10^6 cells/mL), X_V^B, the viable cell density in the bioreactor (x 10^6 cells/L) and t is time (days). Specific nutrient uptake and metabolite production rates were computed from

$$q = \frac{F_m}{VX_V^B}\left(C_{in} - C_{out}\right) \tag{9.2}$$

where q represents the specific uptake or production rate (mol/10^9cells-day) and C_{in} and C_{out} are the bioreactor inlet and outlet concentrations (mol/L) of the nutrients or metabolites.

9.3.4 Estimation of Metabolic Fluxes

The bioreaction network used in the study was similar to the one proposed for CHO cells [5] with modifications to include reactions for all amino acids. It included a total of 65 reactions and 40 metabolites and the uptake/production rates of 27 of the metabolites were measured. The stoichiometric matrix was of full rank and the bioreaction network was characterized by 2 degrees of freedom and 2 redundant measurements. A series of mass balance equations

were written for each of the metabolites in the bioreaction network resulting in

$$\mathbf{A}\dot{\mathbf{x}} = \mathbf{r} \tag{9.3}$$

where $\mathbf{A}$ is the stoichiometric coefficient matrix, $\mathbf{x}$, the vector of unknown metabolic fluxes, and $\mathbf{r}$, the vector of uptake and production rates. Nutrient consumption and metabolite production rates were incorporated in $\mathbf{r}$ and intermediate metabolite production rates were assumed to be zero based on the pseudo-steady-state hypothesis [21]. As the stoichiometric matrix, $\mathbf{A}$, was not square, and estimation of the metabolic flux vector, $\mathbf{x}$, was done using the weighted least squares approach

$$\mathbf{x} = \left(\mathbf{A}^{\mathbf{T}}\psi^{-1}\mathbf{A}\right)^{-1}\mathbf{A}^{\mathbf{T}}\psi^{-1}\mathbf{r} \tag{9.4}$$

where ψ is the variance-covariance matrix associated with the rate vector $\mathbf{r}$. Once the metabolic flux vector was estimated, the sensitivity of the metabolic fluxes to the measurements was estimated from

$$\frac{\partial \mathbf{x}}{\partial \mathbf{r}} = \left(\mathbf{A}^{\mathbf{T}}\psi^{-1}\mathbf{A}\right)^{-1}\mathbf{A}\psi^{-1} \tag{9.5}$$

9.3.5 Computer Implementation

To obtain metabolic flux estimates in a quasi-real-time fashion for on-line physiological state identification, the computation of metabolic fluxes was integrated with on-line data acquisition and process monitoring. A schematic of this approach is shown in Figure 9.2. Specifically, LabVIEW (National Instruments, TX) was used for on-line data acquisition and process control while all flux calculations were performed using FluxAnalyzer [22] in MATLAB (Mathworks, Natick, MA). Seamless integration between these two environments allowed transfer of specific rate data from LabView to MATLAB followed by subsequent transfer of the computed metabolic fluxes in the reverse direction.

Information on cell density could be obtained in real-time from optical density measurements and this information coupled with the bleed rate helped estimate the specific growth rate of the cells. Oxygen and carbon dioxide concentrations in the bioreactor were monitored in real-time as well as their concentrations in the inlet and exit gas streams. This information was used in global mass balance expressions that were developed for the perfusion system to estimate the oxygen uptake rate (OUR) and carbon-dioxide evolution rate (CER). Concentrations of glucose, lactate, ammonia and amino acids were estimated off-line using the analytical techniques described earlier. Given available labor and equipment, all these measurements could be performed within one hour. This combination of on-line and

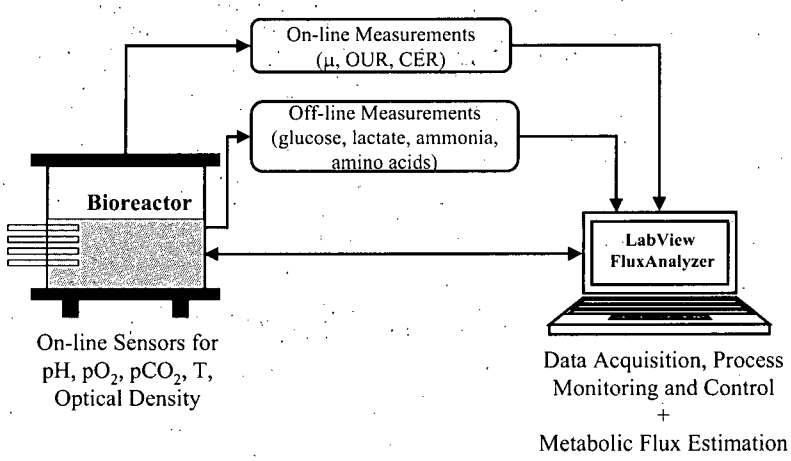

Figure 9.2: Illustration of the framework for quasi real-time metabolic flux estimation

off-line data were initially transferred to LabVIEW and subsequent flux estimations that were performed using FluxAnalyzer were initiated from the LabVIEW environment itself. This interface between LabVIEW and MATLAB was designed to approximate real-time MFA such that on-line information from new sensors could be seamlessly incorporated. Results of the computations included a table containing the fluxes for all the reactions in the bioreaction network along with a graphical depiction of the fluxes through the metabolic network. These metabolic fluxes were archived to observe trends of key metabolic fluxes over the course of the experiment.

9.4 Results

The framework presented above was applied to study the metabolism of CHO cells in perfusion culture at high cell densities. Medium composition and perfusion rates were modified to obtain 6 different states designated as A through F (Table 9.1). The resulting metabolic responses from the cells were subsequently quantified through metabolic flux analysis. The cells were exposed to increasing amounts of glucose and glutamine when switched from state A to B. However, in C, D, and E, the cells were exposed to progressively decreasing amounts of glucose and glutamine. States F and B had identical feed medium composition and perfusion rates. This helped quantify the effect of lower nutrient concentration (in states B, C, and D) on cellular metabolism through a comparison of metabolic fluxes in states B and F.

9.4.1 Cell Density, Glucose, and Lactate Concentrations

Cell densities for states A through C were approximately 20 x 10^6 cells/mL while states E and portions of D were characterized by values in the 5 – 10 x 10^6 cells/mL range (Figure 9.3). State F, which was identical to state B in terms of medium feed and dilution rate was characterized by cell densities between 10 and 30 x 10^6cells/mL. These changes in cell densities were a consequence of the changes made to the cell bleed set-point. The motivation for these changes was to investigate the performance of the process in the neighborhood of 20 x 10^6 cells/mL, the standard operating cell density for this process.

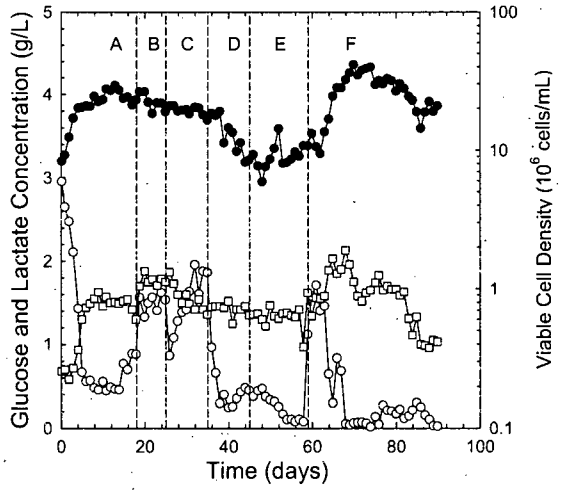

Figure 9.3: Bioreactor viable cell density and glucose and lactate concentrations over the course of the experiment. Medium composition and perfusion rates of states A through F are defined in Table 8.1. [(•) bioreactor cell density; (o) glucose; (□) lactate].

9.4.2 Metabolic Fluxes at States A through F

Recognizing the dynamic nature, especially of states D, E, and F, 4 – 6 data points towards the end of the 6 states A through F were used to compute extracellular rates using Eqs.(9.1) and (9.2). These calculated extracellular rates were averaged to obtain a single value for each state. This information was subsequently used to compute intracellular metabolic fluxes for states A through F from Eq.(9.4). A plot of the pyruvate flux into the TCA cycle versus the pyruvate flux into lactate for each of the six states is shown in Figure 9.4. States A, B and C cluster in the region of high lactate and low TCA flux while states D, E and F lie in the region where the lactate flux is relatively lower and the TCA cycle flux

is correspondingly higher, indicative of a more efficient metabolic state. High values of the pyruvate flux into the TCA cycle flux are desirable as this results in the production of energy. Pyruvate flux to lactate is not desirable since lactate is a waste metabolite. It appears that as the cells progressed from state B to F, there was a shift in metabolism towards a more efficient state as seen from the increase in the pyruvate flux into the TCA cycle.

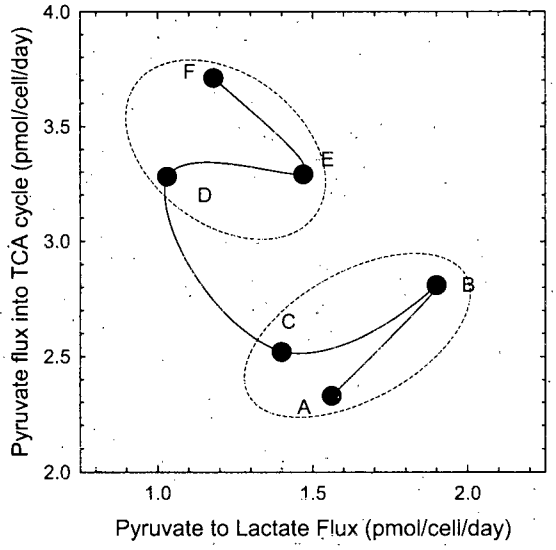

Figure 9.4: Profile of the two pyruvate fluxes at states A through F

Another approach to quantify the shift in metabolism due to changes in dilution rate is by examination of flux distribution around the pyruvate branch point [23]. Figure 9.5 shows a time course of the glycolytic flux plus the TCA cycle reflux divided by the inlet flux to the TCA cycle around the pyruvate branch point. Low values of this ratio indicate more efficient cycling of the carbon flux from pyruvate while high values correspond to increased production of waste metabolites such as lactate. It follows from Figure 9.5 that this ratio decreases with decreasing dilution rate suggesting a shift towards more efficient metabolism at lower dilution rates.

A comparison of metabolic fluxes through the TCA cycle for states B and F that were characterized by the same medium composition and dilution rates revealed that the TCA cycle fluxes in state F were at least 30 % higher than those in B. Hence, two different physiological states were observed under similar reactor operating conditions. No significant change in specific protein productivity was observed during the course of the experiment

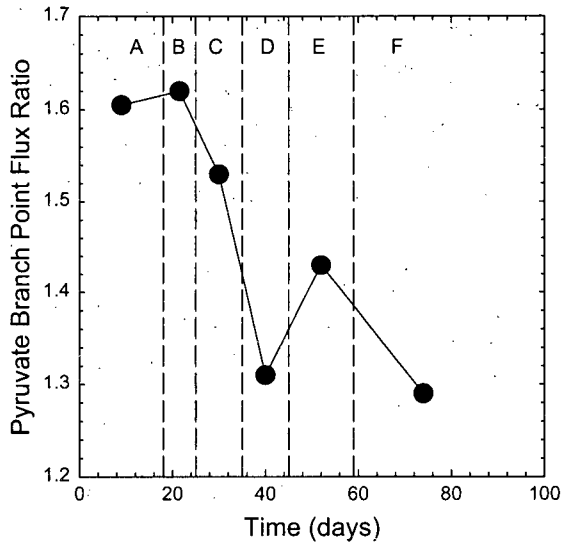

Figure 9.5: Metabolic flux distribution around the pyruvate branch point during the course of the experiment. Higher values are indicative of waste metabolism while low values correspond to increased carbon flux through the TCA cycle

(data not shown). This has significant implications for reactor design and operation since lower production of waste metabolites such as lactate allow use of lower perfusion rates. This can translate into reduced medium costs and a more concentrated harvest stream thereby minimizing the volume of material that needs to be processed in subsequent purification steps.

9.4.3 Sensitivity Analysis for the Practical Realization of QRT-MFA

One approach to overcoming some limitations of metabolite balancing is through the application of sensitivity analysis where information on the effects of measured variables on key metabolic fluxes can be quantified [19]. Sensitivities of the pyruvate kinase, pyruvate dehydrogenase and citrate synthase fluxes to the various uptake and production rates are shown in Figure 9.6 for states B and F. Glucose uptake rate, lactate production rate and oxygen uptake rate have the most significant impact on the above mentioned fluxes for both states B and F. For instance, a 1% change in OUR would cause a 1.5% change in the pyruvate dehydrogenase flux for state B. The glucose uptake rate had a significant influence on the pyruvate kinase and pyruvate dehydrogenase fluxes but only a minor effect on the TCA cycle flux. This sensitivity is similar to that of glutamine for the same fluxes. Once

important metabolic fluxes are identified, the sensitivity of these fluxes to various input data can be estimated and this information can be used to rank the input measurements. An important observation in this study was that most of the amino-acids had only a minor influence on the fluxes of central metabolism. Thus if only central metabolism fluxes are of interest, off-line analysis of amino acids on a daily basis should be adequate for computing the metabolic fluxes with reasonable accuracy. This is an important simplification for the practical realization of QRT-MFA.

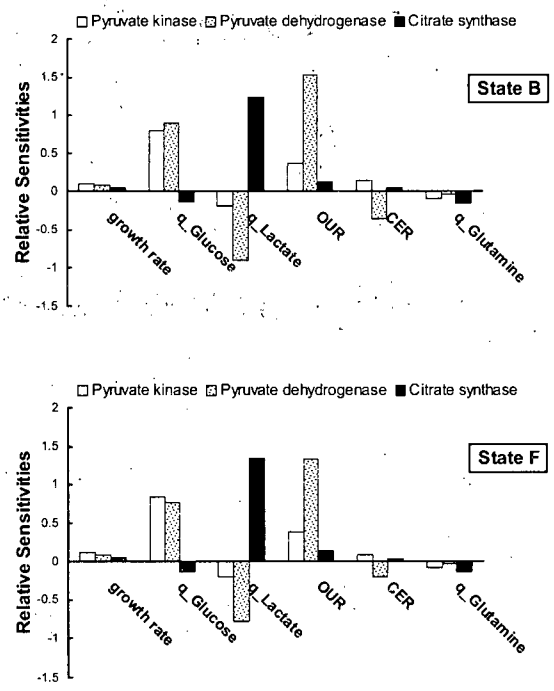

Figure 9.6: Relative sensitivities of the calculated pyruvate kinase, pyruvate dehydrogenase, and citrate synthase fluxes with respect to measured specific rates. Only those specific rates with relative sensitivities greater than 0.05 are shown

9.5 Discussion

9.5.1 Steady State Multiplicity

Exposing the cells to progressively decreasing amounts of glucose and glutamine by varying either the medium composition or the perfusion rate caused a shift in metabolism towards a more efficient state as seen by increased pyruvate flux to the TCA cycle coupled with

decreased lactate production. This manifested as a reduction in the pyruvate branch point flux ratio for the metabolically efficient state (F). Our observations on steady-state multiplicity are consistent with earlier chemostat studies where similar shifts in metabolism were observed at lower dilution rates [23–25].

Glucose and glutamine utilization characteristics of mammalian cells can be influenced by their respective concentrations [4, 26–28]. Generally, high concentrations of glucose result in increased glucose uptake rates with most of the glucose being converted to lactate. Even if this phenomenon is not accompanied by deceased specific protein productivities, it is undesirable because it will result in increased lactate concentration in the bioreactor that can adversely effect cell growth [29]. Reduced lactate levels in a perfusion system can be achieved either by a decrease in cell density or an increase in perfusion rate. However, neither of these changes is desirable. As protein production is directly linked to cell concentration, reduction in cell density will decrease protein production while increased perfusion rates will result in a more dilute harvest stream. This can greatly increase the fluid volume that has to be processed in subsequent purification operations. Alternatively, if cellular metabolism can be altered to reduce lactate production when its accumulation is limiting, high cell densities can be maintained and perfusion rates can be lowered, resulting in harvest streams with higher protein concentrations.

9.5.2 Quasi-Real-Time Metabolic Flux Analysis

We have presented results on the shifts in metabolism of CHO cells in perfusion culture as a response to changes in experimental conditions. There exist several other avenues for the application of metabolic flux analysis at the bioprocess level and these include clone selection, medium optimization and optimization of physical parameters such as pH, temperature, shear and DO among others. Moreover, metabolic flux analysis can also be used in a process evaluation and control mode where changes to set-points can be made based on the estimates of some key metabolic fluxes. However, to fully realize the potential of metabolic flux analysis for these applications, there is a need for rapid evaluation of the fluxes, ideally, in an on-line fashion. This directly translates into a need for reliable on-line sensors for measuring concentrations of key nutrients, metabolites and amino-acids.

9.5.3 Sensors for RT-MFA

Based on results from the sensitivity analysis described above, on-line estimation of oxygen uptake as well as glucose and lactate concentrations should be given high priority because of the significant influence they exert on central metabolism fluxes. This can be followed

by glutamine and ammonia concentrations that are also usually measured in an off-line fashion. Given the rather complex nature of amino-acid analysis, on-line analysis should only be considered under special conditions when the application demands this information.

Flow injection analysis has been used for real-time measurement of glucose and ammonia [17] while real-time measurement of glucose and lactate has been demonstrated by automatically drawing samples from the bioreactor through a circulation loop followed by sample filtration to remove biomass and subsequent analysis using standard analyzers [30]. These approaches typically require the deployment of dedicated analyzers for each bioreactor which becomes impractical in a process development scenario where a number of bioreactors are operated simultaneously. Moreover, the presence of additional flow loops can increase the contamination risk, especially for perfusion systems given their long operation times.

There has been progress in on-line estimation of glucose, lactate, glutamine, and ammonia through the use of near-infrared (NIR) and mid-infrared (MIR) spectroscopic measurements [31, 32]. However, these measurements were characterized by high standard errors which may limit their practical use in experiments such as those performed in this study. Specifically, the lowest standard errors in the NIR measurements for glucose, lactate, glutamine and ammonia were 0.82, 0.94, 0.55, and 0.76 mM, respectively [31] while in the MIR measurements, standard errors for lactate measurements ranged from 1 to 3 mM, and those for glucose were approximately 1 mM [32]. The average concentrations of glucose, lactate, glutamine, and ammonia in this study were 4.03, 16.3, 2.74, and 3.4 mM, respectively, requiring the use of more accurate methods of analysis. Conventional off-line analytical instruments such as the YSI 7100 MBS (YSI Inc., Yellow Springs, OH) with precision on the order of 0.11, 0.22, 0.1 and 0.1 mM for glucose, lactate, glutamine, and ammonia, respectively, are better suited for analysis where the concentrations of these nutrients and metabolites are low and when increased precision is desired. Thus despite the significant progress in bioprocess monitoring over the past few decades [20], there is still a need for reliable sensors that would allow for on-line estimation of the concentrations of key metabolites and amino acids. The applicability of new on-line sensors for real-time flux analysis is currently being investigated in our laboratory.

9.5.4 Metabolite Balancing and Isotope Tracer Approaches as Applied to QRT-MFA

As QRT-MFA requires the rapid analysis of experimental data for estimation of metabolic fluxes, it is not practical to use isotope tracer studies for estimating metabolic fluxes since this technique is laborious both from experimental and analytical standpoints. It is well

known that metabolite balancing alone is not sufficient to estimate all the intracellular metabolic pathway fluxes because the set of linear equations defined by these mass balances is underdetermined [11, 33, 34]. Some of these limitations can be overcome through the use of additional constraints such as including the mass balance expressions of the co-metabolites ATP or NAD(P)H, assuming the irreversibility of certain reactions, or through the use of objective functions [35]. Moreover, the metabolite balancing technique can be augmented with a few carefully planned isotope tracer studies that could validate the use of nutrient and metabolite mass balances alone for the estimation of metabolic fluxes.

9.5.5 Implementation of QRT-MFA in this Study

An intuitive and visual approach towards estimating metabolic fluxes was used in this study. Computation of metabolic fluxes was initiated from the process monitoring and control environment in LabVIEW through a graphical user interface. The input information consisting of rates of growth, glucose and oxygen consumption, metabolite production, carbon-dioxide evolution and uptake/production rates of amino acids was provided. While there is a provision in the software to record and use this data in real-time, a combination of on-line and off-line data was currently used as illustrated in Figure 9.2. Subsequent metabolic flux calculations were performed using FluxAnalyzer in the MATLAB environment and the results displayed both in graphical and tabular format. The graphical display (Figure 9.7) showed the metabolic flux map along with values of key metabolic fluxes. Features of the graphical display include a distinction between computed fluxes and those obtained from experimental data, and lines in the metabolic map with thickness proportional to the magnitude of the flux. The tabular depiction lists the magnitude of the fluxes through all the reactions in the metabolic pathway and has a provision for normalizing these fluxes based on any nutrient/metabolite of choice.

Seamless integration between the process monitoring and control environment (LabVIEW) and the flux analysis computing environment (MATLAB) allowed easy access to metabolic flux information in addition to other commonly measured experimental variables such as pH, temperature and DO along with some calculated variables such as cell growth rate and specific uptake/production rates of key nutrients and metabolites. As perfusion experiments are often carried out over extended periods of time, this information can be archived allowing for trending of key metabolic fluxes. Thus, changes in cellular metabolism can be readily identified and once a cause-effect relationship has been established, this information can be used to make appropriate modifications to process conditions that will result in the desired improvement in the process.

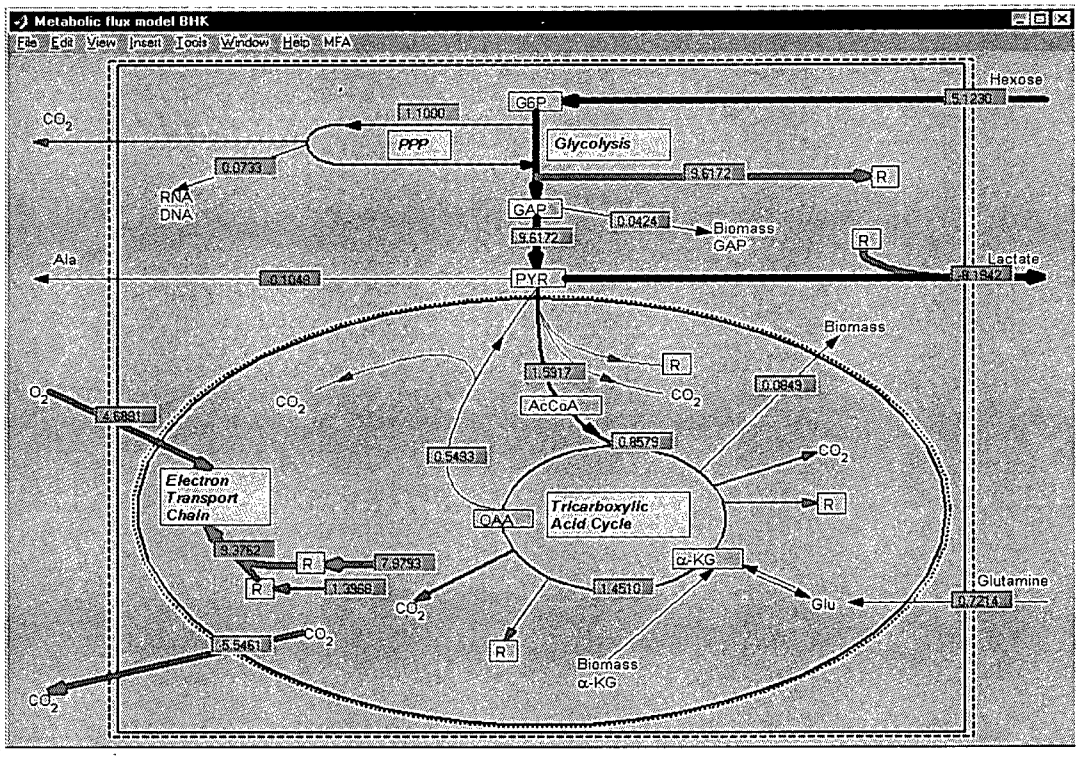

Figure 9.7: Graphical representation of the results of metabolic flux analysis. Distinction is made between experimentally measured and calculated fluxes through use of color and the thickness of the flux lines correspond to the magnitude of the respective fluxes

Currently, the time from sampling the bioreactor to obtaining all the necessary analytical data for computing the metabolic fluxes through a combination of on-line and off-line measurements is approximately 1 hour. Hence there is a 1 hour delay in obtaining a metabolic snapshot of the bioreactor at any given time. This delay can be reduced significantly as more data become reliably available on-line thereby enabling the transition from quasi-real-time to real-time estimation of metabolic fluxes.

9.5.6 Practical Implications of QRT-MFA

Current industrial practice for cultivating mammalian cells in perfusion culture involves bioreactor operation at desired set points for process variables such as cell specific perfusion rate, pH, temperature, and dissolved oxygen concentration. Process characterization involves off-line estimation of prime variables such as cell density, nutrient, metabolite and product concentrations. Control schemes are typically based on values of the prime vari-

ables alone. For instance, the bioreactor cell density control loop maintains constant cell density by bleeding cells from the bioreactor. This can be readily accomplished as long there is an on-line indicator of cell density such as an optical density probe. Indirect indicators of cell density such as oxygen consumption rates could also be used for this purpose. It is important to note that current operational protocols do not rely on detailed information on cellular metabolism.

When metabolic fluxes can be estimated rapidly, a significant amount of quantitative information on cellular metabolism becomes available which can be used in various process control loops to guide bioreactor performance in the desired direction. For instance, a decrease in the stoichiometric ratio between lactate production and glucose consumption from 1.36 mol/mol in normal culture to 0.04 mol/mol in a metabolically altered culture was seen where the amount of glucose available to hybridoma cells in fed-batch culture was reduced [24]. Based on their results, the authors suggest initiation of cultivation in fed-batch mode and exposing cells to reduced amounts of glucose so that lactate production is minimized resulting in very efficient cellular metabolism as seen by increased flux through the TCA cycle. Once this shift in metabolism has occurred, the bioreactor can be operated in a continuous mode and the advantages of efficient metabolism can be leveraged. As seen earlier, reduced lactate yields from glucose allow operation at lower perfusion rates resulting in a concentrated protein stream for subsequent purification processes.

For robust implementation of such a control strategy that is based largely on the metabolism of cells, it is necessary to obtain frequent snapshots of cellular metabolism that will provide valuable feedback on the efficacy of the process control strategy. In the initial fed-batch phase of the process, metabolic flux information would be necessary to follow the shift in metabolism from the high lactate producing state to one that is highly energy efficient as seen by increased flux through the TCA cycle. The feeding strategy for glucose could be based on the relative distribution of fluxes at the pyruvate branch point. During the next phase of the experiment where it is desired to maintain the efficient metabolic state of the cells, metabolic fluxes provide the information necessary to characterize the physiological state of the cells. Again glucose feeding during the perfusion phase can be based on flux distribution at the pyruvate branch point. While it can be argued that the above control strategy can be based on glucose concentration alone, that would be representative of indirect control of cellular metabolism. With rapid estimation of metabolic fluxes, it is possible to directly control cellular metabolism by feeding glucose at a rate that ensures a fixed distribution of fluxes at the pyruvate branch point. This concept of direct estimation and control of cellular metabolism in an industrial mammalian cell bioreactor is novel and more work is necessary to demonstrate the usefulness of this approach towards accelerated

process development and optimized bioreactor operation.

Other applications of QRT-MFA include medium optimization and clone selection that are usually labor-intensive and time consuming approaches. For both these applications, initial screening is usually done in a high throughput fashion followed by evaluation of a small subset of high performers in bioreactors. Traditionally, specific protein productivity and cell growth rate and viability have been regarded as the most important indicators of cell performance and we believe that inclusion of metabolic fluxes in this selection criteria provides an extra line of evidence for selection of a particular medium formulation or clone.

9.6 Conclusions

We have presented a general framework for quasi-real-time estimation of metabolic fluxes in a perfusion bioreactor. The concept is general and as it relies on metabolite balancing alone, it can be readily applied to both laboratory and industrial-scale bioreactors of practically any configuration. The utility of this approach towards monitoring shifts in cellular metabolism was demonstrated using CHO cells cultivated in perfusion reactors where exposure to lower nutrient concentrations shifted cellular metabolism towards a more efficient state as seen by increased flux into the TCA cycle. This new state was characterized by lower production of waste metabolites with significant implications for reactor design and operation. There exist several other scenarios such as clone selection, medium optimization, and bioreactor environment optimization, among others, where MFA can be applied to optimize the operation of mammalian cell bioreactors. While the framework provided in this study allows real-time computation of metabolic fluxes, it is limited by the lack of accurate and reliable sensors for on-line estimation of key nutrient and metabolite concentrations. Once such sensors become available, they will enable the full realization of metabolic flux analysis in real-time. This MFA implementation will substantially increase the quality of information obtained from experiments in process development bioreactors resulting in additional insights into cellular physiology and metabolism. This information can play a significant role in the design of operational strategies for the production bioreactor where the therapeutic protein will finally be made.

Bibliography

[1] Konstantinov, K.; Chuppa, S.; Sajan, E.; Tsai, Y.; Yoon, S.; Golini, F. Real-time biomass-concentration monitoring in animal-cell cultures. *Trends Biotechnol*, **1994**, *12*(8), 324–33.

[2] Trampler, F.; Sonderhoff, S.; Pui, P.; Kilburn, D.; Piret, J. Acoustic cell filter for high density perfusion culture of hybridoma cells. *Bio/Technology*, **1994**, *12*(3), 281–284.

[3] Glacken, M.; Huang, C.; Sinskey, A. J. Mathematical description of hybridoma culture kinetics. III. Simulation of fed-batch reactors. *J. Biotechnol.*, **1989**, *10*, 39–66.

[4] Zhou, W. C.; Rehm, J.; Europa, A. F.; Hu, W. S. Alteration of mammalian cell metabolism by dynamic nutrient feeding. *Cytotechnology*, **1997**, *24*, 99–108.

[5] Nyberg, G. B.; Balcarcel, R. R.; Follstad, B. D.; Stephanopoulos, G.; Wang, D. I. Metabolism of peptide amino acids by Chinese hamster ovary cells grown in a complex medium. *Biotechnol Bioeng*, **1999**, *62*(3), 324–35.

[6] Bonarius, H.; de Gooijer, C.; Tramper, J.; Schmid, G. Determination of the respiration quotient in mammalian cell culture in bicarbonate buffered media. *Biotechnol. Bioeng.*, **1995**, *45*, 524–535.

[7] Stephanopoulos, G.; Vallino, J. J. Network rigidity and metabolic engineering in metabolite overproduction. *Science*, **1991**, *252*(5013), 1675–1681.

[8] Zupke, C.; Sinskey, A. J.; Stephanopoulos, G. Intracellular flux analysis applied to the effect of dissolved oxygen on hybridomas. *Appl. Microbiol. Biotechnol.*, **1995**, *44*(1-2), 27–36.

[9] Vallino, J. J; Stephanopoulos, G. Metabolic flux distributions in Corynebacterium glutamicum during growth and lysine production. *Biotechnol. Bioeng.*, **1993**, *41*, 633–646.

[10] Varma, A.; Palsson, B. Metabolic flux balancing: Basic concepts, scientific and practical use. *Bio/Technology*, **1994**, *12*, 994–998.

[11] Wiechert, W. 13C Metabolic flux analysis. *Metab. Eng.*, **2001**, *3*, 195–206.

[12] Cooney, C.; Wang, H. Y.; Wang, D. I. Computer-aided material balancing for prediction of fermentation parameters. *Biotechnol. Bioeng.*, **1977**, *19*, 55–67.

[13] Wang, H.; Cooney, C.; Wang, D. Computer-aided baker's yeast fermentations. *Biotechnol. Bioeng.*, **1977**, *19*, 69–86.

[14] Wang, H.; Cooney, C.; Wang, D. I. Computer control of baker's yeast production. *Biotechnol. Bioeng.*, **1979**, *21*, 975–995.

[15] Erickson, L. Application of mass-energy balance in on-line data analysis. *Biotechnol. Bioeng. Symp.*, **1979**, *9*, 48–60.

[16] Spruytenburg, R.; Dunn, I.; Bourne, J. Computer control of glucose feed to a continuous culture of Sacchromyces cerevisiae using the respiratory quotient. *Biotechnol. Bioeng. Symp.*, **1979**, *9*, 359.

[17] Herwig, C.; Marison, I.; Stockar, U. On-line stoichiometry and identification of metabolic state under dynamic process conditions. *Biotechnol. Bioeng.*, **2001**, *75*, 345–354.

[18] Konstantinov, K. Monitoring and control of the physiological state of cell cultures. *Biotechnol. Bioeng.*, **1996**, *52*(2), 271–289.

[19] Stephanopoulos, G.; Aristodou, A.; Nielsen, J. *Metabolic Engineering. Principles and Methodologies.* Academic Press, San Diego, 1998.

[20] Schügerl, K. Progress in monitoring, modeling and control of bioprocesses during the last 20 years. *J. Biotechnol.*, **2001**, *85*, 149–173.

[21] Zupke, C.; Stephanopoulos, G. Intracellular flux analysis in hybridomas using mass balances and In Vitro 13C NMR. *Biotechnol. Bioeng.*, **1995**, *45*, 292–303.

[22] Klamt, S.; Schuster, S.; Gilles, E. Calculability analysis in underdetermined metabolic networks illustrated by a model of the central metabolism in purple nonsulfur bacteria. *Biotechnol. Bioeng.*, **2002**, *77*, 734–751.

[23] Follstad, B. D.; Balcarcel, R. R.; Stephanopoulos, G.; Wang, D. I. Metabolic flux analysis of hybridoma continuous culture steady state multiplicity. *Biotechnol Bioeng*, **1999**, *63*(6), 675–83.

[24] Europa, A. F.; Gambhir, A.; Fu, P. C.; Hu, W. S. Multiple steady states with distinct cellular metabolism in continuous culture of mammalian cells. *Biotechnol Bioeng*, **2000**, *67*(1), 25–34.

[25] Cruz, H. J.; Moreira, J. L.; Carrondo, M. J. Metabolic shifts by nutrient manipulation in continuous cultures of BHK cells. *Biotechnol Bioeng*, **1999**, *66*(2), 104–13.

[26] Zhou, W. C.; Rehm, J.; Hu, W. S. High viable cell concentration fed-batch cultures of hybridoma cells through on-line nutrient feeding. *Biotechnol. Bioeng.*, **1995**, *46*, 579–587.

[27] Zielke, H.; Ozand, P.; Tildon, J.; Sevdalian, D.; Cornblath, M. Reciprocal regulation of glucose and glutamine utilization by cultured human diploid fibroblasts. *J. Cell. Physiol.*, **1978**, *95*, 41–48.

[28] Zielke, H.; Zielke, C.; Ozand, P. Glutamine: A major energy source for cultured mammalian cells. *Fed. Proc.*, **1984**, *43*, 121–125.

[29] Hassel, T.; Gleave, S.; Butler, M. Growth inhibition in animall cell culture: The effect of lactate and ammonia. *Appl. Biochem. Biotechnol.*, **1991**, *30*, 29–41.

[30] Ozturk, S.; Thrift, J.; Blackie, J.; Naveh, D. Real-time monitoring and control of glucose and lactate concentrations in a mammalian cell perfusion reactor. *Biotechnol. Bioeng.*, **1997**, *53*, 372–378.

[31] Rhiel, M.; Cohen, M.; Murhammer, D.; Arnold, M. Nondestructive near-infrared spectroscopic measurement of multiple analytes in undiluted samples of serum-based cell culture media. *Biotechnol. Bioeng.*, **2002**, *77*, 73–82.

[32] Rhiel, M.; Ducommun, P.; Bolzonella, I.; Marison, I.; von Stockar, U. Real-time in situ monitoring of freely suspended and immobilized cell cultures based on mid-infrared spectroscopic measurements. *Biotechnol. Bioeng.*, **2002**, *77*, 174–185.

[33] Schmidt, K.; Marx, A.; de Graaf, A. A.; Wiechert, W.; Sahm, H.; Nielsen, J.; Villadsen, J. 13C tracer experiments and metabolite balancing for metabolic flux analysis: Comparing two approaches. *Biotechnol. Bioeng.*, **1998**, *58*, 254–257.

[34] Bonarius, H.; Houtman, J.; de Gooijer, C.; Tramper, J.; Schmid, G. Activity of glutamate dehydrogenase is increased in ammonia-stressed hybridoma cells. *Biotechnol Bioeng*, **1998**, *57*(4), 447–453.

[35] Bonarius, H.; Schmid, G.; Tramper, J. Flux analysis of underdetermined metabolic networks: the quest for the missing constraints. *Trends Biotechnol.*, **1997**, *15*, 308–314.

Part V

Conclusions and Future Work

Chapter 10

Conclusions

The study of cell physiology and metabolism is the unifying theme in this work. Metabolic flux analysis was used to quantify cell metabolism and both the metabolite balancing and isotope tracer methods were evaluated (Chapters 2, 3, 7 – 9). This approach was used to study metabolism at high and low bioreactor pCO_2 concentrations and significant differences were observed (Chapter 4). Information on OUR and CER was necessary for metabolic flux analysis and methods for estimating them in perfusion cultivations were developed (Chapter 5). For reliable application of metabolic flux analysis to batch and fed-batch cultures, robust specific rates are necessary since these comprise the input data set. Current methods of specific rate estimation have multiple limitations and the logistic modeling framework was proposed to address these limitations (Chapter 6).

Despite significant advances in the mammalian cell cultivation techniques, several challenges remain and some of them were addressed in this investigation. The adverse effects of high bioreactor pCO_2 on cell growth and protein productivity are well documented but controlling bioreactor pCO_2 closer to physiological levels is a challenge, especially in high-density perfusion cultures. Examination of bioreactor pCO_2 sources indicated that cellular CO_2 production accounted for ~25% of bioreactor pCO_2 with the remaining due to $NaHCO_3$ addition to neutralize the lactate produced by the cells. A simple pCO_2 reduction strategy based on $NaHCO_3$ elimination was investigated and consistent pCO_2 reduction on the order of 70% was achieved in multiple experiments. This was accompanied by 68 – 123% increase in growth rate and 58 – 92% increase in protein productivity. These results were reproduced at the manufacturing-scale confirming the robustness of this simple pCO_2 reduction approach. In addition, this method of pCO_2 reduction is general and can be readily applied to fed-batch cultivations.

Mass balance expressions for oxygen and carbon dioxide in a perfusion bioreactor were

developed enabling estimation of cell-specific oxygen uptake (OUR) and carbon dioxide evolution rates (CER). Speciation of CO_2 into H_2CO_3* and HCO_3^- was taken into account and the equilibrium constants were corrected for temperature and ionic strength effects to ensure accurate CER estimation. Concentrations of oxygen and carbon dioxide in the exit gas stream were continuously monitored allowing real-time OUR and CER estimation. In addition to providing useful information on cell physiology, this data enabled quasi-real-time estimation of metabolic fluxes providing additional information on the cell physiological state.

Recognizing the need for rapid and reliable modeling of data from early stage process development experiments, logistic equations were used to fit data from batch and fed-batch experiments. Since the logistic equations were analytically differentiable, derivatives and hence specific rates were readily computed. In contrast to other modeling approaches such as polynomial fitting and discrete derivative evaluation, logistic specific rates were smooth and logically constrained to the expected trends. The superiority of logistic modeling over current methods was demonstrated by examining 55 batch and fed-batch data sets spanning 3 cell lines and 0.1 – 300 L reactor volumes. This robustness coupled with simplicity of application could make logistic modeling the method of choice for quantitatively characterizing batch and fed-batch data.

Metabolic flux analysis was used to quantify cell physiology and metabolism in perfusion bioreactors. Metabolic models were developed for BHK and CHO cells and fluxes were estimated in quasi-real-time using a combination of on-line and off-line measurements by the metabolite balancing method. Reliability of the metabolic flux estimates by the metabolite balancing method was ensured by comparison with data from isotope tracer studies. Routine monitoring of laboratory and manufacturing-scale bioreactors was possible using this method and this was also used to analyze transient changes in cell metabolism when bioreactor pH and DO were varied. This method of rapid flux analysis can also be used to analyze the impact of excursions in licensed manufacturing processes thereby helping product disposition. Discarding excursion-associated product is expensive and the impact of excursions are typically evaluated from a protein quality standpoint. Metabolic flux data will quantify the excursion impact on cell physiology and this information can augment protein quality data providing a more comprehensive view of the excursion impact.

10.1 Extensions of This Study

10.1.1 MFA Application to a Licensed Manufacturing Process

Metabolic fluxes would be most useful if they could be linked to protein productivity and quality as they can serve as surrogates in quasi real-time. This is a challenging proposition and is further complicated by the low recombinant protein concentration in mammalian cell culture, often less than 0.1% of the total protein. Moreover, the pathways of central carbon metabolism (whose fluxes are estimated by metabolic flux analysis) may not necessarily be coupled with those of protein glycosylation which makes it difficult to establish direct flux - product quality correlations. However, if correlations between flux and product quality data are established from a large number of experiments, metabolic fluxes can be used to empirically predict product quality significantly enhancing the impact of metabolic flux analysis. Preliminary data (Appendix J) has indicated no adverse impact on protein quality from pH and DO changes and more detailed carbohydrate and associated analyses could be pursued to search for where flux analysis might be consistently correlated with quality changes. This would enable MFA to have a greater impact on mammalian cell process monitoring and control.

10.1.2 Metabolite Profiling

Metabolic flux analysis provides information on intracellular rates but not on the concentration of intracellular metabolites. Information on intracellular metabolite concentrations enables improved characterization of the metabolic phenotype and can provide insight into the thermodynamic feasibility of reactions in the biochemical network (Appendix I). This approach would be particularly useful if some intracellular metabolites could serve as markers for protein productivity and quality attributes such as glycosylation. Using a combination of GC-MS and LC-MS analysis several hundred intracellular metabolites can be identified in a high throughput fashion [1–5]. These techniques are new and can be expected to improve substantially in the near future resulting in reliable measurement of additional metabolites. Upon archival of such metabolomic data, statistical techniques can be used to classify experiments based on intracellular metabolite concentrations. Ongoing experiments can be compared with these classifications to see if the experiment is in the desirable cluster and appropriate corrective action can be taken if necessary.

10.1.3 GS-MS for Isotope Tracer Studies

Cell metabolism was characterized by a combination of metabolite balancing and isotope tracer analysis by NMR in this study. Albeit powerful, NMR analysis requires a substantial amount of labeled glucose in the cultivation medium making it expensive and subsequent sample analysis and flux computation are complicated. Some of these difficulties can be overcome by using GC-MS since the amount of labeled substrate in the medium can be reduced and sample analysis is easier [6–13]. It must however be recognized that GC-MS and NMR can be complementary techniques in some instances and the information from GC-MS analysis could be slightly different than that from NMR. Recent developments in the application of GC-MS for metabolic flux analysis coupled with lower GC-MS equipment costs should make this method more attractive for metabolic flux analysis.

10.1.4 Flux Analysis from Transient Data

Most isotope tracer experiments to date are based on the assumption that cells are at isotopic steady state. Thus, experiments with labeled substrate must be conducted for several days before a sample can be drawn for analysis, greatly increasing experimental costs. If transient data following the introduction of an isotope tracer could be used for flux analysis, it would greatly reduce the requirement of labeled substrate. Moreover, metabolic shifts in any experiment can be investigated by injecting a pulse of labeled substrate and analyzing a sample shortly thereafter. This approach, however, presents modeling and computational challenges because fractional enrichment of the isotope isomers is time dependent and must be described by a system of nonlinear differential equations [14]. It is likely that several thousand differential equations and hundreds of parameters will be necessary to describe a typical mammalian cell bioreaction network. Moreover, this system is likely to be stiff and very sensitive to parameter values which would make their robust estimation very difficult. This problem is perhaps best addressed by first considering a very simple network for which analytical solutions of the differential equations are available. This simplifies parameter estimation and can help establish the validity of flux estimation from transient data. The model can subsequently be extended to include additional reactions such that numerical solutions of the differential equations will become necessary. Extensive statistical testing will be needed to prove that the resulting flux estimates are reliable and representative of cell metabolism.

10.1.5 Low CSPR Cultivation

High throughput perfusion cultivation is especially attractive for unstable molecules because their residence time at cultivation temperature can be reduced by increasing the perfusion rate. While this is a major advantage, this mode of operation will not compare favorably with a fed-batch process for stable molecules because of low protein concentration in the harvest. If stable proteins are produced by cells with non-growth associated kinetics, substantial reduction of the perfusion rate is possible without compromising cell viability and protein productivity and quality. Operation at these low perfusion rates combines the advantages of perfusion and fed-batch processes resulting in stable high product concentration over many months of operation. The conceptual framework of low perfusion rate cultivation and comparison with fed-batch cultivation has been developed and demonstrated for hybridoma cells producing antibodies against tumor necrosis factor [15]. Application to other stable molecules will further illustrate the advantages of low perfusion rate cultivation.

Bibliography

[1] Fiehn, O.; Kopka, J.; Dormann, P.; Altmann, T.; Trethewey, R.; Willmitzer, L. Metabolite profiling for plant functional genomics. *Nat. Biotechnol.*, **2000**, *18*, 1157–1168.

[2] Kopka, J.; Fernie, A.; Weckwerth, W.; Gibson, Y.; Stitt, M. Metabolic Profiling in plant biology: platforms and destinations. *Genome Biology*, **2004**, *5*, 104–115.

[3] Roessner, U.; Wagner, C.; Kopka, J.; Trethewey, R.; Willmitzer, L. Simultaneous analysis of metabolites in potato tuber by gas chromatography-mass spectrometry. *Plant J.*, **2000**, *23*, 131–142.

[4] Villas-Boas, S.; Delicado, D.; Akesson, M.; Nielsen, J. Simultaneous analysis of amino and nonamino organic acids as methyl chloroformate derivatives using gas chromatography-mass spectrometry. *Anal. Biochem.*, **2003**, *322*, 134–138.

[5] Villas-Boas, S.; Moxley, J.; Akesson, M.; Stephanopoulos, G.; Nielsen, J. High-throughput metabolic state analysis: the missing link in integrated functional genomics of yeasts. *Biochem. J.*, **2005**, *388*, 669–677.

[6] Arauzo-Bravo, M.; Shimizu, K. An improved method for statistical analysis of metabolic flux analysis using isotopomer mapping matrices with analytical expressions. *J. Biotechnol.*, **2003**, *105*, 117–133.

[7] Fischer, E.; Sauer, U. Metabolic flux profiling of Escherichia coli mutants in central carbon metabolism using GC-MS. *Eur J Biochem*, **2003**, *270*(5), 880–891.

[8] Klapa, M. I.; Aon, J.-C.; Stephanopoulos, G. Ion-trap mass spectrometry used in combination with gas chromatography for high-resolution metabolic flux determination. *BioTechniques*, **2003**, *34*, 832–849.

[9] Park, S.; Shaw-Reid, C. A.; Sinskey, A. J.; Stephanopoulos, G. Elucidation of anaplerotic pathways in Corynebacterium glutamicum via 13C-NMR spectroscopy and GC-MS. *Appl. Microbiol. Biotechnol.*, **1997**, *47*, 430–440.

[10] Park, S. M.; Klapa, M. I.; Sinskey, A. J.; Stephanopoulos, G. Metabolite and isotopomer balancing in the analysis of metabolic cycles: II. Applications. *Biotechnol Bioeng*, **1999**, *62*(4), 392–401.

[11] van Dien, S.; Strovas, T.; Lidstrom, M. Quantification of central metabolic fluxes in the facultative methylotrop Methylobacterium extorquens AM1 using 13C-label tracing and mass spectrometry. *Biotechnol. Bioeng.*, **2003**, *84*, 45–55.

[12] Wittmann, C.; Heinzle, E. Application of MALDI-TOF MS to lysine-producing Corynebacterium glutamicum: A novel approach for metabolic flux analysis. *Eur J Biochem*, **2001**, *268*(8), 2441–2455.

[13] Zhao, J.; Shimizu, K. Metabolic flux analysis of Escherichia coli K12 grown on 13C-lebeled acetate and glucose using GC-MS and powerful flux calculation method. *J. Biotechnol.*, **2003**, *101*, 101–117.

[14] Nöh, K.; Wiechert, W. Experimental design principles for isotopically instationary 13C labeling experiments. *Biotechnol. Bioeng.*, **2006**, *94*, 234–251.

[15] Konstantinov, K.; Goudar, C.; Ng, M.; Meneses, R.; Thrift, J.; Chuppa, S.; Matanguihan, R.; Michaels, J.; Naveh, D. The "Push-to-Low" approach for optimization of high-density perfusion cultures of animal cells. *Adv Biochem Eng Biotechnol*, **2006**, *101*, In Press.

Appendix A

Computer Program for Flux Estimation

The steps involved in flux estimation by the metabolite balancing and isotope tracer methods have been presented in Chapter 3. The isotope tracer method requires sophisticated computational strategies while those for the metabolite balancing method are simple. The following is a simple MATLAB® program that computes fluxes in the simplified bioreaction network of Chapter 3. The program also performs redundancy and consistency analysis from which improved flux estimates can be obtained through modified (improved) specific rate data.

mfa_balancing.m (Flux Estimation in Overdetermined systems)

```
% mfa_balancing.m Computes Metabolic Fluxes for Mammalian Cells
% Reaction Network is from Balcarcel and Clark % (B.Prog.,19, 98-108 2003)
% Measurements include glucose, lactate, O2, and CO2

clear all

% 1. MATRIX DEFINITIONS
% Stoichiometirc Matrix, GT
GT = [-1 0 0 0 -1 0 0 0 0 0; 0 -1 0 0 0 1 0 0 0 0;...
    0 0 -1 0 0 0 3 0 0 0; 0 0 0 -1 0 0 0 -0.5 -0.5 0;...
    0 0 0 0 0 2 -1 -1 0 0 0; 0 0 0 0 0 2 -1 4 -1 0 0;...
    0 0 0 0 0 0 0 1 0 -1 0; 0 0 0 0 0 2 0 1 2.5 1.5 -1];

% rank and condition number of GT
```

```
rankGT = rank(GT); condGT = cond(GT);

% Rate Vector, v
v = [-1.4788 1.7293 5.8333 -5.1369 0 0 0 0 0 0]';

%2. FLUX ESTIMATION
% Separation of G into Gm and Gc
GmT = GT(:,1:4); GcT = GT(:,5:10);

% Separation of v into vm and vc
vm = v(1:4,1); vc = v(5:10,1);

% Unknown Rate Vector (vc) Estimation
vc = -pinv(GcT)*GmT*vm;

% 3. ERROR DIAGNOSIS
% Redundancy Matrix
R  = GmT - GcT*pinv(GcT)*GmT; rankR = rank(R);

% Reduced redundancy matric
Rr = [0.8099    0.4049   -0.2250   -0.3599
   -0.3679   -0.1839   -0.6745   -0.6131];

% Delta, e and F estimation
measurement_error = 0.1*ones(1,4)';
delta     = vm.*measurement_error;
e1        = Rr*vm;
delta1    = delta*delta';
F         = zeros(length(vm),length(vm));
for i=1:length(vm) F(i,i) = delta1(i,i); end

% Var-Cov Matrix of residuals and h estimation
tsi = Rr*F*Rr'
h   = e1'*pinv(tsi)*e1

% Improved vm and vc estimates
```

```
vm_new = (eye(4) - F*Rr'*inv(tsi)*Rr)*vm
vc_new = -pinv(GcT)*GmT*vm_new
```

Appendix B

Solution Chemistry in a Perfusion Bioreactor

Accurate quantitative description of the solution chemistry in a perfusion bioreactor is essential to meaningfully interpret pCO_2 reduction due to medium and base changes. Carbon dioxide and and lactic acid are products of cellular metabolism that reduce bioreactor pH. Base addition (usually NaOH, $NaHCO_3$ or Na_2CO_3) becomes necessary to maintain bioreactor pH at the predefined setpoint (typically close to neutral). The complex nature of the chemistry of CO_2 dissociation must be modeled to close the CO_2 mass balance in a perfusion reactor. Since carbon dioxide evolution rate and RQ calculations are performed using the CO_2 mass balance expression, CO_2 dynamics in the perfusion system must be accurately accounted for. While carbon dioxide dissociation dynamics play a central role, the roles of other acids and bases such as lactic acid and ammonia are also important and will be examined in this section.

B.1 Computer Porgrams for Solution Chemistry Calculations

Perfusion bioreactors are operated at temperatures close to 37° C with medium ionic strengths in excess of 0.1 M due to the presence of salts such as NaCl. This complicates calculations because equilibrium constants must be corrected for temperature and ionic strength (most literature data are at 25° C and zero ionic strength). Computer programs were written to perfom these calculation and are described below.

B.1.1 Temperature Correction for Equilibrium Constants

Most equilibrium constants available in databases and textbooks are for standard temperature (25° C) and these are not directly applicable to mammalian cell cultivations that are typically around 37° C. The Van't Hoff equation describes the temperature dependence of the equilibrium constant

$$K = K_{ref} \exp\left\{\left(\frac{\Delta H^0}{R}\right)\left(\frac{1}{T_{ref}} - \frac{1}{T}\right)\right\} \tag{B.1}$$

where K is the unknown equilibrium constant at temperature T, K_{ref} the known equilibrium at the reference temperature, T_{ref} (usually 25° C), ΔH^0 the standard enthalpy change for the reaction and R the gas constant. All other factors affecting the equilibrium constant are assumed to be constant at the two temperatures. For the conversion of $CO_{2(g)}$ to H_2CO_3*, the K_{ref} and T_{ref} values are $10^{-1.47}$ and 298 K, respectively and R is 1.98 x 10^{-3} kcal/(mole-K). The standard enthalpy change, ΔH^0, can be estimated as

$$\Delta H^0 = \left(\sum v_i \overline{H}_i^0\right)_{\text{products}} - \left(\sum v_i \overline{H}_i^0\right)_{\text{reactants}} \tag{B.2}$$

where v_i is the stoichiometric coefficient and $\overline{H}_i^0$ the enthalpy of formation of species i at 25 °C and 1 atm pressure. Substituting -167, -94.05 and -68.32 kcal/mole for the $\overline{H}_i^0$ values of H_2CO_3*, $CO_{2(g)}$ and H_2O, respectively, Eq.(B.2) becomes

$$\Delta H^0 = (-167)_{\text{products}} - (-94.05 - 68.32)_{\text{reactants}} = 4.63 \text{ kcal/mole} \tag{B.3}$$

Substituting for ΔH^0, R, K_{ref} and T_{ref} in Eq.(B.1) results in $K_g = 10^{-1.60}$

For the dissociation of H_2CO_3* to HCO_3^-, the K_{ref} and T_{ref} values are $10^{-6.35}$ and 298 K, respectively and R is 1.98 x 10^{-3} kcal/(mole-K). The standard enthalpy change, ΔH^0, can be estimated as

$$\Delta H^0 = (-165.18 + 0)_{\text{products}} - (-167)_{\text{reactants}} = 1.82 \text{ kcal/mole} \tag{B.4}$$

Substituting for ΔH^0, R, K_{ref} and T_{ref} in Eq.(B.1) results in $K = 10^{-6.30}$.

$$K = 10^{-6.35} \exp\left\{\left(\frac{1.82}{1.98 \text{ x } 10^{-3}}\right)\left(\frac{1}{298} - \frac{1}{310}\right)\right\} = 10^{-6.30} \tag{B.5}$$

For the dissociation of HCO_3^- to CO_3^{2-}, ΔH^0, can be estimated as

$$\Delta H^0 = (-167 + 0)_{\text{products}} - (-161.63)_{\text{reactants}} = -5.37 \text{ kcal/mole} \tag{B.6}$$

which upon substitution into Eq.(B.1) results in $K = 10^{-10.48}$. The temperature corrected (for 37 °C) equilibrium constants, K_g, K_1 and K_2 are thus $10^{-1.60}$, $10^{-6.30}$ and $10^{-10.48}$, respectively. The program vanthoff.m computes K from known values of K_{ref}, ΔH^0 and T_{ref} using Eq.(B.1).

Temperature Correction for Equilibrium Constants (vanthoff.m)

```
% USAGE: Type "vanthoff" at the Matlab command prompt
%
% PURPOSE:
% Computes equilibrium constant at a desired temperature
% ln(k/kref) = dHO/R [1/Tref - 1/T]      OR
% k = kref exp {dHO/R [1/Tref - 1/T]}
%
% INPUTS
% 1. kref: Equilibrium constant at the reference temperature
% 2. Tref: Reference temperature (C)
% 3. T   : Temperature at which equilibrium constant is desired (C)
% 4. dHO : Enthalpy change (KJ/mole)

% OUTPUTS
% 1. k:    Equilibrium constant at temperature T

% % Last Modified 07/10/2004

% INPUT INFORMATION
prompt1  = {'Reference (known) value of the equilibrium constant',...
            'Reference Temperature, (C)',...
            'Temperature at which equilibrium constant is desired, (C)',...
            'Change in Enthalpy, (KJ/mole)'};

title1   = 'Input For the Vant Hoff Equation';
lineNo1  = 1;
input1   = inputdlg(prompt1,title1,lineNo1);
```

```
kref     = str2num(input1{1,1});
trefc    = str2num(input1{2,1});
tnewc    = str2num(input1{3,1});
dh0      = str2num(input1{4,1});

% CALCULATIONS
k=fvanthoff(kref,trefc,tnewc,dh0);

% RESULT DISPLAY
disp('The new value of the equilibrium constant is')
disp(k)
```

B.1.2 Ionic Strength Calculation

The ionic strength of a solution can be calculated as

$$I = -\frac{1}{2}\sum C_i z_i^2 \tag{B.7}$$

where C_i and z_i are charge and concentration of species i, respectively. Ideally all species in the medium must be accounted for to get a representative ionic strength estimate. While this can be cumbersome for a complex medium formulation, 3 – 5 species with the highest concentration are responsible for the bulk of the ionic strength and using them in Eq.(B.7) should be adequate for most practical purposes.

Computing Ionic Strength of a Solution (ionicstrength.m)

```
% USAGE: Type "ionicstrength" at the Matlab command prompt
% PURPOSE:
% Computes Ionic Strength of a system
%% INPUTS
%
% 1. The no of species in the system
% 2. Concentration and Charge of each species
%
% OUTPUTS
% 1. Ionic Strength
```

```
% % Last Modified 03/14/2004

prompt1  = ('Please enter the number of species');
title1   = 'Input For Ionic strength calculations';
lineNo1  = 1;
input1   = inputdlg(prompt1,title1,lineNo1);

nospecies   = str2num(input1{1,1});
inpstr = input1{1,1};

conc = input('Please enter species concentrations. Eg [0.01;0.01]: ');
charge = input('Please enter species charges. Eg [1;2]: ');

if length(conc) ~= nospecies
   disp('concentration values not consistent with the number of species')
   elseif length(charge) ~= nospecies
   disp('Charge values not consistent with the number of species')
else

istrength = fionicstrength(conc,charge);
answer=['The Ionic Strength is ' num2str(istrength,4)];
disp(answer)

end
```

B.1.3 Activity Coefficient Calculation

Species activities are a function of solution ionic strength with unity activity coefficients at zero ionic strength. Thus species concentration and activity can be assumed to be equivalent in solutions with very low ionic strength. Ionic strengths of typical cell culture media are usually in exces of 0.1 M due to the presence of salts (especially NaCl) such that species activity coefficients are substantially different than 1. Activity coefficients can be calculated using the Debye-Huckel, extended Debye-Huckel, Guntelberg and Davies equations depending upon the solution ionic strength. The driver program is actcoeff.m where the user provides input data and chooses the appropriate activity coefficient equation. Activity coefficients are estimated in separate function files for each correlation. Only the

Davies equation is presented below as it is adequate to describe most mammalian cell culture systems.

Driver Program for Computing Activity Coefficients (actcoeff.m)

```
% USAGE: Type "actcoeff" at the Matlab command prompt
%
% PURPOSE:
% Computes Activity Coefficients based on Debye-Huckel,
% Extended Debye-Huckel, Guntelberg, and Davies Equations.
%
% INPUTS
% A combination of
% 1. Ionic Strength
% 2. Charge of the ion
% 3. Temperature
% 4. Hydrated Ion size
%
% OUTPUTS
% 1. Activity Coefficient

% % Last Modified 07/11/2004
%%%%%%%%%%%%%%%%%%%%%%%%%%%%%%%%%%%%%%%%%%%%%%%%%%%%%%%%%%%%%%%%%%%%%%%%%%%

% Information on the applicability of the various Correlations
select1=menu('Choose an Equation to Calculate Activity Coefficients',...
             'Debye-Huckel Equation: (I < 0.01 M)',...
             'Extended Debye-Huckel Equation: (I < 0.1 M)',...
             'Guntelberg Equation: (I < 0.1 M)',...
             'Davies Equation: (I < 0.5 M)',...
             'Activity Coefficients for a Neutral Species: (I < 5 M)');

%%%%%%%%%%%%%%%%%%%%%%%%%%%%%%%%%%%%%%%%%%%%%%%%%%%%%%%%%%%%%%%%%%%%%%%%%%%
% 1. Debye-Huckel Equation

if select1==1
```

```
   prompt1  = {'Ionic Strength','Charge of the Ion','Temperature, (C)'};
   title1   = 'Input For the Debye-Huckel Equation';
   lineNo1  = 1;
   input1   = inputdlg(prompt1,title1,lineNo1);

   ionstr   = str2num(input1{1,1});
   charge   = str2num(input1{2,1});
   temp1    = str2num(input1{3,1});

   if ionstr > 0.01;
      disp('WARNING: Ionic Strength > 0.01 M')
      disp('Activity coefficients will not be accurate')
   end

   activity=fdebyehuckel(ionstr,charge,temp1);
   answer=['The Activity Coefficient is ' num2str(activity,4)];
   disp(answer)
%%%%%%%%%%%%%%%%%%%%%%%%%%%%%%%%%%%%%%%%%%%%%%%%%%%%%%%%%%%%%%%%%%%%%%%%%%%

%%%%%%%%%%%%%%%%%%%%%%%%%%%%%%%%%%%%%%%%%%%%%%%%%%%%%%%%%%%%%%%%%%%%%%%%%%%
% 2. Extended Debye-Huckel Equation

elseif select1==2

   prompt1  = {'Ionic Strength','Charge of the Ion',...
       'Hydrated Ion Size (Angstroms)','Temperature, (C)'};
   title1   = 'Input For the Extended Debye-Huckel Equation';
   lineNo1  = 1;
   input1   = inputdlg(prompt1,title1,lineNo1);

   ionstr   = str2num(input1{1,1});
   charge   = str2num(input1{2,1});
   a        = str2num(input1{3,1});
   temp1    = str2num(input1{4,1});

   if ionstr > 0.1;
```

```
      disp('WARNING: Ionic Strength > 0.1 M')
      disp('Activity coefficients will not be accurate')
   end

   activity=fextdebyehuckel(ionstr,charge,a,temp1);
   answer=['The Activity Coefficient is ' num2str(activity,4)];
   disp(answer)
%%%%%%%%%%%%%%%%%%%%%%%%%%%%%%%%%%%%%%%%%%%%%%%%%%%%%%%%%%%%%%%%%%%%%%%%%%%

%%%%%%%%%%%%%%%%%%%%%%%%%%%%%%%%%%%%%%%%%%%%%%%%%%%%%%%%%%%%%%%%%%%%%%%%%%%
% 3. Guntelberg Equation

elseif select1==3
   prompt1  = {'Ionic Strength','Charge of the Ion','Temperature, (C)'};
   title1   = 'Input For the Guntelberg Equation';
   lineNo1  = 1;
   input1   = inputdlg(prompt1,title1,lineNo1);

   ionstr   = str2num(input1{1,1});
   charge   = str2num(input1{2,1});
   temp1    = str2num(input1{3,1});

   if ionstr > 0.1;
      disp('WARNING: Ionic Strength > 0.1 M')
      disp('Activity coefficients will not be accurate')
   end

   activity=fguntelberg(ionstr,charge,temp1);
   answer=['The Activity Coefficient is ' num2str(activity,4)];
   disp(answer)
%%%%%%%%%%%%%%%%%%%%%%%%%%%%%%%%%%%%%%%%%%%%%%%%%%%%%%%%%%%%%%%%%%%%%%%%%%%

%%%%%%%%%%%%%%%%%%%%%%%%%%%%%%%%%%%%%%%%%%%%%%%%%%%%%%%%%%%%%%%%%%%%%%%%%%%
% 4. Davies Equation

elseif select1==4
```

```
   prompt1  = {'Ionic Strength','Charge of the Ion','Temperature, (C)'};
   title1   = 'Input For the Davies Equation';
   lineNo1  = 1;
   input1   = inputdlg(prompt1,title1,lineNo1);

   ionstr   = str2num(input1{1,1});
   charge   = str2num(input1{2,1});
   temp1    = str2num(input1{3,1});

   if ionstr > 0.5;
      disp('WARNING: Ionic Strength > 0.5 M')
      disp('Activity coefficients will not be accurate')
   end

      activity=fdavies(ionstr,charge,temp1);
   answer=['The Activity Coefficient is ' num2str(activity,4)];
   disp(answer)
%%%%%%%%%%%%%%%%%%%%%%%%%%%%%%%%%%%%%%%%%%%%%%%%%%%%%%%%%%%%%%%%%%%%%%%%%%%%

%%%%%%%%%%%%%%%%%%%%%%%%%%%%%%%%%%%%%%%%%%%%%%%%%%%%%%%%%%%%%%%%%%%%%%%%%%%%
% 5. Neutral Species

elseif select1==5
   prompt1  = {'Ionic Strength'};
   title1   = 'Input For Computing Activity Coefficients for a Neutral...
   Species';
   lineNo1  = 1;
   input1   = inputdlg(prompt1,title1,lineNo1);

   ionstr   = str2num(input1{1,1});

   if ionstr > 5.0;
      disp('WARNING: Ionic Strength > 5.0 M')
      disp('Activity coefficients will not be accurate')
   end
```

```
   activity=fneutral(ionstr);
   answer=['The Activity Coefficient is ' num2str(activity,4)];
   disp(answer)
%%%%%%%%%%%%%%%%%%%%%%%%%%%%%%%%%%%%%%%%%%%%%%%%%%%%%%%%%%%%%%%%%%%%%%%%%%%%

end
```

Function File for the Davies Equation (fdavies.m)

```
function y = fdavies(ionstr,charge,temp1)
%
% FDAVIES ia a function file that that computes the activity coefficient
% using the Davies equation
%
% fdavies(ionstr,charge) computes activity coefficients at 25 C
% fdavies(ionstr,charge,temp1) computes activity coefficients at temp1 C

% Last Modified 03/12/2004

if nargin == 2
   temp2 = 273.15;
elseif nargin == 3
   temp2=temp1+273.15;
else
   disp('Inappropriate number of input arguements')
end

 temp2    = temp1+273.15;
 A        = 1.825.*10.^6.*(78.3808.*temp2).^(-1.5);
 activity = 10.^(-A.*charge.^2.*((ionstr.^0.5./(1 + ionstr.^0.5))...
-0.2.*ionstr));

y=activity;
```

Function File for Neutral Species (fneutral.m)

```
function y = fneutral(ionstr)
%
```

```
% FNEUTRAL ia a function file that that computes the activity coefficient
% of a neutral species
%
% fneutral(ionstr) returns the activity coefficient of a neutral species
% at an ionic strength of ionstr

% Start 06/23/1999; Last Modified 03/12/2004

activity=10.^(0.1.*ionstr);

y=activity;
```

B.1.4 Ionization Fractions

Ionization fractions provide information on the relative amounts of various species at any given pH[1]. For instance, CO_2 produced by the cells exists in solution as H_2CO_3*, HCO_3^- and CO_3^{2-} with their relative amounts dependent on solution pH. At a temperature of 37° C and a pH of 6.8 (typical cultivation condtions), H_2CO_3*, HCO_3^- and CO_3^{2-} make up 15.69, 84.26 and 5 x 10^{-4}% of the total CO_2 in solution. This composition changes drastically with pH variation such that H_2CO_3* is the dominant species under acidic conditions and CO_3^{2-} makes up the majority of the solution CO_2 under alkaline conditions. Estimating ionization fractions is cumbersome, especially when correction for temperature and ionic strength need to be made, and the following programs perform these calculations for monoprotic, diprotic and triprotic systems.

Driver Program for Ionization Fraction Estimation (ionfrac.m)

```
% USAGE: Type "ionfrac" at the Matlab command prompt
%
% PURPOSE:
% Computes ionization fractions for monoprotic, diprotic and triprotic acids
% under non-standard conditions of temperature and ionic strength
%
% INPUTS
% 1. pH:   System pH
% 3. pKa:  System pKa value(s)
%
```

[1]Stumm, W., and Morgan, J. J. (1996). Aquatic Chemistry, John Wiley and Sons, New York.

```
% OUTPUTS
% 1. a0,a1:        Monoprotic system ionization fractions
% 2. a0,a1,a2:     Diprotic system ionization fractions
% 3. a0,a1,a2,a3:  Triprotic system ionization fractions

% Last Modified: 7/11/2004

a=menu('Choose an acid','Monoprotic','Diprotic','Triprotic');

%%%%%%%%%%%%%%%%%%%%%%%%%%%%%%%%%%%%%%%%%%%%%%%%%%%%%%%%%%%%%%%%%%%%%%%%
% MONOPROTIC ACID

if a==1

   prompt1  = {'System pH',...
               'System pKa at 25 C',...
               'New Temperature (C)',...
               'Enthalpy Change (KJ/mole)',...
               'Ionic Strength (M)'};

title1   = 'Input For Monoprotic System Ionization Fraction Calculation';
lineNo1  = 1;
input1   = inputdlg(prompt1,title1,lineNo1);
ph       = str2num(input1{1,1});
pka1std  = str2num(input1{2,1});
tnew     = str2num(input1{3,1});
dh01     = str2num(input1{4,1});
ionstr   = str2num(input1{5,1});

pka1     = fpka1itoc(pka1std,tnew,ionstr,dh01);

   A=fionfrac(ph,pka1);
   disp('The ionization fractions [a0, a1] for the monoprotic system...
   are as follows')
   disp(A)
%%%%%%%%%%%%%%%%%%%%%%%%%%%%%%%%%%%%%%%%%%%%%%%%%%%%%%%%%%%%%%%%%%%%%%%%
```

```
%%%%%%%%%%%%%%%%%%%%%%%%%%%%%%%%%%%%%%%%%%%%%%%%%%%%%%%%%%%%%%%%%%%%%%%%%%%%
% DIPROTIC ACID

elseif a==2

   prompt1  = {'System pH',...
               'Ionic Strength (M)',...
               'System pKa1 at 25 C',...
               'System pKa2 at 25 C',...
               'New Temperature (C)',...
               'Enthalpy Change for first reaction (KJ/mole)',...
               'Enthalpy Change for second reaction (KJ/mole)'};

title1   = 'Input For Diprotic System Ionization Fraction Calculation';
lineNo1  = 1;
input1   = inputdlg(prompt1,title1,lineNo1);

ph       = str2num(input1{1,1});
ionstr   = str2num(input1{2,1});
pka1std  = str2num(input1{3,1});
pka2std  = str2num(input1{4,1});
tnew     = str2num(input1{5,1});
dh01     = str2num(input1{6,1});
dh02     = str2num(input1{7,1});

pka1     = fpka1itoc(pka1std,tnew,ionstr,dh01);
pka2     = fpka2itoc(pka2std,tnew,ionstr,dh02);

   A=fionfrac(ph,pka1,pka2);
   disp('The ionization fractions [a0, a1, a2] for the diprotic system...
   are as follows')
   disp(A)
%%%%%%%%%%%%%%%%%%%%%%%%%%%%%%%%%%%%%%%%%%%%%%%%%%%%%%%%%%%%%%%%%%%%%%%%%%%%

%%%%%%%%%%%%%%%%%%%%%%%%%%%%%%%%%%%%%%%%%%%%%%%%%%%%%%%%%%%%%%%%%%%%%%%%%%%%
```

```
% TRIPROTIC ACID

elseif a==3

     prompt1  = {'System pH',...
                 'Ionic Strength (M)',...
                 'System pKa1 at 25 C',...
                 'System pKa2 at 25 C',...
                 'System pKa3 at 25 C',...
                 'New Temperature (C)',...
                 'Enthalpy Change for FIRST reaction (KJ/mole)',...
                 'Enthalpy Change for SECOND reaction (KJ/mole)',...
                 'Enthalpy Change for THIRD reaction (KJ/mole)'};

title1   = 'Input For Diprotic System Ionization Fraction Calculation';
lineNo1  = 1;
input1   = inputdlg(prompt1,title1,lineNo1);

ph       = str2num(input1{1,1});
ionstr   = str2num(input1{2,1});
pka1std  = str2num(input1{3,1});
pka2std  = str2num(input1{4,1});
pka3std  = str2num(input1{5,1});
tnew     = str2num(input1{6,1});
dh01     = str2num(input1{7,1});
dh02     = str2num(input1{8,1});
dh03     = str2num(input1{9,1});

pka1     = fpka1itoc(pka1std,tnew,ionstr,dh01);
pka2     = fpka2itoc(pka2std,tnew,ionstr,dh02);
pka3     = fpka3itoc(pka3std,tnew,ionstr,dh03);


A=fionfrac(ph,pka1,pka2,pka3);
   disp('The ionization fractions for the triprotic system...
   [a0, a1, a2, a3] are as follows')
```

```
   disp(A)
%%%%%%%%%%%%%%%%%%%%%%%%%%%%%%%%%%%%%%%%%%%%%%%%%%%%%%%%%%%%%%%%%%%%%%%%%%%%

end
```

Function file for Ionization Fraction Calculation (fionfrac.m)

```
function y = fionfrac(ph,pka1,pka2,pka3)
%
% FIONFRAC ia a function file that computes ionization fractions for
% monoprotic diprotic and triprotic systems
%
% fionfrac(ph,pka1) computes ionization fractions for a monoprotic system
% fionfrac(ph,pka1,pka2) computes ionization fractions for a diprotic system
% fionfrac(ph,pka1,pka2,pka3) computes ionization fractions for a triprotic
% system

%Last Modified 03/05/2004

if nargin == 2
   h=10.^(-ph); ka1=10.^(-pka1);
   a0=h/(h+ka1); a1=ka1/(h+ka1);
   A=[a0,a1];

elseif nargin == 3
   h=10.^(-ph); ka1=10.^(-pka1); ka2=10.^(-pka2);
   b=h^2+h*ka1+ka1*ka2;
   a0=h^2./b; a1=h*ka1/b; a2=ka1*ka2/b;
   A=[a0,a1,a2];

elseif nargin == 4
   h=10.^(-ph); ka1=10.^(-pka1); ka2=10.^(-pka2); ka3=10.^(-pka3);
   c=h^3+h^2*ka1+h*ka1*ka2+ka1*ka2*ka3;
   a0=h^3/c; a1=h^2*ka1/c; a2=h*ka1*ka2/c; a3=ka1*ka2*ka3/c;
   A=[a0,a1,a2,a3];

else
```

```
   disp('Inappropriate number of input arguements for computing...
   ionization fractions ')
end

y=A;
```

Correction of pka1 for Temperature and Ionic Strength (fpka1itoc.m)

```
function y = fpka1itoc(pka1std,tnew,ionstr,dh01)
%
% FPKA1ITOC converts the Ka at standard conditions to that at a defined
% temperature
% and ionic strength
%
% Last Modified 07/11/2004

ka1std    = 10^(-pka1std);
ka1temp   = fvanthoff(ka1std,25.0,tnew,dh01);
act1      = fdavies(ionstr,1,tnew);
actneut   = fneutral(ionstr);
ka1ionstr = ka1std.*(actneut./(act1.*act1));
pka1      = -log10(ka1ionstr);

y = pka1;
```

Correction of pka2 for Temperature and Ionic Strength (fpka2itoc.m)

```
function y = fpka2itoc(pka2std,tnew,ionstr,dh02)
%
% FPKA2ITOC converts the Ka2 at standard conditions to that at a defined
% temperature
% and ionic strength
%
% Last Modified 07/11/2004

ka2std    = 10^(-pka2std);
ka2temp   = fvanthoff(ka2std,25.0,tnew,dh02);
act2      = fdavies(ionstr,2,tnew);
```

```
ka2ionstr = ka2temp./act2;
pka2      = -log10(ka2ionstr);

y = pka2;
```

Correction of pka3 for Temperature and Ionic Strength (fpka3itoc.m)

```
function y = fpka3itoc(pka3std,tnew,ionstr,dh03)
%
% FPKA3ITOC converts the Ka3 at standard conditions to that at a defined
% temperature
% and ionic strength
%
% Last Modified 07/11/2004

ka3std    = 10^(-pka3std);
ka3temp   = fvanthoff(ka3std,25.0,tnew,dh03);
act1      = fdavies(ionstr,1,tnew);
act2      = fdavies(ionstr,2,tnew);
act3      = fdavies(ionstr,3,tnew);
ka3ionstr = ka3temp.*(act2./(act1.*act2));
pka3      = -log10(ka3ionstr);

y = pka3;
```

B.1.5 pC-pH Diagrams

pC-pH diagrams are a plot of the log of the species concentration as a function of system pH. They are an excellent visual representation of the relative amounts of various species at varying pH values and are an integral part of solution chemistry calculations. The programs below provide pC-pH diagrams for monoprotic, diprotic and triprotic systems for any temperature and ionic strength values.

Driver Program for Construction of pC-pH Diagrams (pcphclosed.m)

```
% USAGE: Type "pcphclosed" at the Matlab command prompt
%
% PURPOSE:
% Constructs pC-pH diagrams for mono di and triprotic acids in closed
```

```
% systems.
%
% INPUTS
%
% 1. The molar concentration
% 2. System pKa(s)
% 3. Temperatute
% 4. Ionic strength
%
% OUTPUTS
% 1. pC-PH diagram

% Last Modified 03/16/2004

a11=menu('Closed System pC-pH diagrams: Choose one of the following...
        options',...
        'Standard Conditions (Temperature = 25C; Ionic Strength = 0)',...
        'Non-Standard Conditions ');

% 1. STANDARD CONDITIONS

  if a11==1
    a1=menu('Closed System pC-pH diagrams: Choose one of the following...
    acids',...
    'Monoprotic Acid at Standard Conditions (T= 25 C, I=0)',...
    'Diprotic Acid at Standard Conditions (T= 25 C, I=0)',...
    'Triprotic Acid at Standard Conditions: T= 25 C, I=0');


   if a1==1
   prompt1  = {'Enter the Molar Concentration','Enter the pKa'};
   title1   = 'Input For Monoprotic System';
   lineNo1  = 1;
   input1   = inputdlg(prompt1,title1,lineNo1);
   ctot     = str2num(input1{1,1});
   pka1     = str2num(input1{2,1});
```

```
   a12=fpcphmonostd(ctot,pka1);

elseif a1==2
   prompt1  = {'Enter the Molar Concentration','Enter the pKa1','Enter...
   the pka2'};
   title1   = 'Input For Diprotic System';
   lineNo1  = 1;
   input1   = inputdlg(prompt1,title1,lineNo1);
   ctot = str2num(input1{1,1});
   pka1  = str2num(input1{2,1});
   pka2  = str2num(input1{3,1});

   a12=fpcphdistd(ctot,pka1,pka2);

elseif a1==3
   prompt1  = {'Enter the Molar Concentration','Enter the pKa1',...
   'Enter the pka2','Enter the pKa3'};
   title1   = 'Input For Triprotic System';
   lineNo1   = 1;
   input1   = inputdlg(prompt1,title1,lineNo1);
   ctot  = str2num(input1{1,1});
   pka1  = str2num(input1{2,1});
   pka2  = str2num(input1{3,1});
   pka3  = str2num(input1{4,1});


   a12=fpcphtristd(ctot,pka1,pka2,pka3);

end


% 2. TEMPERATURE AND IONIC STRENGTH CORRECTIONS

      elseif a11==2
         a1=menu('Closed System pC-pH diagrams: Choose one of the...
```

```
                following acids',...
            'Monoprotic Acid with Temperature and Ionic Strength...
             Corrections',...
            'Diprotic Acid with Temperature and Ionic Strength...
             Corrections',...
            'Triprotic Acid with Temperature and Ionic Strength...
             Corrections');

if a1==1

   prompt1  = {'Enter the Molar Concentration','Enter the pKa at 25C',...
               'Enter the ionic Strength'...
               'Enter the Temperature','Enter the enthalpy change...
                (dH, Kcal/M) of the reaction'};
   title1   = 'Input For Monoprotic System';
   lineNo1  = 1;
   input1   = inputdlg(prompt1,title1,lineNo1);
   ctot     = str2num(input1{1,1});
   pka125   = str2num(input1{2,1});
   ionstr   = str2num(input1{3,1});
   temp     = str2num(input1{4,1});
   deltah   = str2num(input1{5,1});

   a12=fpcphmonocor(ctot,pka125,ionstr,temp,deltah);

elseif a1==2

   prompt1  = {'Enter the Molar Concentration','Enter the pKa1 at 25C',...
               'Enter the pKa2 at 25C',...
              'Enter the ionic Strength','Enter the Temperature',...
              'Enter the enthalpy change (dH, Kcal/M) for the first...
               reaction'...
              'Enter the enthalpy change (dH, Kcal/M) for the second...
               reaction'};

   title1   = 'Input For Diprotic System';
```

```
   lineNo1 = 1;
   input1  = inputdlg(prompt1,title1,lineNo1);
   ctot    = str2num(input1{1,1});
   pka125  = str2num(input1{2,1});
   pka225  = str2num(input1{3,1});
   ionstr  = str2num(input1{4,1});
   temp    = str2num(input1{5,1});
   deltah1 = str2num(input1{6,1});
   deltah2 = str2num(input1{7,1});

   a12=fpcphdicor(ctot,pka125,pka225,ionstr,temp,deltah1,deltah2);


elseif a1==3

   prompt1  = {'Enter the Molar Concentration','Enter the pKa1 at 25C',...
               'Enter the pKa2 at 25C','pKa3 at 25C',...
              'Enter the ionic Strength','Enter the Temperature',...
              'Enter the enthalpy change (dH, Kcal/M) for the first...
               reaction'...
              'Enter the enthalpy change (dH, Kcal/M) for the second...
               reaction'...
              'Enter the enthalpy change (dH, Kcal/M) for the third...
               reaction'};

   title1  = 'Input For Diprotic System';
   lineNo1 = 1;
   input1  = inputdlg(prompt1,title1,lineNo1);
   ctot    = str2num(input1{1,1});
   pka125  = str2num(input1{2,1});
   pka225  = str2num(input1{3,1});
   pka325  = str2num(input1{4,1});
   ionstr  = str2num(input1{5,1});
   temp    = str2num(input1{6,1});
   deltah1 = str2num(input1{7,1});
   deltah2 = str2num(input1{8,1});
```

```
   deltah3 = str2num(input1{9,1});

   a12=fpcphtricor(ctot,pka125,pka225,pka325,ionstr,temp,deltah1,...
   deltah2,deltah3);

end

end
```

Function File for Monoprotic Systems (fpcphmonocor.m)

```
function y = fpcphmonocor(ctot,pka25,ionstr,temp,deltah)
%
% FPCPHMONOCOR ia a function file that that computes the pC-pH diagram
% for a monoprotic acid at specified temperature and ionic strength
%
% fpcphmonocor(ctot,pka25,ionstr,temp,deltah) computes the pC-pH diagram
% for a monoprotic acid at temperature TEMP and ionic strength IONSTR

% Last Modified 03/16/2004


% Temperature Corrections
%%%%%%%%%%%%%%%%%%%%%%%%%%%%%%%%%%%%%%%%%%%%%%%%%%%%%%%%%%%%%%%%%%%
tempnew=temp+273.15;

kwater=(10.^(-14)).*exp(6723.704.*((1./298.15)-(1./tempnew)));
pkwnew=-log10(kwater);

ka25=10.^(-pka25);
kanew=fvanthoff(ka25,25,temp,deltah);
pkanew=-log10(kanew);
%%%%%%%%%%%%%%%%%%%%%%%%%%%%%%%%%%%%%%%%%%%%%%%%%%%%%%%%%%%%%%%%%%%

% COMPUTING ACTIVITY COEFFICIENTS
%%%%%%%%%%%%%%%%%%%%%%%%%%%%%%%%%%%%%%%%%%%%%%%%%%%%%%%%%%%%%%%%%%%
% Species Charge = 1
```

```
charge1 = 1;
act=fdavies(ionstr,charge1,temp); logact=log10(act);

%NEUTRAL SPECIES
actn=fneutral(ionstr);

%%%%%%%%%%%%%%%%%%%%%%%%%%%%%%%%%%%%%%%%%%%%%%%%%%%%%%%%%%%%%%%%%%%%%%%

% [H+] CONCENTRATION
%%%%%%%%%%%%%%%%%%%%%%%%%%%%%%%%%%%%%%%%%%%%%%%%%%%%%%%%%%%%%%%%%%%%%%%
ph=linspace(0,14,141)'; h=10.^(-ph); logh=-ph;
%[OH-] CONCENTRATION
logoh=ph-pkwnew-logact-logact;
%%%%%%%%%%%%%%%%%%%%%%%%%%%%%%%%%%%%%%%%%%%%%%%%%%%%%%%%%%%%%%%%%%%%%%%

% AT NEW TEMPERATURE AND IONIC STRENGTH
%%%%%%%%%%%%%%%%%%%%%%%%%%%%%%%%%%%%%%%%%%%%%%%%%%%%%%%%%%%%%%%%%%%%%%%
overact=(actn./(act.*act));
kanewact=kanew.*overact;
pkanewact=-log10(kanewact);

a=(ctot.*kanewact)./(h+kanewact);
loga=log10(a);

ha=(ctot.*h)./(h+kanewact);
logha=log10(ha);
%%%%%%%%%%%%%%%%%%%%%%%%%%%%%%%%%%%%%%%%%%%%%%%%%%%%%%%%%%%%%%%%%%%%%%%

spointx1=linspace(pka25,pka25,50)';
spointy1=linspace(0,-14,50)';
spointx2=linspace(pkanewact,pkanewact,50)';

%%%%%%%%%%%%%%%%%%%%%%%%%%%%%%%%%%%%%%%%%%%%%%%%%%%%%%%%%%%%%%%%%%%%%%%
% AT NEW TEMPERATURE AND IONIC STRENGTH
plot(ph,logh,'k',ph,logoh,'r',ph,logha,'b',ph,loga,'m',spointx1,...
spointy1,'b--',spointx2,spointy1,'m--')
```

```
axis([0 14 -14 0])
xlabel('pH')
ylabel('Log C')
title('pC-pH diagram for [HA] <----> [H+] + [A-]')
legend('[H+]','[OH-]','[HA]','[A-]','pKa(Std)','pKa(New)',-1)
%%%%%%%%%%%%%%%%%%%%%%%%%%%%%%%%%%%%%%%%%%%%%%%%%%%%%%%%%%%%%%%%

y1=pka25;
disp('The pka at 25 C and I=0 is'), disp(y1)

y=pkanewact;
disp('The new pka is'), disp(y)
```

Function File for Diprotic Systems (fpcphdicor.m)

```
   function  y = fpcphdicor(ctot,pka125,pka225,ionstr,temp,deltah1,deltah2);
%
% FPCPHDICOR ia a function file that that computes the pC-pH diagram
% for a diprotic acid at specified temperature and ionic strength
%
% fpcphdicor(ctot,pka125,pka225,ionstr,temp,deltah1,deltah2) computes...
% the pC-pH diagram
% for a diprotic acid at temperature TEMP and ionic strength IONSTR

% Last Modified 03/16/2004


% TEMPERATURE CORRECTIONS
%%%%%%%%%%%%%%%%%%%%%%%%%%%%%%%%%%%%%%%%%%%%%%%%%%%%%%%%%%%%%%%%
tempnew=temp+273.15;

kwater=(10.^(-14)).*exp(6723.704.*((1./298.15)-(1./tempnew)));
pkwnew=-log10(kwater);

ka125=10.^(-pka125);
ka1new=fvanthoff(ka125,25,temp,deltah1);
pka1new=-log10(ka1new);
```

```
ka225=10.^(-pka225);
ka2new=fvanthoff(ka225,25,temp,deltah2);
pka2new=-log10(ka2new);
%%%%%%%%%%%%%%%%%%%%%%%%%%%%%%%%%%%%%%%%%%%%%%%%%%%%%%%%%%%%


% COMPUTING ACTIVITY COEFFICIENTS
%%%%%%%%%%%%%%%%%%%%%%%%%%%%%%%%%%%%%%%%%%%%%%%%%%%%%%%%%%%%
% Species Charge = 1
charge1 = 1;
act1=fdavies(ionstr,charge1,temp); logact1=log10(act1);

% Species Charge = 2
charge2 = 2;
act2=fdavies(ionstr,charge2,temp); logact2=log10(act2);

%NEUTRAL SPECIES
actn=fneutral(ionstr); logactn=log10(actn);

% OVERALL ACTIVITIES
overact1=(1/(act1*act1)); overact2=actn/(act1*act1); overact3=1/act2;
%%%%%%%%%%%%%%%%%%%%%%%%%%%%%%%%%%%%%%%%%%%%%%%%%%%%%%%%%%%%

% [H+] CONCENTRATION
%%%%%%%%%%%%%%%%%%%%%%%%%%%%%%%%%%%%%%%%%%%%%%%%%%%%%%%%%%%%
% AT 25 C AND I=0
ph25=linspace(0,14,141)'; h25=10.^(-ph25); logh25=-ph25; logoh25=ph25-14;

% AT THE NEW TEMPERATURE
ph=linspace(0,14,141)'; h=10.^(-ph); logh=log10(h);
%%%%%%%%%%%%%%%%%%%%%%%%%%%%%%%%%%%%%%%%%%%%%%%%%%%%%%%%%%%%

%[OH-] CONCENTRATION
logoh=ph-pkwnew-logact1-logact1;
%%%%%%%%%%%%%%%%%%%%%%%%%%%%%%%%%%%%%%%%%%%%%%%%%%%%%%%%%%%%
```

```
% CONCENTRATION BASED pKa's AFTER ADJUSTMENTS FOR IONIC STRENGTH
%%%%%%%%%%%%%%%%%%%%%%%%%%%%%%%%%%%%%%%%%%%%%%%%%%%%%%%%%%%%%%%%
ka1newconc=ka1new.*overact2;
pka1newconc=-log10(ka1newconc);

ka2newconc=ka2new.*overact3;
pka2newconc=-log10(ka2newconc);
%%%%%%%%%%%%%%%%%%%%%%%%%%%%%%%%%%%%%%%%%%%%%%%%%%%%%%%%%%%%%%%%

% ACID CONCENTRATIONS AT NEW TEMPERATURE AND IONIC STRENGTH
%%%%%%%%%%%%%%%%%%%%%%%%%%%%%%%%%%%%%%%%%%%%%%%%%%%%%%%%%%%%%%%%
h2a=ctot./(1 + ka1newconc./h + (ka1newconc.*ka2newconc)./(h.^2));
logh2a=log10(h2a);

ha=ctot./(1+ h./ka1newconc + ka2newconc./h);
logha=log10(ha);

a=ctot./(1 + h.^2./(ka1newconc.*ka2newconc) + h./ka2newconc);
loga=log10(a);
%%%%%%%%%%%%%%%%%%%%%%%%%%%%%%%%%%%%%%%%%%%%%%%%%%%%%%%%%%%%%%%%


% CONSTRUCTING pKa's
%%%%%%%%%%%%%%%%%%%%%%%%%%%%%%%%%%%%%%%%%%%%%%%%%%%%%%%%%%%%%%%%
spointx1=linspace(pka125,pka125,50)';
spointx2=linspace(pka225,pka225,50)';
spointx3=linspace(pka1newconc,pka1newconc,50)';
spointx4=linspace(pka2newconc,pka2newconc,50)';
spointy1=linspace(0,-14,50)';
%%%%%%%%%%%%%%%%%%%%%%%%%%%%%%%%%%%%%%%%%%%%%%%%%%%%%%%%%%%%%%%%


% PLOTS
%%%%%%%%%%%%%%%%%%%%%%%%%%%%%%%%%%%%%%%%%%%%%%%%%%%%%%%%%%%%%%%%
plot(ph,logh,'k',ph,logoh,'g',ph,logh2a,'r',ph,logha,'b',ph,loga,'m',...
```

```
spointx1,spointy1,'r--',spointx2,spointy1,'g--',...
   spointx3,spointy1,'b--',spointx4,spointy1,'m--')
axis([0 14 -14 0])
xlabel('pH')
ylabel('Log C')
title('pC-pH diagram for the Diprotic Acid [H2A]')
legend('[H+]','[OH-]','[H2A]','[HA-]','[A2-]','pKa1(std)','pKa2(std)',...
'pKa1(new)','pKa2(new)',-1)
%%%%%%%%%%%%%%%%%%%%%%%%%%%%%%%%%%%%%%%%%%%%%%%%%%%%%%%%%%%%%%%%%%%%%%%

y1=[pka125, pka225];
disp('The pkas at 25 C and I = 0 are [pKa1, pKa2] are');
disp(y1);

y=[pka1newconc, pka2newconc];
disp('The new pkas [pKa1, pKa2] are');
disp(y);
```

Function File for Triprotic Systems (fpcphtricor.m)

```
function  y = fpcphtricor(ctot,pka125,pka225,pka325,ionstr,temp,deltah1,...
deltah2,deltah3);
%
% FPCPHTRICOR ia a function file that that computes the pC-pH diagram
% for a diprotic acid at specified temperature and ionic strength
%
% fpcphtricor(ctot,pka125,pka225,pka325,ionstr,temp,deltah1,deltah2,deltah3)
% computes the pC-pH diagram
% for a triprotic acid at temperature TEMP and ionic strength IONSTR

% Last Modified 03/18/2004

% TEMPERATURE CORRECTIONS
%%%%%%%%%%%%%%%%%%%%%%%%%%%%%%%%%%%%%%%%%%%%%%%%%%%%%%%%%%%%%%%%%%%%%%%
tempnew=temp+273.15;

kwater=(10.^(-14)).*exp(6723.704.*((1./298.15)-(1./tempnew)));
```

```
pkwnew=-log10(kwater);

ka125=10.^(-pka125);
ka1new=fvanthoff(ka125,25,temp,deltah1);
pka1new=-log10(ka1new);

ka225=10.^(-pka225);
ka2new=fvanthoff(ka225,25,temp,deltah2);
pka2new=-log10(ka2new);

ka325=10.^(-pka325);
ka3new=fvanthoff(ka325,25,temp,deltah3);
pka3new=-log10(ka3new);
%%%%%%%%%%%%%%%%%%%%%%%%%%%%%%%%%%%%%%%%%%%%%%%%%%%%%%%%%%%%%%%%%%%%%%%%%%%%


% COMPUTING ACTIVITY COEFFICIENTS
%%%%%%%%%%%%%%%%%%%%%%%%%%%%%%%%%%%%%%%%%%%%%%%%%%%%%%%%%%%%%%%%%%%%%%%%%%%%
% Species Charge = 1
charge1 = 1;
act1=fdavies(ionstr,charge1,temp); logact1=log10(act1);

% Species Charge = 2
charge2 = 2;
act2=fdavies(ionstr,charge2,temp); logact2=log10(act2);

% Species Charge = 3
charge3 = 3;
act3=fdavies(ionstr,charge3,temp); logact3=log10(act3);

%NEUTRAL SPECIES
actn=fneutral(ionstr); logactn=log10(actn);

% OVERALL ACTIVITIES
overact1=actn/(act1*act2); overact2=1/act2; overact3=act2/(act1*act3);
%%%%%%%%%%%%%%%%%%%%%%%%%%%%%%%%%%%%%%%%%%%%%%%%%%%%%%%%%%%%%%%%%%%%%%%%%%%%
```

```
% [H+] CONCENTRATION
%%%%%%%%%%%%%%%%%%%%%%%%%%%%%%%%%%%%%%%%%%%%%%%%%%%%%%%%%%%%%%%%%%%%%%%%
% AT THE NEW TEMPERATURE
ph=linspace(0,14,141)'; h=10.^(-ph); logh=log10(h);

%[OH-] CONCENTRATION
logoh=ph-pkwnew-logact1-logact1;
%%%%%%%%%%%%%%%%%%%%%%%%%%%%%%%%%%%%%%%%%%%%%%%%%%%%%%%%%%%%%%%%%%%%%%%%

% CONCENTRATION BASED pKa's AFTER ADJUSTMENTS FOR IONIC STRENGTH
%%%%%%%%%%%%%%%%%%%%%%%%%%%%%%%%%%%%%%%%%%%%%%%%%%%%%%%%%%%%%%%%%%%%%%%%
ka1newconc=ka1new.*overact1;
pka1newconc=-log10(ka1newconc);

ka2newconc=ka2new.*overact2;
pka2newconc=-log10(ka2newconc);

ka3newconc=ka3new.*overact3;
pka3newconc=-log10(ka3newconc);

%%%%%%%%%%%%%%%%%%%%%%%%%%%%%%%%%%%%%%%%%%%%%%%%%%%%%%%%%%%%%%%%%%%%%%%%

% ACID CONCENTRATIONS AT NEW TEMPERATURE AND IONIC STRENGTH
%%%%%%%%%%%%%%%%%%%%%%%%%%%%%%%%%%%%%%%%%%%%%%%%%%%%%%%%%%%%%%%%%%%%%%%%
h2a=ctot./(1 + ka1newconc./h + (ka1newconc.*ka2newconc)./(h.^2));
logh2a=log10(h2a);

ha=ctot./(1+ h./ka1newconc + ka2newconc./h);
logha=log10(ha);

a=ctot./(1 + h.^2./(ka1newconc.*ka2newconc) + h./ka2newconc);
loga=log10(a);
%%%%%%%%%%%%%%%%%%%%%%%%%%%%%%%%%%%%%%%%%%%%%%%%%%%%%%%%%%%%%%%%%%%%%%%%

% ACID CONCENTRATIONS AT NEW TEMPERATURE AND IONIC STRENGTH
```

```
%%%%%%%%%%%%%%%%%%%%%%%%%%%%%%%%%%%%%%%%%%%%%%%%%%%%%%%%%%%%%%%%%%%%%%%%%%%%%%%%
h3a=ctot./(1 + ka1newconc./h + (ka1newconc.*ka2newconc)./(h.^2) + ...
   (ka1newconc.*ka2newconc.*ka3newconc)./(h.^3));
logh3a=log10(h3a);

h2a=ctot./(h./ka1newconc + 1 + ka2newconc./h + (ka2newconc.*ka3newconc)...
./(h.^2));
logh2a=log10(h2a);

ha=ctot./((h.^2)./(ka1newconc.*ka2newconc) + h./ka2newconc + 1 +...
ka3newconc./h);
logha=log10(ha);

a=ctot./((h.^3)./(ka1newconc.*ka2newconc.*ka3newconc) + (h.^2)./...
(ka2newconc.*ka3newconc) + h./ka3newconc + 1);
loga=log10(a);
%%%%%%%%%%%%%%%%%%%%%%%%%%%%%%%%%%%%%%%%%%%%%%%%%%%%%%%%%%%%%%%%%%%%%%%%%%%%%%%%


% CONSTRUCTING pKa's
%%%%%%%%%%%%%%%%%%%%%%%%%%%%%%%%%%%%%%%%%%%%%%%%%%%%%%%%%%%%%%%%%%%%%%%%%%%%%%%%
spointx1=linspace(pka125,pka125,50)';
spointx2=linspace(pka225,pka225,50)';
spointx3=linspace(pka325,pka325,50)';
spointx4=linspace(pka1newconc,pka1newconc,50)';
spointx5=linspace(pka2newconc,pka2newconc,50)';
spointx6=linspace(pka3newconc,pka3newconc,50)';
spointy1=linspace(0,-14,50)';
%%%%%%%%%%%%%%%%%%%%%%%%%%%%%%%%%%%%%%%%%%%%%%%%%%%%%%%%%%%%%%%%%%%%%%%%%%%%%%%%


% PLOTS
%%%%%%%%%%%%%%%%%%%%%%%%%%%%%%%%%%%%%%%%%%%%%%%%%%%%%%%%%%%%%%%%%%%%%%%%%%%%%%%%
plot(ph,logh,'y',ph,logoh,'m',ph,logh3a,'c',ph,logh2a,'r',ph,logha,...
'g',ph,loga,'b',spointx1,spointy1,'y--',spointx2,spointy1,'m--',...
spointx3,spointy1,'c--',spointx4,spointy1,'r--',spointx5,spointy1,'g--',...
```

```
   spointx6,spointy1,'b--')
axis([0 14 -14 0])
xlabel('pH')
ylabel('Log C')
title('pC-pH diagram for the Triprotic Acid [H3A]')
legend('[H+]','[OH-]','[H3A]','[H2A]','[HA-]','[A2-]','pKa1(std)',...
'pKa2(std)','pKa3(std)','pKa1(new)',   'pKa2(new)','pKa3(new)',-1)
%%%%%%%%%%%%%%%%%%%%%%%%%%%%%%%%%%%%%%%%%%%%%%%%%%%%%%%%%%%%%%%%

y1=[pka125, pka225, pka325];
disp('The pkas at 25 C and I = 0 are [pKa1, pKa2, pKa3] are');
disp(y1);

y=[pka1newconc, pka2newconc, pka3newconc];
disp('The new pkas [pKa1, pKa2, pKa3] are');
disp(y);
```

Appendix C

pCO_2 Contributors in a Perfusion System

C.1 Acids, Bases and Buffering Action

C.1.1 Carbon dioxide

Cells produce CO_2 that reduces culture pH and detailed information on CO_2 dynamics has been presented in Chapter 4. Figure C.1 shows the pC-pH diagram for the carbonate system. At pH = 6.8, 85% of the CO_2 exists as HCO_3^- with 15% as H_2CO_3* and CO_3^{2-} virtually non-existent. Thus a significant amount of the CO_2 produced by the cells is converted to HCO_3^- and this conversion is accompanied by the release of H^+ that will reduce bioreactor pH in the absence of buffering ability.

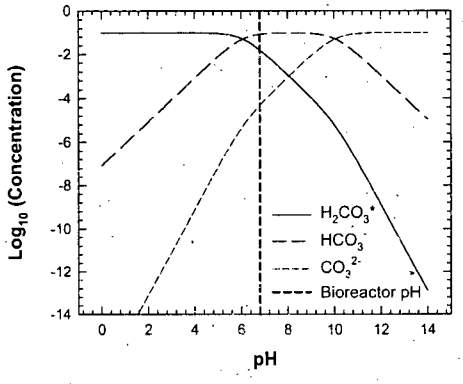

Figure C.1: pC-pH diagram for the bicarbonate system.

C.1.2 Lactic Acid

Cells convert a significant amount of glucose to lactic acid which subsequently dissociates to lactate releasing a hydrogen ion

$$C_3H_6O_3 \leftrightarrow C_3H_5O_3 + H^+; \qquad K_1 = 10^{-3.86} \tag{C.1}$$

The pC-pH diagram for lactate is shown in Figure C.2 from which it is clear that dissociation of lactic acid to lactate virtually proceeds to completion under culture conditions. Thus each mole of lactic acid produced by the cells results in the formation of an H^+ ion that must be neutralized either by the buffering action of the medium or by base addition.

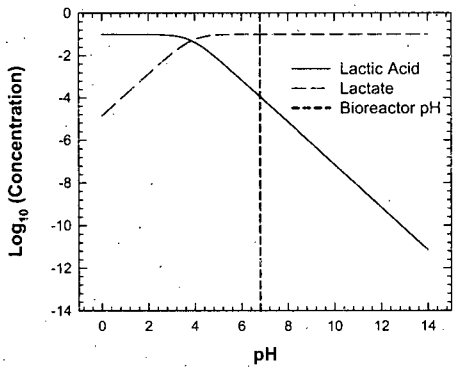

Figure C.2: pC-pH diagram for lactic acid.

C.1.3 Ammonia

Cellular conversion of glutamine to glutamate is accompanied by ammonia production and abiotic glutamine degradation also results in the formation of ammonia. Ammonia can take up a hydrogen ion forming ammonium

$$NH_3 + H^+ \leftrightarrow NH_4^+; \qquad K_1 = 10^{9.256} \tag{C.2}$$

Figure C.3 shows concentration profiles of ammonia and ammonium as a function of pH. At pH = 6.8, >99% is present as ammonium with negligible amount present as ammonia. Conversion of ammonia to ammonium according to Eq.(C.2) essentially proceeds to completion and helps neutralize some of the H^+ ions produced by the conversion of lactic acid to lactate. However, ammonia production alone cannot provide adequate buffering action

against lactic acid. For BHK cells in perfusion culture, the cell-specific lactate production rate was 5-6 fold higher than the total ammonia production rate (cell and glutamine degradation combined) suggesting that additional buffering either through a medium component or base addition is necessary for pH control.

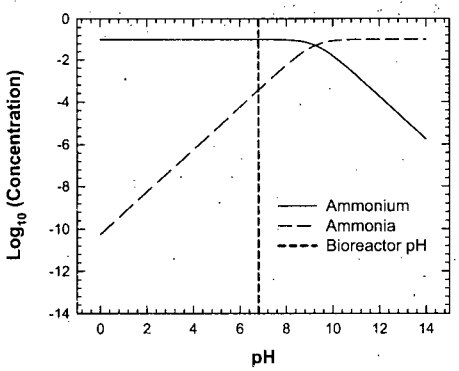

Figure C.3: pC-pH diagram for ammonia.

C.1.4 Base Addition

The combination of CO_2 and lactate production results in an excess of H^+ ions that must be neutralized to maintain bioreactor pH at the set point. This is done using a combination of buffer in the cultivation medium and base for pH control. Sodium bicarbonate is most commonly used both in the medium and as base with Na_2CO_3 and NaOH the other choices for base. Elimination of $NaHCO_3$ will significantly reduce bioreactor pCO_2 (Chapter 4) and this is especially attractive for high-density perfusion systems. In the medium, $NaHCO_3$ can be replaced by an organic buffer such as MOPS while Na_2CO_3 and NaOH can be used as base for pH control.

Appendix D

Closed Loop pCO_2 Control

Elimination of $NaHCO_3$ from the medium and base resulted in ~70% reduction in bioreactor pCO_2 such that the final bioreactor pCO_2 was 68 – 85 mm Hg (Chapter 4). Despite the absence of closed loop pCO_2 control, pCO_2 levels remained relatively steady over the course of a perfusion cultivation as the cell density was held constant. If further pCO_2 reduction and set point control are desired, a closed loop control strategy must be used.

D.1 pCO_2 Control Strategy

Reduction in bioreactor pCO_2 is possible by stripping with air, nitrogen or oxygen. A 25% pCO_2 reduction was seen in a manufacturing reactor when oxygen was sparged at 0.015 vvm (Chapter 4). There is an upper limit on the sparging rate because cell damage will occur at very high rates. Moreover, sparging will affect bioreactor dissolved oxygen whose set point control is of greater importance than pCO_2 control. Recognizing this interdependence of DO and pCO_2 we propose a cascade-control strategy based on manipulating gas flows for pCO_2 control in combination with DO and pH control (Figure D.1).

The idea is to introduce a slow loop for pCO_2 control. When bioreactor pCO_2 exceeds the set-point, the total gas flow is increased to facilitate CO_2 stripping and bring the pCO_2 value closer to the set-point. As oxygen and nitrogen make up the total gas flow, any changes to this value will affect the bioreactor DO concentration. A cascade control loop is thus necessary to ensure that bioreactor DO is maintained at its set-point despite total gas flow changes associated with pCO_2 control. Given the rapid DO dynamics, a fast loop is necessary for DO control while a much slower loop will be adequate for pCO_2 control. If CO_2 gas is used as an acid for bioreactor pH control, the CO_2 flow rate can be determined by the pCO_2 controller as well.

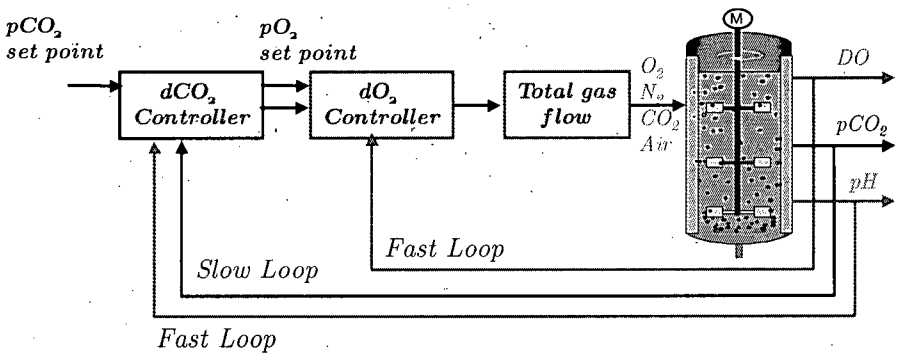

Figure D.1: Illustration of the pCO_2 control strategy proposed in this study

D.2 Results from pCO_2 Control

Bioreactor pCO_2 reduction on the order of 15 – 20% were observed using the above strategy. When $NaHCO_3$ was present in both the medium and the base, bioreactor pCO_2 dropped from ~250 mm Hg to a value in the 200 - 210 mm Hg range. No beneficial metabolic and productivity responses were seen after this reduction. Upon $NaHCO_3$ removal from both the medium and base, bioreactor pCO_2 dropped from 84 mm Hg to 60 mm Hg bringing it closer to the physiological range of 30 – 50 mm Hg (Chapter 4). However, there were no changes in metabolism and productivity when bioreactor pCO_2 decreased from 84 to 60 mm Hg. For the BHK cells examined in this study, it appears that benefits from closed loop pCO_2 control are minimal. A majority of the pCO_2 reduction was due to $NaHCO_3$ elimination that resulted in substantial productivity increases (Chapter 4).

Appendix E

RQ Estimation in Perfusion Systems

E.1 Liquid Stream Contributions to OUR

Only gas phase contributions to OUR are accounted for in Eq.(5.1). The following analysis will show that the liquid stream contributions are negligible and Eq.(5.1) indeed provides accurate OUR estimates. Eq.(5.1) can be modified to include liquid streams

$$\text{OUR} = \text{Gas Stream Contributions} + \text{Liquid Stream Contributions} \tag{E.1}$$

$$\text{OUR} = \left\{F_{O_2}O_2^{in} - F_{O_2}O_2^{out}\right\} + \left\{\left(F_m C_l^m + F_{base}C_l^{base} + F_r C_l^r\right) - \left(F_d C_l^b + F_r C_l^b + F_h C_l^h\right)\right\} \tag{E.2}$$

where F_m, F_{base}, F_r, F_d, F_h are the medium, base, recycle, cell discard and harvest flow rates, respectively (L/day), and C_l^m, C_l^{base}, C_l^r, C_l^b, C_l^h the oxygen concentrations in the medium, base, recycle, bioreactor and harvest, respectively (mol/L). Liquid stream flow rates in the above equation can be rewritten as

$$F_m + F_{base} = F_d + F_h = F' \tag{E.3}$$

Assuming that the medium and base streams are saturated with air (this was verified with pO_2 measurements in a blood gas analyzer) oxygen concentration in the liquid streams may be rewritten as

$$C_l^m + C_l^{base} = 2C_l^b \tag{E.4}$$

when the DO concentration in the bioreactor is 50%. Substituting Eqs.(E.3) and (E.4) in Eq.(E.2) results in

$$\text{OUR} = \left\{F_{O_2}O_2^{in} - F_{O_2}O_2^{out}\right\} + \left\{F'C_l^b + F_r\left(C_l^r - C_l^b\right)\right\} \tag{E.5}$$

Assuming a cell density of 20 x10^6 cells/mL and an OUR of 5 pmol/cell-d, the daily consumption of oxygen in a bioreactor with a 10 L working volume is 1 mol/day. For the experiments in this study, F' was approximately 35 L/day (30 L/day perfusion + 5 L/day cell discard) and C_l^b was 50% air saturation or 1.12 x 10^{-4} mol/L. The product $F'C_l^b$ is thus 3.9 x 10^{-3} mol/day which is only 0.39% of the daily consumption of oxygen. If no biological activity is assumed in the settler, $C_l^r = C_l^b$ and the contribution of the $F_r\left(C_l^r - C_l^b\right)$ term is zero. However, in reality, there is oxygen consumption in the settler and experimental data indicate that the pO_2 in the settler return stream (C_l^r) is approximately 10 mm Hg or 1.3% air saturation. Since C_l^r is very small when compared to C_l^b, the contribution of the second term in the liquid stream can be readily approximated as $F_rC_l^b$ which corresponds to –1.34 x 10^{-2} mol/day or 1.34% of the daily consumption of oxygen.

It is clear from the above analysis that the liquid stream, $F'C_l^b$, accounts for 0.39% of the OUR while the liquid stream, $F_r\left(C_l^r - C_l^b\right)$, accounts for –1.34 %. Together, these two liquid streams account for only 1% of the oxygen consumption in the bioreactor. It is thus reasonable to conclude that there will be no significant loss in accuracy when Eq.(5.1) is used for OUR estimation.

E.2 k_La Estimation from OUR Data

An interesting feature of the mass balance approach is that while it does not require k_La values for determining OUR, it actually allows k_La estimation once the OUR has been determined. An expression for oxygen accumulation in the bioreactor may be written as

$$\text{Oxygen Accumulation} = \text{OTR - OUR} \tag{E.6}$$

where OTR transfer rate defined as

$$\text{OTR} = k_La\left(C^* - C_l^b\right) \tag{E.7}$$

where C* is the oxygen concentration in equilibrium with the gas phase. Since bioreactor DO concentration is controlled at a predetermined set point (usually 50%), there is no accumulation of oxygen in the bioreactor. Thus OUR = OTR and k_La can be determined

from

$$k_L a = \frac{\text{OUR}}{(C^* - C_l^b)} \tag{E.8}$$

where $C^* = \frac{p}{H}$, p the oxygen partial pressure and H the Henry's constant. Since C_l^b is usually measured as % saturation, it can be converted to mol/L using

$$C_l^b\ (mol/L) = \frac{0.209\left(\frac{C_l^b\ (\%\ saturation)}{100}\right)760}{H} \tag{E.9}$$

E.3 Effect of Medium and Base Composition on the Exit Gas Flow Rate

When carbonate species ($NaHCO_3$ or Na_2CO_3) are present in the medium and base, they are an abiotic source of CO_2 production. Since both the medium and base enter the perfusion system as liquids, they make no CO_2 contributions to the inlet gas stream. They do, however, contribute CO_2 to the exit gas stream which should result in an increase in the exit gas flow rate over the inlet gas stream. The OUR and CER mass balance expressions derived above assume identical inlet and exit gas stream flow rates and the error introduced by this assumption is examined in this section. Cellular CO_2 production does not cause a net increase in gas flow rates because it is a consequence of oxygen consumption. As mammalian cell RQ values are close to unity, oxygen uptake results in an equivalent amount (on a mole basis) of CO_2 production.

E.3.1 Medium with 2 g/L $NaHCO_3$ and 6% $NaHCO_3$ as Base

This combination represents the worst case scenario since abiotic CO_2 contribution from both the medium and base are the highest. This results in a bioreactor pCO_2 of 225 mm Hg and a 5% CO_2 concentration in the exit gas at a CER value of 4.89 pmol/cell-d. If we make a conservative assumption that all exit gas CO_2 is from the medium and base, the exit gas flow rate has to be 5% higher than the inlet stream. To get a true estimate of CO_2 sources for the exit gas streams, cellular contribution must be accounted for. Using the CO_2 mass balance expressions developed in Chapter 5, the following inlet and outlet steam CO_2 compositions can be calculated

The medium and base streams make up 84% of the $[CO_2]_T$ in the inlet stream and are thus responsible for 84% of $[CO_2]_T$ in the outlet stream as well. Since the CO_2 flow rate in the exit stream in 5%, we expect to see a 4.2% increase in exit gas flow rate (84% of 5) when both the medium and base contain $NaHCO_3$. While the error in gas flow measurement may

Table E.1: Carbon dioxide contributions from the inlet and outlet streams when both medium and base streams contain sodium bicarbonate

Stream	$[CO_2]_T$ (mol/d)	% Contribution
Inlet Streams		
Medium	3.45	38
Base	4.18	46
Cells	1.47	16
Outlet Streams		
Harvest	7.38	81
Cell Discard	0.25	3
Exit Gas	1.47	16

be $> 4.2\%$, it is still important to correct the exit gas flow rate to minimize the error in OUR and CER estimation. It must be noted that the exit gas stream carries 16% of $[CO_2]_T$ leaving the system reflective of the distribution between $H_2CO_3{}^*$ and HCO_3^-. This number is very close to the theoretically predicted value of 15.69% from Eq.(5.13).

E.3.2 Bicarbonate-free Medium and 6% Na_2CO_3 as Base

This is a preferred combination since CO_2 contributions from the medium and base are minimized resulting in lower bioreactor pCO_2. Under these conditions, bioreactor pCO_2 is 73 mm Hg at a CER of 4.87 pmol/cell-d with 1.5% CO_2 concentration in the exit gas. The $[CO_2]_T$ concentrations in the inlet and outlet streams are

Table E.2: Carbon dioxide contributions from the inlet and outlet streams with bicarbonate-free medium and sodium carbonate as base

Stream	$[CO_2]_T$ (mol/d)	% Contribution
Inlet Streams		
Medium	0	0
Base	1.45	50
Cells	1.46	50
Outlet Streams		
Harvest	2.39	82
Cell Discard	0.08	3
Exit Gas	0.44	15

The base and cellular respiration contribute equally to $[CO_2]_T$ in the inlet streams such

that half the CO_2 in the exit stream is from base addition. We should thus expect a 0.75% increase in the exit gas flow rate (50% of 1.5) when the medium is bicarbonate-free and Na_2CO_3 is used as base. This increase is very small and can be neglected with minimal impact on OUR and CER estimates. Just as the case with bicarbonate present both in the medium and base, the exit gas stream carried 15% of $[CO_2]$, very close to the 15.69% theoretical prediction.

E.4 Computer Programs for OUR and CER Estimation

henryo2.m (Computes Henry's constant for oxygen at the desired temperature)

```
function y = henryo2(temp)
%HENRYO2   Computes Henry's constant for O2 at a desired temperature
%   Return results in mmHg-L/mole

%   Last Modified: 07/31/04

% Constants for Bunsen Coefficients
a   = 4.9e-2;
b   = -1.335e-3;
c   = 2.759e-5;
d   = -3.235e-7;
e   = 1.614e-9;

% Calculation of Bunsen Coefficient
alpha = a + b*temp + c*temp.^2 + d*temp.^3 + e*temp.^4;

% Calculation of Henry's Constant
hdim        = 273.15./(alpha.*(temp+237.15));
hkpalmole   = (101.3*22.395)./alpha;
hatmlmole   = hkpalmole*0.009869233;
hmmhglmole  = hkpalmole*7.500617;

y = hmmhglmole;
```

henryco2.m (Computes Henry's constant for CO2 at the desired temperature)

```
function y = henryco2new(temp)
%HENRYCO2   Computes Henry's constant for CO2 at a desired temperature
%   Return results in mmHg-L/mole

%   Last Modified: 01/29/04

% Coefficients of Power series for Bunsen Coefficients
% (Eq.21 in Schumpe et al, (1982) Adv. Biochem. Eng. 24: 1-83)
a   = 1.720;
b   = -6.689e-2;
c   = 1.618e-3;
d   = -2.284e-5;
e   = 1.394e-7;

% Calculation of Bunsen Coefficient
alpha = a + b*temp + c*temp^2 + d*temp^3 + e*temp^4;

% Calculation of Henry's Constant
hdim        = 273.15/(alpha*(temp+237.15));
hkpalmole   = (101.3*22.395)/alpha;
hatmlmole   = hkpalmole*0.009869233;
hmmhglmole  = hkpalmole*7.500617;
%y = hmmhglmole;
```

our.m (Computes OUR using global mass balances)

```
% OUR ESTIMATION IN PERFUSION SYSTEMS USING THE GLOBAL MASS BALANCE APPROACH
% Only gas phase contributions are used for OUR estimation

% SECTION 1: INPUT DATA

% O2 Flows (L/min)
o2prompt={'Inlet Total Gas Flow Rate (L/min)',...
          'Inlet O2 Flow Rate (L/min)',...
```

```
            '% O2 in Exit Gas (%)'...
            'Bioreactor Viable Cell Density (x10^6 cells/ml)',...
            'Bioreactor Volume (L)'};

o2def={'0.1','0.041','25.7','20','12'};

o2Title='Oxygen Flow Rate Data For OUR Estimation From Global Mass Balance';
lineNo=1;
o2input=inputdlg(o2prompt,o2Title,lineNo,o2def);

gasflow          = str2double(o2input(1));
o2flowin         = str2double(o2input(2));
yo2              = str2double(o2input(3));
fvcd             = str2double(o2input(4));
vol              = str2double(o2input(5));

% SECTION 2. CALCULATIONS

% Gas Phase Calculations
% Inlet
o2flowin = o2flowin*60*24;                      %(L/day)
o2flowin = 1*o2flowin/(0.08206*298.15);         %(moles/day)

% Outlet
o2flowout = (yo2/100)*gasflow;                  %(L/min)
o2flowout = o2flowout*60*24;                    %(L/day)
o2flowout = 1*o2flowout/(0.08206*298.15);       %(moles/day)

% Total Gas Flows
totalo2in  = o2flowin;                          %(moles/day)
totalo2out = o2flowout;                         %(moles/day)

% Global Mass Balance
our1 = o2flowin - o2flowout;                    %(moles/day)
our2 = our1*1e12/(fvcd*1e6*vol*1000);           %(pM/cell-d)
```

```
%3. RESULT DISPLAY

disp('The OUR in moles/day'), disp(our1)
disp('The OUR in pmole/cell/day'), disp(our2)
```

cerr.m (Computes CER using global mass balances)

```
% CER ESTIMATION IN PERFUSION SYSTEMS USING A COMBINATION OF GAS AND
% LIQUID PHASE MASS BALANCES
% Program modified to compute Real-time CER using data from Fermworks

% Last Modified 09/22/2005

clear all

% SECTION 1: ONLINE VARIABLES FROM FERMWORKS
pH_reactor      = 6.8;   % (-)
temp_reactor    = 35.5;  % (C)
vol_reactor     = 15;    % (L)

flow_base       = 2;     % (L/day)
flow_purge      = 5;     % (L/day)
flow_harvest    = 150;   % L/day

total_gasflow   = 0.5;   % (L/min)
co2_flowin      = 0;     % (L/min)
co2_out         = 1.5;   % (%)

% SECTION 2: OFFLINE VARIABLES ENTERED INTO FERMWORKS
pCO2_reactor    = 72.7;  % mm Hg
vcd_reactor     = 20;    % 10^6 cells/mL

% SECTION 3. CALCULATIONS
% Rate Constants Corrected for temperature and ionic strength effects
k1              = 10^(-6.07);   % (-)
k2              = 10^(-10.04);  % (-)
```

```
% Computing [CO2]T concentrations (moles/L)
% Medium: Determine [CO2]T from [H2CO3*]
hconc = 10^(-pH_reactor);  % Bioreactor [H+]
convfactor = 1 + k1./hconc + (k1.*k2)./hconc.^2;
a=1.720; b=-6.689e-2; c= 1.618e-3; d=-2.284e-5; e=1.394e-7;
temp         = temp_reactor;
alpha = a + b*temp + c*temp^2 + d*temp^3 + e*temp^4;
hkpalmole    = (101.3*22.395)/alpha;
hmmhglmole   = hkpalmole*7.500617;
clbioreactor = convfactor.*(pCO$_{\text{2}}$_reactor/hmmhglmole);

% Other [CO2]T Calculations (moles/L)
clpurge      = clbioreactor;
clharvest    = clbioreactor;
clmedium     = 0;     % NaHCO$_{\text{3}}$-free medium
clbase       = 0.723; % 6% Na2CO3


% Calculation of Liquid Phase [CO2]T Flows (moles/day)
% Inlet
co2medium    = flow_harvest*clmedium;
co2base      = flow_base*clbase;
inletliquid  = co2medium + co2base;
inletflows   = [co2medium,co2base]';

% Outlet
co2purge     = flow_purge*clbioreactor;
co2harvest   = flow_harvest*clharvest;
outletliquid = co2purge + co2harvest;
outletflows = [co2purge,co2harvest]';

% Gas Phase Calculations
% Inlet
co2flowin = co2_flowin*60*24;                    %(L/day)
co2flowin = 1*co2flowin/(0.08206*298.15);        %(moles/day)
```

```
% Outlet
co2flowout = (co2_out/100)*total_gasflow;          %(L/min)
co2flowout = co2flowout*60*24;                     %(L/day)
co2flowout = 1*co2flowout/(0.08206*298.15);        %(moles/day)

% Combined Gas and Liquid Phase Mass Balance
cer1 = (co2flowout - co2flowin) + (outletliquid - inletliquid);%(moles/day)
cer2 = cer1*1e12/(vcd_reactor*1e6*vol_reactor*1000);    %(pmole/cell/day)

% SECTION 4. RESULT DISPLAY

disp('The CER in moles/day'), disp(cer1)
disp('The CER in pmole/cell/day'), disp(cer2)

disp('    Medium   Carbonate   Cellular Activity  (moles/day)')
sources = [co2medium, co2base, cer1];
disp(sources)

disp('    Harvest   Purge     Basket Stripping    (moles/day)')
sinks = [co2harvest, co2purge, co2flowout];
disp(sinks)
```

Appendix F

Logistic Equation Modeling

Detailed information of the analysis of data from mammalian cell batch cultures using logistic equations is presented in Chapter 6. Computer programs developed for this analysis can be classified into the following categories

- Logistic equation simulation
- Polynomial fitting of batch culture data
- Nonlinear parameter estimation in logistic models

F.1 Logistic Equation Simulation

Programs in this category provide a means of graphically visualizing time profiles of the dependent variable when the time vector and model parameters are known.

F.1.1 Generalized Logistic Equation

The 4-parameter generalized logistic equation has been used to fit cell density as it can describe both the ascending and decending portions of the viable cell density profile in a batch culture. The following programs compute the viable cell density and growth rate and also provide a graphical representation of the output

```
% gle_simulation.m
% Simulates growth curves from the 4-parameter
% generalized logistic equation
% Inputs: time range, model parameters
% Outputs: vectors of dependent variable, its
```

```
% derivative, and the growth rate
% Uses gle_equation for function evaluation

% Chetan Goudar
% Last Modified: 6/18/04

% Model Parameters
k=[0.03057 4.84939 0.92957 2.03765];
c1 = k(1); d1 = k(2); c2 = k(3); d2 = k(4);

% Definition of the time vector
tlow  = 0;
thigh = 11;
t     = linspace(tlow,thigh,51)';

% Function evaluation
fvcd = gle_equation(k,t);

% Derivative and growth rate computaion
term1 = (c2/d2).*exp(-t./d2);
term2 = (c1/d1).*exp(t./d1);
dydt  = (fvcd.^2).*(term1 - term2);
mu    = dydt./fvcd;

subplot(2,1,1)
plot(t,fvcd)

subplot(2,1,2)
plot(t,mu)
%%%%%%%%%%%%%%%%%%%%%%%%%%%%%%%%%%%%%%%%%%%%%%%%%%%%%%%%%%%%%%%%%%%%%%%%

function y = gle_equation(k,t)
% function y = gle_equation(k,time)
% Evaluates the 4-parameter generalized logistic equation
% Inputs: model parameters, time vector
% Outputs: dependent variable vector
```

```
% Chetan Goudar
% Last Modified: 6/18/04

c1 = k(1); d1 = k(2); c2 = k(3); d2 = k(4);
x  = 1./(c1.*exp(t./d1) + c2.*exp(-t./d2));
y  = x;
```

F.1.2 Logistic Growth Equation

The logistic growth equation has been used to describe variables that monotonically increase during cultivation. These include lactate, ammonium and the product concnetration.

```
% lge_simulation.m
% Simulates logistic GROWTH curves
% Inputs: time range, model parameters
% Outputs: vectors of dependent variable and its derivatives
% Uses lge_equation for function evaluation

% Chetan Goudar
% Last Modified: 6/18/04

% Model Parameters
k=[0.01053 0.44560 1.05743];

c1 = k(1); c2 = k(2); d2 = k(3);

% Definition of the Time Vector
tlow=0;
thigh = 10;
t = linspace(tlow,thigh,50)';

% Function Computation
y = lge_equation(k,t)

% Derivative and Specific Rate Computation
term1 = (c2/d2);
```

```
term2 = exp(-t./d2);
dydt  = (y.^2).*term1.*term2;
%%%%%%%%%%%%%%%%%%%%%%%%%%%%%%%%%%%%%%%%%%%%%%%%%%%%%%%%%%%%%%%%%%%%%%%%%%%%

function y = lge_equation(k,t)
% function y = lge_equation(k,time)
% Evaluates the 3-parameter logistic growth equation
% Inputs: model parameters, time vector
% Outputs: dependent variable vector

% Chetan Goudar
% Last Modified: 6/18/04

c1 = k(1); c2 = k(2); d2 = k(3);
x  = 1./(c1 + c2.*exp(-t./d2));
y  = x;
```

F.1.3 Logistic Decline Equation

The logistic decline equation has been used to describe the nutrients glucose and glutamine that monotonically decrease during cultivation.

```
% lde_simulation.m
% Simulates logistic DECLINE curves
% Inputs: time range, model parameters
% Outputs: vectors of dependent variable and its derivatives
% Uses lde_equation for function evaluation

% Chetan Goudar
% Last modified: 6/18/04

% Model Parameters
k=[0.07141 4.61711 0.00000];
c1 = k(1); d1 = k(2); c2 = k(3);

% Definition of the Time Vector
tlow  = 0;
```

```
thigh = 11;
t = linspace(tlow,thigh,51)';

% Function Computation
y = lde_equation(k,t);

% Derivative and Specific Rate Computation
term1 = (-c1/d1);
term2 = exp(t./d1);
dydt  = (y.^2).*term1.*term2;
%%%%%%%%%%%%%%%%%%%%%%%%%%%%%%%%%%%%%%%%%%%%%%%%%%%%%%%%%%%%%%%%%%%%%%%

function y = lde_equation(k,t)
% function y = lde_equation(k,time)
% Evaluates the 3-parameter logistic decline equation
% Inputs: model parameters, time vector
% Outputs: dependent variable vector

% Chetan Goudar
% Last Modified: 6/18/04

c1 = k(1); d1 = k(2); c2 = k(3);
x  = 1./(c1.*exp(t./d1) + c2);
y  = x;
```

F.2 Polynomial Fitting of Batch Culture Data

The programs in this section describe the fitting of cell culture data to polynomial functions. This method is frequently used in the literature and is conceptually similar to the logistic approach in that a functional form is used to approximate experimental data.

F.2.1 Fermentor Viable Cell Density

Polynomials of order 3 and 4 (4 and 5 parameters, respectively) were used to fit viable cell density data so that a comparison could be made between fits from the 4-parameter logistic equation.

```
%%%%%%%%%%%%%%%%%%%%%%PROGRAM START%%%%%%%%%%%%%%%%%%%%%%%%%%%%%%%%%%%%
% vcd_polyfit.m
% Fits polynomials to viable cell density data
% Inputs: vcd vs. time data
% Outputs: dependent variable, its derivatives and growth rate

% Chetan Goudar
% Last modified: 6/20/04

clear all

% Experimental Data

% Bayer CHO Data (1)
%t = [0.010 0.938 2.000 2.826 4.097 5.010 6.035 6.989 7.917...
%    8.722 9.826 10.951]';
%x = [0.97 1.69 2.27 3.65 5.35 5.87 6.23 6.67 5.14 5.88 3.66 ...
%     3.45]';       rsse = 1.6710;

% Bayer CHO Data (2)
%t = [0.000 0.917 2.003 2.878 4.128 5.184 6.142 6.986 8.038...
%    8.955 9.854]';
%x = [1.07 1.83 2.99 3.91 5.6 8.1 7.29 8.5 7.49 4.87 3.83]';
%    rsse = 2.3159;

% Bayer CHO Data (3)
%t = [0.000 1.104 2.042 3.003 4.035 5.080 5.962 7.021 8.031...
%    8.997 9.833 10.969]';
%x = [1.13 2.12 3.35 5.01 8.12 9.1 12 11.72 8.15 7.88 6.32 4.42]';
%rsse = 4.0789;

% Bree et al
%t = [0.050 0.850 1.850 2.980 3.880 4.860 5.820 6.820 7.810...
%    8.800 9.800 10.880]';
%x = [0.280 0.380 0.780 1.270 2.010 2.360 1.920 1.420 1.100...
%    0.560 0.480 0.290]'; rsse = 0.0586;
```

```
% Dalili et al
t = [0.029 0.429 0.666 1.557 1.888 2.440 2.971 3.456 3.963 4.518...
    4.969 5.536 6.651]';
x = [0.073 0.452 0.608 0.948 2.809 5.038 5.920 4.395 1.738 0.995...
    0.175 0.001 0.141]'; rsse = 0.8051;

% Linz et al
%t = [0.088 0.891 1.446 1.964 2.474 2.895 3.989 4.932 5.454 6.499...
%    7.029]';
%x = [0.283 0.346 0.913 1.036 1.502 1.705 1.526 1.690 1.611...
%    1.473 1.090]'; rsse = 0.1595

%%%%%%%%%%%%%%%%%%%%%%%%%%%%%%%%%%%%%%%%%%%%%%%%%%%%%%%%%%%%%%%%%%%%%%%%%%%%

% Polynomial Generation
p4 = polyfit(t,x,3);
p5 = polyfit(t,x,4);

% Generating Curves from Polynomial Fits
x4 = polyval(p4,t);
x5 = polyval(p5,t);

% Plotting the Data
plot(t,x,'o',t,x4,t,x5)
legend('Experimental Data','Order 3 Fit','Order 4 Fit',0)
title('Experimental Viable Cell Density Data and Polynomial Fits')
xlabel('Time (days)')
ylabel('Viable Cell Density (x E06 cells/mL)')

% Computing RSSE Values
rsse4 = sum((x4-x).^2);
rsse5 = sum((x5-x).^2);

rssedisplay = [rsse rsse4 rsse5]'
```

```
% COMPUTING mu' VALUES
% for p4
tfinal = 7.0;

t1  = linspace(0,tfinal,50)';
x4a = polyval(p4,t1);

a1 = p4(1); a2 = p4(2); a3 = p4(3);
dxdt4a = 3*a1*(x4a.^2) + 2*a2.*x4a + a3;
mu4a = dxdt4a./x4a;

dxdt4 = 3*a1*(x4.^2) + 2*a2.*x4 + a3;
%mu4 = dxdt4./x4

% for p5
tfinal = 7.0;

t1  = linspace(0,tfinal,50)';
x5a = polyval(p5,t1);

b1 = p5(1); b2 = p5(2); b3 = p5(3); b4 = p5(4);
dxdt5a = 3*a1*(x4a.^2) + 2*a2.*x4a + a3;
mu5a = dxdt5a./x5a;
%%%%%%%%%%%%%%%%%%%%%%PROGRAM END%%%%%%%%%%%%%%%%%%%%%%%%%%%%%%%%%%%%
```

F.2.2 Glucose

Glucose concentration is fit using polynomials of order 2 and 3 and the results are compared with those from the 3-parameter logistic decline equation.

```
%%%%%%%%%%%%%%%%%%%%%%PROGRAM START%%%%%%%%%%%%%%%%%%%%%%%%%%%%%%%%%%%%
% glucose_polyfit.m
% Fits polynomials to glucose data
% Inputs: glucose vs. time data
% Outputs: dependent variable, SSE

% Chetan Goudar
```

```
% Last modified: 6/20/04


clear all
% Experimental Data
% Bayer CHO Data (1)
%t = [0.01 0.94 2.00 2.83 4.10 5.01 6.03 6.99 7.92 8.72 9.83 10.95]';
%x = [62.05 61.90 57.36 53.02 46.77 41.01 36.94 33.49 31.52 30.03...
%26.15 26.08]'; rsse = 31.7931;

% Bayer CHO Data (2)
%t = [0.00 0.92 2.00 2.88 4.13 5.18 6.14 6.99 8.04 8.95 9.85]';
%x = [74.21 70.07 68.30 62.09 45.41 30.43 20.37 16.32 10.30 5.50...
%3.09]';     rsse = 31.0813;

% Bayer CHO Data (3)
%t = [0.000 1.104 2.042 3.003 4.035 5.080 5.962 7.021 8.031 8.997...
%9.833 10.969]';
%x = [70.758 70.284 66.701 62.123 52.451 43.706 27.389 20.338...
%13.195 8.401 4.931 1.500]';   rsse = 25.5818;

% Linz et al
t = [0.038 0.902 1.434 1.921 2.407 2.893 3.902 4.908 5.433 5.861...
        6.385 7.005]';
x = [9.084 8.016 6.797 5.164 3.669 2.173 0.973 0.185 0.067 0.084...
        0.103 0.127]';     rsse = 0.1145;

%%%%%%%%%%%%%%%%%%%%%%%%%%%%%%%%%%%%%%%%%%%%%%%%%%%%%%%%%%%%%%%%%%%%%%%%%%%%

% Polynomial Generation
p3 = polyfit(t,x,2);
p4 = polyfit(t,x,3);

% Generating Curves from Polynomial Fits
x3 = polyval(p3,t);
x4 = polyval(p4,t);
```

```
% Plotting the Data
plot(t,x,'o',t,x3,t,x4)
legend('Experimental Data','Order-2 Fit','Order-3 Fit')
title('Experimental Glucose Data and Polynomial Fits')
xlabel('Time (days)')
ylabel('Glucose (mM)')

% Computing RSSE Values
rsse3 = sum((x3-x).^2);
rsse4 = sum((x4-x).^2);
rssedisplay = [rsse rsse3 rsse4]'
%%%%%%%%%%%%%%%%%%%%%%PROGRAM END%%%%%%%%%%%%%%%%%%%%%%%%%%%%%%%%%%%%
```

F.2.3 Glutamine

Just as with glucose, glutamine concnetration data is fit with polynomials of order 2 and 3 and the results are compared with those obtained from the logistic decline equation

```
%%%%%%%%%%%%%%%%%%%%%%PROGRAM START%%%%%%%%%%%%%%%%%%%%%%%%%%%%%%%%%%%%
% glutamine_polyfit.m
% Fits polynomials to glutamine data
% Inputs: glucose vs. time data
% Outputs: dependent variable, SSE

% Chetan Goudar
% Last modified: 6/20/04

clear all
% Experimental Data
% Bayer CHO Data (1)
%t = [0.010 0.938 2.000 2.826 4.097 5.010 6.035 6.989 7.917 8.722...
%     9.826 10.951]';
%x = [13.766 11.472 9.901 7.747 5.366 4.034 3.077 2.645 2.715...
%    2.593 2.094 2.245]';        rsse = 3.4126;

% Bayer CHO Data (2)
```

```
%t = [0.000 0.917 2.003 2.878 4.128 5.184 6.142 6.986 8.038 8.955 9.854]';
%x = [14.130 12.103 9.968 7.520 3.572 1.444 0.716 0.951 0.950 1.008...
%       0.899]';       rsse = 2.8701;

% Bayer CHO Data (3)
%t = [0.000 1.104 2.042 3.003 4.035 5.080 5.962 7.021 8.031 8.997...
%       9.833 10.969]';
%x = [13.903 11.900 9.976 7.843 5.234 2.868 1.742 1.212 0.936...
%       0.932 0.943 0.825]';       rsse = 1.7139;

% Bree et al
%t = [0.07 0.85 1.85 2.96 3.9 4.85 5.82 6.81 7.8 8.79 9.81]';
%x = [2.65 2.49 1.95 1.13 0.67 0.09 0.1 0.05 0.17 0.11 0.08]';
%rsse = 0.0765;

% Dalili et al
t = [0.02 0.45 0.674 1.565 1.937 2.934 3.422 3.896 4.459 5.615 6.623]';
x = [0.498 0.492 0.394 0.298 0.193 0.008 0 0.006 0.005 0.009 0.007]';
rsse = 0.00491;

% Linz et al
%t = [0.095 0.947 1.468 1.989 2.462 2.936 3.883 4.972 5.445 5.966...
%   6.392 7.055]';
%x = [4.977 3.954 3.628 3.116 2.698 2.326 2.093 1.861 1.628 1.349...
%   1.07 0.837]'; rsse = 0.2336
%%%%%%%%%%%%%%%%%%%%%%%%%%%%%%%%%%%%%%%%%%%%%%%%%%%%%%%%%%%%%%%%%%%%%%%%%%%%%%%

% Polynomial Generation
p3 = polyfit(t,x,2);
p4 = polyfit(t,x,3);

%Generating Curves from Polynomial Fits
x3 = polyval(p3,t);
x4 = polyval(p4,t);

%Plotting the Data
```

```
plot(t,x,'o',t,x3,t,x4)
legend('Experimental Data','Order-2 Fit','Order-3 Fit',0)
title('Experimental Glutamine Data and Polynomial Fits')
xlabel('Time (days)')
ylabel('Glutamine (mM)')

% Computing RSSE Values
rsse3 = sum((x3-x).^2);
rsse4 = sum((x4-x).^2);
rssedisplay = [rsse rsse3 rsse4 rsse5]'

% Computing Degrees of Freedom
d4 = n-4;
d5 = n-5;

% COMPUTING SIMULATED GLUTAMINE VALUES
tfinal = 7.0;
t1  = linspace(0,tfinal,50)';
x3a = polyval(p3,t1)
x4a = polyval(p4,t1);
%%%%%%%%%%%%%%%%%%%%%%PROGRAM END%%%%%%%%%%%%%%%%%%%%%%%%%%%%%%%%%%%%
```

F.2.4 Lactate

The concnetration of lactate increases monotonically and polynomials of order 2 and 3 have been used to describe this profile. These are subsequently compared with results from the 3-parameter logistic growth equation.

```
%%%%%%%%%%%%%%%%%%%%%%PROGRAM START%%%%%%%%%%%%%%%%%%%%%%%%%%%%%%%%%%%%
% lactate_polyfit.m
% Fits polynomials to lactate data
% Inputs: lactate vs. time data
% Outputs: dependent variable, SSE

% Chetan Goudar
% Last modified: 6/20/04
```

```
clear all
% Experimental Data
% Bayer CHO Data (1)
%t = [0.01 0.94 2.00 2.83 4.10 5.01 6.03 6.99 7.92 8.72 9.83 10.95]';
%x = [0.84 4.87 10.92 15.67 23.22 26.44 27.56 28.89 29.11 30.67...
%     30.00 30.56]';   rsse = 5.3675;

% Bayer CHO Data (2)
%t = [0.00 0.92 2.00 2.88 4.13 5.18 6.14 6.99 8.04 8.95 9.85]';
%x = [0.94 2.79 5.28 10.13 19.78 24.11 26.22 28.33 29.22 31.56...
%     33.11]';  rsse = 11.9479;

% Bayer CHO Data (3)
%t = [0.000 1.104 2.042 3.003 4.035 5.080 5.962 7.021 8.031 8.997...
%       9.833 10.969]';
%x = [1.033 2.956 4.944 8.500 13.556 17.778 21.333 23.333 25.111...
%26.000 26.889 26.333]'; rsse = 0.9818;

% Linz et al
t = [0.038 0.902 1.434 1.921 2.407 2.893 3.902 4.908 5.433 5.861...
        6.385 7.005]';
x = [0.002 2.098 4.457 7.503 7.521 9.88 11.708 14.358 13.413...
        13.022 12.35 12.373]';     rsse = 7.0979;

%%%%%%%%%%%%%%%%%%%%%%%%%%%%%%%%%%%%%%%%%%%%%%%%%%%%%%%%%%%%%%%%%%%%%%%%%%%%

% Polynomial Generation
p3 = polyfit(t,x,2);
p4 = polyfit(t,x,3);

% Generating Curves from Polynomial Fits
x3 = polyval(p3,t);
x4 = polyval(p4,t);

% Plotting the Data
plot(t,x,'o',t,x3,t,x4)
```

```
legend('Experimental Data','Order-2 Fit','Order-3 Fit',0)
title('Experimental Lactate Data and Polynomial Fits')
xlabel('Time (days)')S
ylabel('Lactate (mM)')

% Computing RSSE Values
rsse3 = sum((x3-x).^2);
rsse4 = sum((x4-x).^2);
rssedisplay = [rsse rsse3 rsse4]'
%%%%%%%%%%%%%%%%%%%%%%PROGRAM END%%%%%%%%%%%%%%%%%%%%%%%%%%%%%%%%%%%%
```

F.2.5 Ammonium

Polynomial fitting for the ammonium data set is similar to that for lactate given their similar monotonically increasing profiles

```
%%%%%%%%%%%%%%%%%%%%%%PROGRAM START%%%%%%%%%%%%%%%%%%%%%%%%%%%%%%%%%%%%
% ammonium_polyfit.m
% Fits polynomials to lactate data
% Inputs: ammonium vs. time data
% Outputs: dependent variable, SSE

% Chetan Goudar
% Last modified: 6/20/04

clear all
% Experimental Data
% Bayer CHO Data (1)
%t = [0.010 0.938 2.000 2.826 4.097 5.010 6.035 6.989 7.917 8.722...
%       9.826 10.951]';
%x = [0.175 1.050 1.938 3.363 4.425 4.519 5.719 6.206 6.656 6.850...
%       7.400 6.656]';        rsse = 1.3834;

% Bayer CHO Data (2)
%t = [0.000 0.917 2.003 2.878 4.128 5.184 6.142 6.986 8.038 8.955...
%       9.854]';
%x = [1.120 1.990 2.990 4.270 5.630 9.140 7.500 7.960 8.960 9.280...
```

```
%       8.600]';        rsse = 4.3601;

% Bayer CHO Data (3)
%t = [0.000 1.104 2.042 3.003 4.035 5.080 5.962 7.021 8.031 8.997...
%       9.833 10.969]';
%x = [0.480 2.060 4.210 5.160 5.460 7.200 13.500 14.200 16.160...
%       17.360 17.560 19.360]'; rsse = 12.4441;

% Bree et al
%t = [0.07 1.84 2.96 3.87 4.85 5.82 6.81 7.82 8.77 9.81]';
%x = [0.78 1.28 1.71 2.18 2.65 2.23 2.45 2.43 2.44 2.65]';
% rsse = 0.2278;

% Linz et al
t = [0.047 0.852 1.42 1.894 2.367 2.983 3.883 4.972 5.445 5.966...
        6.44 7.008]';
x = [0.279 0.744 0.977 1.256 1.488 1.721 2.093 2.326 2.837...
        3.349 3.814 4]';     rsse = 0.3573;

%%%%%%%%%%%%%%%%%%%%%%%%%%%%%%%%%%%%%%%%%%%%%%%%%%%%%%%%%%%%%%%%%%%%%%%%%%%%

% Polynomial Generation
p3 = polyfit(t,x,2);
p4 = polyfit(t,x,3);

% Generating Curves from Polynomial Fits
x3 = polyval(p3,t);
x4 = polyval(p4,t);

% Plotting the Data
plot(t,x,'o',t,x3,t,x4)
legend('Experimental Data','Order-2 Fit','Order-3 Fit',0)
title('Experimental Ammoniumn Data and Polynomial Fits')
xlabel('Time (days)')
ylabel('Ammonia (mM)')
```

```
% Computing RSSE Values
rsse3 = sum((x3-x).^2);
rsse4 = sum((x4-x).^2);
rssedisplay = [rsse rsse3 rsse4 rsse5]'
%%%%%%%%%%%%%%%%%%%%%%PROGRAM END%%%%%%%%%%%%%%%%%%%%%%%%%%%%%%%%%%%%
```

F.2.6 Product

Product concentration is described by polynomials of order 2 and 3 and these results are compared with those from the logistic growth equation.

```
%%%%%%%%%%%%%%%%%%%%%%PROGRAM START%%%%%%%%%%%%%%%%%%%%%%%%%%%%%%%%%%%%
% product_polyfit.m
% Fits polynomials to product data
% Inputs: product vs. time data
% Outputs: dependent variable, SSE

% Chetan Goudar
% Last modified: 6/20/04

clear all
% EXPERIMENTAL DATA

% Bayer CHO1 Data (1)
t = [0.010 0.938 2.000 2.826 4.097 5.010 6.035 6.989 7.917 8.722...
    9.826 10.951]';
x = [12.000 12.000 16.000 19.000 66.000 51.000 63.000 95.000 119.000...
    150.000 194.000 182.000]';  rsse = 1630.66;

% Bayer CHO Data (2)
%t = [0.000 0.917 2.003 2.878 4.128 5.184 6.142 6.986 8.038 8.955 9.854]';
%x = [6.100 6.100 10.800 24.500 51.400 74.600 83.200 87.600 91.100
%    95.500 96.600]';rsse = 42.2229;

% Bayer CHO Data (3)
%t = [0.000 1.104 2.042 3.003 4.035 5.080 5.962 7.021 8.031 8.997 9.833...
%    10.969]';
```

```
%x = [6.100 6.100 14.200 31.800 53.400 80.000 115.000 120.000 125.000...
%    126.000 129.000 135.000 ]'; rsse = 170.2958;

% Bree et al
%t = [0.02 0.83 1.82 2.93 3.85 4.82 5.8 6.81 7.82 8.82 9.83 10.91]';
%x = [0.08 0.11 0.12 0.36 21.94 43.93 69.22 90.39 103.48 104.37 104.38...
%    104.46]';     rsse = 79.7789;

% Dalili et al
%t = [0 0.398 0.681 1.531 1.918 2.942 3.448 3.928 4.453 5.588 6.665]';
%x = [0 0.526 0.671 1.746 2.675 6.382 7.525 6.393 5.83 6.553 5.995]';
%rsse = 2.6924

%%%%%%%%%%%%%%%%%%%%%%%%%%%%%%%%%%%%%%%%%%%%%%%%%%%%%%%%%%%%%%%%%%%%%%%%%%%%

% POLYNOMIAL GENERATION
p3 = polyfit(t,x,2);
p4 = polyfit(t,x,3);

% GENERATING CURVES FROM POLYNOMIAL FITS
x3 = polyval(p3,t);
x4 = polyval(p4,t);

% PLOTTING THE DATA
plot(t,x,'o',t,x3,t,x4)
legend('Experimental Data','Order 2 Fit','Order 3 Fit',0)
title('Experimental Titer Data and Corresponding Polynomial Fits')
xlabel('Time (days)')
ylabel('Titer (Arbitrary Units)')
%ylabel('Titer (mg/L)')

% COMPUTING RSSE VALUES
rsse3 = sum((x3-x).^2);
rsse4 = sum((x4-x).^2);
rssedisplay = [rsse rsse3 rsse4]'
```

```
% COMPUTING SIMULATED TITER VALUES
tfinal = 7.0;
t1  = linspace(0,tfinal,50)';
x3a = polyval(p3,t1);
x4a = polyval(p4,t1);


% COMPUTING DERIVATIVES
a1 = p3(1); a2 = p3(2);
dxdt3a = 2*a1.*x3a + a2;

b1 = p4(1); b2 = p4(2); b3 = p4(3);
dxdt4a = 3*b1*(x4a.^2);
%%%%%%%%%%%%%%%%%%%%%%PROGRAM END%%%%%%%%%%%%%%%%%%%%%%%%%%%%%%%%%%%%
```

F.3 Nonlinear Parameter Estimation in Logistic Models

The generalized logistic equation and its reduced forms are nonlinear and an itereative approach is required to estimate their parameters. The following program describes fitting experimental data to the 4-parameter GLE and an identical approach can be used for the LGE and LDE.

F.3.1 Generalized Logistic Equation

```
%%%%%%%%%%%%%%%%%%%%%%PROGRAM START%%%%%%%%%%%%%%%%%%%%%%%%%%%%%%%%%%%%
% gle_fit.m
% Fits VCD data to the logistic equation
% Inputs: fvcd vs. time data, parameter estimates
% Outputs: best fit parameters, fit stastics

% Chetan Goudar
% Last modified: 6/20/04

% USES curvefit1, gle_solution
% curvefit1 uses cubici11,cubici31,lsint1,searchq1
```

```
%%%%%%%%%%%%%%%%%%%%%%%%%%%%%%%%%%%%%%%%%%%%%%%%%%%%%%%%%%%%%%%%%%%%%%%%%%%%
%INPUT INFORMATION
prompt1  = {'datafile: Name of file containing experimental data'};
title1   = 'Input for gle_fit';
lineNo1  = 1;
input1   = inputdlg(prompt1,title1,lineNo1);
datafile = num2str(input1{1,1});

%%%%%%%%%%%%%%%%%%%%%%%%%%%%%%%%%%%%%%%%%%%%%%%%%%%%%%%%%%%%%%%%%%%%%%%%%%%%

% READING EXPERIMENTAL DATA
fid=fopen(datafile,'r');
A=fscanf(fid,'%e %e',[2,inf])';
fclose(fid);
t=A(:,1);
fvcd=A(:,2);
%%%%%%%%%%%%%%%%%%%%%%%%%%%%%%%%%%%%%%%%%%%%%%%%%%%%%%%%%%%%%%%%%%%%%%%%%%%%

% NONLINEAR PARAMETER ESTIMATION

% Initial kinetic parameter estimates
k0=[1 1 1 1]';

disp('Initial Kinetic Parameter Estimates')
disp(k0')
disp('Computing "Optimal" Kinetic Parameters. Please Wait')
disp('')

% Optimization
[kfinal,options,error,jac]=...
   curvefit1('gle_solution',k0,t,fvcd);

iters=options(10);
disp('Number of Iterations')
```

```
      disp(iters)


% 1. GENERAL OUTPUT
error;
ymodel=fvcd+error;
disp('Final Estimates of Kinetic Parameters')
disp(kfinal')

% 2. STATISTICAL OUTPUT
ydata=fvcd;
yfit=ymodel;
param=kfinal;

% 2.1 RESIDUAL SUM OF SQUARES ERROR (rsse)
     e=yfit-ydata;
     rsse=e'*e;
     disp('Residual Sum of Squares Error')
     disp(rsse)

% 2.2 RESUDUAL MEAN SQUARE (rms)
     m=length(yfit);
     n=length(param);

if (m~=n)
   rms=rsse./(m-n);
else
   var=NaN;
end
     disp('Residual Mean Square')
     disp(rms)

% 2.3 COVARIANCE MATRIX (cm)
      xtx=jac'*jac;
      cm=inv(xtx);
      disp('Covariance Matrix')
```

```
      disp(cm)

% 2.4 VARIANCE INFLATION FACTOR (varinf)
      varinf = diag(cm);

% 2.5 PARAMETER CORRELATION MATRIX, PCM (pcm)
      pcm = cm./sqrt(varinf*varinf');
      disp('Correlation Matrix for Parameters ')
      disp(pcm)

% 2.6 STANDARD ERROR OF PARAMETERS (std)
      vcv=cm.*rms;
      std=sqrt(diag(vcv));
      disp('Standard Error for Parameters ')
      disp(std')
      disp('95% Confidence Interval for Parameters ')
      disp(2*std')

% PLOTTING THE OUTPUT

% 1. EXPERIMENTAL DATA vs MODEL PREDICIONS

figure
subplot(2,1,1)
plot(t,ymodel,t,yfit,'o')
xlabel('Time');ylabel('FVCD')
legend('Model Prediction', 'Experimental data')
title('Comparison of Experimental Data and Model Fit')

% 2. RESIDUAL PLOT
yzero=linspace(0,0,m);
subplot(2,1,2)
plot(t,yzero,t,error,'o')
xlabel('Time'); ylabel('Error')
title('Residual Plot')
%%%%%%%%%%%%%%%%%%%%%%%%PROGRAM END%%%%%%%%%%%%%%%%%%%%%%%%%%%%%%%%%%%%
```

F.4 Integral Viable Cell Density

An approximation to the integral viable cell density can be obtained by integrating Eq.(6.5)

$$\int X dt = \frac{Ae^{Dt}}{CD} H(t) \tag{F.1}$$

where

$$H(t) = F\left\{1, \frac{D}{B+D}, \frac{B+2D}{B+D}, -\frac{e^{(B+D)t}}{C}\right\} \tag{F.2}$$

is a hypergeometric function of the form $F\{a, b, c, z\}$with the series expansion

$$F\{a, b, c, z\} = \sum_{k=0}^{\infty} (a)_k \frac{(b)_k z^k}{(c)_k k!} \tag{F.3}$$

Appendix G

Parameter Estimation in Logistic Equations

Application of the logistic equations for describing batch and fed-batch data has been presented in Chapter 6. All 3 logistic equations (4 parameter generalized, logistic growth and logistic decline) are nonlinear with respect to their parameters requiring the use of nonlinear least squares for parameter estimation. Since nonlinear least squares is iterative, initial parameter estimates are necessary. It is important the initial estimates be reasonably accurate because the exponential terms in the logistic equations make the model sensitive to parameter variation. Since solution convergence during nonlinear parameter estimation is often influenced by the choice of initial estimates, a consistent method of initial parameter estimation is desirable. Methods to obtain initial parameter estimates are presented and a comparison between commonly used nonlinear parameter estimation algorithms is also made.

G.1 Initial Parameter Estimates

Initial parameter estimates in nonlinear equations are typically obtained by a linear transformation followed by linear least squares analysis. The 4-parameter generalized logistic equation describes cell density profiles in batch and fed-batch cultures

$$X = \frac{A}{\exp(Bt) + C\exp(-Dt)} \tag{G.1}$$

where X, the cell density, is a nonlinear function of the unknown parameters A, B, C and D and t is time. Eq.(G.1) can describe both the cell growth and death phases and can be

modified to reflect only the growth phase as

$$X = \frac{A}{C\exp(-Dt)} \tag{G.2}$$

which can be rearranged as

$$\ln(X) = Dt + \ln\left(\frac{A}{C}\right) \tag{G.3}$$

It follows from Eq.(G.3) that a plot of $\ln(X)$ versus t is linear with a slope of D and $\ln\left(\frac{A}{C}\right)$ as intercept. Eq.(G.1) can be simplified to reflect only the death phase

$$X = \frac{A}{\exp(Bt)} \tag{G.4}$$

which can be linearized as

$$\ln(X) = -Bt + \ln(A) \tag{G.5}$$

such that a plot of $\ln(X)$ versus t has $-B$ as slope and $\ln(A)$ as intercept. Thus initial estimates of A and B can be obtained from a plot of Eq.(G.5) and those for C and D from Eq.(G.3).

The logistic growth equation describes monotonically increasing quantities such as lactate, ammonium and product concentrations (P) in batch and fed-batch systems

$$P = \frac{A}{1 + C\exp(-Dt)} \tag{G.6}$$

Setting $\frac{dP}{dt} = 0$ results in $A = P_{\max}$, the maximum value of P such that Eq.(G.6) can be rewritten as

$$\ln\left(\frac{P_{\max} - P}{P}\right) = -Dt + \ln(C) \tag{G.7}$$

Estimates of C and D can be obtained from the intercept and slope of Eq.(G.7).

The logistic decline equation describes monotonically decreasing quantities such as glucose and glutamine concentrations

$$N = \frac{A}{\exp(-Bt) + C} \tag{G.8}$$

and can be reduced to a form analogous to the logistic growth equation by substituting $\frac{A}{C} = A'$, $-B = B'$, $\frac{1}{C} = C'$

$$N = \frac{A'}{1 + C'\exp(-B't)} \tag{G.9}$$

Initial parameter estimates for the logistic decline equation can be obtained from an expression analogous to Eq.(G.7).

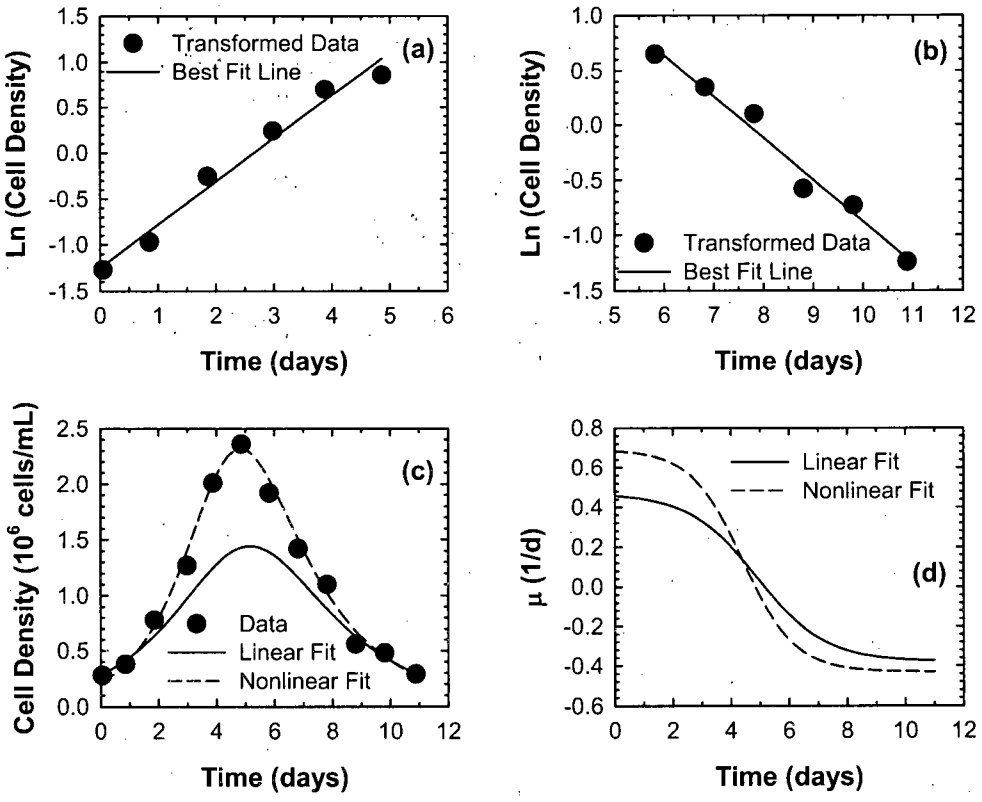

Figure G.1: Parameter estimation by the linear and nonlinear methods for cell density data of Bree et al., (1988).

G.2 Final Parameter Estimation

A comparison was made between three commonly used nonlinear parameter estimation techniques. The Levenberg-Marquardt (LM) method requires gradient calculation and is the most widely used algorithm for nonlinear parameter estimation. The simplex method does not require derivatives and can sometimes be more robust than gradient-based methods. Most commercial nonlinear regression software use the Levenberg-Marquardt and Simplex methods. The generalized reduced gradient (GRG) method was also evaluated as it is used by the Solver utility in Microsoft Excel. Since Microsoft Excel is widely used to record

experimental data, success with the GRG method would greatly simplify analysis of batch and fed-batch data.

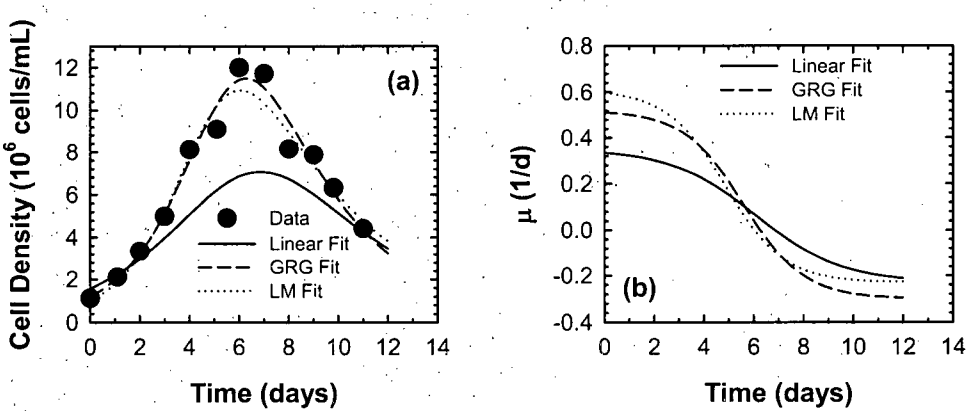

Figure G.2: Comparison of linear and 2 nonlinear fits to batch CHO cell density data.

G.3 Generalized Logistic Equation

The 4-parameter generalized logistic equation has been used to fit cell density data from multiple batch and fed-batch data sets (Chapter 6). A total of 16 cell density data sets were examined and the results are shown in Tables G1 – G3. In 14 of the 16 data sets, estimates of parameters A, B, C and D by the LM method were different than those from the simplex and GRG methods (Parameter estimates from the simplex and GRG methods were virtually identical for all data sets). While a reduction in the residual sum of squares error (RSSE) was seen for all 3 nonlinear parameter estimation methods when compared to the initial estimates, RSSE values from the simplex and GRG methods were lower than those for the LM method. Based on this difference, we can conclude that the simplex and GRG methods better fit experimental cell density data. It is important to note that the solutions converged for all 16 data sets examined indicating that the proposed linearization of the GLE resulted in representative initial parameter estimates.

Figure G.1 shows application of the nonlinear parameter estimation procedure to the cell density data in Bree et al., (1998). Linearized plots for the cell growth and death phases corresponding to Eqs.(G.3) and (G.5) are shown in Figures G.1a and G.1b, respectively, where log-transformed experimental data are well described by the linear fits. Linear and nonlinear fits to experimental data are shown in Figure G.1c and clearly highlight the

superiority of the nonlinear fit. This is an important observation because the inadequacy of the linear fit in Figure G.1c is not evident in the linear fits to transformed data in Figure G.1a and G.1b (This general trend was true for all other data sets and is also reflected in the lower RSSE values for the nonlinear fits). Substantial differences in growth rate time courses are seen (Figure G.1d) for the linear and nonlinear fits. The Figure G.1 results cleary indicate that linearization alone will not provide satisfactory fits to experimental cell density data and improvement of these initial parameter estimates by nonlinear least squares is necessary.

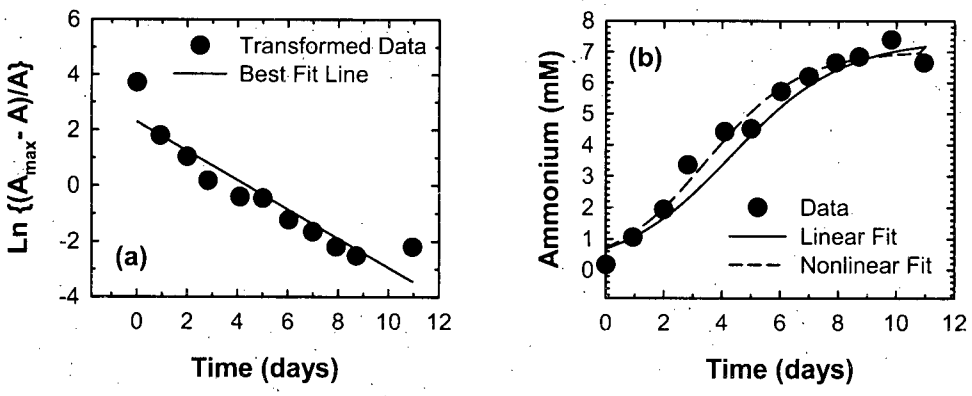

Figure G.3: Initial parameter estimation (panel a) and comparison of linear and nonlinear fits (panel b) to ammonium concentration data for CHO cells in batch culture.

Parameter estimates from the LM method were in most cases different than those from the simplex and GRG methods (Tables G1 – G3). The impact of these differences on the ability to describe experimental data is shown in Figure G.2 for CHO cells in batch culture The corresponding parameter estimates are in Table G1, CHO cells (C). While both nonlinear fits were substantial improvements over the linear fit, the GRG fit was visually a slightly better fit to experimental data than the LM method (Figure G.2a). This is also reflected in the lower RSSE for the GRG method (4.08 versus 5.36; Table G1).

G.4 Logistic Growth Equation

The logistic growth equation describes monotonically increasing quantities such as ammonium, lactate and product concentrations in batch and fed-batch cultures. Eq.(G.7) was used to obtain initial parameter estimates for 6 sets of ammonium concentration data which

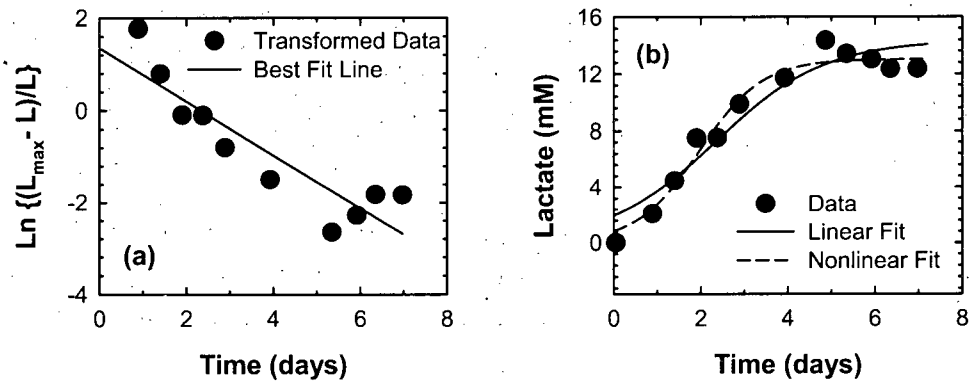

Figure G.4: Initial parameter estimation (panel a) and comparison of linear and nonlinear fits (panel b) for lactate concentration data of Linz et al., (1997).

were subsequently used as starting points for nonlinear parameter estimation. Unlike with the GLE, nonlinear parameter estimates from all 3 methods were identical and a comparison with the initial estimates is shown in Table G4. All nonlinear fits had lower RSSE values than the corresponding linear fits suggesting improved description of experimental data (Table G4). A comparison of linear and nonlinear fits for CHO cells in batch culture is shown in Figure G.3.

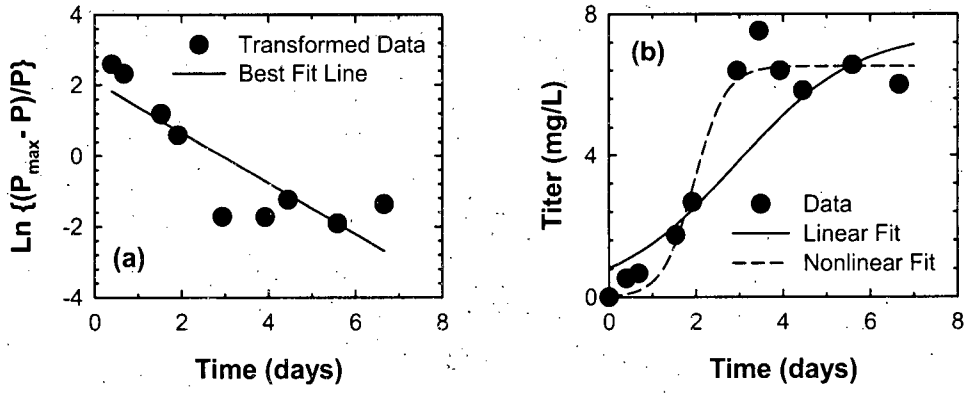

Figure G.5: Initial parameter estimation (panel a) and comparison of linear and nonlinear fits (panel b) for product concentration data of Dalili et al., (1990).

Lactate concentration data from 5 different studies were also described by the logistic

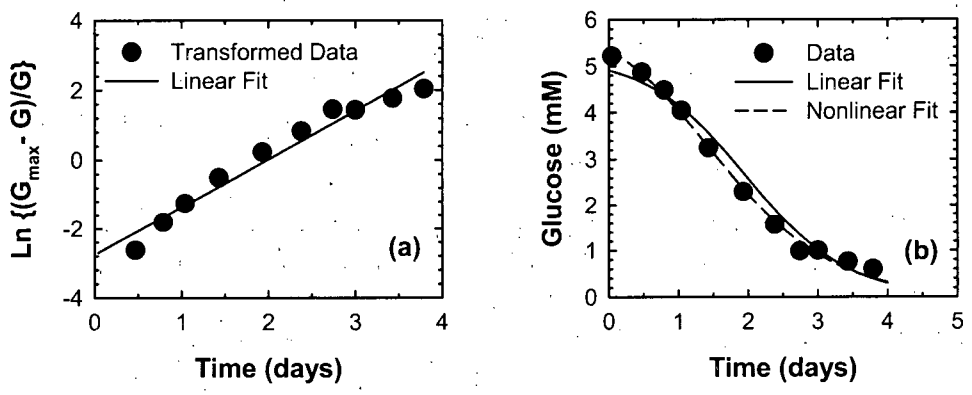

Figure G.6: Initial parameter estimation (panel a) and comparison of linear and nonlinear fits (panel b) for glucose concentration data of Ljumggren and Häggström (1994).

growth equation and estimates of A, C and D from the 3 nonlinear methods were identical (Table G5). Substantial RSSE reduction was seen for all data sets reflecting improved fits to experimental data. A plot of the linear fit to transformed lactate concentration data is shown in Figure G.4a and a comparison of linear and nonlinear fits to lactate concentration data is shown in Figure G.4b.

Six product concentration data sets were also described by the logistic growth equation and the results as shown in Table G6. As with previous data from the LGE (Tables G4 and G5), the nonlinear fits were characterized by substantially reduced RSSE and were better fits to experimental data. The linear fit to transformed product concentration data from Dalili et al., (1990) is shown in Figure G.5a and the linear and nonlinear fits to product concentration data in Figure G.5b. The nonlinear fit was clearly a much improved representation of the experimental data (Figure G.5b).

G.5 Logistic Decline Equation

Monotonically decreasing glucose and glutamine concentrations were described by the LDE and the inital parameter estimation method was identical to that for the LGE using modified parameter definitions (Eq. G.9). A total of 5 glucose concentration data sets were analyzed and the results are shown in Table G7 and Figure G.6. Parameter estimates from the Simplex and GRG methods were identical but different from the LM estimates. Both sets of estimates, however, had lower RSSE values than the corresponding linear fits (Table G7).

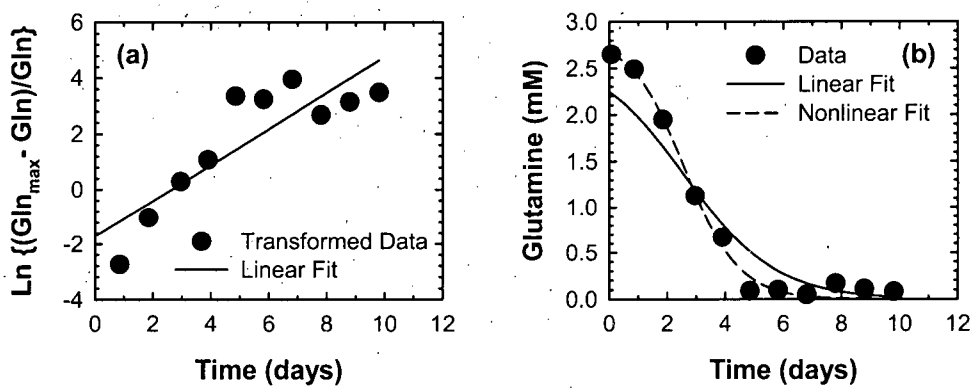

Figure G.7: Initial parameter estimation (panel a) and comparison of linear and nonlinear fits (panel b) for glutamine concentration data of Bree et al., (1988).

Six glutamine concentration data sets were also described by the LDE. As with the glucose data sets in Table G7, parameter estimates from the Simplex and GRG methods were identical and different from the LM method (Table G8). Both sets of estimates, however, were substantial improvements over the linear parameter estimates (Figure G.7).

G.6 Conclusions

A simple approach for fitting logistic equations to batch and fed-batch data was presented and verified. Linearized forms of the logistic equations were derived from which initial parameter estimates were obtained. These initial estimates were used as starting points for nonliner least squares and three commonly used algorithms were tested. For all 44 data sets examined, the nonlinear parameter estimation algorithms converged on a solution suggesting that the logistic equations can be reliably used to describe experimental data. Parameter estimates from the Simplex and GRG methods were in most cases very similar but different than those from the LM method. In all cases, the Simplex/GRG estimates were characterized by lower RSSE values and hence were better fits to experimental data. For robust logistic modeling, we recommend initial parameter estimation using the linearization approaches presented in this sudy. These preliminary parameter estimates can be refined using either the Simplex or GRG methods resulting in robust fits to experimental data from which specific rates can be determined.

Table G.1: Comparison of GLE Parameter Estimates for Cell Density Data from Linear and Non-linear Parameter Estimation

Data Source	**Parameter**	**Parameter Estimation Method**			
		Linear	GRG	LM	Simplex
Bree et al., (1988)	A	18.52	30.13	29.39	30.13
	B	0.38	0.43	0.43	0.43
	C	64.78	140.52	139.43	140.53
	D	0.47	0.69	0.69	0.69
	RSSE	1.93	0.06	0.06	0.06
Dalili et al., (1990)	A	119.49	1708.69	124.59	1710.2
	B	1.09	1.7	0.98	1.7
	C	432.29	12166.06	649.08	12172.4
	D	1.09	1.54	1.56	1.54
	RSSE	21.20	0.81	4.0511	0.81
Linz et al., (1997)	A	4.36	3.02	3.03	3.02
	B	0.18	0.12	0.12	0.12
	C	18.97	15.93	15.93	15.93
	D	0.74	1.25	1.25	1.25
	RSSE	1.02	0.16	0.16	0.16
CHO Cells (A)	A	21.35	32.7	22.19	32.71
	B	0.17	0.21	0.17	0.21
	C	13.30	30.40	22.79	30.40
	D	0.23	0.49	0.56	0.49
	RSSE	38.43	1.67	1.81	1.67
CHO Cells (B)	A	70.80	334.46	70.28	335.00
	B	0.29	0.45	0.28	0.45
	C	49.62	242.92	62.19	243.24
	D	0.34	0.37	0.48	0.37
	RSSE	25.99	2.32	3.19	2.32
CHO Cells (C)	A	56.77	119.13	60.37	115.46
	B	0.23	0.30	0.23	0.30
	C	35.14	99.07	59.95	94.46
	D	0.35	0.52	0.61	0.52
	RSSE	70.37	4.08	5.36	4.34

Table G.2: Comparison of GLE Parameter Estimates for Cell Density Data from Linear and Nonlinear Parameter Estimation

Data Source	Parameter	Parameter Estimation Method			
		Linear	GRG	LM	Simplex
Dowd et al., (2000)	A	49.29	38.21	46.44	35.32
(Figure 4; batch data)	B	1.06	1.00	1.03	0.98
	C	207.18	209.93	212.52	195.31
	D	0.56	0.87	0.77	0.88
	RSSE	0.16	0.02	0.02	0.02
Dowd et al., (2000)	A	20.59	72.29	25.31	71.62
(Figure 5; batch data)	B	0.75	1.00	0.77	1.00
	C	88.61	395.21	150.76	391.9
	D	0.68	0.86	0.97	0.86
	RSSE	0.38	0.01	0.02	0.01
Dowd et al., (2000)	A	1.91	2.81	2.68	2.81
(Figure 2; 3 pmol case)	B	0.13	0.19	0.18	0.19
	C	8.40	19.52	18.73	19.51
	D	0.45	0.96	0.98	0.96
	RSSE	0.77	0.08	0.08	0.08
Dowd et al., (2000)	A	3.75	6.82	5.18	6.83
(Figure 2; 4 pmol case)	B	0.24	0.32	0.27	0.32
	C	16.01	37.62	29.75	37.62
	D	0.45	0.72	0.78	0.72
	RSSE	0.65	0.01	0.01	0.01
Dowd et al., (2000)	A	9.70	13.02	9.73	13.02
(Figure 2; 5 pmol case)	B	0.43	0.48	0.43	0.48
	C	53.34	114.71	83.31	114.73
	D	0.49	0.80	0.81	0.80
	RSSE	0.47	0.20	0.20	0.20
Dowd et al., (2000)	A	4.41	9.53	5.98	9.60
(Figure 4; case E)	B	0.23	0.34	0.27	0.34
	C	15.88	57.16	33.99	57.36
	D	0.43	0.77	0.82	0.77
	RSSE	1.21	0.18	0.20	0.18

Table G.3: Comparison of GLE Parameter Estimates for Cell Density Data from Linear and Non-linear Parameter Estimation

Data Source	**Parameter**	**Parameter Estimation Method**			
		Linear	GRG	LM	Simplex
Dowd et al., (2000)	A	8.93	32.15	14.39	32.57
(Figure 4; Case F)	B	0.33	0.48	0.37	0.48
	C	20.80	107.47	52.91	108.81
	D	0.27	0.48	0.56	0.47
	RSSE	1.44	0.08	0.10	0.08
Dowd et al., (2000)	A	3.73	21.48	7.58	21.7
(Figure 4; Case G)	B	0.23	0.46	0.30	0.46
	C	8.74	95.18	34.05	96.03
	D	0.30	0.65	0.76	0.65
	RSSE	2.43	0.31	0.39	0.30
Dowd et al., (2000)	A	14.72	26.38	20.83	26.53
(Figure 5; fed-batch)	B	0.29	0.38	0.34	0.38
	C	63.31	166.18	137.48	166.34
	D	0.72	0.98	1.03	0.99
	RSSE	3.11	0.07	0.08	0.07
Ljumggren and Häggström (1994)	A	3.29	5.68	4.12	6.92
	B	0.38	0.53	0.43	0.58
	C	22.29	61.43	41.68	63.68
	D	0.93	1.57	1.61	1.43
	RSSE	0.80	0.01	0.01	0.01

Table G.4: Comparison of LGE Parameters for Ammonium Concentration Data from Linear and Nonlinear Parameter Estimation

Data Source	**Parameter**	**Parameter Estimation Method**	
		Linear	Nonlinear
Bree et al., (1988)	A	2.65	2.55
	C	1.86	2.94
	D	0.40	0.68
	RSSE	0.46	0.23
Linz et al., (1997)	A	4.00	7.68
	C	9.95	11.62
	D	0.67	0.36
	RSSE	0.88	0.36
CHO Cells (A)	A	7.40	7.04
	C	9.88	8.87
	D	0.52	0.62
	RSSE	3.39	1.38
CHO Cells (B)	A	9.28	8.98
	C	5.76	8.01
	D	0.52	0.71
	RSSE	6.99	4.36
CHO Cells (C)	A	19.36	20.05
	C	19.75	16.90
	D	0.57	0.52
	RSSE	12.97	12.44
Ljumggren and Häggström (1994)	A	3.59	4.51
	C	7.52	6.28
	D	1.45	0.89
	RSSE	0.76	0.26

Table G.5: Comparison of LGE Parameters for Lactate Concentration Data from Linear and Nonlinear Parameter Estimation

Data Source	**Parameter**	**Parameter Estimation Method**	
		Linear	Nonlinear
Linz et al., (1997)	A	14.36	13.04
	C	6.32	14.70
	D	0.79	1.38
	RSSE	17.81	7.10
CHO Cells (A)	A	30.67	29.89
	C	10.45	11.88
	D	0.71	0.91
	RSSE	38.77	5.37
CHO Cells (B)	A	33.11	31.42
	C	19.99	21.05
	D	0.69	0.81
	RSSE	34.76	11.95
CHO Cells (C)	A	26.89	26.75
	C	19.54	18.07
	D	0.71	0.71
	RSSE	1.66	0.98
Ljumggren and Häggström (1994)	A	4.00	3.84
	C	1.28	1.43
	D	1.44	1.92
	RSSE	0.20	0.09

Table G.6: Comparison of LGE Parameters for Product Concentration Data from Linear and Nonlinear Parameter Estimation

Data Source	Parameter	Parameter Estimation Method	
		Linear	Nonlinear
Bree et al., (1988)	A	104.46	105.32
	C	5351.16	430.47
	D	1.64	1.17
	RSSE	303.67	79.78
Dalili et al., (1990)	A	7.53	6.51
	C	8.19	229.91
	D	0.72	2.77
	RSSE	20.50	2.69
CHO Cells (A)	A	194.00	248.85
	C	25.55	30.39
	D	0.50	0.43
	RSSE	2503.83	1630.66
CHO Cells (B)	A	96.60	94.46
	C	25.72	42.32
	D	0.81	0.95
	RSSE	75.19	42.22
CHO Cells (C)	A	135.00	131.49
	C	26.32	53.34
	D	0.70	0.91
	RSSE	472.59	170.30
Dowd et al., (2000)	A	130.71	130.51
	C	13.32	7.29
	D	1.76	1.46
	RSSE	119.08	23.26

Table G.7: Comparison of LDE Parameter Estimates from Linear and Nonlinear Parameter Estimation for Glucose Concentration Data

Data Source	**Parameter**	**Parameter Estimation Method**		
		Linear	GRG/Simplex	LM
Linz et al., (1997)	A	107.01	145.44	111.99
	C	1.15	1.34	1.23
	D	11.78	14.88	11.07
	RSSE	1.64	0.11	0.16
CHO Cell (A)	A	760.98	102.62	668.60
	C	0.30	0.12	0.29
	D	12.26	0.58	10.24
	RSSE	175.07	31.79	147.42
CHO Cell (B)	A	2430.98	1545.57	2266.56
	C	0.68	0.64	0.70
	D	32.76	19.67	29.81
	RSSE	77.87	31.08	39.62
CHO Cell (C)	A	7485.01	2358.42	6756.41
	C	0.78	0.63	0.80
	D	105.78	31.79	96.46
	RSSE	142.19	25.58	74.41
Ljumggren and Häggström (1994)	A	82.58	36.63	76.26
	C	1.39	1.17	1.47
	D	15.82	5.83	13.87
	RSSE	0.75	0.16	0.35

Table G.8: Comparison of LDE Parameter Estimates from Linear and Nonlinear Parameter Estimation for Glutamine Concentration Data

Data Source	**Parameter**	**Parameter Estimation Method**		
		Linear	GRG/Simplex	LM
Bree et al., (1997)	A	14.75	46.67	28.08
	C	0.65	1.07	0.93
	D	5.57	16.37	9.29
	RSSE	0.75	0.08	0.09
Dalili et al., (1990)	A	1.34	21.41	6.42
	C	1.01	2.20	1.62
	D	2.69	43.39	11.74
	RSSE	0.08	0.00	0.01
Linz et al., (1997)	A	21.43	3.65	4.34
	C	0.43	0.19	0.21
	D	4.31	0.28	0.14
	RSSE	1.39	0.21	0.22
CHO Cell (A)	A	31.96	12.27	16.38
	C	0.27	0.20	0.24
	D	2.32	0.13	0.18
	RSSE	33.05	3.37	3.59
CHO Cell (B)	A	60.29	125.42	63.2
	C	0.52	0.78	0.61
	D	4.27	7.99	3.40
	RSSE	20.32	2.87	3.72
CHO Cell (C)	A	66.51	77.57	67.51
	C	0.47	0.58	0.55
	D	4.78	4.57	3.81
	RSSE	14.90	1.71	1.76

Appendix H

Error in Specific Rates and Metabolic Fluxes

Error propagation from prime variables into specific rates and subsequently into metabolic fluxes was analyzed in Chapter 7. For specific rates, these results were largely based on adding normally distributed error to the prime variables and determining their impact on specific rate errors. To characterize error propagation into metabolic fluxes, error was added to error-free specific rate values followed by flux estimation. Application of the Gaussian method for error estimation is illustrated using specific growth rate as an example and other specific rates can be similarly analyzed. Specific rate espressions are derived first and computer programs for error estimation by both the Gaussian and Monte-Carlo approaches are also presented in this Chapter.

H.1 Specific Growth Rate

In a perfusion system, the bioreactor cell density is maintained at a constant value by offsetting cell growth with a combination of cell loss in the harvest stream (uncontrolled) and controlled bleeding of cells from the bioreactor. Cellular mass balances across the bioreactor and the cell retention device help quantify these dynamics and can be used to obtain an expression for specific growth rate. A schematic of the perfusion system is shown in Figure H.1.

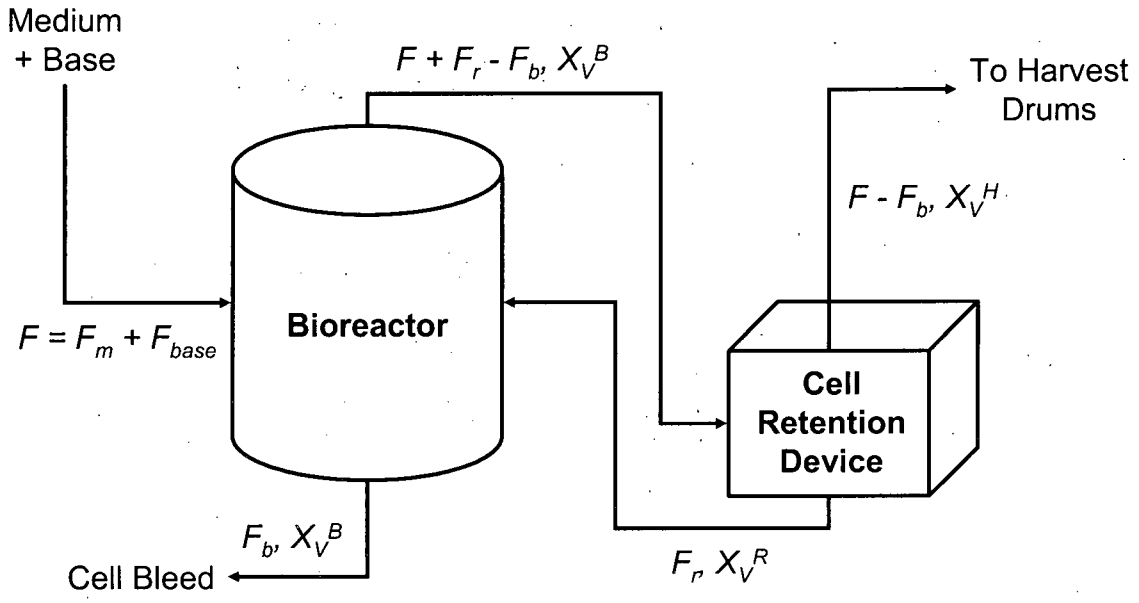

Figure H.1: Schematic of a perfusion system with the various flow streams and their respective viable cell concentrations.

H.1.1 Mass Balance on Viable Cells in the Bioreactor

There are three inlet and two outlet streams for a typical perfusion bioreactor. The inlets include the cell retention device return stream (Flow rate = F_r; Cell density = X_V^R), the inlet medium stream (Flow rate = F_m) and the base addition stream (Flow rate = F_{base}). As base addition is typically a very small percentage of medium addition, these streams can be combined into a single stream, F ($F = F_m + F_{base}$) for convenience. The outlet streams include the cell bleed stream (Flow rate = F_b; Cell density = X_V^B) and the cell retention device feed stream (Flow rate = $F + F_r - F_b$; Cell density = X_V^B). The mass balance expression for viable cells in the bioreactor can now be written in terms of the following general expression

$$Accumulation = Input - Output + Generation - Decay \tag{H.1}$$

$$V\frac{dX_V^B}{dt} = \{(F)\,0 + (F_r)\,X_V^R\} - \{(F_b)\,X_V^B + (F + F_r - F_b)\,X_V^B\} + \{(\mu V)\,X_V^B\} - \{(k_d V)\,X_V^B\} \tag{H.2}$$

where V is the bioreactor volume (L), X_V^B the viable cell density in the bioreactor (10^9 cells/L), X_V^R the viable cell density in the return stream from the cell retention device (10^9

cells/L), μ the specific growth rate (1/d) and k_d the specific death rate (1/d). Eq.(H.2) can be rewritten as

$$\frac{dX_V^B}{dt} = \left(\frac{F_r}{V}\right) X_V^R - \left(\frac{F}{V} + \frac{F_r}{V}\right) X_V^B + (\mu)\, X_V^B - (k_d)\, X_V^B \tag{H.3}$$

Combining the specific growth rate, μ, and the specific death rate, k_d, an apparent growth rate μ' (1/d) can be defined as

$$\mu' = \mu - k_d \tag{H.4}$$

Eq.(H.4) can now be rewritten in terms of the apparent growth rate

$$\mu' = \frac{1}{X_V^B}\frac{dX_V^B}{dt} + \left(\frac{F}{V}\right)\frac{X_V^B}{X_V^R} + \left(\frac{F_r}{V}\right)\left(X_V^R - X_V^B\right) \tag{H.5}$$

Eq.(H.5) has limited utility for specific growth calculations because the viable cell density in the return stream from the cell retention device, X_V^R, is not routinely measured. It is desirable to express X_V^R in terms of experimentally measured quantities and this can be done by performing a mass balance on viable cells across the cell retention device.

H.1.2 Mass Balances on Viable Cells in the Cell Retention Device

Assuming no cell growth in the cell retention device, a generalized mass balance for viable cells can be written as

$$0 = \left\{(F + F_r - F_b)\, X_V^B\right\} - \left\{(F - F_b)\, X_V^H + (F_r)\, X_V^B\right\} \tag{H.6}$$

where X_V^H is the viable cell density in the harvest (10^9 cells/L). Eq.(H.6) can be rearranged to obtain an expression for X_V^R

$$X_V^R = X_V^B + \left(\frac{F - F_b}{F_r}\right)\left(X_V^B - X_V^H\right) \tag{H.7}$$

H.1.3 Expression for Apparent Specific Growth Rate

Substituting Eq.(H.7) in Eq.(H.5) and simplifying results in the following expression for the apparent specific growth rate

$$\mu' = \frac{F_b}{V} + \left(\frac{F_h}{V}\right)\frac{X_V^H}{X_V^B} + \frac{1}{X_V^B}\frac{dX_V^B}{dt} \tag{H.8}$$

The apparent specific growth rate is now expressed in terms of the bioreactor volume, discard and harvest flow rates and the bioreactor and harvest cell densities. Estimating μ' from Eq.(H.8) is straightforward as all these quantities are routinely measured during a perfusion cultivation.

H.2 Specific Glucose Consumption

Glucose is a major source of carbon and energy for mammalian cells and is a key component of cell culture medium. A mass balance for glucose in the bioreactor can be written following the general representation in Eq.(H.1)

$$V\frac{dG}{dt} = \{(F)\,G_m + (F_r)\,G\} - \{(F_b)\,G + (F + F_r - F_b)\,G\} - \left\{\left(VX_V^B\right)q_G\right\} \tag{H.9}$$

where G is the glucose concentration in the bioreactor (mol/L), G_m the glucose concentration in the medium and q_G the specific glucose consumption rate (pmol/cell-d). Dividing throughout by V and simplifying, the specific glucose consumption rate can be computed using

$$q_G = \frac{1}{X_V^B}\left\{\frac{F\,(G_m - G)}{V} - \frac{dG}{dt}\right\} \tag{H.10}$$

H.3 Specific Glutamine Consumption

Glutamine is the second source of carbon and energy for the cells and is also present in cell culture medium. In addition to cell consumption, glutamine undergoes abiotic degradation at cell cultivation temperatures which must be taken into account while writing the mass balance expression

$$\begin{aligned} V\frac{dGln}{dt} &= \{(F)\,Gln_m + (F_r)\,Gln\} - \{(F_b)\,Gln + (F + F_r - F_b)\,Gln\} \\ &\quad - \left\{\left(VX_V^B\right)q_{Gln} - (VK_{Gln})\,Gln\right\} \end{aligned} \tag{H.11}$$

where Gln_m and Gln are glutamine concentrations in the medium and bioreactor, respectively (mol/L), q_{Gln} the specific glutamine consumption rate (pmol/cell-d) and K_{Gln} the first order rate constant for glutamine degradation (1/d). Dividing throughout by V and simplifying, the specific glucose consumption rate can be expressed as

$$q_{Gln} = \frac{1}{X_V^B}\left\{\frac{F\,(Gln_m - Gln)}{V} - \frac{dGln}{dt}\right\} \tag{H.12}$$

H.4 Specific Lactate Production

The majority of lactate produced in mammalian cell culture is a result of glucose metabolism and a mass balance for lactate can be written as

$$V\frac{dL}{dt} = \{(F_r)\,L\} - \{(F_b)\,L + (F + F_r - F_b)\,L\} + \left\{\left(VX_V^B\right)q_L\right\} \tag{H.13}$$

where L is the lactate concnetration in the bioreactor (mol/L) and q_L the specific lactate production rate (pmol/cell-d). Eq.(H.13) can be simplified to obtain an expression for q_L

$$q_L = \frac{1}{X_V^B}\left\{\frac{FL}{V} + \frac{dL}{dt}\right\} \tag{H.14}$$

H.5 Specific Ammonium Production

Ammonium is produced during the metabolism of glutamine to glutamate and also during the abiotic degradation of glutamine resulting in the following mass balance expression

$$V\frac{dA}{dt} = \{(F_r)\,A\} - \{(F_b)\,A + (F + F_r - F_b)\,A\} + \left\{\left(VX_V^B\right)q_A + (VK_{Gln})\,Gln\right\} \tag{H.15}$$

where A is the ammonium concnetration in the bioreactor (mol/L) and q_A the specific ammonium production rate (pmol/cell-d) which can be estimated from

$$q_A = \frac{1}{X_V^B}\left\{\frac{FA}{V} + \frac{dA}{dt} - K_{Gln}Gln\right\} \tag{H.16}$$

H.6 Specific Productivity

The mass balance for protein production can be writtten in an analogous fashion to those for lactate and ammonium production

$$V\frac{dP}{dt} = \{(F_r)\,P\} - \{(F_b)\,P + (F + F_r - F_b)\,P\} + \left\{\left(VX_V^B\right)q_P\right\} \tag{H.17}$$

where P is the product concnetration (g/L) and q_P the specific protein production rate that is commonly refered to as specific productivity (pg/cell-d). From Eq.(H.17), an expression

for specific productivity can be obtained as

$$q_P = \frac{1}{X_V^B}\left\{\frac{FP}{V} + \frac{dP}{dt}\right\} \tag{H.18}$$

H.7 Gaussian Method of Error Estimation

H.7.1 General Expression for Error

Using only the first derivatives in the Taylor series expansion of a function $f(x_1, x_2, ...x_n)$, the error in f can be expressed in terms of that in the independent variables

$$\Delta f(x_1, x_2, ...x_n) \cong \left|\frac{\partial f}{dx_1}\right| \Delta x_1 + \left|\frac{\partial f}{dx_2}\right| \Delta x_2 + ... \left|\frac{\partial f}{dx_n}\right| \Delta x_n \tag{H.19}$$

where $\Delta x_1, \Delta x_2, ...\Delta x_n$ are the errors in $x_1, x_2, ...x_n$, respectively. The standard deviation can be calculated from

$$\Delta f^2 = \sum \left|\frac{\partial f}{dx_i}\right|^2 \Delta x_i^2 \tag{H.20}$$

If the relative error of x_i is defined as $r_{x_i} = \frac{\Delta x_i}{\bar{x}_i}$, that for f can be derived as

$$\left(r_f.\bar{f}\right) = \sum \left|\frac{\partial f}{dx_i}\right|^2 \left(r_{x_i}.\bar{x}_i\right)^2 \tag{H.21}$$

where $\bar{f}$ and $\bar{x}_i$ are the true values.

H.7.2 Error Estimation in Specific Growth Rate

The derivative in that expression can be estimated using finite forward differences

$$\left(\frac{dX_V^B}{dt}\right)_{(j+1)} = \frac{X_{V(j+1)}^B - X_{V(j)}^B}{t_{(j+1)} - t_{(j)}} \tag{H.22}$$

where $X_{V(j)}^B$ and $X_{V(j+1)}^B$ are bioreactor cell density measurements at time $t_{(j)}$ and $t_{(j+1)}$, respectively. The relative error for the specific growth rate can now be written as

$$\begin{aligned}\left(r_\mu.\bar{\mu}'\right)^2 &= \left(\frac{1}{V}\right)^2 \left(r_{F_d}.\bar{F}_b\right)^2 + \left(\frac{\bar{F}_h}{VX_V^B}\right)^2 \left(r_{X_V^H}.\bar{X}_V^H\right)^2 \\ &+ \left(\frac{\bar{F}_h \bar{X}_V^H}{V\left(X_V^B\right)^2}\right)^2 + \frac{1}{\left(t_{(j+1)} - t_{(j)}\right)^2}\left(\frac{2}{X_V^B}\right)^2 \left(r_{X_V^B}.\bar{X}_V^B\right)^2\end{aligned} \tag{H.23}$$

Using F_d = 6 L/day, F_h = 120 L/day, V = 12 L, X_V^B = 20 x 10^6 cells/mL and X_V^H = 0.2 x 10^6 cells/mL, μ' can be calculated from Eq.7.3 as 0.6 1/day.

Substituting for V and F_b in Eq.(H.23), the relative error of μ' with respect to error in F_b is

$$\left(r_{\mu}.\bar{\mu}'\right)^2 = \left(\frac{1}{V}\right)^2 \left(r_{F_b}.\bar{F}_b\right)^2 = \left(\frac{1}{12}\right)^2 \left(r_{F_b}.6\right)^2 \tag{H.24}$$

which simplifies to

$$r_{\mu} = (0.8333)\, r_{F_b} \tag{H.25}$$

Eq.(H.23) can be simplfied to include only the effect of errors in harvest cell density on the apparent specific growth rate

$$\left(r_{\mu}.\bar{\mu}'\right)^2 = \left(\frac{\bar{F}_h}{V X_V^B}\right)^2 \left(r_{X_V^H}.\bar{X}_V^H\right)^2 \tag{H.26}$$

which upon substitution and simplification results in

$$r_{\mu} = (0.1666)\, r_{X_V^H} \tag{H.27}$$

When bioreactor viable cell density data are in error Eq.(H.23) can be simplfied as

$$\left(r_{\mu}.\bar{\mu}'\right)^2 = \left(\frac{\bar{F}_h \bar{X}_V^H}{V\left(X_V^B\right)^2}\right)^2 + \frac{1}{\left(t_{(j+1)} - t_{(j)}\right)^2} \left(\frac{2}{X_V^B}\right)^2 \left(r_{X_V^B}.\bar{X}_V^B\right)^2 \tag{H.28}$$

which upon substitution and simplification results in

$$r_{\mu} = (2.36)\, r_{X_V^B} \tag{H.29}$$

H.8 Computer Programs for Specific Rate Error Estimation

H.8.1 Comparison of Gaussian and Monte-Carlo Methods

A comparison of the Gaussian and Monte-Carlo methods indicated that the Gaussian method underpredicted specific rate errors when the prime variable errors were high. This was due to the truncation of higher order terms in the Gaussian method. While including these terms will improve accuracy, the expressions involving higher order terms are complex and difficult to use. The program compare_mc_gauss compares error estimates from these two methods. It calls separate function files to calculate the Gaussian error for differnt specific rates.

compare_mc_gauss.m (Compares error between Gaussian and Monte-Carlo Methods)

```
%%%%%%%%%%%%%%%%%%%%%%PROGRAM START%%%%%%%%%%%%%%%%%%%%%%%%%%%%%%%%%%%%
% compare_mc_gauss.m
% m-file which compares the results of the gaussian error analysis and
% monte-carlo simulation

% Chetan Goudar
% Last modified: 12/18/05
%%%%%%%%%%%%%%%%%%%%%%%%%%%%%%%%%%%%%%%%%%%%%%%%%%%%%%%%%%%%%%%%%%%%%%%

clear all
figure
hold on
% ERROR-FREE QUANTITIES
vf = 12; fh = 120.0; fvcd = 20; gm=1.0; gf=0.5;

dt=1;
dgdt = (gf-0.5)./dt;
c1 = 1000/180;
c2 = (fh/vf)*((gm-gf)/fvcd);
c3 = dgdt/fvcd;
qg   = c1*(c2 + c3);

% ADDING ERRORS TO PRIME VARIABLES AND COMPUTING MU
% Specifying magnitude of errors
sdvf = 0.0*vf;
r_fh = 0.0;
sdfh = r_fh*fh;
%sdfvcd = 0.0*fvcd;
%sdg = 0.25*gm;
% r_g = 2.0;
% r_gm = 2.0;
% sdg = r_g/100*gf;
% sdgm = r_gm/100*gm;
```

```
% Error introduction

n=25000;
perdiff=ones(n,1); %increases the calculation speed
qg1=ones(n,1); %increases the calculation speed

%r_g    = 0:2:10;
r_g     =    0;
r_gm    = r_g;
r_gm    = r_gm*0;
r_fvcd = 0:2:20;

for i1=1:length(r_g)
    sdg = r_g(i1)/100*gf;
    sdgm = r_gm(i1)/100*gm;


for i2=1:length(r_fvcd)
    sdfvcd = (r_fvcd(i2)/100).*fvcd;

for j=1:n
   vf1    = vf + randn(1).*sdvf;
   fh1    = fh + randn(1).*sdfh;
   fvcd1 = fvcd + randn(1).*sdfvcd;

   gf1    = gf + randn(1).*sdg;
   gf2    = gf + randn(1).*sdg;
   gm1    = gm + randn(1).*sdgm;

% Computation of qg
dgdt1 = (gf1-gf2)./1;
c4     = (fh1/vf1)*((gm1-gf1)/fvcd1);
c5     = dgdt1/fvcd1;c5=0;
qg1(j)    = c1*(c4 + c5);
```

```
% Computing differences in qg
qgdiff  = abs(qg-qg1(j));
perdiff(j) = (qgdiff./qg)*100;
end

perdiff;
avgperdiff = mean(perdiff);
av_qg1 = mean(qg1);
%disp(avgperdiff)
%disp([av_qg1,avgperdiff,std(qg1)/av_qg1*100])
r_qg_mc(i2)=std(qg1)/qg*100;
%disp([av_qg1,avgperdiff,r_qg_mc(i2)])
end

[d_qg,r_qg] = err_qg(qg,gm,gf,fh,vf,fvcd,r_g(i1)/100,r_gm(i1)/100,...
r_fh/100,r_fvcd/100,dt);

plot(r_fvcd,r_qg_mc,r_fvcd,r_qg*100)
end

xlabel('Error in XvF (%)')
ylabel('Error in q_{Glucose} (%)')
title('Specific glucose consumption rate')
legend('Monte Carlo Simulation','Gaussian Error propagation',2)

r_fvcd'
r_qg_mc'
r_gauss = 100*r_qg'
%%%%%%%%%%%%%%%%%%%%%%%%%%%%%%%%%%%%%%%%%%%%%%%%%%%%%%%%%%%%%%%%%%%%%%%%%%%%%%%
```

err_mu.m (Function file that computes growth rate error by the Gaussian method)

```
function [d_mu,r_mu]=err_mu(mu,Fp,Fh,Vf,XvF,XvH,r_Fp,r_Fh,r_XvF,r_XvH,dt)
%
% Error analysis for the specific growth rate calculation
%
```

```
%mu (1/d) specific growth rate
%Fp (l/d) Purge rate
%Fh (l/d) Harvest rate
%Vf (l) Fermentor volume
%XvF (1e6 cells/ml) Fermentor viable cell density
%XvH (1e6 cells/ml) Harvest viable cell density
%r_i relative errors
%dt (d) sample time interval

dFp=r_Fp*Fp;         %(l/d) standard deviation purge rate
dFh=r_Fh*Fh;         %(l/d) standard deviation harvest rate
dXvF=r_XvF*XvF;      %(1e6 cells/ml) standard deviation fvcd
dXvH=r_XvH*XvH;      %(1e6 cells/ml) standard deviation hvcd

% Error for specific growth rate
d_mu = sqrt(1/Vf^2.*dFp.^2 + (XvH/XvF/Vf)^2.*dFh.^2 + (Fh/Vf/XvF)^2.*...
dXvH.^2 + ((Fh*XvH/Vf/XvF^2)^2 + 2/dt^2/XvF^2).*dXvF.^2);
% relative error for specific growth rate
r_mu = 1/mu * d_mu;
%%%%%%%%%%%%%%%%%%%%%%%%%%%%%%%%%%%%%%%%%%%%%%%%%%%%%%%%%%%%%%%%%%%%%%%%%%%%
```

err_qg.m (Function file that computes glucose consumption rate error by the Gaussian method)

```
function [d_qG,r_qG]=err_qg(qG,G_medium,G_fermentor,Fh,Vf,XvF,r_G,...
r_Gm,r_Fh,r_XvF,dt)
%
% Error analysis for the specific rate calculation
% Error for specific glucose consumption rate
%
%qG (pmole/cell/d) Glucose specific consumption rate
%G_medium (g/l) Glucose concentration medium
%G_fermentor (g/l) Glucose concentration fermentor
%Fp (l/d) Purge rate
%Fh (l/d) Harvest rate
%Vf (l) Fermentor volume
%XvF (1e6 cells/ml) Fermentor viable cell density
```

```
%r_i relative errors
%dt (d) sample time interval

dFh=r_Fh*Fh;         %(1/d) standard deviation harvest rate
dXvF=r_XvF*XvF;      %(1e6 cells/ml) standard deviation fvcd
dG=r_G*G_fermentor; %(g/l) standard deviation for bioreactor glucose
dGm=r_Gm*G_medium;  %(g/l) standard deviation for medium glucose

% Error for specific glucose consumption rate (pmole/cell/d)
d_qG = 1000/180*sqrt(((G_medium-G_fermentor)/XvF/Vf)^2.*dFh.^2 ...
        + ((Fh/Vf/XvF)^2 + 2/dt^2/XvF^2).*dG.^2 + ((Fh/Vf/XvF)^2).*...
       dGm.^2 + (Fh*(G_medium-G_fermentor)/Vf/XvF^2)^2.*dXvF.^2);
% d_qG = 1e3/180*sqrt(((G_medium-G_fermentor)/XvF/Vf)^2.*dFh.^2 +...
((Fh/Vf/XvF)^2).*dG.^2 + (Fh*(G_medium-G_fermentor)/Vf/XvF^2)^2.*dXvF.^2);
% relative error for specific glucose consumption rate
r_qG = 1/qG * d_qG;
%%%%%%%%%%%%%%%%%%%%%%%%%%%%%%%%%%%%%%%%%%%%%%%%%%%%%%%%%%%%%%%%%%%%%%%%%%%
```

err_qgln.m (Function file that computes glutamine consumption rate error by the Gaussian method)

```
function [d_qGln,r_qGln]=err_qgln(qGln,Gln_medium,Gln_fermentor,Fh,...
Vf,XvF,r_Gln,r_Gln_m,r_Fh,r_XvF,dt)
%
% Error analysis for the specific rate calculation
% Error for specific glutamine consumption rate
%
%
k=1;                 %(1/d) Glutamine decay rate
%qGln (pmole/cell/d) glutamine specific consumption rate
%Gln_medium (mM) glutamine concentration medium
%Gln_medium (mM) glutamine concentration fermentor
%Fp (l/d) Purge rate
%Fh (l/d) Harvest rate
%Vf (l) Fermentor volume
%XvF (1e6 cells/ml) Fermentor viable cell density
%r_i relative errors
```

```
%dt (d) sample time interval
%
dFh=r_Fh*Fh;          %(l/d) standard deviation harvest rate
dXvF=r_XvF*XvF;       %(1e6 cells/ml) standard deviation fvcd
dGln=r_Gln*Gln_fermentor;   %(mM) SD for bioreactor glutamine
dGln_m=r_Gln_m*Gln_medium;   %(mM) SD for medium glutamine

% Error for specific glutamine consumption rate (pmole/cell/d)
d_qGln = sqrt(((Gln_medium-Gln_fermentor)/XvF/Vf)^2.*dFh.^2 ...
        + ((Fh/Vf/XvF)^2 + 2/dt^2/XvF^2 + (k/XvF)^2).*dGln.^2...
+ ((Fh/Vf/XvF)^2).*dGln_m.^2 + (((Fh*(Gln_medium-Gln_fermentor)...
/Vf/XvF^2)^2 + (k/XvF^2)^2)).*dXvF.^2);
% relative error for specific glutamine consumption rate
r_qGln = 1/qGln * d_qGln;
%%%%%%%%%%%%%%%%%%%%%%%%%%%%%%%%%%%%%%%%%%%%%%%%%%%%%%%%%%%%%%%%%%%%%%%%%%%%%%%
```

err_qlac.m (Function file that computes lactate production rate error by the Gaussian method)

```
function [d_qLac,r_qLac]=err_qlac(qLac,Lac_fermentor,Fh,Vf,XvF...
,r_Lac,r_Fh,r_XvF,dt)
%
% Error analysis for the specific rate calculation
% Error for specific lactate production rate
%
%qLac (pmole/cell/d) lactate specific production rate
%Lac_fermentor (g/l) lactate concentration fermentor
%Fh (l/d) Harvest rate
%Vf (l) Fermentor volume
%XvF (1e6 cells/ml) Fermentor viable cell density
%r_i relative errors
%dt (d) sample time interval

dFh=r_Fh*Fh;          %(l/d) standard deviation harvest rate
dXvF=r_XvF*XvF;       %(1e6 cells/ml) SD fermentor viable cell density
dLac=r_Lac*Lac_fermentor;   %(g/l) SD for lactate concentration
```

```
% Error for specific lactate production rate (pmole/cell/d)
d_qLac = 1e3/90*sqrt((Lac_fermentor/XvF/Vf)^2.*dFh.^2 +...
((Fh/Vf/XvF)^2 + 2/dt^2/XvF^2).*dLac.^2 ...
+ (Fh*Lac_fermentor/Vf/XvF^2)^2.*dXvF.^2);
d_qLac = 1e3/90*sqrt((Lac_fermentor/XvF/Vf)^2.*dFh.^2 +...
((Fh/Vf/XvF)^2).*dLac.^2 ...
        + (Fh*Lac_fermentor/Vf/XvF^2)^2.*dXvF.^2);
% relative error for specific lactate production rate
r_qLac = 1/qLac * d_qLac;
%%%%%%%%%%%%%%%%%%%%%%%%%%%%%%%%%%%%%%%%%%%%%%%%%%%%%%%%%%%%%%%%%%%%%%%%%%%%
```

err_qnh3.m (Function file that computes ammonium production rate error by the Gaussian method)

```
function [d_qNH3,r_qNH3]=err_qnh3(qNH3,NH3_fermentor,Fh,Vf,XvF,...
r_NH3,r_Fh,r_XvF,dt)
%
% Error analysis for the specific rate calculation
%
%qNH3 (pmole/cell/d) ammonia specific production rate
%NH3_fermentor (mM) ammonia concentration fermentor
%Fh (1/d) Harvest rate
%Vf (l) Fermentor volume
%XvF (1e6 cells/ml) Fermentor viable cell density
%r_i relative errors
%dt (d) sample time interval

dFh=r_Fh*Fh;         %(1/d) SD harvest rate
dXvF=r_XvF*XvF;      %(1e6 cells/ml) SD fermentor viable cell density
dNH3=r_NH3*NH3_fermentor;   %(mM) SD for ammonia concentration

% Error for specific ammonia production rate (pmole/cell/d)
d_qNH3 = sqrt((NH3_fermentor/XvF/Vf)^2.*dFh.^2 +...
((Fh/Vf/XvF)^2 + 2/dt^2/XvF^2).*dNH3.^2 ...
       + (Fh*NH3_fermentor/Vf/XvF^2)^2.*dXvF.^2);
% relative error for specific ammonia production rate
r_qNH3 = 1/qNH3 * d_qNH3;
```

```
%%%%%%%%%%%%%%%%%%%%%%%%%%%%%%%%%%%%%%%%%%%%%%%%%%%%%%%%%%%%%%%%%%%%%%%%%%%%
```

err_qo2.m (Function file that computes oxygen uptake rate error by the Gaussian method)

```
function [d_qO2,r_qO2]=err_qo2(qO2,O2_in,O2_out,Fg,Vf,XvF,...
r_O2,r_Fg,r_XvF,dt)
%
% Error analysis for the specific rate calculation
% Error for specific oxygen uptake rate
%
%qO2 (pmole/cell/d) Oxygen uptake rate
%O2_in (mM) O2 concentration fermentor inlet
%O2_out (mM) O2 concentration fermentor outlet
%Fg (l/d) Aeration rate
%Vf (l) Fermentor volume
%XvF (1e6 cells/ml) Fermentor viable cell density
%r_i relative errors
%dt (d) sample time interval

dFg=r_Fg*Fg;          %(l/d) SD aeration rate
dXvF=r_XvF*XvF;       %(1e6 cells/ml) SD fermentor viable cell density
dO2=r_O2*O2_out;      %(mM) SD for O2 concentration

% Error for specific oxygen uptake rate (pmole/cell/d)
d_qO2 = sqrt(((O2_in-O2_out)/XvF/Vf)^2.*dFg.^2 + (Fg/Vf/XvF)^2.*dO2.^2 ...
        + (Fg*(O2_in-O2_out)/Vf/XvF^2)^2.*dXvF.^2);
% relative error for specific oxygen uptake rate
r_qO2 = 1/qO2 * d_qO2;
%%%%%%%%%%%%%%%%%%%%%%%%%%%%%%%%%%%%%%%%%%%%%%%%%%%%%%%%%%%%%%%%%%%%%%%%%%%%
```

err_qp.m (Function file that computes specific productivity error by the Gaussian method)

```
function [d_qp,r_qp]=err_qp(qp,Titer,Fh,Vf,XvF,r_Titer,r_Fh,r_XvF,dt)
%
% Error analysis for the specific rate calculation
%
```

```
%qp (pg/cell/d) specific production rate
%Titer (mg/l) Product titer
%Fh (l/d) Harvest rate
%Vf (l) Fermentor volume
%XvF (1e6 cells/ml) Fermentor viable cell density
%r_i relative errors
%dt (d) sample time interval

dFh=r_Fh*Fh;          %(l/d) SD harvest rate
dXvF=r_XvF*XvF;       %(1e6 cells/ml) SD fermentor viable cell density
dTiter=r_Titer*Titer;       %(mg/l) SD for product titer

% Error for specific production rate (pg/cell/d)
d_qp = 1e6*sqrt((Titer/XvF/Vf)^2.*dFh.^2 + (Fh/Vf/XvF)^2.*dTiter.^2 ...
       + (Fh*Titer/Vf/XvF^2)^2.*dXvF.^2);
% relative error specific production rate
r_qp = 1/qp * d_qp;
%%%%%%%%%%%%%%%%%%%%%%%%%%%%%%%%%%%%%%%%%%%%%%%%%%%%%%%%%%%%%%%%%%%%%%%%%%%%
```

H.8.2 Specific Rate Error Estimation by the Monte-Carlo Method

The inadequacies of the Gaussian method at high prime variable errors were apparent and the Monte-Carlo method was used to generate most of the data in Chapter 8. The following programs estimate specific rate errors by the Gaussian method. The magnitude of prime variable error can be specified and at every prime variable error combination, the programs compute the resulting specific rate error as a mean of 25000 values.

main_qg.m (Computes glucose consumption rate error by the Monte-Carlo method)

```
%%%%%%%%%%%%%%%%%%%%%%%%PROGRAM START%%%%%%%%%%%%%%%%%%%%%%%%%%%%%%%%%%%%
% mainqg_mc.m
% Calculates errors in qG using the Monte-Carlo Approach
% Inputs:  Prime Variables and error specifications
% Outputs: Error in qG

% Chetan Goudar
% Last modified: 1/30/05
```

```
%%%%%%%%%%%%%%%%%%%%%%%%%%%%%%%%%%%%%%%%%%%%%%%%%%%%%%%%%%%%%%%%%%%%%%%%%%%%

clear all

% 1. Prime variables to be error free
Gm  = 1;   % (g/L)
dt  = 1;   % (day) not really a prime variable!

% 2. Prime variables with error
V   = 12;    % (L)
Fh  = 120;   % (L/day)
G   = 0.5;   % (g/L)
XvF = 20;    % (1e6 cells/mL)

% 3. qG Computation
c1  = 1000/180;
c2  = (Fh/V)*((Gm-G)/XvF);
qG  = c1*c2;

% 4. Computing error in qG
% Specifying magnitude of relative errors
r_V   = ones(1,10)*5;
r_Fh  = ones(1,10)*5;
r_G   = 2:2:20;
r_XvF = 0:5:20;

sd_XvF    = (r_XvF(5)/100)*XvF; % must be changed

n=25000;

for i=1:1:10
      sd_V   = (r_V(i)/100)*V;
      sd_Fh  = (r_Fh(i)/100)*Fh;
      sd_G   = (r_G(i)/100)*G;

for j=1:n
```

```
      V1    = V + randn(1).*sd_V;
      Fh1   = Fh + randn(1).*sd_Fh;
      G1    = G + randn(1).*sd_G;
      G0    = G + randn(1).*sd_G;
      XvF1  = XvF + randn(1).*sd_XvF;

% Computation of qg
dgdt1    = (G1-G0)./dt;
c1       = 1000/180;
c4       = (Fh1 /V1)*((Gm-G1)/XvF1);
c5       = dgdt1/XvF1;
qG1(j)   = c1*(c4 + c5);

% Differences in qG
qGdiff     = abs(qG-qG1(j));
perdiff(j) = (qGdiff./qG)*100;
end

avgperdiff(i) = mean(perdiff);
avg_qG1       = mean(qG1);
r_qG_mc(i)    = (std(qG1)/avg_qG1)*100;
end

% 5. Output
r_qG_mc'
plot(r_G,r_qG_mc,'o-')
%%%%%%%%%%%%%%%%%%%%%%%%%%%%%%%%%%%%%%%%%%%%%%%%%%%%%%%%%%%%%%%%%%%%%%%%%%%%%%%
```

main_qgln.m (Computes glutamine consumption rate error by the Monte-Carlo method)

```
%%%%%%%%%%%%%%%%%%%%%%%%PROGRAM START%%%%%%%%%%%%%%%%%%%%%%%%%%%%%%%%%%%%%%%%
% mainqgln_mc.m
% Calculates errors in qGln using the Monte-Carlo Approach
% Inputs:  Prime Variables and error specifications
% Outputs: Error in qGln
```

```
% Chetan Goudar 7/22/04
% Last modified: 7/22/04
%%%%%%%%%%%%%%%%%%%%%%%%%%%%%%%%%%%%%%%%%%%%%%%%%%%%%%%%%%%%%%%%%%%%%%%%%%%%

clear all

% 1. Error-free prime variables
Glnm  = 9;   % (g/L)
dt    = 1;   % (day) not really a prime variable!

% 2. Prime variables with error
V     = 12;    % (L)
Fh    = 120;   % (L/day)
Gln   = 4.5;   % (g/L)
XvF   = 20;    % (1e6 cells/mL)

% 3. qGln Computation
c1   = 1e3;
c2   = (Fh/V)*((Glnm-Gln)/XvF);
c3   = (0.017/XvF)*Gln;
qGln = c1*(c2-c3)

% 4. Computing error in qGln
% Specifying magnitude of relative errors
r_V   = ones(1,10)*5;
r_Fh  = ones(1,10)*5;
r_Gln = 2:2:20;
r_XvF = 0:5:20;

sd_XvF  = (r_XvF(1)/100)*XvF;

n=25000;

for i=1:1:10
      sd_V   = (r_V(i)/100)*V;
      sd_Fh  = (r_Fh(i)/100)*Fh;
```

```
      sd_Gln = (r_Gln(i)/100)*Gln;

for j=1:n
      V1    = V + randn(1).*sd_V;
      Fh1   = Fh + randn(1).*sd_Fh;
      Gln1  = Gln + randn(1).*sd_Gln;
      Gln0  = Gln + randn(1).*sd_Gln;
      XvF1  = XvF + randn(1).*sd_XvF;

% Computation of qGln
dgdt1    = (Gln1-Gln0)./dt;
c4       = (Fh1/V1)*((Glnm-Gln1)/XvF1);
c5       = dgdt1/XvF1;
c6       = (0.017/XvF1)*Gln1;
qGln1(j) = c1*(c4 + c5 - c6);

% Differences in qGln
qGlndiff   = abs(qGln-qGln1(j));
perdiff(j) = (qGlndiff./qGln)*100;
end

avgperdiff(i) = mean(perdiff);
avg_qGln1     = mean(qGln1);
r_qGln_mc(i)  = (std(qGln1)/avg_qGln1)*100;
end

% 5. Output
r_qGln_mc'
plot(r_Gln,r_qGln_mc,'o-')
%%%%%%%%%%%%%%%%%%%%%%%%%%%%%%%%%%%%%%%%%%%%%%%%%%%%%%%%%%%%%%%%%%%%%%%%%%%%%%%
```

main_qlac.m (Computes lactate production rate error by the Monte-Carlo method)

```
%%%%%%%%%%%%%%%%%%%%%%%%PROGRAM START%%%%%%%%%%%%%%%%%%%%%%%%%%%%%%%%%%%%%%%%
% mainqlac_mc.m
% Calculates errors in qGln using the Monte-Carlo Approach
```

```
% Inputs:  Prime Variables and error specifications
% Outputs: Error in qlac

% Chetan Goudar
% Last modified: 1/30/05
%%%%%%%%%%%%%%%%%%%%%%%%%%%%%%%%%%%%%%%%%%%%%%%%%%%%%%%%%%%%%%%%%%%%%%%%%%%%

clear all

% 1. Error-free prime variables
dt    = 1;   % (day) not really a prime variable!

% 2. Prime variables with error
V     = 12;    % (L)
Fh    = 120;   % (L/day)
L     = 1.0;   % (g/L)
XvF   = 20;    % (1e6 cells/mL)

% 3. qL Computation
c1    = 1000/90;
c2    = (Fh*L)/(V*XvF);
qL    = c1*c2;

% 4. Computing error in qL
% Specifying magnitude of relative errors
r_V   = ones(1,10)*5;
r_Fh  = ones(1,10)*5;
r_L   = 2:2:20;
r_XvF = 0:5:20;

sd_XvF  = (r_XvF(5)/100)*XvF;

n=25000;

for i=1:1:10
      sd_V   = (r_V(i)/100)*V;
```

```
      sd_Fh  = (r_Fh(i)/100)*Fh;
      sd_L   = (r_L(i)/100)*L;

for j=1:n
      V1     = V + randn(1).*sd_V;
      Fh1    = Fh + randn(1).*sd_Fh;
      L1     = L + randn(1).*sd_L;
      L0     = L + randn(1).*sd_L;
      XvF1   = XvF + randn(1).*sd_XvF;

% Computation of qGln
dLdt1     = (L1-L0)./dt;
c4        = (Fh1*L1)/(V1*XvF1);
c5        = dLdt1/XvF1;
qL1(j)    = c1*(c4 + c5);

% Differences in qGln
qLdiff      = abs(qL-qL1(j));
perdiff(j) = (qLdiff./qL)*100;
end

avgperdiff(i) = mean(perdiff);
avg_qL1       = mean(qL1);
r_qL_mc(i)    = (std(qL1)/avg_qL1)*100;
end

% 5. Output
r_qL_mc'
plot(r_L,r_qL_mc,'o-')
%%%%%%%%%%%%%%%%%%%%%%%%%%%%%%%%%%%%%%%%%%%%%%%%%%%%%%%%%%%%%%%%%%%%%%%%%%%%%%%
```

main_qo2.m (Computes oxygen uptake rate error by the Monte-Carlo method)

```
%%%%%%%%%%%%%%%%%%%%%%PROGRAM START%%%%%%%%%%%%%%%%%%%%%%%%%%%%%%%%%%%%%%%%%%%
% mainqgo2_mc.m
% Calculates errors in q02 using the Monte-Carlo Approach
% Inputs:  Prime Variables and error specifications
```

```
% Outputs: Error in qO2

% Chetan Goudar
% Last modified: 2/03/05
%%%%%%%%%%%%%%%%%%%%%%%%%%%%%%%%%%%%%%%%%%%%%%%%%%%%%%%%%%%%%%%%%%%%%%%%%%%%

clear all

% 1. Error-free prime variables
o2in   = 9;   % (g/L)
o2out  = 1;   % (day) not really a prime variable!

% 2. Prime variables with error
V     = 12;    % (L)
FO2   = 720;   % (L/day)
O2in  = 4e-3;% (M/L)
O2out = 2e-3;  % (M/L)
XvB   = 20;    % (1e6 cells/mL)

% 3. qO2 Computation
c1   = FO2*(O2in - O2out)*1000;
c2   = V*XvB;
qO2  = c1/c2

% 4. Computing error in qO2
% Specifying magnitude of relative errors
r_V     = ones(1,10)*5;
r_FO2   = ones(1,10)*5;
r_O2out = 2:2:20;
r_XvB   = 0:5:20;

sd_XvB  = (r_XvB(5)/100)*XvB;

n=25000;

for i=1:1:10
```

```
      sd_V     = (r_V(i)/100)*V;
      sd_FO2   = (r_FO2(i)/100)*FO2;
      sd_O2out = (r_O2out(i)/100)*O2out;

for j=1:n
      V1     = V + randn(1).*sd_V;
      FO21   = FO2 + randn(1).*sd_FO2;
      O2out1 = O2out + randn(1).*sd_O2out;
      XvB1   = XvB + randn(1).*sd_XvB;

% Computation of qGln
c1       = FO21*(O2in-O2out1)*1000;
c2       = V1*XvB1;
qO21(j)  = c1/c2;

% Differences in qGln
qO2diff   = abs(qO2-qO21(j));
perdiff(j) = (qO2diff./qO2)*100;
end

avgperdiff(i) = mean(perdiff);
avg_qO21      = mean(qO21);
r_qO2_mc(i)   = (std(qO21)/avg_qO21)*100;
end

% 5. Output
r_qO2_mc'
plot(r_O2out,r_qO2_mc,'o-')
```

H.9 Computer Programs for Metabolic Flux Error Estimation

To estimate error propagation from specific rates into metabolic fluxes, an error-free metabolic flux vector ($\mathbf{x}$) is used to compute the corresponding error-free specific rate vector ($\mathbf{r}$) when the stoichiometric matrix ($\mathbf{A}$) is known ($\mathbf{r} = \mathbf{A}\mathbf{x}$). Subsequently normally distributed error

of known magnitude is added to the error-free specific rate vector and flux calculations are performed. Comparison of these flux estimates with the known eror-free values helps quantify error propagation from specific rates into metabolic fluxes. The program below performs these calculations when all specific rates have the same amount of error. The programs can be easily customized to assign different error values to the specific rates.

h15_mfaerrorall.m (Computes metabolic flux error by the Monte-Carlo method)

```
%%%%%%%%%%%%%%%%%%%%%%PROGRAM START%%%%%%%%%%%%%%%%%%%%%%%%%%%%%%%%
% Computes error associated with metabolic flux estimation
% All specific rates are in error
% Error is added to error-free sepcific rates from which
% the corresponding metabolic fluxes are computed.
% Model based on Nyberg et al (Biotech Bioeng, 62, 324-335 1999)
% H15 Data are used for error estimation

clear all

% 1. GENERATION OF THE "ERROR-FREE" R VECTOR
% Stoichiometric Matrix
A = importdata('nyberg_A.m');
AT = A';
rank_a = rank(A); cond_a = cond(A);
smx = inv(AT*A)*AT;   % Sensitivity Matrix

% absolute sensitivity matrix
smx_abs = abs(smx);
low_sens  = min(smx_abs)';
high_sens = max(smx_abs)';
mean_sens = mean(smx_abs)';
xdata = linspace(1,35,35)';
%semilogy(xdata,low_sens,xdata,mean_sens,xdata,high_sens)

% Known Flux Vector
x_all = importdata('h15_flux_data.m');
x_known = x_all(:,5);  % Std. Conditions 3
```

```
% Error-Free Rate Vector
r_true  = A*x_known;
r_error = r_true;

% 2. INTRODUCTION OF ERROR IN SPECIFIC RATES
err_r = 0.25;
sd_r  = err_r.*r_true;

n=10000;
pererror = 0;
x=ones(33,n);

% 3. FLUX AND ERROR COMPUTATION USING ERROR-CONTAINING SPECIFIC RATES
% Flux Computation

for i=1:n
        r_error = r_true + (randn(35,1).*sd_r);
        x(:,i)  = inv(AT*A)*AT*r_error;
% Error in Fluxes
error = abs(x(:,i)-x_known);
pererror = pererror + (error./x_known).*100;
end

% AVERAGE ERRORS
pererror_new = std(x')./x_known'*100;
newerror = pererror_new'
```

Appendix I

Thermodynamic Analysis of Metabolic Pathways

Analysis of the free energy changes associated with reactions in a biochemical network will provide information that can augment metabolic flux data. The free energy change, ΔG, for the reaction

$$aA + bB \longleftrightarrow cC + dD \tag{I.1}$$

can be determined as

$$\Delta G = \Delta G^{0'} + RT \ln \left(\frac{[\gamma_C]^c [\gamma_D]^d}{[\gamma_A]^a [\gamma_B]^b} \right) \tag{I.2}$$

where $\Delta G^{0'}$ is the free energy changes under standard conditions (25 °C, 1 atm pressure), R the gas constant, T the absolute temperature and $\gamma_A, \gamma_B, \gamma_C$ and γ_D the activities of A, B, C and D. For a reaction at equilibrium, $\Delta G^{0'} = 0$ and Eq.(I.2) reduces to

$$\Delta G^{0'} = -RT \ln \left(\frac{[\gamma_C]^c [\gamma_D]^d}{[\gamma_A]^a [\gamma_B]^b} \right) = -RT \ln (K) \tag{I.3}$$

where K is the equilibrium constant. A cell in a bioreactor, however, is an open system as it interacts with the cultivation medium by consuming nutrients and releasing metabolites resulting in nonequilibrium conditions. The simplification in Eq.(I.3) is hence not applicable to cells cultivated in a bioreactor. It follows from Eq.(I.2) that reactant and product activities determine ΔG and hence the feasibility of biochemical reactions (ΔG must be negative for a reaction to occur).

I.1 Theory of Thermodynamic Feasibility

For single reactions, $\Delta G < 0$ must be true for the reaction to occur. This is also true for metabolic pathways with multiple reactions where $\Delta G < 0$ must be true for all reactions in the pathway. Thermodynamic bottlenecks in metabolic pathways can be identified based on reaction ΔG values and are referred to as localized bottlenecks (single reaction with $\Delta G > 0$) or distributed bottlenecks (multiple reactions with $\Delta G > 0$). When intracellular activities are known, it is desirable to evaluate the thermodynamic feasibility of reactions in the biochemical pathway of interest. A systematic method for such an evaluation has been proposed (Mavrovouniotis, 1993)[1] and is described below.

Consider a biochemical network with the stoichiometry

$$\sum_{i=1}^{n} a_{j,i}\gamma_i = 0; \qquad j = 1, ..., J \tag{I.4}$$

where a is the stoichiometric coefficient, j the number of reactions in the network, n the number of species and γ the species activity. The free energy change for reaction j can be written as

$$\Delta G_j = \Delta G_j^{0'} + \sum_{i=1}^{n} a_{j,i} RT \ln(\gamma_i) \tag{I.5}$$

During mammalian cell cultivation, the activities of nutrients and metabolites such as glucose and lactate can be expected to change while those for cofactors such as ATP and NADH are assumed to be constant due to cellular regulation. These metabolites with constant activities are referred to as currency metabolites and can be grouped separately

$$\Delta G_j = \Delta G_j^{0'} + \sum_{i=1}^{n-n'} a_{j,i} RT \ln(\gamma_i) + \sum_{i=1}^{n'} a_{j,i} RT \ln(\gamma_i) \tag{I.6}$$

where n' is the number of non-currency metabolites whose activities are expected to change during the course of a cultivation. Eq.(I.6) can be rewritten by combining the constant terms

$$\Delta G_j = \Delta G_j^{0''} + \sum_{i=1}^{n'} a_{j,i} RT \ln(\gamma_i) \tag{I.7}$$

where $\Delta G_j^{0''} = \Delta G_j^{0'} + \sum_{i=1}^{n-n'} RT \ln(\gamma_i)$. For the reaction network described by Eq.(I.4) to

[1] Mavrovouniotis, M.L. (1993). Identification of localized and distributed bottlenecks in metabolic pathways. *ISMB* **93**: 273-283.

be feasible, the following must be true

$$\frac{\Delta G_j^{0''}}{RT} + \sum_{i=1}^{n'} a_{j,i} \ln(\gamma_i) < 0 \tag{I.8}$$

While activities of non-currency metabolites can vary, a range for this variation must be defined and the algorithm will determine if the pathway is thermodynamically feasible within these activity ranges. Denoting $\gamma_i^{\min}$ and $\gamma_i^{\max}$ as the minimum and maximum activities, Eq.(I.8) can be rewritten to scale γ_i with the minimum concentration as

$$\frac{\Delta G_j^{0''}}{RT} + \sum_{i=1}^{n'} a_{j,i} \ln\left(\gamma_i^{\min}\right) + \sum_{i=1}^{n'} a_{j,i} \ln\left(\frac{\gamma_i}{\gamma_i^{\min}}\right) < 0 \tag{I.9}$$

which can be further modified to include $\gamma_i^{\max}$

$$\frac{\Delta G_j^{0''}}{RT} + \sum_{i=1}^{n'} a_{j,i} \ln\left(\gamma_i^{\min}\right) + \sum_{i=1}^{n'} a_{j,i} \ln\left(\frac{\gamma_i^{\max}}{\gamma_i^{\min}}\right) \frac{\ln\left(\frac{\gamma_i}{\gamma_i^{\min}}\right)}{\ln\left(\frac{\gamma_i^{\max}}{\gamma_i^{\min}}\right)} < 0 \tag{I.10}$$

substituting

$$h_j = \frac{\Delta G_j^{0''}}{RT} + \sum_{i=1}^{n'} a_{j,i} \ln\left(\gamma_i^{\min}\right) \tag{I.11}$$

$$w_{j,i} = a_{j,i} \ln\left(\frac{\gamma_i^{\max}}{\gamma_i^{\min}}\right) \tag{I.12}$$

$$f_j = \frac{\ln\left(\frac{\gamma_i}{\gamma_i^{\min}}\right)}{\ln\left(\frac{\gamma_i^{\max}}{\gamma_i^{\min}}\right)} \tag{I.13}$$

Eq.(I.10) can be rewritten as

$$H_j = h_j + \sum_{i=1}^{n'} w_{j,i} f_i < 0 \tag{I.14}$$

such that $H_j < 0$ must be satisfied for thermodynamic feasibility and this is influenced by f_i values. The range of f is determined by γ_i such that when $\gamma_i = \gamma_i^{\max}$, $f = 1$ and when $\gamma_i = \gamma_i^{\min}$, $f = 0$. The maximum value of H_j is when $\gamma_i = \gamma_i^{\min}$ for all reactants ($f = 0$)

and $\gamma_i = \gamma_i^{\max}$ $(f = 1)$ for all products

$$H_{j,\max} = h_j + \sum_{i=1}^{n'} w_{j,i}; \qquad w_{j,i} > 0 \tag{I.15}$$

Conversely, H_j is minimum when $\gamma_i = \gamma_i^{\max}$ for all reactants $(f = 1)$ and $\gamma_i = \gamma_i^{\min}$ $(f = 0)$ for all products

$$H_{j,\min} = h_j + \sum_{i=1}^{n'} w_{j,i}; \qquad w_{j,i} < 0 \tag{I.16}$$

Thus for any reaction j in the network, the scaled Gibbs free energy, H_j, varies between $H_{j,\min}$ and $H_{j,\max}$ depending upon the associated reactant and product activities. Since $H_j < 0$ must be true for the reaction to be feasible, it is obvious that the reaction is always feasible when $H_{j,\max} < 0$ and is always unfeasible when $H_{j,\min} > 0$. Determination of the feasibility is not obvious when $H_{j,\max} > 0$ and $H_{j,\min} < 0$ because H_j can be either positive or negative under these conditions.

It has been shown (Mavrovouniotis, 1993) that when two reactions that share a common metabolite are combined, the $H_{\min}$ of the resulting reaction will be greater and the $H_{\max}$ will be lower than the linear combination of the individual reactions. Thus by successively combining reactions with $H_{j,\max} > 0$ and $H_{j,\min} < 0$, it is possible to ultimately determine their thermodynamic feasibility.

I.2 Steps for Determining Reaction Thermodynamic Feasibility

The above concepts can be summarized in the following steps such that the thermodynamic feasibility of biochemical reactions can be determined using a computer program:

1. Formulate the bioreaction network of interest and obtain $\Delta G^{0'}$ values for all reactions
2. Identify the currency and non-currency metabolites in the network
3. Assign constant activity values to the currency metabolites based on published data
4. Assign minimum and maximum activity values for all the non-currency metabolites from published data
5. Compute $\frac{\Delta G_j^{0''}}{RT}$, h_j, $w_{j,i}$, $H_{j,\max}$ and $H_{j,\min}$ for all reactions in the network

6. Eliminate all reactions with $H_{j,\max} < 0$ as they are always thermodynamically feasible
7. Classify all reactions with $H_{j,\min} > 0$ as always thermodynamically unfeasible
8. For the remaining reactions ($H_{j,\max} > 0$ and $H_{j,\min} < 0$) construct a combination of two reactions that share a metabolite and go to step 5. If metabolites are not shared, this combination is not possible and the search must be stopped

I.3 Application to Glycolysis

Application of the above method to reactions in the glycolytic pathway is presented. A total of 11 reactions along with their standard free energies are shown in Table I.1. The non-currency metabolites are ATP, ADP, NAD, P_i and NADH with the rest being currency metabolites.

Table I.1: Glycolytic Reactions and their Standard Free Energies

#	Reaction	$\Delta G^{0'}$ (KJ/mol)
1	Glc + ATP → G6P + ADP	-16.75
2	G6P → F6P	1.67
2	F6P + ATP → FDP + ADP	-14.24
4	FDP → DHAP + GAP	23.99
5	DHAP → GAP	7.66
6	GAP + NAD + Pi → PGP + NADH	6.28
7	PGP + ADP → 3PG + NADH	-18.84
8	3PG → 2PG	4.44
9	2PG → PEP	1.84
10	PEP + ADP → Pyr + ATP	-31.4
11	Pyr + NADH → Lac + NAD	-25.12

Intracellular activities of both the currency and non-currency metabolites are necessary for determining thermodynamic feasibility. While some data are available for cultured mammalian cells, these represent a very small portion of the glycolytic metabolites. A more complete data set is available for the human erythrocyte (Table I.2) and was used in the analysis. Among non-currency metabolites, concentrations of PGP and Lac were not available and were assumed to be 0.01 and 0.05 mM, respectively. For currency metabolites, concentrations of NAD and NADH were not available and were assumed to be 4 and 0.2 mM, respectively.

Lower and upper concentration limits must be defined for the non-currency metabolites before reaction feasibility can be determined. In the absence of extensive published data,

Table I.2: Intracellular Metabolite and Cofactor Concentrations in the Glycolytic Pathway for Human Erythrocyte

Metabolite	Concentration (mM)
Glc	5
G6P	0.083
F6P	0.014
FDP	0.031
DHAP	0.138
GAP	0.019
PGP	0.010
3PG	0.118
2PG	0.030
PEP	0.023
Pyr	0.051
Lac	0.050
ATP	1.850
ADP	0.138
NAD	4.000
P_i	1.000
NADH	0.200

the range for Glc was set as 1 – 10 mM and those for all other non-currency metabolites as 0.01 – 0.2 mM. Results of the thermodynamic feasibility analysis are shown in Table I.3 and are valid only at the above concentration ranges.

Reactions 1, 3, 7, 10 and 11 are always feasible since $H_{j,\max} < 0$. Alternatively, reactions 4 and 5 are always unfeasible ($H_{j,\min} > 0$) and can be classified as two localized bottlenecks. Further analysis of reactions 2, 6, 8 and 9 is necessary to determine if they are feasible or not. Reaction 2 must be feasible because both reactions 1 and 3 cannot be part of a distributed bottleneck (they are both always feasible). Reactions 5 and 6 can be combined to eliminate GAP

$$\text{DHAP} + \text{NAD} + \text{P}_\text{i} \rightarrow \text{PGP} + \text{NADH} \tag{I.17}$$

with a new h value of 2.63. The $H_{\min}$ value for this combined reaction can be estimated as 0.33 and since this value is > 0, reaction 6 is unfeasible. Similarly, reactions 8 and 9 can be combined to eliminate 2PG

$$\text{3PG} \rightarrow \text{PEP} \tag{I.18}$$

with a h value of 2.53 from which the $H_{\min}$ is determined as 0.23. Reactions 8 and 9 thus

Table I.3: Results from Thermodynamics Feasibility Analysis on the Glycolytic Reactions

Reaction #	$\frac{\Delta G_j^{0''}}{RT}$	h_j	$H_{j,\max}$	$H_{j,\min}$	Feasibility
1	-9.35	-13.96	-10.96	-16.26	Yes
2	0.68	0.68	3.67	-2.32	Yes
3	-8.34	-8.34	-5.34	-11.33	Yes
4	9.68	5.07	11.06	2.08	No
5	3.09	3.09	6.09	0.10	No
6	-0.46	-0.46	2.53	-3.46	No
7	-5.00	-5.00	-2.01	-8.00	Yes
8	1.79	1.79	4.79	-1.21	No
9	0.74	0.74	3.74	-2.25	No
10	-10.07	-10.07	-7.08	-13.07	Yes
11	-7.14	-7.14	-4.14	-10.13	Yes

constitute a distributed bottleneck since $H_{\min} > 0$ for the combined reaction.

Thus 5 of the 11 reactions in glycolysis were determined to be thermodynamically unfeasible for assumed metabolite and cofactor concentration ranges. While the standard free energies for these 5 reactions were also positive (Table I.1), this need not be the case and usually the standard free energy provides very little information on reaction feasibility.

I.4 Bioprocess Implications

With increased metabolite profiling and metabolomics research, additional data on metabolite and cofactor intracellular activities will become available allowing reliable determination of pathway thermodynamic feasibility. In addition to providing data on thermodynamic feasibility, the magnitude of ΔG is important because reactions with low ΔG proceed close to equilibrium while those with large negative ΔG values can be thought of as thermodynamically irreversible. Combining metabolite concentration and reaction free energy data with metabolic fluxes will improve our understanding of cell physiological state and can aid bioprocess optimization efforts.

Appendix J

Flux Analysis for Bioprocess Development[1]

J.1 Introduction

High density cultivation of mammalian cells on the order of 20 x 10^6 cells/mL or higher is possible in perfusion systems where cells are retained in a cell retention device and recycled back to the bioreactor [1, 2]. In contrast to transient fed-batch systems that experience substantial changes in nutrient and metabolite concentrations over the course of cultivation, perfusion reactors operate at quasi steady state with relatively constant nutrient and metabolite levels. Cell viability can be maintained high throughout the course of the cultivation and product concentration and quality are also typically consistent.

Variables such as bioreactor pH and dissolved oxygen (DO) have set points that are established in process optimization experiments. While operation at these set points is desirable, process control systems are not ideal and small deviations around the set point are frequent. These fluctuations help define the normal operating range (Figure J.1) which is typically set at 2 – 3 standard deviations of typical variations [3]. Occasionally, variables can drift outside the normal operating range and a maximum operating range must be defined over which product quality is not impacted. These subsequently become the variable specifications and the process must be operated within these ranges for product release. When variables deviate from the maximum operating range, the product cannot be released unless comprehensive additional investigations confirm no adverse impact on

[1] A version of this chapter will be submitted for publication. Goudar, C.T., Piret, J.M. and Konstantinov, K.B. (2006). Applications of QRT-MFA for mammalian culture process development and commercial manufacturing.

product quality. Finally, there is an edge of failure outside which the process is severely compromised and from which recovery is usually not possible.

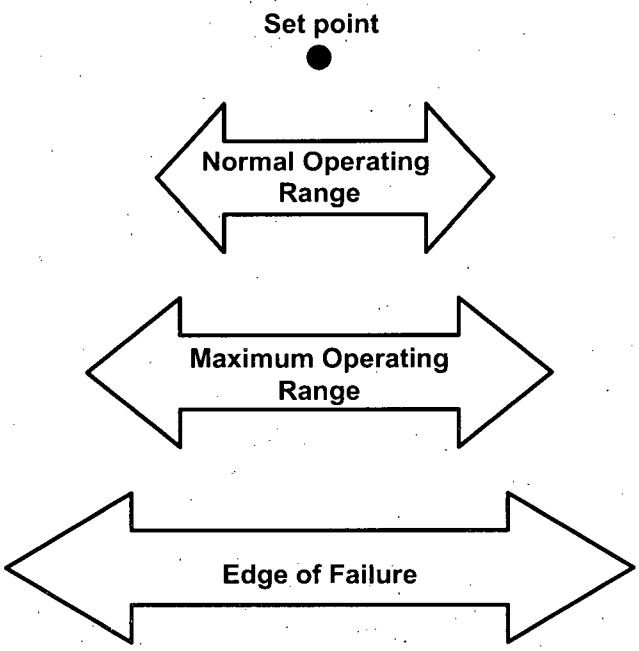

Figure J.1: Ranges of variables such as pH and dissolved oxygen in a perfusion bioreactor. Adapted from [3].

Variable ranges and edges of failure must be established before the process is transferred to clinical material production and commercial manufacturing. Experiments to establish these ranges are typically performed in laboratory-scale bioreactors during late stage process development after variable set points have been established [3, 4]. The testing duration at variable range extremes must be determined and this is challening for perfusion systems given their long operation times. Stabilization of cell growth and metabolism have been used as indicators of steady-state following a change [5] and for a perfusion system, these are often in excess of a week. Thus examination of multiple variable extremes requires extended cultivation times slowing down the process development and transfer process. Simultaneous examination of multiple effects is one approach to reducing development time and the effect of low glucose and high pCO_2 were concurrently examined for CHO cells in perfusion culture [6]. Another approach is scanning non-steady-state responses where it was shown that third day transient values were similar to those when pseudo-steady-state was reached [7]. Given the substantial reduction in development time, a similar approach was used in this study

and variable extremes were evaluated over a period of 48 hours.

Specific protein productivity and protein quality are the primary response parameters that are monitored when variable ranges are explored. Cell growth and specific nutrient consumption and metabolite production are also monitored at the range extremes and some changes in them are usually acceptable as long as product quality is not adversely impacted. The information content in these classical range finding studies can be enhanced with quantitative information on cell metabolism at the range extremes. Albeit of secondary importance when compared with product quality, improved understanding of the cell physiological state rovides additional evidence for establishing process ranges. Moreover, if process deviations outside the maximum operating range do occur, a detailed understanding of cellular metabolism can help investigations that ultimately result in product release.

Metabolic flux analysis provides a framework to obtain quantitative physiological information when nutrient and metabolite specific rate data are available [8]. Rapid flux estimation is possible through quasi real time metabolic flux analysis (QRT-MFA) and is especially attractive because rapid feedback on cell metabolism can be used to characterize the transient phases that accompany variable changes. This improved understanding of metabolism can influence range selection as dramatic variations in the cell physiological state are not desirable even if they are not accompanied by reduced productivity or deterioration of protein quality.

The effect of pH or DO changes on cell metabolism and protein productivity were examined in this study which was aimed at exploring their edges of failure. The pH and DO set points were varied over the course of a perfusion cultivation and the resulting growth, metabolism and productivity responses were characterized. This information was used to determine if the operating ranges examined were indeed the maximum possible for this process.

J.2 Materials and Methods

J.2.1 Cell Line, Medium and Cell Culture System

BHK cells were cultivated in perfusion mode with glucose and glutamine as the main carbon and energy sources. Experiments were conducted in a 15 L bioreactor (Applikon, Foster City, CA) with a 12 L working volume. The temperature was maintained at 35.5 °C and the agitation at 70 RPM. Under standard conditions, the dissolved oxygen (DO) concentration was maintained at 50% air saturation using an oxygen-nitrogen mixture that entered the bioreactor through a silicone membrane. The pH was maintained at 6.8 by the automatic

addition of 0.57 M Na_2CO_3. The bioreactor was inoculated at an initial cell density of 11.7 x 10^6 cells/mL and cells were allowed to accumulate to a steady-state concentration of 20 x 10^6 cells/mL. The steady-state cell density was maintained by automatic cell bleed from the bioreactor.

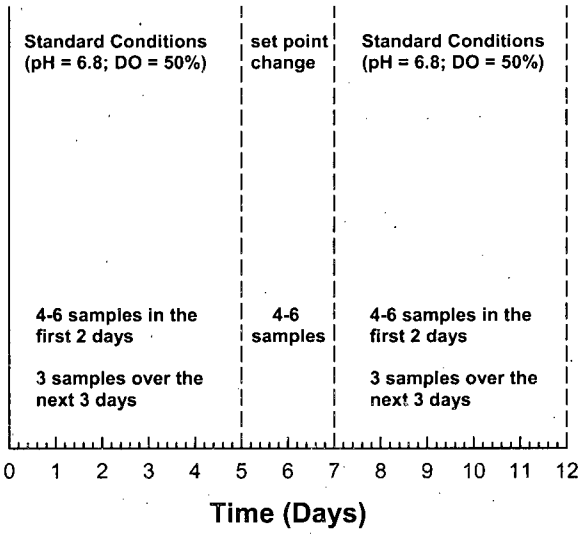

Figure J.2: Sequencing and sampling of the experimental procedure in this study. A total of 4 set point changes (pH = 6.6 and 7.0; DO = 0 and 150%) were examined in a 38 day perfusion cultivation

Once steady-state was reached, bioreactor pH and DO were varied to evaluate cellular responses to these changes. The low pH value was 6.6 and the high was 7.0 while DO values of 0 and 150% air saturation were investigated. Once a set point change was made, the reactor was operated under these altered conditions for 2 days and was sampled 4 – 6 times during this period to capture transient cellular response to set point change. This 2 day operation allowed approximately 2 population doubling times and was much longer than a typical excursion observed in a manufacturing system. The set points were then reset and the reactor was operated at standard conditions for 5 days. Multiple samples (usually 4 – 6) were taken in the first 2 days followed by daily sampling. The 5 day standard condition cultivation allowed 5 doubling times and was followed by another 2 day period of set point change (Figure J.2). This process was repeated until all experimental conditions were evaluated.

J.2.2 Analytical Methods

Samples from the bioreactor were taken for cell density and viability analysis using the CEDEX system (Innovatis, Bielefeld, Germany). The samples were subsequently centrifuged (Beckman Coulter, Fullerton, CA) and the supernatants were analyzed for nutrient and metabolite concentrations. Glucose, lactate, glutamine and glutamate concentrations were determined using a YSI Model 2700 analyzer (Yellow Springs Instruments, Yellow Springs, OH) while ammonium was measured by an Ektachem DT60 analyzer (Eastman Kodak, Rochester, NY). The pH and DO were measured online using retractable electrodes (Mettler-Toledo Inc., Columbus, OH) and their measurement accuracy was verified through off-line analysis in a Rapidlab® 248 blood gas analyzer (Bayer HealthCare, Tarrytown, NY). The same instrument also measured the dissolved CO_2 concentration. On-line measurements of cell density were made with a retractable optical density probe (Aquasant Messtechnik, Bubendorf, Switzerland), calibrated with CEDEX cell density measurements. Concentrations of oxygen and carbon-dioxide in the exit gas were measured using a MGA-1200 Mass Spectrometer (Applied Instrument Technologies, Pomona, CA).

J.2.3 Specific Rate Estimation

Growth rate, nutrient consumption, metabolite production and specific productivity were calculated from mass balance expressions across the bioreactor and cell retention device. Since bioreactor cell density was held constant by bleeding cells from the bioreactor and death rates not accounted for, the apparent growth rate, μ (1/day), was a function of the bleed rate, F_b (L/day), and the viable cell density in the harvest stream, X_V^H (10^6 cells/mL)

$$\mu = \frac{F_b}{V} + \left(\frac{F_h}{V}\right)\frac{X_V^H}{X_V^B} + \frac{1}{X_V^B}\frac{dX_V^B}{dt} \tag{J.1}$$

where V is the bioreactor volume (L), F_h the harvest flow rate (L/day), X_V^B the bioreactor viable cell density (10^6 cells/mL) and t the time (day). The specific rates of glucose consumption and lactate production were determined from their bioreactor concentrations:

$$q_G = \frac{1}{X_V^B}\left\{\frac{F_h\,(G_\mathrm{m} - G)}{V} - \frac{dG}{dt}\right\} \tag{J.2}$$

$$q_L = \frac{1}{X_V^B}\left\{\frac{F_h L}{V} + \frac{dL}{dt}\right\} \tag{J.3}$$

where q_G and q_L are the specific glucose consumption and lactate production rates, respectively, (pmol/cell-day), G_{m} the glucose concentration in the fed medium (mM), G and L their bioreactor concentrations (mM). The expression for specific protein productivity is analogous to that for lactate production.

J.2.4 Metabolic Flux Estimation

A biochemical network previously developed for hybridoma cell cultivation in 24 well plates [9] was used in this study. This is a simplified representation of metabolism and includes fluxes through glycolysis, the TCA cycle and oxidative phosphorylation. The stoichiometric matrix for this reaction network was of full rank with a low condition number of 7.6 indicating that flux estimates were not overly sensitive to specific rate variations. Metabolic fluxes were estimated using weighted least squares

$$\mathbf{x} = \left(\mathbf{A}^{\mathrm{T}}\psi^{-1}\mathbf{A}\right)^{-1}\mathbf{A}^{\mathrm{T}}\psi^{-1}\mathbf{r} \tag{J.4}$$

where $\mathbf{x}$ is the flux vector, $\mathbf{A}$ the stoichiometric matrix, $\mathbf{r}$ the rate vector and ψ the variance-covariance matrix of $\mathbf{r}$.

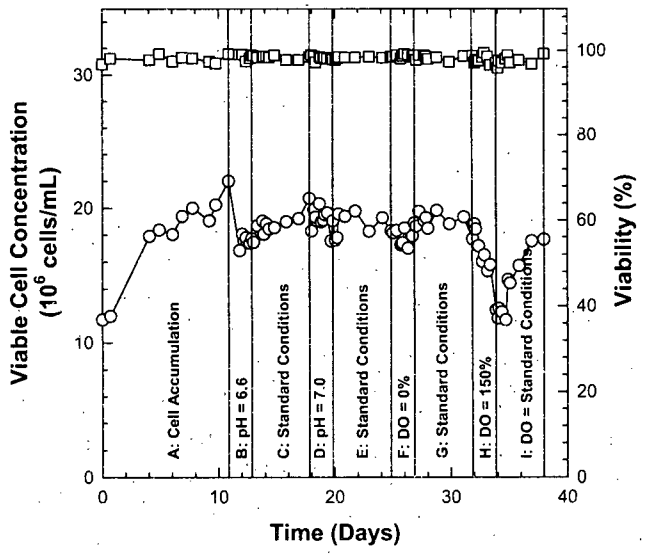

Figure J.3: Time courses of bioreactor viable cell concentration (○) and viability (□) for conditions A – I in the 38 day perfusion cultivation.

J.3 Results

J.3.1 Cell Growth and Viability

Time courses of bioreactor viable cell density and viability are shown in Figure J.3 for experimental conditions A – I. The target cell density was 20 x 10^6 cells/mL and average cell densities were within 10% of the target for all conditions except when the DO was 150% (condition H). Increasing the DO to 150% caused a sharp decrease in growth rate lowering cell density to 12.4 x 10^6 cells /mL at the end of condition H. Cell growth recovered 24 hours after reducing DO to the standard 50% in condition I, reaching a final value of 17.9 x 10^6 cells/mL at day 38. Growth rate reductions on the order of 20 – 30% were also seen when the pH was reduced to 6.6 (condition B) but were not substantial enough to decrease bioreactor cell density. Despite the substantial reduction in growth at 150% DO, cell viability was not affected and was >95% over the entire length of the cultivation (Figure J.3).

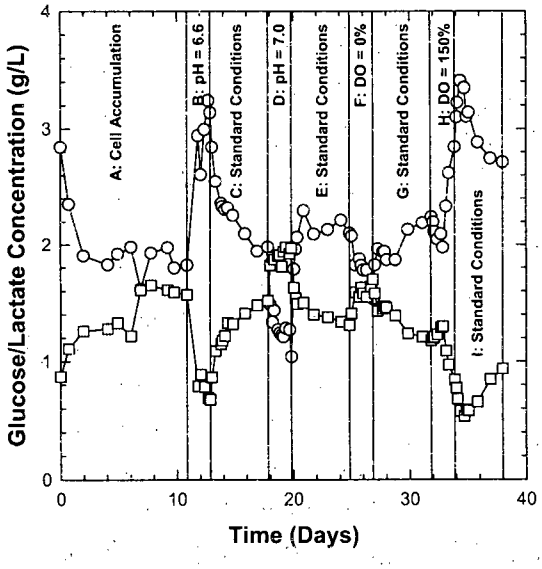

Figure J.4: Time courses of bioreactor glucose (◯) and lactate concnetrations (□) for conditions A – I in the 38 day perfusion cultivation.

J.3.2 Residual Glucose and Lactate Concentrations

Reducing pH from 6.8 to 6.6 reduced lactate concentration from 1.61 ± 0.03 g/L (mean ± standard deviation for last 4 data points in condition A) to 0.76 ± 0.10 g/L towards the end

of condition B (Figure J.4). This was accompanied by a glucose concentration increase to 3.0 ± 0.28 g/L from 1.88 ± 0.08 g/L. Lactate and glucose concentrations rapidly increased and decreased, respectively, when standard conditions (pH = 6.8) were restored (Condition C). Increasing pH from 6.8 to 7 in condition D increased lactate concentration from 1.43 ± 0.09 to 1.95 ± 0.03 g/L while the associated glucose concentration decreased from 2.07 ± 0.14 to 1.20 ± 0.11 g/L. Both changes were reversible when the pH was reduced to 6.8 in condition E. Reducing DO to 0% in condition F caused an increase in lactate concentration from 1.36 ± 0.04 g/L at the end of condition E to 1.62 ± 0.07 g/L at the end of condition F. This was accompanied by an increase in glucose concentration indicating increased glucose uptake and lactate production when oxygen was limiting. Increasing DO to 150% resulted in substantial decrease in the lactate concentration and this was primarily due to cell density reduction in condition H (Figure J.3). Glucose and lactate concentrations recovered after reducing DO to the standard 50% (condition I) but were still quite different from those at the end of condition G. It is possible that more time was necessary for the cells to reach a metabolic state similar to that in condition A, if this was at all possible.

J.3.3 Effect of pH Changes on Metabolic Fluxes

Time profiles of the glycolytic, lactate and TCA cycle fluxes are shown in Figure J.5a for conditions A - C. Substantial decreases are seen for all fluxes when the pH was reduced to 6.6 (condition B) and the values recovered after the pH was increased to 6.8 in condition C. Average flux values from the last 4 data points of each condition and their associated standard deviations are shown in Figure J.5b. Results from a t-test indicated a statistically significant difference ($p<0.05$) for the glycolytic and TCA cycle fluxes across conditions A and C. Increasing pH to 7.0 in condition D resulted in flux increases (Figure J.6a) and this change was reversible once the pH was reduced to 6.8. Average flux values for conditions C - E are shown in Figure J.6b and there was no statistically significant difference ($p<0.05$) in all three fluxes across conditions C and E. Cellular metabolism, while substantially affected by pH increase, returned to levels prior to pH increase suggesting that pH increase over a 48 hour period had no long-term impact on cell metabolism.

Metabolic responses to pH changes were rapid. The bioreactor was sampled 23 hours after reducing pH to 6.6 by which time the glycolytic, lactate and TCA fluxes were down to 3.1, 5.7 and 0.5 pmol/cell-d, respectively, from values of 6.5, 9.5 and 3.5 pmol/cell-d at the end of condition A (Figure J.5a). When the reactor was sampled 4 hours after increasing the pH to 6.8 (condition C) all 3 fluxes were substantially higher and continued to increase in the 24 hour period following the pH increase. Flux values stabilized in the subsequent

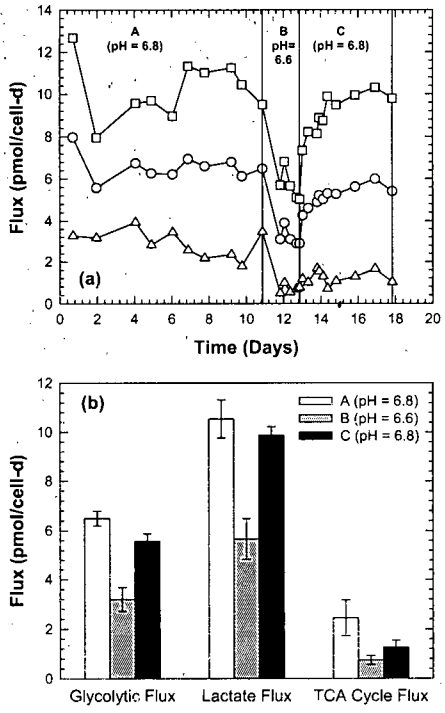

Figure J.5: Effect of pH reduction on cell metabolism. Panel (a) contains time profiles of glycolytic (○), lactate (□) and TCA cycle (△) fluxes for conditions A – C. Average flux values over the last 4 data points of each condition are shown in panel (b) along with their standard deviations.

24 hours (Figure J.5a) and these were considered representative of condition C and used to compute the average values in Figure J.5b. Similar rapid metabolic responses were seen when the pH was increased to 7.0 followed by a decrease to 6.8 (Figure J.6a). A 48 hour period (~2 population doublings) was thus adequate for cell metabolism to adjust to the new pH set point.

J.3.4 Effect of DO Changes on Metabolic Fluxes

Reducing bioreactor DO to 0% (condition F) resulted in an increase in the glycolytic and lactate fluxes while the TCA cycle flux was substantially reduced (Figure J.7) There was a finite TCA cycle flux at 0% DO and this was because oxygen was still being supplied to the system at a rate that was lower than that required by the cells. The glycolytic and lactate fluxes decreased when the DO was increased back to the standard 50% (condition G) while that for the TCA cycle increased. There was no statistically significant difference

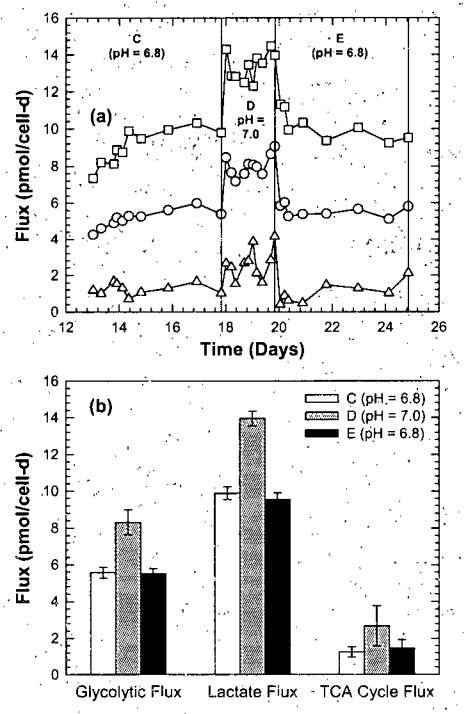

Figure J.6: Effect of pH increase on cell metabolism. Time profiles of of glycolytic (◯), lactate (□) and TCA cycle (△) fluxes are shown in panel (a) for conditions C – E. Average flux values over the last 4 data points of each condition are shown in panel (b) along with their standard deviations.

between conditions E and G for the glycolytic and lactate fluxes. The TCA cycle fluxes for conditions E and G were however, significantly different. DO increase to 150% (condition H) resulted in an increase in all 3 fluxes over the first 24 hours followed by a substantial decline over the next 24 hours (Figure J.8a). This decline extended well into condition I where the DO was reduced to 50%.

Unlike other changes, the DO increase to 150% caused a substantial decrease in the growth rate resulting in a cell density decline (Figure J.3). The cell density decline in the second half of condition H and a gradual increase in condition I is similar to the flux trends in Figure J.8a. Flux recovery following 150% DO was the slowest among the 4 set point changes examined and was also not complete. There was a statistically significant difference ($p < 0.05$) in all 3 flux averages for conditions G and I (Figure J.8b) indicating that a 5 day period following a DO set point of 150% was not adequate to restore cell metabolism to previous levels. While further cultivation may have caused metabolism to reach levels

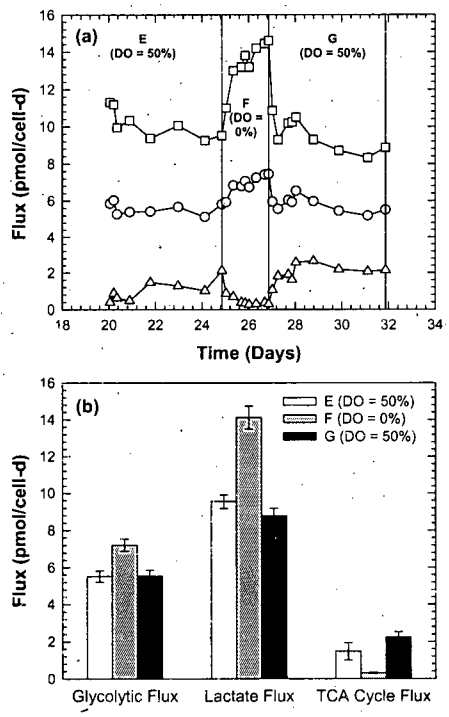

Figure J.7: Effect of DO decrease on cell metabolism. Time profiles of of glycolytic (○), lactate (□) and TCA cycle (△) fluxes are shown in panel (a) for conditions E – G. Average flux values over the last 4 data points of each condition are shown in panel (b) along with their standard deviations.

prior to DO increase, this was not verified in this study.

J.3.5 Cell Size Variation

Cell size was also affected by pH and DO changes (Figure J.9) with pH reduction to 6.6 resulting in a diameter decrease over the first 24 hours that subsequently increased. Increasing pH to 7.0 resulted in a diameter increase which was lowered when the pH was reset to 6.8. A slight diameter decrease was seen at 0% DO while a substantial diameter increase (~2 μm) was seen when the DO was increased to 150% (Figure J.9). Results from the Tukey-Kramer test indicated no significant difference ($p<0.05$) among the control conditions A, C, E and G (condition I was significantly different). Average diameter for condition B (pH=6.6) was not significantly different than conditions A and C while that for condition D (pH = 7.0) was significantly different from condition E but not condition C. Diameter change at 0% DO (condition F) was not significantly different than standard conditions E and G while

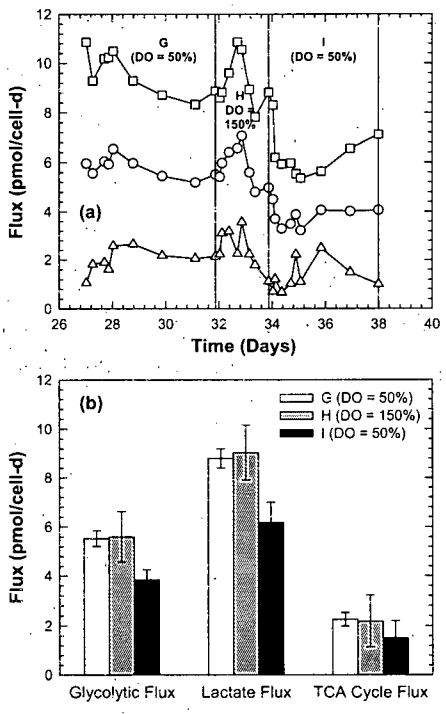

Figure J.8: Effect of DO increase on cell metabolism. Time profiles of of glycolytic (○), lactate (□) and TCA cycle (△) fluxes are shown in panel (a) for conditions G – I. Average flux values over the last 4 data points of each condition are shown in panel (b) along with their standard deviations.

the diameter at 150% DO (condition H) was significantly higher than standard condition G. Overall, pH and DO increases had the most impact on cell diameter and the increases in both cases were significant ($p < 0.05$) compared to one standard condition immediately before or after.

J.3.6 Specific Productivity and Protein Quality

Given the significant variation in cell density, especially for conditions H and I (Figure J.3), product concentrations were normalized to a cell density of 20 x 10^6 cells/mL and are shown in Figure J.10. For the most part, product concentrations were remarkably steady (assay variation is 10 – 15%) despite the substantial metabolic shifts over the course of the experiment (Figures J.5 - J.8). There was no statistically significant difference in product concentration ($p < 0.05$) between the control (condition A) and conditions B – I by the Dunnett's method. When all pairs were compared by the Tukey-Kramer method, condition

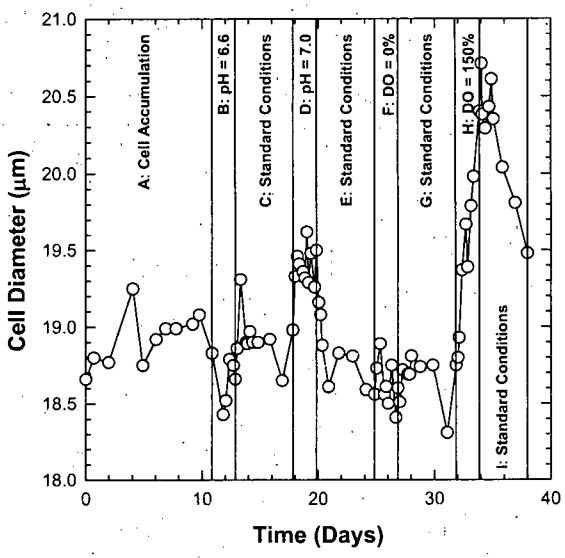

Figure J.9: Effect of pH and DO changes on cell diameter.

H (DO = 150%) was significantly different than conditions B, E, F, G and I. Since condition H was between the conditions G and I and was significantly lower than both of them, we can infer that exposure to 150% DO results in a statistically significant productivity decline. This deduction, however, is not definitive since there was no statistically significant difference between condition H and condition A, the control at the beginning of the experiment.

Figures J.11 - J.13 show protein western blots over the course of the experiment. The last two samples from each experimental condition were analyzed since they would be the most representative of each culture condition. For the standard conditions C, E, G and I that were each of 120 hour duration, the two samples were 116 and 120 hours following the switch to standard conditions while for the test conditions B, D, F and H, the samples were 44 and 48 hours following the transition. Similar banding patterns were seen for the standard and pH = 6.6 and pH = 7.0 conditions in Figure J.11. Perhaps the only difference was the reduced intensity of the lower molecular weight band at pH = 7.0. Banding patterns at DO = 0% were also similar to the standard (Figure J.12) while the lower molecular weight band intensity in standard condition sample E1 was lower than that at DO = 0%. The effect of DO = 150% on protein quality is illustrated in Figure J.13 where condition H is compared with standard conditions G and I. The band intensities were the lowest for samples H1 and H2 and this is because these lanes were loaded with ~30% less protein.

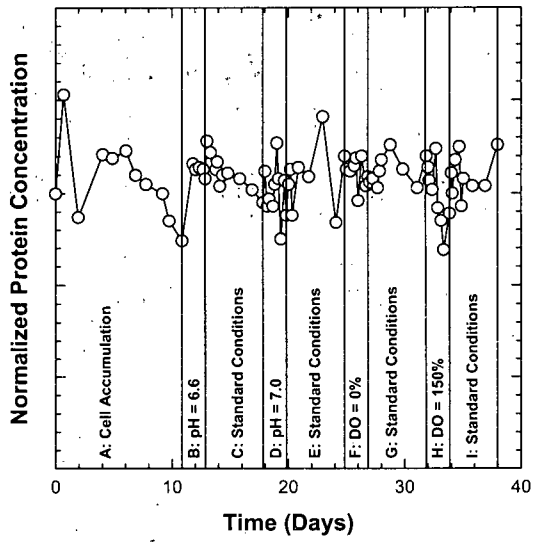

Figure J.10: Time profile of product concentration.

While some degradation of the high molecular weight band was seen for all samples tested, similar degradation was also seen in the reference standard. (Figures J.11 – J.13). We can thus conclude that the pH and DO ranges examined had minimal impact on protein productivity and quality. This is a rather remarkable result given the substantial metabolic changes that resulted from pH and DO variations.

J.4 Discussion

J.4.1 Effect of pH on Metabolism

Mammalian cell growth and metabolism are pH dependent. Reduction of bioreactor pH from 7.6 to 6.8 reduced hybridoma growth, glucose consumption and lactate production in batch culture [10] and similar results were also seen for both batch and continuous culture of hybridoma cells [11]. It has been shown that intracellular pH (pH_i) is lowered when the extracellular (bioreactor) pH is reduced [12] and this cytoplasmic acidification can significantly alter metabolism. A pH_i reduction of 0.2 units has been shown to significantly reduce the glycolytic flux [10, 13] consistent with the observations in this study (Figure J.5).

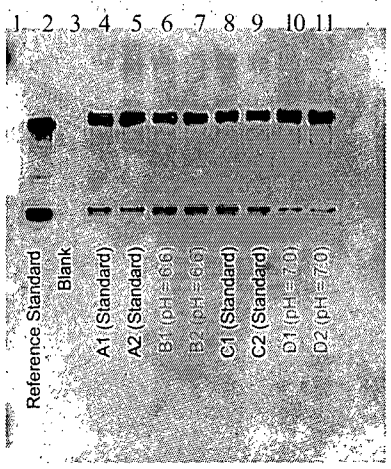

Figure J.11: Western blot for experimental conditions A – D. The last 2 samples from each experimental condition were analyzed such that the two standard condition samples (A1, A2 or C1, C2) were 116 and 120 hours after set point change while those for the test conditions (B1, B2 or D1, D2) were after 44 and 48 hours.

J.4.2 Effect of DO on Metabolism

In most studies to date, low DO (<1%) has been associated with decrease in cell growth and oxygen uptake while glucose uptake and lactate production rates were higher. For mouse LS cells in batch culture, oxygen uptake rate, cell growth and maximum cell density were lowest at DO = 1% while lactate production was the highest [14]. An analysis of the enzyme levels at low DO concentration indicated low levels of isocitrate dehydrogenase and aldolase, and high levels of lactate dehydrogenase [15], indicating a decrease in enzymes involved in terminal respiration and an increase in those associated with glycolysis and the hexose-monophosphate pathway. For hybridoma cells in continuous culture, oxygen uptake rate decreased for DO < 10% and was relatively constant when DO was between 10 and 100% [16]. Low DO concentration also resulted in higher glucose consumption and lactate production rates while glutamine consumption was reduced. In another hybridoma chemostat cultivation [17], DO < 5% was accompanied by reduction in cell growth rate and oxygen uptake while glucose consumption and lactate production rates were higher. Metabolic flux analysis on hybridoma cells in continuous culture indicated a decrease in NAD(P)H-producing fluxes at low DO concentration [18]. Our observation of increased glycolytic and lactate fluxes and reduced TCA cycle fluxes at DO = 0% are thus consistent with those reported previously.

While a few reports indicate high DO (> 100%) tolerance of mammalian cells [19–21],

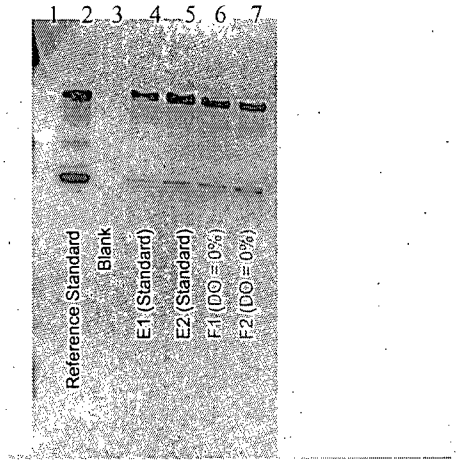

Figure J.12: Western blot for experimental conditions E and F. The last 2 samples from each experimental condition were analyzed such that the two standard condition samples (E1 and E2) were 116 and 120 hours after set point change while those for the test conditions (F1 and F2) were after 44 and 48 hours.

most other studies have observed reduced cell growth [15, 17, 22]. High DO can enhance the formation of reactive oxygen species that can damage DNA, proteins and lipids. A gradual increase in DNA breakage was seen when hybridoma cells were exposed to 200 - 476% DO [23]. It is possible that similar mechanisms were responsible for growth rate reduction and hence the substantial decrease in cell density when the DO was increased to 150% (Figure J.3). High DO however, did not cause a decrease in cell viability.

J.4.3 QRT-MFA Application to Bioprocess Development

The metabolic changes observed as a consequence of pH and DO variation provide additional information to establish operating ranges for these variables. While operating ranges are typically defined such that protein productivity and quality are not impacted, metabolic changes must also be considered and this data is obtained from flux analysis. While minimal impact of pH changes on protein productivity and quality was detected (Figures J.10 – J.13), the metabolic changes were substantial (Figures J.5 –J.8) and must be considered for establishing pH and DO ranges. While the reversibility of the physiological state following a 48 hour exposure to the range extremes reduces the concern, a DO value of 150% cannot serve as a viable upper limit of the maximum operating range in a perfusion system given the substantial decrease in growth rate (This would limit the maximum cell density that can be achieved in a perfusion cultivation). Moreover, the diameter increase at high DO is

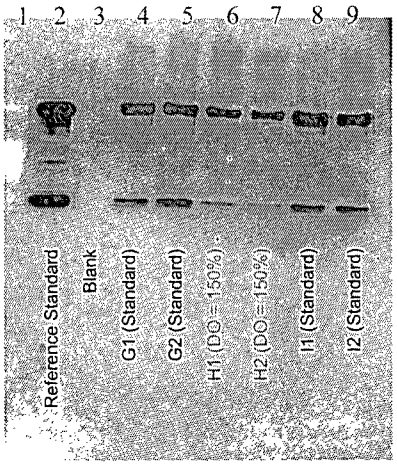

Figure J.13: Western blot for experimental conditions G – I. The last 2 samples from each experimental condition were analyzed such that the two standard condition samples (G1, G2 or I1, I2) were 116 and 120 hours after set point change while those for the test conditions (H1, H2) were after 44 and 48 hours.

a stress response that is undesirable. Similarly, operation at 0% DO virtually shuts down the TCA cycle activity and cannot serve as a viable low limit for DO. Both 0 and 150% DO would classify as beyond the edges of failure despite minimal adverse effects on protein productivity and quality. It is very likely that long term exposure (>5 days) to these extreme DO values will adversely impact productivity and this will be verified in future investigations.

The pH values of 6.6 and 6.8 can serve as maximum operating ranges instead of edges of failure. While growth rate did decrease at pH = 6.6, this reduction did not impact bioreactor cell density. Reduction in glucose consumption and lactate production (Figure J.5) is desirable as long as this metabolic shift has no adverse impact on protein productivity and quality which was indeed the case (Figures J.10 and J.11). The increase in metabolic activity at pH = 7.0 has implications for medium design given the increased demand for nutrients and the high lactate production rate could be a concern for low perfusion rate cultivations. However, these shifts do not classify pH 7.0 as an edge of failure but more as an upper limit of the maximum operating range. It must be recognized that long term cultivation at pH 6.6 and 7.0 and more detailed product quality analysis are necessary to ensure that the observations from this study can be reproduced over extended cultivation times. Thus a combination of protein productivity and quality analysis coupled with information on the cell physiological state can help establish rational ranges for important

process variables in a perfusion cultivation.

J.5 Conclusions

In an attempt to augment conventional variable range studies with physiological information, metabolic flux analysis was used to characterize cell metabolism when bioreactor pH and DO were varied between 6.6 – 7.0 and 0 – 150%, respectively. While substantial metabolic changes were seen at these extreme conditions, the changes were reversible when these variables were restored to set points. The most adverse impact was seen at 150% DO with the largest growth rate reduction and the longest metabolic recovery time. For all other cases, metabolism recovered to levels prior to set point changes within 24 hours, and in most cases, there were no statistically significant metabolic changes before or after set point changes suggesting physiological state reversibility. Surprisingly, productivity and product quality were not affected despite the major central carbon metabolism changes. The exposure time to pH and DO extremes in this study was 48 hours and extended exposure could irreversibly affect metabolism and negatively impact productivity and product quality. Moreover, additional studies are required at intermediate variable values (for instance DO in increments of 20% in the 10 - 130% range; pH in increments of 0.1 in the 6.5 – 7.1 range) to comprehensively map cellular response to variable changes. This information coupled with the findings from this study can help establish a maximum operating range for the perfusion process enabling smooth transfer to clinical manufacturing and commercial production.

Bibliography

[1] Chuppa, S.; Tsai, S.; Yoon, S.; Shackelford, S.; Rozales, C.; Bhat, R.; Tsay, G.; Matanguihan, R.; Konstantinov, K.; Naveh, D. Fermentor temperature as a tool for control of high-density perfusion cultures of mammalian cells. *Biotechnol. Bioeng.*, **1997**, *55*, 328–338.

[2] Trampler, F.; Sonderhoff, S.; Pui, P.; Kilburn, D.; Piret, J. Acoustic cell filter for high density perfusion culture of hybridoma cells. *Bio/Technology*, **1994**, *12*(3), 281–284.

[3] Gardner, A.; Smith, T. in *Biopharmaceutical Process Validation*, Sofer, G.; Zabriskie, D., Eds., p 382. Marcel Dekker, New York, NY, 2000.

[4] Adamson, S.; Leonard, M.; Drapeau, D.; Harrison, S.; O'Connell, B.; Charlebois, T.

in *Biopharmaceutical Process Validation*, Sofer, G.; Zabriskie, D., Eds., p 382. Marcel Dekker, New York, NY, 2000.

[5] Follstad, B. D.; Balcarcel, R. R.; Stephanopoulos, G.; Wang, D. I. Metabolic flux analysis of hybridoma continuous culture steady state multiplicity. *Biotechnol Bioeng*, **1999**, *63*(6), 675–83.

[6] Takuma, S.; Hirashima, C.; Piret, J. in *Animal Cell Technology: Basic and Applied Aspects*, Yagasaki, K.; Miura, Y.; Hatori, M.; Nomura, Y., Eds., pp 99–103. Kluwer Academic Publishers, Netherlands, 2004.

[7] Angepat, S.; Gorenflo, V.; Piret, J. Accelerating perfusion process optimization by scanning non-steady-state responses. *Biotechnol. Bioeng.*, **2005**, *92*, 472–478.

[8] Stephanopoulos, G.; Aristodou, A.; Nielsen, J. *Metabolic Engineering. Principles and Methodologies.* Academic Press, San Diego, 1998.

[9] Balcarcel, R. R.; Clark, L. Metabolic screening of mammalian cell cultures using well-plates. *Biotechnol. Prog.*, **2003**, *19*, 98–108.

[10] McQueen, A.; Bailey, J. E. Effect of ammonium ion and extracellular pH on hybridoma cell metabolism amd antibody production. *Biotechnol. Bioeng.*, **1990**, *35*, 1067–1077.

[11] Miller, W.; Blanch, H.; Wilke, C. A kinetic analysis of hybridoma growth and metabolism in batch and continuous suspension culture: Effect of nutrient concentration, dilution rate and pH. *Biotechnol. Bioeng.*, **1987**, *32*, 947–965.

[12] McQueen, A.; Bailey, J. E. Growth inhibition of hybridoma cells by ammonium ion: Correlation with effect on intracellular pH. *Bioprocess Engineering*, **1990**, *6*, 49–61.

[13] Fidelman, M.; Seeholzer, S.; Walsh, K.; Moore, R. Intracellular pH mediates action of insulin on glycosysis in frog skeletal muscle. *Am. J. Physiol.*, **1982**, *242*, C87–C93.

[14] Kilburn, D.; Lilly, M.; Self, D.; Webb, F. The effect of dissolved oxygen partial pressure on the growth and carbohydrate metabolism of mouse LS cells. *J. Cell Sci.*, **1969**, *4*, 25–37.

[15] Self, D.; Kilburn, D.; Lilly, M. The influence of dissolved oxygen partial pressure on the level of various enzymes in mouse LS cells. *Biotechnol Bioeng*, **1968**, *10*, 815–828.

[16] Miller, W.; Wilke, C.; Blanch, H. Effects of dissolved oxygen concentration on hybridoma growth and metabolism in continuous cultures. *J. Cell. Physiol.*, **1987**, *132*, 524–530.

[17] Ozturk, S.; Palsson, B. Effects of dissolved oxygen on hybridoma cell growth, metabolism, and antibody production kinetics in continuous culture. *Biotechnol. Prog.*, **1990**, *6*, 437–446.

[18] Bonarius, H.; Houtman, J.; Schmid, G.; C.D., d. G.; Tramper, J. Metabolic-flux analysis of hybridoma cells under oxidative and reductive stress using mass balance. *Cytotechnology*, **2000**, *32*, 97–107.

[19] Frank, L.; Iqbal, J.; Hass, M.; Massaro, D. New rest period protocol for inducing tolerance to high O2 exposure in adult rats. *Am. J. Physiol.*, **1989**, *257*, 226–231.

[20] Oller, A.; Buser, C.; Tyo, M.; Thilly, W. Growth of mammalian cells at high oxygen concentrations. *J. Cell Sci.*, **1989**, *14*, 43–49.

[21] van der Valk, P.; Gille, J.; Oostra, A.; Roubous, E.; Sminia, T.; Joenje, H. Characterization of any oxygen-tolerant cell line derived from Chinese Hamster Ovary cells. *Cell Tissue Res.*, **1985**, *239*, 61–68.

[22] Jan, D.; Petch, D.; Huzel, N.; Butler, M. The effect of dissolved oxygen on the metabolic profile of a murine hybridoma grown in serum-free medium in continuous culture. *Biotechnol. Bioeng.*, **1997**, *54*, 153–164.

[23] Cacciuttolo, M.; Trinh, L.; Lumpkin, J.; Rao, G. Hyperoxia induces DNA damage in mammalian cells. *Free Radical Biol. and Med.*, **1993**, *14*, 267–276.